Jörg Peter Dietrich

Combined Weak Lensing and X-Ray Search for Galaxy Clusters
and the Filaments Connecting Them

Dissertation

Jörg Peter Dietrich

Combined Weak Lensing and X-Ray Search for Galaxy Clusters
and the Filaments Connecting Them

Erster Gutachter: Prof. Dr. Peter Schneider
Zweiter Gutachter: Priv-Doz. Dr. Axel Schwope
Tag der Prüfung: 12.7.2006

Diese Dissertation ist auf dem Hochschulschriftenserver der ULB Bonn
`http://hss.ulb.uni-bonn.de/diss_online/` elektronisch
publiziert.

Bonn 2006

Contents

Contents

Introduction

Our understanding of the Universe has made great progress in the last decade. From the first unambiguous detection of a non-negative cosmological constant (Riess et al. 1998; Perlmutter et al. 1999) to the recent 3 year data release of the Wilkinson Microwave Anisotropy Probe (WMAP) satellite a consistent standard model of cosmology is emerging. This concordance cosmology is supported by a number of cosmological probes; some of these are the already mentioned observations of type Ia supernovae as distance indicators and anisotropies of the cosmic microwave background, large cosmological redshift surveys such as the 2dF (Colless et al. 2001) and the Sloan Digital Sky Survey (SDSS, Abazajian et al. 2003), the first detection of cosmological weak lensing (Bacon et al. 2000; Van Waerbeke et al. 2000; Wittman et al. 2000) and numerous later confirmations (e.g., Semboloni et al. 2005; Hoekstra et al. 2005), and measurement of the cosmological power spectrum from the Lyman-α forest (Croft et al. 1998; Gnedin & Hamilton 2002) to only name a few.

While the agreement of such different methods, based on very different physics and emanating from widely different cosmological epochs is overwhelming, we have at the moment no fundamental physical understanding of our Universe. In the current cosmological concordance model, matter in the Universe is dominated by non-baryonic *dark matter* which can only be accounted for in extensions of the standard model of particle physics and which has not been observed in any laboratory on Earth. The total energy content of the Universe is dominated by something often called *dark energy*,

which may be Einstein's cosmological constant and which is equated with the energy of the vacuum. We have no viable model that is able to explain the size of the dark energy.

Given this unsatisfactory state of the art further rigorous tests of the predictions of the concordance model and new experiments aiming at understanding the nature of dark matter and dark energy are needed. Many of these experiments will rely on wide-field imaging surveys. Some of these surveys like the SDSS and the CFHT legacy survey are underway, others like the Kilo-Degree Survey (KIDS) and the Dark Energy Survey (DES) are scheduled to start in the foreseeable future. These surveys generate data volumes and types that are new in astronomy and require new handling and reduction strategies. The thesis presented here aims to make a modest contribution to the areas of automatic data reduction of wide-field images and tests of the standard cold dark matter (CDM) model.

After a *tour de force* through cosmology from the geometry of our Universe to the mass function of galaxy clusters (Chap. 1), I will briefly review the foundations and some techniques of weak gravitational lensing (Chap. 2) used in later Chapters. The technical and scientific results of my work are presented in Chaps. 3–6.

- Chapter 3 presents an outline of the functionality of the "Garching-Bonn Deep Survey" (GABODS) image reduction pipeline, which I co-developed during the work presented here. This Chapter concentrates on my contributions to the pipeline, most notably the nearly fully automated photometric calibration of images. The pipeline as a whole is described in Erben et al. (2005); details about the photometric calibration of coadded images are published in Hildebrandt et al. (2006).

- Chapter 4 aims to provide observational proof for a CDM prediction. In the standard scenario of cosmic structure formation matter collapses into a "web" of sheets and filaments and galaxy clusters form at the nodes of this cosmic web. While this filamentary structure has been observed in galaxy redshift surveys for a long time, no direct evidence for filaments of dark matter has been found so far. I studied the double cluster system Abell 222/223 with the aim of directly mapping

a dark matter filament between the two galaxy clusters. This work was published in Dietrich et al. (2005).

– Chapter 5 presents data obtained during the Xmm-Newton Follow-Up Survey, a public eso survey, conducted on deep public Xmm-Newton fields, with a private extension. I describe in detail the reduction and calibration of the public data. These data, in the form of fully reduced and calibrated images and single passband catalogs, were made available to the world-wide astronomical community. This data release is described in Dietrich et al. (2006). The data release paper also contains a detailed quality assessment of the gabods pipeline described in Chap. 3. Besides the data release, this Chapter also contains a short description of the reduction of the private survey extension.

– The mass function of galaxy clusters is a sensitive cosmological probe of various cosmological parameters, including the evolution of dark energy (Wang & Steinhardt 1998). Studying the mass function in detail requires good knowledge of cluster masses and possible selection biases in constructing a catalog of galaxy clusters. Comparison of the selection function and the cluster masses obtained with different methods is thus an essential step towards a high-precision determination of the equation of state of the dark energy. Using the Xmm-Newton Follow-Up Survey I construct catalogs of galaxy cluster candidates with three different selection methods in Chap. 6: Optical matched filter, X-ray, and weak gravitational lensing. The resulting catalogs will provide a solid foundation for studying possible biases in either selection methods. This work will be submitted for publication to Astronomy and Astrophysics.

I conclude with a summary and an outlook.

It is clear from the outline above that this thesis touches on a very wide variety of topics and methods. Chapters 3 and 5 are more of technical nature; Chapters 4 and 6 concentrate on scientific questions. The combination of X-ray and optical data inevitably means that the reduction of both kinds of data must be described; weak lensing, although by now more than 10 years

old, is still not a standard technique that can be used by anyone as readily as, e.g., photometry or spectroscopy.

Providing a thorough introduction to all techniques and methods would blow the volume of this thesis out of proportion. I therefore decided to keep any introductory material and technical descriptions to a minimum and rather provide references to introductory material where necessary. The obvious exception are those parts that are technical by their nature.

1

Cosmological Framework

The observations and effects described in this thesis take place on large scales and thus the effects of space-time curvature and cosmological expansion must be taken into account. This is a complex and wide field and a full treatment is considerably beyond the scope of this work. Several good books on this matter are available, e.g., Peebles (1993) and Peacock (1999). In the following outline of the cosmological framework used in following chapters I will review the Friedmann-Lemaître-Robertson-Walker (FLRW) cosmological model.

1.1 The Homogeneous Universe

1.1.1 Dynamics of the Expansion

Fundamental to the FLRW model are the postulates that (1) the matter distribution is isotropic on sufficiently large scales and that (2) the Universe is homogeneous, i.e., that every comoving observer sees the same history of the Universe. The geometry of an FLRW Universe with spherical coordinates (r, θ, φ) is described by the Robertson-Walker metric

$$ds^2 = c^2 dt^2 - a^2(t) \left[dr^2 + f_K^2(r) (d\theta^2 + \sin^2 d\varphi) \right] , \tag{1.1}$$

where $a(t)$ is a scale factor, normalized such that at the present epoch t_0 $a_0 \equiv a(t_0) = 1$, and the functional dependence of $f_K(r)$ on the curvature K of the spatial hypersurface is given by

$$f_K(r) = \begin{cases} K^{-1/2} \sin(K^{1/2} r) & (K > 0) , \\ r & (K = 0) , \\ (-K)^{-1/2} \sinh\left[(-K)^{1/2} r\right] & (K < 0) . \end{cases} \tag{1.2}$$

Because spacetime expands a photon emitted with wavelength λ_e at time t_1 and observed at a later time $t_2 > t_1$ is redshifted, i.e., observed with a different wavelength λ_{obs}, given by

$$1 + z = \frac{a(t_2)}{a(t_1)} = \frac{\lambda_{obs}}{\lambda_e} \ .$$

(1.3)

Given the curvature, the kinematics of the Universe is completely described by the scale factor $a(t)$. Inserting the metric (1.1) into Einstein's field equations shows that the stress-energy tensor must contain only the terms of a perfect fluid with density $\rho(t)$ and pressure $p(t)$. The field equations then take the simple form of two independent equations,

$$\left(\frac{\dot{a}}{a}\right)^2 = \frac{8\pi G}{3}\rho - \frac{Kc^2}{a^2} + \frac{\Lambda}{3} \ ,$$

(1.4)

which is called *Friedmann's equation*, and

$$\frac{\ddot{a}}{a} = -\frac{4\pi G}{3}\left(\rho + \frac{3p}{c^2}\right) + \frac{\Lambda}{3} \ .$$

(1.5)

Equations (1.4) and (1.5) can be combined into the *adiabatic equation*

$$c^2 \frac{d}{dt}\left[a^3(t)\rho(t)\right] + p(t)\frac{da^3(t)}{dt} = 0 \ .$$

(1.6)

This equation can be interpreted as follows: The energy contained in a given comoving volume is proportional to $a^3\rho$. The change with time of this internal energy is equal to the change of volume times the pressure in this volume. Equation (1.6) is thus nothing but the first law of thermodynamics in a cosmological context. Models with the metric given by Eq. (1.1) with scale factors obeying Eq. (1.4) and the adiabatic Equation (1.6) are called *Friedmann-Lemaître* Universes. The constant Λ in Eqs. (1.4) and (1.5) is the *cosmological constant* introduced by Einstein to obtain a static solution by fine-tuning its value. After the expansion of the Universe was discovered this term was dismissed for several decades but nowadays evidence points towards an acceleratedly expanding Universe with $\Lambda > 0$.

The foregoing equations are not sufficient to describe the expansion history of the Universe; knowledge of the equations of state of the various

components contributing to the energy density is necessary. These components are

- radiation, which is important in the radiation-dominated era until matter-radiation equivalence at redshift $z \sim 10^4$ but plays no role after recombination. Its equation of state is $p_r = c^2\rho_r/3$, i.e., $\rho_r \propto a^{-4}$. This equation of state also describes relativistic particles such as light neutrinos. The a^{-4} dependence has the following interpretation: number conservation of radiation particles leads to $\rho_r \propto a^{-3}$, their individual energies are decreased by another factor of a^{-1} due to cosmological redshift;

- non-relativistic matter (called "dust") with random (thermal) velocities $\ll c$ and $c^2\rho \gg p$. Setting the pressure in Eq. (1.6) to $p = 0$, yields $\rho_m \propto a^{-3}$, where the decrease as a^{-3} is again owed to number conservation;

- vacuum energy, the cosmological constant, which is constant in time and thus has the equation of state $p_v = -c^2\rho_v$.

The total energy density and pressure of the Universe are given by the sum of these components

$$\rho = \rho_r + \rho_m + \rho_v = \frac{\rho_{r0}}{a^4} + \frac{\rho_{m0}}{a^3} + \rho_v \,, \quad p = \frac{c^2\rho_r}{3} - c^2\rho_v = \frac{c^2\rho_{r0}}{3a^4} - c^2\rho_v \,, \quad (1.7)$$

where the index '0' denotes the values at the present time. The contribution of radiation is negligible at the present day but was – due to the a^{-4} dependence – much higher at earlier times. At some time in the past radiation and dust equally contributed to the energy density. The scale factor at radiation-matter equality is denoted by a_{eq}. The matter dominating the Universe today is generally believed to be *Cold Dark Matter* (CDM). CDM interacts only via gravitation and possibly the weak interaction and has non-relativistic random velocities at a_{eq}.

1.1.2 Cosmological Parameters

The ratio

$$H(t) = \frac{\dot{a}(t)}{a(t)} \tag{1.8}$$

is called the *Hubble parameter* and gives the expansion rate of the Universe. Its value at the present epoch

$$H_0 = \frac{\dot{a}(t_0)}{a(t_0)} = \frac{\dot{a}_0}{a_0} \tag{1.9}$$

is called the *Hubble constant.* The value of the Hubble constant is $H_0 = 100h$ km s^{-1} Mpc^{-1}, where h parameterizes the uncertainty in our knowledge of the actual value of H_0. The current best value is $h \simeq 0.7$ (Freedman et al. 2001).

The geometry of the Universe depends on its total energy density. Setting $\Lambda = 0$ in the Friedmann Eq. (1.4) and assuming a flat geometry $K = 0$, one sees that the Hubble constant is directly related to the current density of the Universe. This density is called the *critical density*

$$\rho_{\text{crit}} \equiv \frac{3H_0^2}{8\pi G} \ . \tag{1.10}$$

This is a characteristic density which we can use to scale the densities of the individual components and define the following cosmological parameters

$$\Omega_{\text{r}} \equiv \frac{\rho_{\text{r}0}}{\rho_{\text{crit}}} \ , \quad \Omega_{\text{m}} \equiv \frac{\rho_{\text{m}0}}{\rho_{\text{crit}}} \ , \quad \Omega_{\Lambda} \equiv \frac{\rho_{\text{v}}}{\rho_{\text{crit}}} = \frac{\Lambda}{3H_0^2} \ . \tag{1.11}$$

The total density parameter of the Universe can then be defined as

$$\Omega_0 = \Omega_{\text{r}} + \Omega_{\text{m}} + \Omega_{\Lambda} \ . \tag{1.12}$$

Inserting the definitions of the density parameters in Eq. (1.11) into the Eqs. (1.7) and (1.4), the Friedmann equation reads

$$H^2 = H_0^2 \left[\frac{\Omega_{\text{r}}}{a^4} + \frac{\Omega_{\text{m}}}{a^3} - \frac{Kc^2}{a^2 H_0^2} + \Omega_{\Lambda} \right] \ . \tag{1.13}$$

If we evaluate the foregoing equation at the present epoch, i.e., at $a = 1$, we obtain an expression for the curvature,

$$K = (\Omega_{\text{m}} + \Omega_{\Lambda} - 1) \frac{H_0^2}{c^2} \ , \tag{1.14}$$

where we made use of the fact that at the present epoch the contribution of radiation to the energy density is negligible. Inserting this back into Eq. (1.13) yields

$$H^2 = H_0^2 \left[\frac{\Omega_r}{a^4} + \frac{\Omega_m}{a^3} + \frac{(1 - \Omega_0)}{a^2} + \Omega_\Lambda \right] . \qquad (1.15)$$

Recent measurements of the cosmic microwave background (CMB) combined with the 2dF galaxy survey (Colless et al. 2001) and the Lyman-α forest give $\Omega_m = 0.24 \pm 0.04$, $\Omega_\Lambda = 0.73 \pm 0.04$ (Spergel et al. 2003), i.e., we live in a flat or nearly flat Universe.

1.1.3 Distance

The notion of "distance" is not unambiguous in a curved, non-static space-time. Unlike Euclidean space where distance is uniquely defined and all methods to measure a distance are defined to give the same result, various possibilities to define a distance measure exist in general spacetime and their values differ. The most important ones are described below.

A small *comoving distance* δD_c between two close objects is the distance that remains constant with time if these objects only follow the Hubble flow and have no peculiar velocities. In other words, the comoving distance is the distance of the worldlines on a spatial hyper-surface $t = t_0$ between two points comoving with the cosmic flow. In the chosen coordinates this distance is $\delta D_c = \mathrm{d}r$. Because light rays travel on null geodesics we set $\mathrm{d}s = 0$ and obtain $c\mathrm{d}t = -a\mathrm{d}r$. This can be transformed to $\mathrm{d}D_c = -a^{-1}c\mathrm{d}t = -c\mathrm{d}a(a\dot{a})^{-1} = -c\mathrm{d}a(a^2 H)^{-1}$ and thus the comoving distance along the line of sight between two points at redshifts z_1 and z_2 is given by the integral

$$D_c(z_1, z_2) = \frac{c}{H_0} \int_{a(z_1)}^{a(z_2)} \mathrm{d}a \left[a\Omega_m + a^2(1 - \Omega_m - \Omega_\Lambda) + a^4\Omega_\Lambda \right] , \quad (1.16)$$

where here and in the following definitions we assume $z_2 > z_1$.

The *angular diameter distance* D_a relates the transverse physical extent δL of an object at redshift z_2 to the angular diameter $\delta\theta$ seen by an observer at redshift z_1 in analogy to the Euclidean case by $D_a = \delta L/\delta\theta$. We consider an object with edges at (r, θ, φ) and $(r, \theta + \delta\theta, \varphi)$. The spatial part of the

metric (1.1) then becomes $a^2(z_2)f_K^2[r(z_1,z_2)]\delta\theta^2 = \delta L^2$ and consequently the angular diameter distance is related to the comoving distance by

$$D_a(z_1,z_2) = a(z_2)f_K[D_c(z_1,z_2)] \ . \tag{1.17}$$

Because the theorems of intercepting lines hold for the angular diameter distance it is the distance measure that is used in gravitational lensing (see Chap. 2), and thus it is worthwhile to point out a couple of its "oddities". The angular diameter does not increase indefinitely as $z_2 \to \infty$. If $z_1 = 0$, objects beyond $z_2 \gtrsim 1$ appear bigger than objects with the same physical diameter at lower redshift. A consequence of this behavior is that $D_a(z_1,z_3) \neq D_a(z_1,z_2) + D_a(z_2,z_3)$.

The *luminosity distance* D_l relates the bolometric flux S of a source at redshift z_2 to the observed bolometric luminosity at redshift z_1,

$$D_l = \sqrt{\frac{L}{4\pi S}} \ . \tag{1.18}$$

It is related to the angular diameter and comoving distance by

$$D_l(z_1,z_2) = \left[\frac{a(z_1)}{a(z_2)}\right]^2 D_a(z_1,z_2) = \frac{a^2(z_1)}{a(z_2)}f_K[D_c(z_1,z_2)] \ , \tag{1.19}$$

where the second equality simply follows from Eq. (1.17). The first equality is intuitively clear: Photons are redshifted and their arrival times delayed due to spacetime expansion. Both effects contribute a factor of $a(z_1)/a(z_2)$. The sphere on which the observer sees the photons expands between emission and absorption by a factor $[a(z_1)/a(z_2)]^2$, leading to a total decrease of the flux by a factor $[a(z_1)/a(z_2)]^4$ or a factor $[a(z_1)/a(z_2)]^2$ relative to the angular diameter distance.

1.2 The Inhomogeneous Universe

The Universe is very homogeneous on very large scales but certainly the assumption of homogeneity breaks down at some point. Inhomogeneities appear on scales smaller than a few hundred Mpc and are observed as a

wealth of structures such as giant walls of galaxies, void, filaments, and galaxy clusters. It is commonly believed that these structures evolved from tiny inhomogeneities, possibly of quantum origin, in the very early Universe. Gravitational instability caused slightly overdense regions to expand slower under the influence of their self-gravity than their surrounding. This further increased their density contrast and led to even slower expansion, and so on. If the initial density contrast was high enough, such regions could eventually stop expansion altogether, re-collapse, and form galaxies or galaxy clusters.

1.2.1 Linear Perturbation Theory

For small density fluctuations linear perturbation theory is sufficient to describe them. To do so it is useful to define the *density contrast*

$$\delta(\boldsymbol{x}, t) \equiv \frac{\rho(\boldsymbol{x}, t) - \overline{\rho}(t)}{\overline{\rho}(t)} , \tag{1.20}$$

where $\overline{\rho}(t)$ is the mean density of the Universe at time t, and $\boldsymbol{x}$ is a comoving spatial coordinate. Linear theory assumes that the density contrast is much smaller than unity. If this is not the case, the linear approximation breaks down and the full non-linear equations of structure evolution must be evaluated numerically.

On scales much smaller than the horizon and for non-relativistic matter, Newtonian physics can be used to describe the evolution of structure. An ideal pressureless fluid interacting only via gravity – as we expect it from the dominating dark matter – can be described by the following standard equations in comoving coordinates (e.g., Peebles 1980),

$$\dot{\rho} + 3H\rho + \frac{1}{a}\nabla_x(\rho\boldsymbol{v}) = 0 \qquad \text{Continuity eq. ,} \tag{1.21}$$

$$\dot{\boldsymbol{v}} + H\boldsymbol{v} + \frac{1}{a}(\boldsymbol{v}\nabla_x)\boldsymbol{v} = -\frac{1}{a}\nabla\phi \qquad \text{Euler eq. ,} \tag{1.22}$$

$$\Delta_x\phi = 4\pi G\rho a^2 + 3a\ddot{a} - \Lambda a^2 \quad \text{Poisson eq.} \tag{1.23}$$

The homogeneous, isotropic Universe is a solution to these equations in which ϕ is the comoving potential and $\boldsymbol{v}$ the peculiar velocity field, defined as the proper velocity $\boldsymbol{u}$ minus the Hubble flow, $\boldsymbol{v} = \boldsymbol{u} - H\boldsymbol{x}$.

Using the definition of the density contrast (1.20), the continuity Eq. (1.21) becomes

$$\dot{\delta} + \frac{1}{a}\nabla_x\big[(1+\delta)\boldsymbol{v}\big] = 0 \, , \tag{1.24}$$

and with the help of Eq. (1.5), the Poisson Eq. (1.23) reads

$$\Delta_x\phi = \frac{3H_0^2\Omega_{\mathrm{m}}}{2a}\delta \, . \tag{1.25}$$

Note that no explicit dependence on the cosmological constant is present anymore in the Poisson equation. A uniform energy background has no effect on the evolution of density perturbations.

With the requirements that only small perturbations in density and velocity are allowed we can consider only terms linear in δ and $\boldsymbol{v}$. The continuity equation then further simplifies from (1.24) to

$$\dot{\delta} + \frac{1}{a}\nabla_x\boldsymbol{v} = 0 \, , \tag{1.26}$$

and the Euler Eq. (1.22) becomes

$$\dot{\boldsymbol{v}} + H\boldsymbol{v} = -\frac{1}{a}\nabla_x\phi \, . \tag{1.27}$$

Combining these two equations. with the Poisson Eq. (1.25), we obtain a second order linear differential equation for the evolution of the density contrast

$$\ddot{\delta} + 2H\dot{\delta} - \frac{3H_0^2\Omega_{\mathrm{m}}}{2a^3}\delta = 0 \, . \tag{1.28}$$

Because the coefficients in this differential equation do not depend on spatial coordinates, the general solution is given by the factorisation

$$\delta(\boldsymbol{x}, t) = D_+(t)\Delta_+(\boldsymbol{x}) + D_-(t)\Delta_-(\boldsymbol{x}) \, , \tag{1.29}$$

where one solution, by convention D_-, corresponds to the *decaying mode* that plays no role in structure formation because density perturbations in this mode quickly decrease. D_+ corresponds to the *growing mode* and is called the *linear growth factor*. One finds that it is

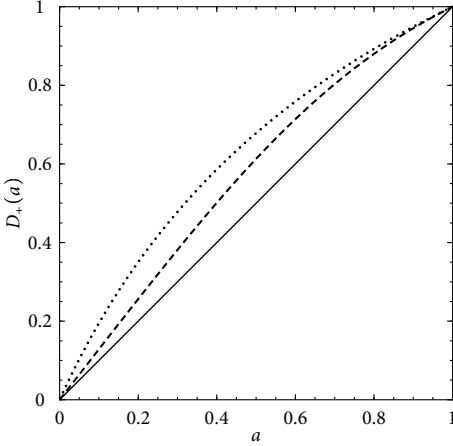$$D_+ \propto H(a) \int \frac{\mathrm{d}a'}{[a'H(a')]^3} \tag{1.30}$$

Figure 1.1: The evolution of the linear growth factor D_+ as a function of the scale factor a for various cosmological models. The solid line represents an EDS Universe ($\Omega_m = 1.0$, $\Omega_\Lambda = 0$), the dashed line a Universe with $\Omega_m = 0.3$, $\Omega_\Lambda = 0.7$, and the dotted line an open Universe with $\Omega_m = 0.3$, $\Omega_\Lambda = 0$. The curves have been calculated using the fitting formula of Carroll et al. (1992).

by solving the differential Eq. (1.28). The proportionality factor is chosen such that $D_+(t_0) = 1$. For an Einstein-de Sitter (EDS) Universe ($\Omega_m = 1.0$, $\Omega_\Lambda = 0$) $D_+ = a(t)$; for Universes with lower matter density $D_+ \geq a(t)$. This behavior is shown in Fig. 1.1. With $\delta_0 \equiv \delta(\boldsymbol{x}, t_0)$ one has

$$\delta(\boldsymbol{x}, t) = D_+(t)\delta_0(\boldsymbol{x}) \ . \tag{1.31}$$

1.2.2 Matter Power Spectrum

It will never be possible to compute the evolution of the density field of the Universe we live in as this would require knowledge of the exact density field at some earlier time $\delta(t_i < t_0)$. What cosmology can aim for is a comparison of the statistical properties of the observed matter distribution with predictions of the density field.

The early density fluctuations from which structure evolved are usually assumed to be Gaussian with random phases in Fourier space. In this case the density field is uniquely specified by its two-point correlation function $\xi(|\boldsymbol{x} - \boldsymbol{x}'|) = \langle \delta(\boldsymbol{x})\delta^*(\boldsymbol{x}') \rangle$. Defining $\hat{\delta}(\boldsymbol{k}, t)$ to be the Fourier transform of the density contrast field, $\hat{\delta}(\boldsymbol{k}, t) = D_+(t)\hat{\delta}_0(k)$ follows immediately from

Eq. (1.31) and consequently

$$P(k, t) = D_+^2(t) P_0(k) , \qquad (1.32)$$

where P_0 is the linearly evolved power spectrum at the present time.

When talking about the linearly evolved power spectrum this of course bears the question, linearly evolved from what? The answer is based on two assumptions: First, at some very early time t_i all fluctuations must have been larger than the horizon scale. If this is the case no characteristic length scale was available, a condition satisfied by a power law $P(k) \propto k^n$. The second argument, which determines the value of n is a bit more involved. We first define the dimensionless power spectrum

$$\Delta^2(k) = 4\pi k^3 P(k) , \qquad (1.33)$$

which is the variance of fluctuations per logarithmic bin, $d\langle \delta^2 \rangle / d\ln k \propto k^3 P(k)$. Before a_{eq} the density fluctuations grew proportional to a^2 on superhorizon scales (Peacock 1999), i.e., $\Delta^2 \propto a^4$ or $\Delta \propto d_{\mathrm{H}}^4$, as the horizon size is proportional to the scale factor. Combining this with Eq. (1.33) leads to an expression for fluctuations on the horizon scale,

$$\Delta^2 \left(k = \frac{1}{d_{\mathrm{H}}} \right) = d_{\mathrm{H}}^{-(3+n)} d_{\mathrm{H}}^4 , \qquad (1.34)$$

If one now requires that fluctuations entering the horizon, which provides the only length scale, are *scale-invariant*, i.e., always have the same amplitude, the index of the power spectrum is fixed to $n = 1$, so that $\Delta^2(1/d_{\mathrm{H}}) = 1$. The $P(k) \propto k$ spectrum is called the *Harrison-Zeldovich* spectrum (Harrison 1970; Zeldovich 1972).

Equation (1.32) describes the *linear* evolution of the power spectrum and is not valid in a number of situations. First, the obvious one is where the density contrast approaches unity and linear perturbation theory is not applicable. Second, because the horizon scales grows with time, perturbations larger than the horizon existed at all times. These superhorizon fluctuations cannot be described with Newtonian theory but require a linearization of Einstein's field equations. Finally, for $a < a_{\mathrm{eq}}$ radiation dominated and its equation of state has to be used instead of the equation of state for matter that has been used in the derivation of (1.32).
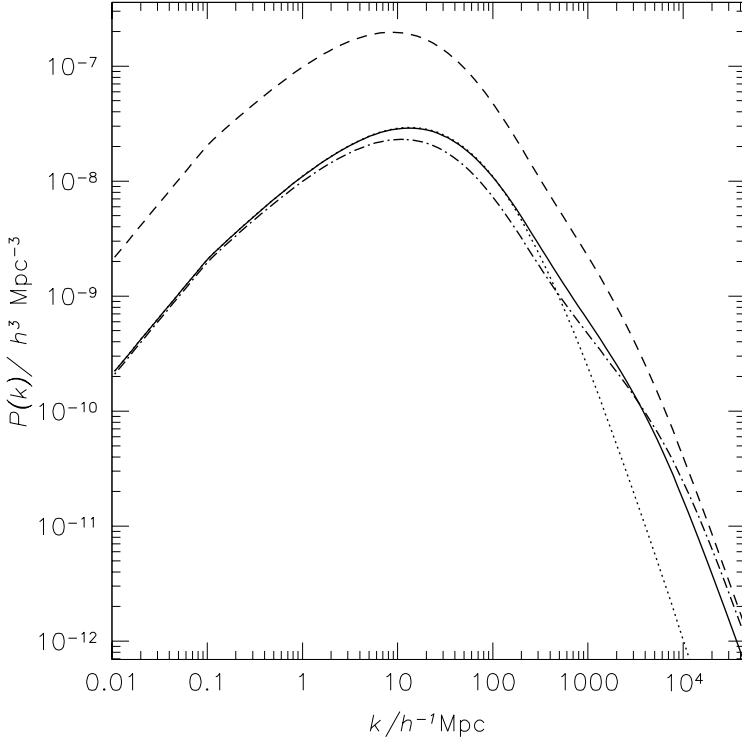
Figure 1.2: The power spectrum of cosmological density fluctuations at the present epoch for various cosmological models. The solid line corresponds to a ΛCDM Universe with $\Omega_m = 0.3$, $\Omega_\Lambda = 0.7$. The dotted line shows the linear power spectrum in the same cosmology for comparison. The dashed line is for an EDS Universe with $\Omega_m = 1$, $\Omega_\Lambda = 0$. The dot-dashed line represents an OCDM Universe with $\Omega_m = 0.3$, $\Omega_\Lambda = 0$. For all models the normalization is $\sigma_8 = 0.85$, and the shape parameter $\Gamma = 0.21$. The non-linear evolution of the power spectrum was calculated following the prescription of Peacock & Dodds (1996).

The effects of superhorizon fluctuations and the radiation dominated era are taken care of by defining a *transfer function $T(k)$* such that

$$P(k, t) = T^2(k) \left(\frac{D_+(t)}{D_+(t_i)} \right)^2 P(k, t_i) , \qquad (1.35)$$

where t_i is an early time at which all Fourier modes of interest are smaller than the horizon size. The transfer function can be calculated and fitting formulae exist (e.g., Eisenstein & Hu 1998). In a CDM Universe for small scales, i.e., large k, $T(k) \propto k^{-2}$. For large scale, i.e., small k, $T(k) \sim 1$. The transition region is described by the *shape parameter*

$$\Gamma = h\Omega_{\mathrm{m}} \exp \left[-\Omega_{\mathrm{b}} \left(1 + \sqrt{2h}\Omega_{\mathrm{m}}^{-1} \right) \right] , \qquad (1.36)$$

where the exponential function accounts for the small contribution of the baryonic matter density Ω_{b}.

The shape of the power spectrum is completely determined by the spectral index n and the shape parameter. What remains to be fixed is the normalization of the power spectrum, usually expressed as the rms of density fluctuations in sphere with radius $8h^{-1}$ Mpc, σ_8. One way to determine σ_8 will be presented in Sect. 1.2.4.

The non-linear evolution of the power spectrum is in practice modelled with N-body simulations. Each simulation yields one realization of the non-linearly evolved density field starting from an initial random Gaussian field with Harrison-Zeldovich spectrum. These simulations can be used to derive fitting formulae for the non-linear power spectrum. For example, Hamilton et al. (1991, 1995) derived an equation relating the linear to the non-linearly evolved power spectrum. Based on this work, the refinements of Peacock & Dodds (1996) and Smith et al. (2003) give accurate description of the non-linear power spectrum for all times and Fourier modes.

1.2.3 Spherical Collapse Model

A simple, analytically solvable model of non-linear structure evolution is the spherical collapse model. Although the model is very simple it is able to yield the characteristic overdensity of clusters of galaxies. The model

assumes a spherically symmetric overdensity embedded in an FLRW Universe. It follows from Birkhoff's theorem that the evolution of the overdense region depends only on the local density. Surrounding matter influences the selected region only via tidal fields, which are higher order effects and neglected here. For simplicity we assume an EDS Universe. Eke et al. (1996) generalized this model to cosmologies with a cosmological constant but the important numbers can be found already for the simpler case considered here. In fact, numerical simulation seem to indicate that this case is sufficient (Jenkins et al. 2001).

The overdense region will evolve like a closed sub-universe and can thus be described by the Friedmann equation for this case,

$$\ddot{r} = -\frac{GM}{r^2} \, , \tag{1.37}$$

where the proper radius of the sphere r takes on the role of the scale factor and M is the total mass of the overdense region. The solution is the well known cycloid

$$r(\theta) = A(1 - \cos\theta) \, , \quad t(\theta) = B(\theta - \sin\theta) \, . \tag{1.38}$$

The constants A and B are related via $A^3/B^2 = GM$.[1]

For small times t the solution (1.38) can be expanded to

$$r \simeq \left(\frac{9}{2}GMt^2\right)^{1/3} \left[1 - \frac{1}{20}\left(\frac{6t}{B}\right)^{2/3}\right] \, . \tag{1.39}$$

Neglecting the square bracket term this equation simply reproduces the evolution of the scale factor $a \propto t^{2/3}$ in an EDS Universe. Further expansion to first order yields an expression for the mean density

$$\rho = \frac{3M}{4\pi r^3} \simeq \frac{1}{6\pi Gt^2}\left[1 + \frac{3}{20}\left(\frac{6t}{B}\right)^{2/3}\right] \, , \tag{1.40}$$

where by the same argument as above $1/6\pi Gt^2$ is the evolution of the background density $\bar{\rho}$. Thus, the linear density contrast is

$$\delta \simeq \frac{3}{20}\left(\frac{6t}{B}\right)^{2/3} \, . \tag{1.41}$$

---

[1]This is of course nothing else but Kepler's Third Law.

The true density contrast evolves differently and can be calculated by

$$1 + \delta_{\text{true}} \equiv \frac{\rho}{\bar{\rho}} = \left(\frac{r_{\text{b}}}{r}\right)^3 , \tag{1.42}$$

where r_{b} is the radius of a sphere with the background matter density $\bar{\rho}$ in which the total mass equals M. It follows from combining Eqs. (1.38) and (1.42) that

$$1 + \delta_{\text{true}} = \frac{9(\theta - \sin \theta)^2}{2(1 - \cos \theta)^3} . \tag{1.43}$$

We can now investigate the difference of the non-linear behavior from the linear approximation (1.41) by looking at some characteristic points. The sphere reaches its maximum radius at $\theta = \pi$, $t = \pi B$. After this time the sphere does not any further participate in the general expansion but starts to contract. At this point the true density contrast is $\delta_{\text{true}} = 9\pi^2/16 - 1 \simeq 4.55$, while linear theory predicts $\delta = (3/20)(6\pi)^{2/3} \simeq 1.06$.

In the absence of dissipative effects a perfect sphere would collapse into a singularity at $\theta = 2\pi$. Linear theory predicts $\delta_{\text{c}} = (3/20)(12\pi)^{2/3} \simeq 1.69$ for this moment, while the "true" overdensity formally diverges.

In reality deviations from spherical symmetry of course prohibit a complete collapse and direct particles onto non-radial orbits. Random motion of particles will eventually lead to virialization and a stable equilibrium state. The density of this virialized region can be estimated using the virial theorem $V = -2K$, V being the potential energy given by $V = -GM/r_{\text{vir}}$, and K being the kinetic energy. The true overdensity of a virialized region depends on the time virialization is complete. A lower bound is provided by the time the solution (1.38) fulfils the virial theorem. This occurs at $\theta = 3\pi/2$ and the corresponding density contrast is $\delta_{\text{true}} = (9\pi + 6)^2/8 \simeq 146$, while linear theory predicts $\delta \simeq 1.58$. Random motions of particles, however, will delay the collapse to r_{vir}. If virialization occurs at the time of collapse $\theta = 2\pi$, $\delta_{\text{true}} \simeq 177$.

In practice one works with a radius r_{200} enclosing a sphere of mean overdensity 200 to estimate the virial radius.

1.2.4 Number Density of Collapsed Halos

The Press-Schechter Argument

Galaxy clusters are highly non-linear structures with overdensities of at least several hundreds. Nevertheless, a relatively simple analytic approach is able to give reasonably accurate predictions of the mass function of collapsed halos. The argument is due to Press & Schechter (1974, PS) and is based on the spherical collapse model and the initial density field. Sheth et al. (2001) later generalized this argument to ellipsoidal halos.

If the initial Gaussian density field is smoothed with a top-hat filter with comoving radius R, typical structures in the filtered field will have sizes $\sim R$ and masses $M \sim 4\pi R^3 \rho_{m0}/3$. The smoothed field is still Gaussian and has a variance

$$\sigma(M) = \frac{1}{2\pi^2} \int_0^\infty \mathrm{d}k \; k^2 P(k) W(k; M) \;, \qquad (1.44)$$

where $W(k; M)$ is the Fourier transformed top-hat filter function with a radius that corresponds to an enclosed mass M.

According to the spherical collapse model all overdensities with linearly extrapolated density contrasts δ_0 in excess of the critical density contrast $\delta_c \simeq 1.69$ have collapsed by t_0. The condition to have collapsed at an earlier redshift z is $\delta_0 > \delta_c(1 + z)$. The probability for a given point being inside a collapsed halo of mass $> M$ is thus

$$P\left(\delta(z) > \delta_c(z); M\right) = \frac{1}{\sqrt{2\pi}\sigma(M)} \int_{\delta_c(z)}^\infty \mathrm{d}\delta \; e^{-\delta(z)^2/2\sigma^2(M)} \;. \qquad (1.45)$$

The PS argument is now that all objects that exist at a given epoch are those that have just reached the critical density contrast. Objects that have $\delta > \delta_c$ on some mass scale M will have $\delta = \delta_c$ on a larger scale and will be counted as objects in the larger scale. This argument has the problem that half of the mass, namely the mass in initially underdense regions, is ignored. Press & Schechter argue that this mass will later be accreted into neighboring lumps and simply multiplied the probability (1.45) by 2.

The number density of halos of a given mass M is the product of the number density ρ_0/M if all mass in the Universe were in halos of mass M and the probability for a halo to have this mass $\mathrm{d}P/\mathrm{d}M$. We know this

probability because Eq. (1.45) implicitly depends on M. Thus, the mass function is

$$\frac{\mathrm{d}n}{\mathrm{d}M}\mathrm{d}M = \frac{\rho_0}{M}\frac{\mathrm{d}\sigma}{\mathrm{d}M}\frac{\mathrm{d}P}{\mathrm{d}\sigma}\mathrm{d}M \; . \tag{1.46}$$

Evaluating $\mathrm{d}P/\mathrm{d}\sigma$ and defining $\nu = \delta_\mathrm{c}/\sigma(M)$ we obtain the PS mass function in its usual form,

$$\frac{\mathrm{d}n}{\mathrm{d}M} = \sqrt{\frac{2}{\pi}}\frac{\rho_0}{M}\left|\frac{\mathrm{d}\nu}{\mathrm{d}M}\right|\nu e^{-\nu^2/2} \; . \tag{1.47}$$

Equation (1.47) – and all other mass functions for that matter – opens an avenue to normalizing the power spectrum. Massive clusters of galaxies contain about as much mass as a comoving sphere of size $8h^{-1}$ Mpc, so that the cluster abundance is a direct measure of σ_8 (e.g., Eke et al. 1996). Comparing the predicted number of clusters with the observed one provides normalizations of the form

$$\sigma_8 = (0.52 \pm 0.04)\,\Omega_\mathrm{m}^{-0.52+0.13\Omega_\mathrm{m}} \; , \tag{1.48}$$

for flat cosmologies with $\Omega_\mathrm{m} + \Omega_\Lambda = 1$. The challenge for this method lies in obtaining a well-selected cluster sample with unbiased mass estimates.

Figure 1.3 shows the PS mass function in comparison with those obtained by Sheth & Tormen (1999) and Jenkins et al. (2001) discussed below.

The Jenkins Fitting Formula

The formation of halos is a very complex and non-linear process that cannot be fully described by analytical approximations such as the spherical collapse model. While more advanced methods like Lagrangian perturbation theory (e.g., Zeldovich 1970) are successful, the full complexity of the problem can only be tackled numerically. N-body simulations compute the full non-linear evolution of the density field from very high redshifts to the present time.

The most extensive study of the mass function from numerical simulations to date has been done using the N-body simulations of the VIRGO consortium (Jenkins et al. 1998). Jenkins et al. (2001) studied the mass function from a number of numerical simulations for two cosmologies, a CDM Universe with $\Omega_\mathrm{m} = 1.0$, $\Omega_\Lambda = 0$, and the concordance ΛCDM with
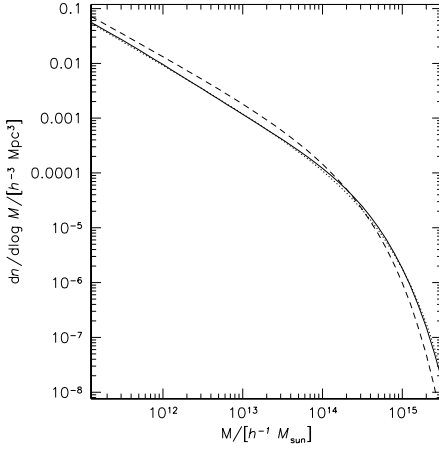
Figure 1.3: The mass function in a standard ΛCDM Universe at redshift $z = 0$ computed with different methods. The solid line is the Jenkins et al. mass function which is in good agreement with the Sheth & Tormen mass function (dotted line). The PS mass function slightly over-predicts the number of small halos and underestimates the number of massive halos.

$\Omega_m = 0.3$, $\Omega_\Lambda = 0.7$, to obtain a fit for the mass function over more than four orders of magnitude in mass. These simulations differed in volume, number of particles, and mass per particle.

Jenkins et al. find a universal mass function that is expressed in terms of the variance of the mass $\sigma(M)$ instead of the mass M itself. Their mass function,

$$\frac{dn}{dM} = 0.315 \frac{\overline{\rho}}{M^2} \left| \frac{d \ln \sigma(M)}{d \ln M} \right| \exp\left(-|0.61 - \ln \sigma(M)|^{3.8} \right), \qquad (1.49)$$

fits the simulated number density of halos over the range $-1.2 \le \ln \sigma^{-1} \le 1.05$ with an accuracy of better than 20%. This corresponds to a mass range of 3×10^{11} to $5 \times 10^{15} h^{-1} M_\odot$ at redshift 0. The fitting formula (1.49) has been tested for redshift and density ranges $0 \le z \lesssim 0.5$ and $0.3 \lesssim \Omega_m \lesssim 1$.

1 Cosmological Framework

2

Gravitational Lensing

The deflection of light in gravitational fields is one of the predictions of Einstein's "General Theory of Relativity" and was the subject of its first experimental test. Dyson et al. (1920) verified the prediction of the lensing effect by observing the positional shift of stars close to the sun during a solar eclipse. This experiment did not only show the expected deflection but also confirmed the effect's predicted magnitude, which is twice as big as one would expect from a simple Newtonian approach. Zwicky (1937) was the first to propose to use the gravitational lens effect to measure the masses of clusters of galaxies. However, it was not until 1979, when Walsh et al. observed the doubly imaged quasar Q 0957+561, that gravitational lensing was seen on cosmological scales. The first observations of gravitational lensing by a galaxy cluster was reported by Soucail et al. (1987a,b).

In the following I will review the fundamentals of (weak) gravitational lensing and its applications, important to this thesis. For a more extensive review see, e.g., Schneider (2006).

2.1 Gravitational Lens Theory

Computing the propagation of light through a universe with clumpy mass concentrations is hardly possible using Einstein's full theory. Luckily, a number of approximations can made, which turn gravitational lensing, as needed for this thesis, into a relatively easy, linear theory. Figure 2.1 provides a simplified sketch of the lens geometry. A source $\mathcal{S}$ at an angular position $\boldsymbol{\beta}$ and at an angular diameter distance D_s from the observer $\mathcal{O}$ emits a light ray. The light ray is deflected by an angle $\hat{\boldsymbol{\alpha}}$ when it passes the lens, which is at a distance D_d from the observer, at the impact vector $\boldsymbol{\xi}$. In the *thin*
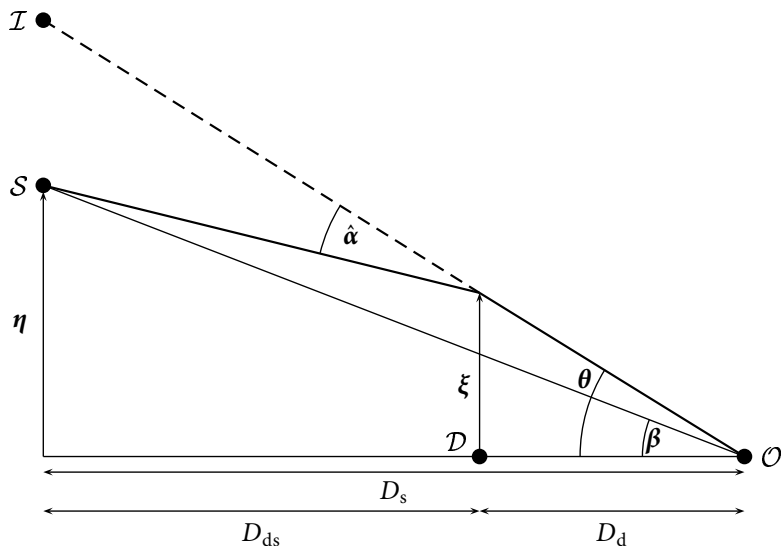
Figure 2.1: Simple sketch of a gravitational lens system. A light ray is emitted from the source $\mathcal{S}$. When it passes the gravitational lens $\mathcal{D}$ it is deflected and seen by the observer $\mathcal{O}$ as coming from the image $\mathcal{I}$. The distances D_d, D_s, and D_ds are the angular diameter distances from the observer to the deflector, to the source, and from the deflector to the source, respectively.

lens approximation we assume that the spatial extent of the lens $\mathcal{D}$ is much smaller than the distances D_s, D_d, and D_ds, the distance from the deflector to the source. This is a well justified assumption, e.g., for galaxy clusters, which have radii typically of a few Mpc, while the distances D_d, D_s and D_ds are on the order of several hundred Mpc. Accordingly, we treat the deflection as instantaneous and the light ray can be considered as a piecewise straight line. After deflection the observer sees an image of the source at an angular position $\boldsymbol{\theta}$.

We make the further assumption that the impact parameter is much larger than the Schwarzschild radius of a point lens with mass M, $|\boldsymbol{\xi}| \gg 2GMc^{-2}$. The field equations of General Relativity can then be linearized and the

deflection angle is the superposition of the deflection angles of the individual mass elements of a lens:

$$\boldsymbol{\alpha}(\boldsymbol{\xi}) = \frac{4G}{c^2} \int d^2\xi' \, \Sigma(\boldsymbol{\xi}') \frac{\boldsymbol{\xi} - \boldsymbol{\xi}'}{\left|\boldsymbol{\xi} - \boldsymbol{\xi}'\right|^2} \, . \tag{2.1}$$

Here $\Sigma(\boldsymbol{\xi})$ is the surface mass density, that is the projection of the three-dimensional mass distribution of the lens onto a plane perpendicular to the line of sight,

$$\Sigma(\boldsymbol{\xi}) = \int dr_3 \, \rho(\boldsymbol{\xi}, r_3) \, . \tag{2.2}$$

The condition on the impact parameter also implies that $\hat{\boldsymbol{\alpha}} \ll 1$, leading to the simple geometric relation

$$\boldsymbol{\eta} = \frac{D_s}{D_d} \boldsymbol{\xi} - D_{ds}\hat{\boldsymbol{\alpha}}(\boldsymbol{\xi}) \, , \tag{2.3}$$

which one can read off from Fig. 2.1. Here $\boldsymbol{\eta}$ is the position of the source in the source plane. Using the relations $\boldsymbol{\eta} = D_s\boldsymbol{\beta}$ and $\boldsymbol{\xi} = D_d\boldsymbol{\theta}$, Eq. (2.3) takes the form

$$\boldsymbol{\beta} = \boldsymbol{\theta} - \frac{D_{ds}}{D_s}\hat{\boldsymbol{\alpha}}(D_d\boldsymbol{\theta}) = \boldsymbol{\theta} - \boldsymbol{\alpha}(\boldsymbol{\theta}) \, , \tag{2.4}$$

where we have defined the scaled deflection angle $\boldsymbol{\alpha}(\boldsymbol{\theta})$ in the last step. Equation (2.4) is called the *lens equation*. In it the properties of the lens appear only as the (scaled) deflection angle. This in turn depends on the surface mass distribution, as we see from Eq. (2.1), suggesting to define a characteristic surface mass density

$$\Sigma_{crit} = \frac{c^2}{4\pi G} \frac{D_s}{D_d D_{ds}} \, , \tag{2.5}$$

called the *critical surface mass density*, and henceforth work with the dimensionless surface mass density, also called *convergence*

$$\kappa(\boldsymbol{\theta}) = \frac{\Sigma(D_d\boldsymbol{\theta})}{\Sigma_{crit}} \, . \tag{2.6}$$

The scaled deflection angle can now also be expressed in terms of κ by inserting its definition and Eq. (2.5) into Eq. (2.1),

$$\boldsymbol{\alpha}(\boldsymbol{\theta}) = \frac{1}{\pi} \int d^2\theta' \; \kappa(\boldsymbol{\theta}') \frac{\boldsymbol{\theta} - \boldsymbol{\theta}'}{|\boldsymbol{\theta} - \boldsymbol{\theta}'|^2} \; . \tag{2.7}$$

We see from this expression that $\boldsymbol{\alpha}$ can be expressed as the gradient of a two-dimensional potential

$$\boldsymbol{\alpha}(\boldsymbol{\theta}) = \nabla\psi(\boldsymbol{\theta}) \qquad \text{with} \qquad \psi(\boldsymbol{\theta}) = \frac{1}{\pi} \int d^2\theta' \; \kappa(\boldsymbol{\theta}') \ln|\boldsymbol{\theta} - \boldsymbol{\theta}'| \; . \tag{2.8}$$

In analogy to the three-dimensional Newtonian potential the *deflection potential* ψ satisfies a Poisson equation,

$$\nabla^2\psi(\boldsymbol{\theta}) = 2\kappa(\boldsymbol{\theta}) \; . \tag{2.9}$$

If $\kappa > 1$ for at least one source position $\boldsymbol{\theta}$ the lens equation (2.4) has multiple solutions, i.e., the lens will produce multiple images of the source. In this case the lens is said to be 'strong'. Note, however, that $\kappa > 1$ is a sufficient but not a necessary condition for the occurrence of multiple images. If $\kappa \ll 1$ the lens is called 'weak'.

The shapes of background sources will be distorted by the lens because light bundles are deflected differentially. In general, the shape of objects must be determined by solving the lens equation (2.4). Under the assumption that the source is smaller than the angular scale on which the lens properties change, the lens equation can be locally linearized. The distortion of images is then described by its Jacobian matrix

$$\mathcal{A}(\boldsymbol{\theta}) = \frac{\partial\boldsymbol{\beta}(\boldsymbol{\theta})}{\partial\boldsymbol{\theta}} = \left(\delta_{ij} - \frac{\partial^2\psi(\boldsymbol{\theta})}{\partial\theta_i\theta_j} \right) = \begin{pmatrix} 1 - \kappa - \gamma_1 & -\gamma_2 \\ -\gamma_2 & 1 - \kappa + \gamma_1 \end{pmatrix} , \tag{2.10}$$

where in the last step we used the components of the complex *shear* $\gamma = \gamma_1 + i\gamma_2 = |\gamma| e^{2i\varphi}$, which are defined by

$$\gamma_1 = \frac{1}{2} \left(\psi_{,11} - \psi_{,22} \right) \qquad \text{and} \qquad \gamma_2 = \psi_{,12} \; . \tag{2.11}$$
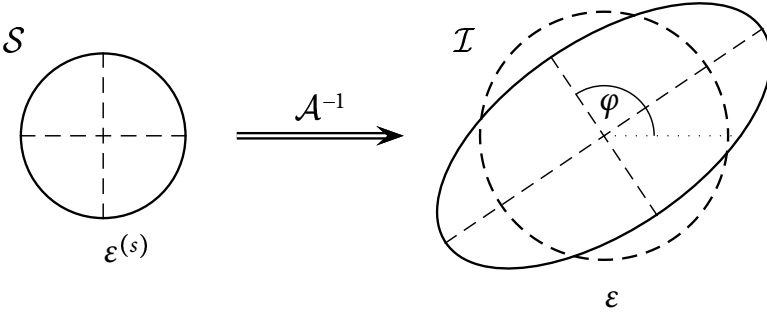
Figure 2.2: The effects of convergence and shear. A circular background source on the left is transformed by the lens mapping. The convergence κ alone causes an isotropic magnification (dashed circle). The combination of convergence and shear γ leads to the elliptical image on the right.

Defining the *reduced* shear

$$g(\boldsymbol{\theta}) = \frac{\gamma(\boldsymbol{\theta})}{1 - \kappa(\boldsymbol{\theta})} \; , \tag{2.12}$$

and inserting this definition into Eq. (2.10) it is easy to understand the effects of convergence and shear onto an image. See also Fig. 2.2. The factor $(1 - \kappa)$ yields an isotropic magnification of the image but does not alter its shape. The components of $g = g_1 + ig_2$ determine the shape of the image. In particular, a circular background source with radius r will be mapped to an ellipse with semi-axes

$$a = r|(1 - \kappa)(1 - |g|)|^{-1}$$
$$b = r|(1 - \kappa)(1 + |g|)|^{-1} \tag{2.13}$$

It follows from Liouville's theorem and the conservation of photon number in gravitational deflection, that gravitational lensing leaves the surface brightness of objects unchanged. If $I^{(s)}(\boldsymbol{\beta})$ is the intensity distribution in the source plane an observer sees the intensity

$$I(\boldsymbol{\theta}) = I^{(s)}\left[\boldsymbol{\beta}(\boldsymbol{\theta})\right] \; . \tag{2.14}$$

We locally linearize this expression around a point $\boldsymbol{\beta}_0 = \boldsymbol{\beta}(\boldsymbol{\theta}_0)$ and obtain

$$I(\boldsymbol{\theta}) = I^{(s)} \left[\boldsymbol{\beta}_0 + \mathcal{A}(\boldsymbol{\theta}_0) \cdot (\boldsymbol{\theta} - \boldsymbol{\theta}_0) \right] \; . \tag{2.15}$$

The effects of shear and convergence are illustrated in Fig. 2.2 for a source with circular isophotes. The convergence κ causes an isotropic magnification, while the shear γ, in addition to also contributing to the magnification effect, distorts the object, leading to an image with elliptical isophotes, with an axis ratio given by the ratio of the inverse of the eigenvalues $1 - \kappa \pm |\gamma|$ of $\mathcal{A}$.

2.2 Measuring Shear

We saw in the previous section that the properties of a lens are completely determined by its surface mass density distribution κ. Measuring the total mass of objects and its distribution is a common problem in astrophysics. The convergence, however, is not an observable but the shear γ can be estimated from observable quantities. A rough outline of this procedure is given in this section, a more detailed outline can be found in Bartelmann & Schneider (2001); how to obtain maps of surface mass density from shear fields will be described in the following section.

To estimate the shear we make use of the fact that the shapes of faint background galaxies (FBG) are distorted when their light passes the tidal field of massive structures. If FBG were intrinsically circular we could immediately determine the shear at the galaxy's position by measuring its axis ratio. Unfortunately, galaxies are intrinsically not circular and measuring the shape of an individual galaxy will not provide significant information about the tidal gravitational field. If we, however, assume that the unlensed ellipticity distribution of galaxies is random, the shear can be estimated from the net ellipticity of a localized galaxy sample.

While many galaxies in the local Universe are well described by elliptical profiles, the FBGs from which we want to estimate the shear are often irregular galaxies, which cannot be reasonably approximated with elliptical isophotes. An additional complication arises from the pixelization of CCD cameras. We thus have to develop a measure for ellipticity that works well for irregular shaped galaxies and can be used with discrete brightness values at CCD pixels.
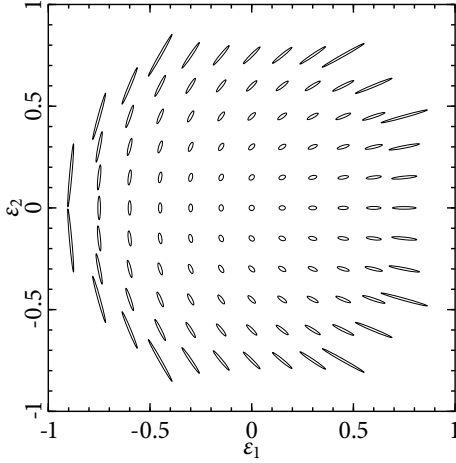
Figure 2.3: The shape of the image ellipse in dependence on the ellipticity components ε_1 and ε_2. Note that the image is rotated by 90° if $\varepsilon \mapsto -\varepsilon$.

First, we define the center $\overline{\boldsymbol{\theta}}$ of an image with brightness distribution $I(\boldsymbol{\theta})$,

$$\overline{\boldsymbol{\theta}} = \frac{\int \mathrm{d}^2\theta \, w \left[I(\boldsymbol{\theta})\right] \boldsymbol{\theta}}{\int \mathrm{d}^2\theta \, w \left[I(\boldsymbol{\theta})\right]} \, , \qquad (2.16)$$

where w is a weight function. For example, if $w(I) = H(I - I_{\mathrm{lim}})$ is the Heaviside step function, $\overline{\boldsymbol{\theta}}$ is the center of light within the limiting isophote I_{lim}. Using this center we define the tensor of second brightness moments

$$Q_{ij} = \frac{\int \mathrm{d}^2\theta \, w \left[I(\boldsymbol{\theta})\right] (\theta_i - \overline{\theta}_i)(\theta_j - \overline{\theta}_j)}{\int \mathrm{d}^2\theta \, w \left[I(\boldsymbol{\theta})\right]} \quad \text{with} \quad i, j \in \{1, 2\} \, , \qquad (2.17)$$

which we utilize in the definition of two quantities, which are both called complex ellipticity,

$$\chi = \frac{Q_{11} - Q_{22} + 2iQ_{12}}{Q_{11} + Q_{22}} \quad \text{and} \quad \varepsilon = \frac{Q_{11} - Q_{22} + 2iQ_{12}}{Q_{11} + Q_{22} + 2\sqrt{Q_{11}Q_{22} - Q_{12}^2}} \, . \qquad (2.18)$$

Both ellipticities have the same orientation as they have the same numerator; only their absolute values differ. Which one is more convenient to use depends on the context. The image ellipticity in dependence on the

components ε_1 and ε_2, which we will use from now on, is shown in Fig. 2.3. An image with elliptical isophotes with an axis ratio $r \leq 1$ has the ellipticity

$$\varepsilon = \frac{1-r}{1+r}e^{2i\vartheta} \ . \tag{2.19}$$

The phase factor 2ϑ corresponds to the symmetry of the ellipse, which is invariant under rotations by 180°. Figure 2.3 shows that ε changes to $-\varepsilon$ if the image is rotated by 90°.

Seitz & Schneider (1997) showed that the relation

$$\varepsilon^{(s)} = \begin{cases} \frac{\varepsilon-g}{1-g^*\varepsilon} & |g| \leq 1 \ , \\ \frac{1-g\varepsilon^*}{\varepsilon^*-g^*} & |g| > 1 \ , \end{cases} \tag{2.20}$$

holds, where the asterisk denotes complex conjugation. The inverse transformation is obtained by $g \mapsto -g$ and exchanging source and image ellipticities.

If we assume that the intrinsic distribution of galaxies is random, i.e., that the expectation value of $\varepsilon^{(s)}$ vanishes,

$$E\left(\varepsilon^{(s)}\right) = 0 \ , \tag{2.21}$$

the expectation value of ε becomes

$$E\left(\varepsilon\right) = \begin{cases} g & |g| \leq 1 \ , \\ 1/g^* & |g| > 1 \ , \end{cases} \tag{2.22}$$

which one obtains by averaging over the source ellipticities in Eq. (2.20). The foregoing relation means that ε is an unbiased estimator of the local reduced shear. In the case of weak lensing, $\kappa \ll 1$, $|\gamma| \ll 1$, and thus $|g| \ll 1$, Eq. (2.20) simply becomes $\varepsilon \approx \varepsilon^{(s)} + g$, under the condition that $|\varepsilon| \approx |\varepsilon^{(s)}| \lesssim 1/2$. The noise of the estimator is determined by the dispersion of the intrinsic ellipticity distribution

$$\sigma_\varepsilon = \sqrt{\left\langle \varepsilon^{(s)}\varepsilon^{(s)*}\right\rangle} \ . \tag{2.23}$$

2.3 Mass Reconstruction

Shear and convergence are both second derivatives of the deflection potential. By combining Eqs. (2.8) and (2.11) we can relate the shear γ to the surface

mass density κ,

$$\gamma(\boldsymbol{\theta}) = \frac{1}{\pi} \int d^2\theta' \, \mathcal{D}(\boldsymbol{\theta} - \boldsymbol{\theta}')\kappa(\boldsymbol{\theta}') \, . \tag{2.24}$$

The kernel

$$\mathcal{D}(\boldsymbol{\theta}) = \frac{\theta_2^2 - \theta_1^2 - 2i\theta_1\theta_2}{|\theta|^4} = \frac{-1}{(\theta_1 - i\theta_2)^2} \, , \tag{2.25}$$

is the shear exerted by a unit point mass at $\boldsymbol{\theta} = 0$. Equation (2.24) thus means that the shear of a mass distribution $\kappa(\boldsymbol{\theta})$ is given by the convolution of this mass distribution with the shear of a point mass. This implies that by Fourier-transforming and applying the convolution theorem the surface mass density can be determined from the shear alone.

The Fourier transform $\hat{\kappa}(\boldsymbol{l})$ of the surface mass density is given by

$$\hat{\kappa}(\boldsymbol{l}) = \int_{\mathbb{R}^2} d^2\theta \, \kappa(\boldsymbol{\theta}) \exp(i\boldsymbol{l} \cdot \boldsymbol{\theta}) \, , \tag{2.26}$$

and its inverse by

$$\kappa(\boldsymbol{\theta}) = \frac{1}{(2\pi)^2} \int_{\mathbb{R}^2} d^2l \, \hat{\kappa}(\boldsymbol{l}) \exp(-i\boldsymbol{l} \cdot \boldsymbol{\theta}) \, . \tag{2.27}$$

The Fourier transforms $\hat{\gamma}$ of the shear and of the deflection potential $\hat{\psi}$ and their inversions are defined in analogy to Eqs. (2.26) and (2.27). We note that differentiation in real space with respect to the component θ_i amounts to a multiplication with $-il_i$ in Fourier space. Thus, the Poisson equation (2.9) becomes

$$- |\boldsymbol{l}|^2 \, \hat{\psi}(\boldsymbol{l}) = 2\hat{\kappa}(\boldsymbol{l}) \, , \tag{2.28}$$

and the Fourier transform of the shear reads

$$\hat{\gamma}(\boldsymbol{l}) = - \left(\frac{l_1^2 - l_2^2}{2} + il_1l_2 \right) \hat{\psi}(\boldsymbol{l}) \, . \tag{2.29}$$

Combining the previous two equations and requiring that $|\boldsymbol{l}| \neq 0$, we get the Fourier transform of the kernel $\mathcal{D}$,

$$\hat{\mathcal{D}}(\boldsymbol{l}) = \pi \frac{l_1^2 - l_2^2 + 2il_1l_2}{|l|^2} \, . \tag{2.30}$$

Solving for $\hat{\kappa}(\boldsymbol{l})$ in Fourier space and transforming back leads to

$$\kappa(\boldsymbol{\theta}) - \kappa_0 = \frac{1}{\pi} \int d^2\theta' \, \mathcal{D}^*(\boldsymbol{\theta} - \boldsymbol{\theta}')\gamma(\boldsymbol{\theta}') \,, \tag{2.31}$$

where the asterisk denotes complex conjugation. Because κ is a real quantity the foregoing equation is commonly written as

$$\kappa(\boldsymbol{\theta}) - \kappa_0 = \frac{1}{\pi} \int d^2\theta' \, \mathfrak{R}\left[\mathcal{D}^*(\boldsymbol{\theta} - \boldsymbol{\theta}')\gamma(\boldsymbol{\theta}')\right] \,. \tag{2.32}$$

The equivalence of Eqs. (2.31) and (2.32) is easily checked by verifying that $\mathfrak{I}(\hat{\mathcal{D}}^*\hat{\gamma}) \equiv 0$. This inversion formula was first derived by Kaiser & Squires (1993, KS93) .

A number of difficulties with this method are evident from Eq. (2.32). Most of them are caused by this specific inversion methods, while one is a fundamental limitation of weak lensing mass reconstructions. The additive constant κ_0 remains undetermined. Its physical interpretation, the correspondence to an $|\boldsymbol{l}| = 0$ mode in Fourier space, is that a sheet of constant surface mass density κ_0 does not exert any shear and thus is undetermined from shear measurements alone. This is called the *mass-sheet degeneracy* and is a fundamental limitation of all inversion methods that solely rely on shear information.

Another problem of the KS93 inversion method is that γ can only be estimated at discrete points, namely the positions of the FBG. As already noticed by KS93 it is not possible to simply convert Eq. (2.32) into a sum over individual shear estimators. This approach would yield an estimator for κ that has infinite variance due to the sampling noise introduced by the random positions of the FBG. The remedy for this problem is to smooth the data to obtain a shear field. When smoothing with a Gaussian kernel of scale θ_s the covariance of the resulting mass map is given by

$$\mathrm{Cov}\left(\kappa(\boldsymbol{\theta}), \kappa(\boldsymbol{\theta}')\right) = \frac{\sigma_\varepsilon^2}{4\pi\theta_s^2 n} \exp\left(-\frac{|\boldsymbol{\theta} - \boldsymbol{\theta}'|^2}{2\theta_s^2}\right) \,, \tag{2.33}$$

where n is the number density of FBG (van Waerbeke 2000). Smoothing the shear field with a Gaussian kernel amounts to a convolution of the mass map with the same kernel. Therefore, the choice of the smoothing scale is a

trade-off between suppressing noise and preserving structure in the mass maps.

We saw in Sect. 2.2 that the observed ellipticities are unbiased estimators of the reduced shear g and not of the shear γ. The KS93 algorithm, however, makes use of γ. Recalling eq. (2.12) we can rewrite eq. (2.32) as

$$\kappa(\boldsymbol{\theta}) - \kappa_0 = \frac{1}{\pi} \int d^2\theta' \left[1 - \kappa(\boldsymbol{\theta}')\right] \Re\left[\mathcal{D}^*(\boldsymbol{\theta} - \boldsymbol{\theta}')g(\boldsymbol{\theta}')\right] . \tag{2.34}$$

This integral can be solved by iteration, using (2.32) to obtain a first estimate of κ and employing this to compute g. Experience shows that this procedures converges quickly. With Eq. (2.34) the inversion has become a non-linear process and the undetermined constant κ_0 corresponds no longer to adding a uniform mass sheet. The transformation

$$\left[1 - \kappa'(\boldsymbol{\theta})\right] = \lambda\left[1 - \kappa(\boldsymbol{\theta})\right] \tag{2.35}$$

changes the shear $\gamma \mapsto \gamma' = \lambda\gamma$ and thus leaves g unchanged. Equation (2.35) is the full form of the mass-sheet degeneracy.

The integral in Eq. (2.32) extends over $\mathbb{R}^2$ but observations are only available on finite fields. To be able to compute the integral the shear outside the field-of-view is set to zero. This leads to systematic errors at the borders and especially at the corners where the influence of this "invented data" is biggest. This problem has been addressed in a number of ways and finite field inversion methods exist (see, e.g., Seitz & Schneider 1996, for a comparison of several methods). We will present one such method, which is used in this work.

We note that

$$\nabla\kappa = \begin{pmatrix} \gamma_{1,1} + \gamma_{2,2} \\ \gamma_{2,1} - \gamma_{1,2} \end{pmatrix} , \tag{2.36}$$

which can be obtained by partially differentiating Eq. (2.11) and combining suitable terms (Kaiser 1995). A similar relation holds for the reduced shear. We define $K(\boldsymbol{\theta}) \equiv \ln[1 - \kappa(\boldsymbol{\theta})]$ and assume that we are in the weak lensing regime, i.e. $\kappa < 1$. Then

$$\nabla K(\boldsymbol{\theta}) = \frac{-1}{1 - g_1^2 - g_2^2} \begin{pmatrix} 1 - g_1 & -g_2 \\ -g_2 & 1 + g_1 \end{pmatrix} \begin{pmatrix} g_{1,1} + g_{2,2} \\ g_{2,1} - g_{1,2} \end{pmatrix} \equiv \boldsymbol{u}_g(\boldsymbol{\theta}) . \tag{2.37}$$

Equation (2.37) can be integrated by formulating it as a von Neumann boundary problem on the data field $\mathcal{U}$ (Seitz & Schneider 2001)

$$\nabla^2 \kappa = \nabla \cdot \boldsymbol{u}_g \quad \text{with} \quad \boldsymbol{n} \cdot \nabla \kappa = \boldsymbol{n} \cdot \boldsymbol{u}_g \text{ on } \partial \mathcal{U} \, , \qquad (2.38)$$

where $\boldsymbol{n}$ is the outward pointing normal vector on the boundary $\partial \mathcal{U}$. The practical implementation of solving Eq. (2.38) follows these steps:

1. The galaxy ellipticities are spatially smoothed. The reduced shear at the position $\boldsymbol{\theta}$ is calculated from

$$g(\boldsymbol{\theta}) = \frac{\sum_{i=1}^{N_g} w(|\boldsymbol{\theta} - \boldsymbol{\theta}_i|) \varepsilon_i}{\sum_{i=1}^{N_g} w(|\boldsymbol{\theta} - \boldsymbol{\theta}_i|)} \, , \qquad (2.39)$$

   where ε_i is the ellipticity of the ith galaxy at position $\boldsymbol{\theta}_i$. N_g is the number of all galaxies and $w(\theta)$ is a suitably chosen weight function. Seitz & Schneider (2001) set

$$w(\theta) = \begin{cases} \exp\left(-\frac{\theta^2}{(\theta_s)^2}\right) - \exp(-q) & \theta \le \sqrt{q}\theta_s \\ 0 & \text{otherwise} \, , \end{cases} \qquad (2.40)$$

   with the constant q fixed at $q = 9$, so that the smoothing is nearly Gaussian and w is continuous at $\theta = \sqrt{q}\theta_s$.

2. The vector field $\boldsymbol{u}_g$ is computed by finite differencing using Eq. (2.37).

3. The von Neumann problem (2.38) is solved using successive overre-laxation (Press et al. 1992).

2.4 The Aperture Mass Statistic

Often one is not interested in mapping the mass distribution but only in the most significant mass peaks, typically clusters of galaxies, in an observed field. For mass-to-light ratios, e.g., one wants to measure the mass of a cluster of galaxies inside a circle of given radius. Due to the mass-sheet degeneracy this is not possible if using parameter-free methods and shear

data alone. A statistic that provides a related quantity is the aperture mass M_{ap} (Schneider 1996), defined as the weighted integral over the surface density around a point $\boldsymbol{\theta}_0$

$$M_{\mathrm{ap}}(\boldsymbol{\theta}_0) = \int_{\mathrm{sup}\,U} \mathrm{d}^2\theta\,\kappa(\boldsymbol{\theta})U(\boldsymbol{\theta}-\boldsymbol{\theta}_0)\,, \tag{2.41}$$

where $U(\boldsymbol{\theta})$ is a weight function. To avoid the linear mass-sheet-degeneracy we require that the weight function is compensated, i.e., that it has zero total weight,

$$\int_{\mathrm{sup}\,U} \mathrm{d}^2\theta\,U(\boldsymbol{\theta}) = 0\,. \tag{2.42}$$

An example of a weight function U satisfying this condition is

$$U(\vartheta) = U(|\boldsymbol{\theta}-\boldsymbol{\theta}_0|) = \begin{cases} \frac{1}{\pi\vartheta_1^2} & 0 \le \vartheta \le \vartheta_1\,, \\ -\frac{1}{\pi(\vartheta_2^2-\vartheta_1^2)} & \vartheta_1 < \vartheta \le \vartheta_2\,, \\ 0 & \text{otherwise}\,. \end{cases} \tag{2.43}$$

This recovers the ζ-statistic of Kaiser (1995), which is the average mass in a circular aperture minus the average mass in an annulus around the aperture. In this case the aperture mass can provide a lower bound for the mass of a galaxy cluster.

For the sake of simplicity and relevance to later chapters in this work, I will from now on limit the discussion to radial symmetric weight functions $U(\vartheta) = U(|\boldsymbol{\theta}-\boldsymbol{\theta}_0|)$, although the M_{ap}-statistic can be computed in much more general apertures as was shown by Schneider & Bartelmann (1997). The aperture mass in Eq. (2.41) is defined in terms of the surface mass density κ. It is possible to find an expression that directly relates the observable shear γ with M_{ap}.

$$M_{\mathrm{ap}}(\boldsymbol{\theta}_0) = \int_{\mathrm{sup}\,Q} \mathrm{d}^2\theta\,Q(\vartheta)\gamma_{\mathrm{t}}(\boldsymbol{\theta};\boldsymbol{\theta}_0)\,, \tag{2.44}$$

where we define the tangential shear γ_{t} relative to a point $\boldsymbol{\theta}_0$ by

$$\gamma_{\mathrm{t}}(\boldsymbol{\theta};\boldsymbol{\theta}_0) = -\Re\left[\gamma(\boldsymbol{\theta}+\boldsymbol{\theta}_0)\mathrm{e}^{-2\mathrm{i}\varphi}\right]\,, \tag{2.45}$$

where (ϑ, φ) are polar coordinates with respect to $\boldsymbol{\theta}_0$, and the weight function $Q(\vartheta)$ is related to $U(\vartheta)$ by

$$Q(\vartheta) = \frac{2}{\vartheta^2} \int_0^\vartheta d\vartheta' \, \vartheta' U(\vartheta') - U(\vartheta) . \qquad (2.46)$$

On real data the aperture mass can be estimated by a sum over the N_g galaxy ellipticities inside the aperture,

$$M_{\mathrm{ap}}(\boldsymbol{\theta}_0) = \frac{1}{n} \sum_{i=1}^{N_g} Q(\vartheta_i) \varepsilon_{ti} . \qquad (2.47)$$

Here n is the number density of FBG and the tangential component of the ellipticity has been defined in analogy to Eq. (2.45).

The significance of a peak in maps of aperture mass can be estimated in two ways. Either numerically by randomizing the orientation of the FBG while keeping their positions and ellipticity moduli fixed and estimates the variance from the scatter of a number of realizations, or analytically by using the fact that in the case of no lensing $\langle M_{\mathrm{ap}}^2 \rangle \equiv 0$ holds. Then the RMS dispersion of the M_{ap}-statistic becomes $\sigma_{M_{\mathrm{ap}}} = \sqrt{\langle M_{\mathrm{ap}} \rangle^2}$, which is

$$\sigma_{M_{\mathrm{ap}}} = \frac{\sigma_\varepsilon}{\sqrt{2}n} \left[\sum_{i=1}^{N_g} Q^2(\theta_i) \right]^{1/2} , \qquad (2.48)$$

using

$$\langle \varepsilon_i \varepsilon_j \rangle = \frac{\sigma_\varepsilon^2}{2} \delta_{ij} . \qquad (2.49)$$

What remains to be fixed is the shape of the weight function. Several proposals with varying suitability for galaxy cluster observations are available in the literature. Schneider et al. (1998) propose a family of polynomial functions,

$$Q_P(x) = \frac{(1+l)(2+l)}{\pi \theta_{\mathrm{max}}^2} x^2 (1-x^2)^l H(1-x) , \qquad (2.50)$$

where $x = \vartheta / \theta_{\mathrm{max}}$ is a dimensionless coordinate in units of the maximal filter radius θ_{max} and $H(x)$ is the Heaviside step function. While functionally

simple and fast to compute this function is far from ideal if one wants to use the aperture mass statistic to search for galaxy clusters (Schirmer 2004; Hennawi & Spergel 2005, HS05) . To increase the signal-to-noise ratio of a galaxy cluster the filter function Q should follow the shear profile of the cluster as closely as possible. The aperture mass then becomes a *matched filter technique* for weak lensing detections of galaxy clusters. N-body simulations predict the shape of collapsed halos to follow an NFW profile (Navarro et al. 1997) . The shear of an NFW profile can be computed analytically (Bartelmann 1996; Wright & Brainerd 2000) but the resulting expressions are complex and time-consuming to evaluate. Schirmer (2004) proposed a simple approximation to the NFW shear profile

$$Q_{\mathrm{NFW}}(x) = \frac{\tanh x}{x} \, , \qquad (2.51)$$

that is much faster to compute than the full expression. The foregoing equation is not used directly for the computation of M_{ap} but exponential cut-offs are multiplied to Eq. (2.51) as $x \to 0$ and $x \to \infty$,

$$Q_{\mathrm{NFW}}(x; x_{\mathrm{c}}) = \frac{1}{1 + e^{6-150x} + e^{-47+50x}} \frac{\tanh(x/x_{\mathrm{c}})}{x/x_{\mathrm{c}}} \, . \qquad (2.52)$$

The purpose of these cut-offs is (1) to avoid finite field effects as the weight function (2.51) formally extends to infinity but data is only available on a finite field; and (2) to downweight the signal close to the cluster core where cluster dwarf galaxies may pollute the signal and where the reduced shear g rather than the shear γ should be used. The parameter x_{c} in Eq. (2.52) controls the shape of the filter function. For small values of x_{c} more weight is put to smaller filter scales. In the absence of the exponential cut-offs variations in x_{c} and θ_{max} are obviously degenerate but the exponential cut-off makes the weight function (2.52) a two parameter family. Hetterscheidt et al. (2005) find that the optimal value of $x_{\mathrm{c}} = 0.15$ for a range of cluster masses and redshifts and I will use this value throughout this thesis.

Schirmer (2004) finds that the function (2.52) is much more efficient than the polynomial filter (2.50).[1] This observation is confirmed by HS05 who

---

[1] In cluster searches the efficiency is the percentage of cluster detections that are true clusters (1 – fraction of false positives). The completeness is the fraction of true clusters that generated a cluster signal (1 – fraction of false negatives).
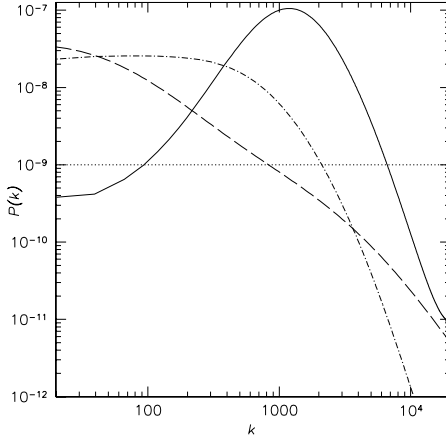
Figure 2.4: The construction of the $M_{\rm ap}$ filter function proposed by Maturi et al. (2005). The dot-dashed line is the square of the cluster shear $|\gamma|^2$. The dotted curve is the white noise contribution of the FBG, while the dashed line is the power spectrum of the effective convergence. The thick solid line is the resulting filter.

use a similar analytical approximation to the NFW shear profile to test weak lensing cluster searches on ray-tracing simulations. Hennawi & Spergel find that a filter following the NFW shear profile has 2–3 times fewer false positives in weak lensing cluster searches than the polynomial filter.

The projection of large-scale structure (LSS) along the line of sight is a serious contaminant for every weak lensing observation of galaxy clusters. Such projections of sheets and filaments inevitably lead to false cluster detections at all significance levels expected from real clusters (HS05) and missed cluster detection except for the most massive systems (Hamana et al. 2004). It was shown by HS05 that even in the absence of shape noise the efficiency of a weak lensing search for galaxy clusters does not exceed 80%. The efficiency of such a survey depends on the shape of the filter function.

Maturi et al. (2005) proposed to treat the projection of LSS as another noise source and constructed a filter that follows the NFW profiles as closely as possibly while downweighting the cosmic shear signal on scales of interest. The general solution of this problem has the following form in Fourier space,

$$\hat{Q}_{\rm LSS}(k) = \frac{1}{2\pi} \left[\int \mathrm{d}^2 k \, \frac{|\hat{\tau}(\boldsymbol{k})|^2}{P_{\rm N}(k)} \right]^{-1} \frac{\hat{\tau}(k)}{P_{\rm N}(k)} \, , \qquad (2.53)$$

where $P_{\rm N}$ is the power spectrum of all noise sources and τ is the expected
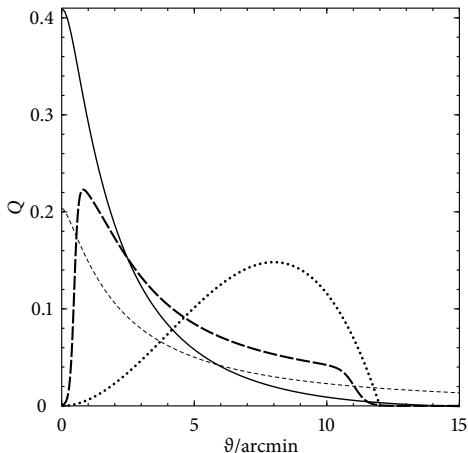
Figure 2.5: Comparison of filter functions. The solid line is the M_{ap} kernel proposed by Maturi et al. (2005). The long-dashed line is the NFW filter with exponential cut-offs by Schirmer (2004). The dotted line is the polynomial of Schneider et al. (1998). The shear profile of an NFW halo is given by the thin short-dashed line for comparison.

shear profile of an NFW halo. The components contributing to P_N are the shape noise of the FBG P_ε and the power spectrum of the effective convergence P_κ. The former is described by Poisson noise and is hence constant for all Fourier modes. Its value is determined by the intrinsic ellipticity dispersion and the number density of galaxies

$$P_\varepsilon(k) = \frac{\sigma_\varepsilon^2}{2n} \ . \tag{2.54}$$

The latter, P_κ, needs to be computed from the three-dimensional power spectrum of cosmological density fluctuations. Figure 2.4 shows the various components contributing to the construction of Q_{LSS}. As one would expect, P_κ has a lot of power on those scales where the signal $|\hat{\tau}|^2$ is located. Consequentially, a perfect separation of the cluster signal and the LSS signal is not possible. This is also intuitively clear since clusters are part of the LSS and their contribution is contained in P_κ. The resulting filter is narrower than Q_{NFW} because the signal will be suppressed on larger scales where the cosmic shear noise dominates over the cluster signal.

Figure 2.5 shows a comparison of the three M_{ap} kernels discussed in this section, as well as the shear signal of an NFW profile.

3

Image Reduction Pipeline

During the last decade the design of CCD cameras for optical astronomy has fundamentally changed. In the early days of CCD cameras detectors of only a few hundred pixels side length were the norm, whereas CCD chips with up to 4000 × 4000 pixels are available today. Due to technical limitations in the manufacturing process larger chips cannot be feasibly produced and cameras requiring larger detector arrays are built as *multi-chip cameras*. In these cameras several CCD chips are placed in the detector plane to cover a larger area. An example is of the layout of such a camera is shown in Fig. 3.1. The development of these *wide-field imagers* with fields-of-view (FOV) of up to 1 square degree is a fundamental necessity for current and future imaging surveys like the CFHT Legacy Survey and KIDS.

Compared to single-chip cameras these new instruments produce an enormous data volume. For example a raw data frame from the Wide-Field Imager (WFI) at the ESO/MPG-2.2 m telescope in La Silla has 135 MB; nightly data volumes including calibration files are around 20 GB. This data flow can be handled with current computers and harddisks but it was a serious obstacle when WFI was commissioned in 1999. Likewise, the data flow of newer wide-field imagers like Megacam at the CFHT or, starting in the first half of 2007, ΩCam at the VST is a challenge for hardware currently available to the average observer.

In addition to the data volume, the multi-chip layout of the cameras adds a new layer of complexity in the reduction and calibration of data. Contrary to the first impression one might have, a multi-chip camera cannot simply be treated as a collection of N single-chip cameras, i.e., there are steps in the reduction in which the detectors cannot be treated individually. We have to account for the mosaic structure with its gaps, not perfectly aligned chips, curvature of the focal plane, and differential image distortion across the field
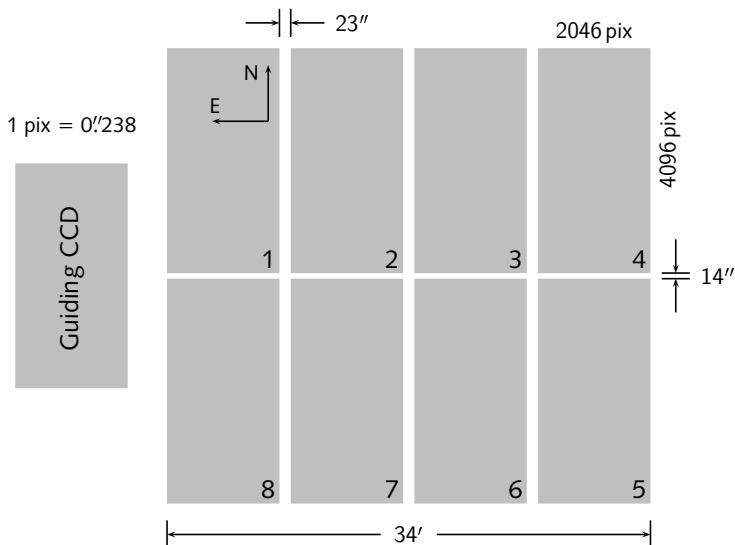
Figure 3.1: The CCD layout (not to scale) of the ESO Wide-Field Imager at the the ESO/MPG-2.2 m telescope. The chip array is shown as it is projected on the sky with north up and east to the left.

of view. In addition, to achieve a homogeneous photometric calibration, the differences in sensitivity, gain, and noise properties of the chips pose new challenges for calibration techniques.

These issues are non-trivial as is illustrated by the history of WFI. After WFI went into operation in January 1999, only 35 refereed papers based on data taken with this instrument were published until the end of 2002. Recently, the number of papers based on WFI data has risen but the publication rate is still behind that of other ESO instruments. The existing papers demonstrate that WFI is a powerful instrument that can lead to exciting scientific results. This fact, combined with the high pressure factor on WFI, which is among the highest of all ESO instruments, shows that the low number of publications is due to challenges in data handling and volume and not the quality of the instrument or the science that can be done with it.

Although wide-field imagers have been available for the community for more than five years, only now a consensus on *standard* reduction techniques to attack these new problems is beginning to emerge. This is stimulated by public releases of at least two pipelines for the reduction of single- and multi-chip camera data and discussion among the "power users" of such pipelines, e.g., within the AstroWise consortium[1]. A comparison of the results of the "Garching-Bonn Deep Survey" (GABODS) pipeline (Erben et al. 2005, ESD) described in this Chapter and the EIS/MVM pipeline (Vandame 2004), whose functionality is outlined in Chap. 5.1 and App. C, is presented in Chapter 5.3.

During the thesis work presented here I participated in the development of the GABODS pipeline, an automatic image reduction system for optical single and multi-chip instruments. This pipeline is described in detail by ESD. It was used for the image reduction of the B- and V- band data in Chap. 4 and the data of the XMM-Newton follow-up survey presented in Chap. 5. While this Chapter describes the pipeline in general, it focusses on the areas in which I significantly contributed. Namely, these are the automatic photometric calibration of images (single and coadded), strategies for de-fringing, and the reduction of medium-band filter data. The photometric calibration of coadded images is also described in Hildebrandt et al. (2006). Quality control of the reduced and calibrated products by comparing with an independent reduction is covered in Chap. 5.3. Other areas of the pipeline are described as well to give a full overview of the data reduction for later chapters. For the details of reduction steps, the interested reader can refer to ESD. This chapter is not meant as an introduction to the reduction of optical imaging data, nor is it a manual of the many programs used in the GABODS pipeline. The reader in need of the former is recommended to read, e.g., "A User's Guide to CCD Reduction with IRAF"[2], while the reader wishing to be informed about the inner workings of such programs should consult the appropriate manuals.

The GABODS pipeline has been tested with a number of instruments – single- and multi-chip – but the discussion in this work focusses on the reduction of data from WFI, for which the pipeline was primarily developed.

---

[1] http://www.astro-wise.org
[2] http://iraf.noao.edu/iraf/ftp/iraf/docs/ccduser3.ps.Z

Most of the instrument specific information like number and size of the chips, orientation, size of the overscan area is described in an instrument definition file. This allows to quickly adapt the pipeline to new instruments.

3.1 Pipeline Characteristics

No automated pipeline reduction will lead to the best possible result in all circumstances. The optimal reduction strategy for any given data set depends on the science goals, observing strategy, and instrument characteristics. It is therefore important to keep the design goals of the GABODS pipeline in mind when discussing the reduction algorithms.

The primary science driver behind the development of the GABODS pipeline is weak gravitational lensing. Weak lensing data is typically taken on empty fields at high galactic latitude and this is what the pipeline is optimized for. Nevertheless, it is possible to reduce crowded fields or fields with extended objects using this pipeline, but some modifications might be necessary. The intended application also defines the main requirements on the pipeline. Weak lensing crucially depends on the accurate shape measurement of very faint and small objects, leading to the following requirements:

- a very accurate alignment of subsequent (dithered) exposures before the final stacking process. This requires good knowledge of the astrometric distortions;

- a re-mapping of subsequent exposures with sub-pixel accuracy to allow an accurate measurement of object shapes;

- a good knowledge of the noise properties across the field. This is important to detect as many faint galaxies as possible without a large number of spurious objects. This also requires a sky background that is as flat as possible.

It can be seen from this list that the main challenges are astrometry and flat-fielding. Good photometry is not a top priority for weak lensing applications. Nevertheless, routines for photometric calibration of single nights and the propagation of these night solutions to stacked images were developed and integrated into the pipeline.

The pipeline is to a large degree based on previously existing programs and libraries. For example, programs to obtain image statistics exist in large numbers. A fundamental design decision of the GABODS pipeline was to use such programs as much as possible. These programs are then "glued" together with shell scripts. This leads to a very modular structure of the pipeline. The advantage of this approach is that a lot of time can be saved during development because not everything has to be written from scratch. Also, if for a particular data set the science goals differ from the ones outlined above, replacing individual modules with more suited reduction strategies is a relatively simple process. The obvious disadvantage of this approach is the large amount of disk IO needed to transfer intermediate results between modules, significantly slowing the pipeline in comparison to a monolithic design.

Many of the algorithms used are similar to those developed during the EIS (ESO Imaging Survey) Wide Survey carried out 1997–1999. The main pillars of our pipeline are the following software modules:

– The LDAC software: The Leiden Data Analysis Centre (LDAC) software[3] was developed for the DENIS survey (Epchtein et al. 1997). It provides tools for the handling of FITS-LDAC catalogs, and astrometric and photometric calibration of mosaic data.

– TERAPIX software (Bertin et al. 2002): The pipeline uses `SExtractor` (Bertin & Arnouts 1996) for catalog generation in the astrometric and photometric calibration. `SExtractor` can produce a number of diagnostic *check-images*. These are described in the `SExtractor` manual (Bertin 2005). They are used at various places, including the creation of "super"-flats. `EYE` and `weightwatcher` are used for the detection of cosmic rays and the creation of mask and weight images. `SWarp` is used to re-sample images to a common reference grid.

– Eclipse and qfits tools (Devillard 2001): The pipeline makes use of several tools from the `Eclipse` library to read and modify FITS headers. Tools based on the `qfits` library are used in the early reduction stages.

---

[3] `ftp://ftp.strw.leidenuniv.nl/pub/ldac/software`

– Astrometrix: The `Astrometrix` package[4] is another module for the astrometric calibration of images.

– Imcat tools: From Nick Kaiser's imcat tools[5] the image calculator `ic` and the image statistic tool `stat` are used in the pipeline.

All the tools, with the exception of `Astrometrix`, which is written in `perl`, are written in the C programming language. Together with the shell scripts connecting the pipeline modules and some other modules written in `python`, this choice of programming languages makes the pipeline as a whole portable to a wide variety of Unix based systems

A large portion of the reduction processes is performed independently on the individual images associated with a chip, e.g., bias frames are created independently for each chip. It is an obvious choice to parallelize the steps that do not require global camera information. Parallelization is straight-forward because the independent processes need no message passaging or synchronization scheme. The only synchronization that is necessary is that the pipeline waits at the end of the parallelized reduction step until all jobs are finished, i.e., all data from all chips are processed.

In practice, parallel processing is implemented by a *parallel manager* process that distributes the tasks per chip to different processors or nodes, in the case of cluster environment. For example, for the 8 chip wfi and a 4 cpu machine, the parallel manager will instruct cpu1 to process frames from chips 1 and 5, cpu2 from chips 2 and 6, and so on. The case of having only one cpu is in this framework just an extreme case for the parallel manager, which does not require a conceptually different treatment than 2, 4, or 8 cpus. The parallel manager provides a single interface for running the pipeline, whether it is in serial or in parallel mode. The advantage of this mode of parallel processing is simplicity of implementation. The obvious disadvantage is that the available computing resources are not ideally used in a number of circumstances. For this scheme to be effective the number of chips must be divisible by the number of nodes/cpus. Having more nodes/cpus than chips does not lead to further speed enhancements as the additional nodes/cpus will remain unused.

---

[4]`http://www.na.astro.it/~radovich/wifix.html`
[5]`http://www.ifa.hawaii.edu/~kaiser/imcat/`

3.2 Terminology

Before I describe the data flow in the pipeline and the algorithms used, it is helpful to define a few terms:

- – Chip, CCD: an individual detector in a (wide-field) camera;

- – Exposure: a single shot/observation with the whole camera;

- – Image, frame: the part of an exposure associated with an individual CCD;

- – BIAS: image with zero seconds exposure time;

- – DARK: image with non-zero exposure time with closed shutter;

- – FLAT: image of a uniformly illuminated area; this can be a white screen in the telescope dome (DOMEFLAT), or the sky during twilight (SKYFLAT);

- – SCIENCE: image of the actual target of scientific interest;

- – SUPERFLAT: image created from properly stacked SCIENCE images to correct for large scale illumination inhomogeneities;

- – STANDARD: image of photometric standard stars;

- – Names of other calibration images will appear in SMALLCAPS; their meaning will be clear within the context;

- – Mosaic: the final coadded image, or synonymous with exposure;

- – Dithering: off-setting the telescope between exposures;

- – Stack: set of n images from one chip that have been combined pixel by pixel;

- – Run: set of images sharing the same calibration files;

- – Set: set of images taken with one instrument configuration, e.g., filter or objective, that have the same target.

The division of the processing into *run-* and *set-processing* is an important concept of the GABODS pipeline and deserves further explanation. The first steps of SCIENCE frame reduction like de-biasing and flat-fielding are independent of the pointing position. Thus, all SCIENCE images taken during a limited time interval with the same instrument configuration, e.g., filter, are processed together. For example, typically all R-band exposures from a night will be reduced as a group. The defining feature of these groups being reduced together is that they use the same calibration data. The time interval for which this is possible depends on the stability of the instrument and the ambient conditions. For WFI typical intervals for B-band exposures are one week or even more, and 2–3 nights for R-band data. In I-band the fast time variability of the fringe pattern intensity can lead to several runs per night.

The final data reduction steps depend on the pointing position of the telescope. These include, e.g., joint astrometric calibration of a set of dithered images, scaling to a common photometric system, and mapping of images to a common reference grid. This is done during set-processing in which all reduced SCIENCE images of a target observed with the same instrument configuration are collected and processed together.

3.3 Run-Processing

3.3.1 From Raw to Flatfielded Images

Data from different instruments comes in a variety of formats. While virtually all raw astronomical data from optical cameras is stored as FITS images, further specifics like header keywords are not standardized. The first step of run-processing has to be standardization of the data structure and header content, so that any further processing is independent of the camera specific raw data format.

Data from multi-chip cameras is often stored in multiple extension FITS (MEF) format, with one chip per extension. As the very first step, exposures are split into individual images. All further run-processing is performed on images. The parallelization of the pipeline also depends on the simultaneous execution of tasks on different images.

The original FITS header is replaced with a minimal set of header keywords necessary for the automated pipeline reduction. As this involves the generation of new keywords with values derived from the original header, this part is very instrument specific. For example the entry for filter, which varies across many ESO instruments and developed with time, is brought to a standard format in the FILTER keyword. An example of such a standard pipeline header is given in App. A.

All images are overscan corrected by estimating the mean of the data in the overscan region defined by the instrument definition file of the pipeline and subtracting it. The overscan corrected BIAS images are stacked to produce a master BIAS frame. The stacking is performed by estimating the median value of the input images with a rejection of high and low values. The master BIAS frame is subtracted from all images.

To produce master FLAT images all SKYFLAT, or DOMEFLAT in the absence of the preferable SKYFLAT images, are scaled to a common median, and then stacked using the same algorithm as for the BIAS frames.

These master FLAT frames are very good for taking out small-scale, pixel-to-pixel variations in the SCIENCE frames. Experience shows, however, that in wide-field images often large-scale variations in the background intensity remain after dividing the SCIENCE frames by the master FLAT image rescaled to unity. To eliminate these, the technique of SUPERFLATS can be used. SUPERFLATS are flatfield images produced directly from the SCIENCE images by the following steps:

1. The creation of SUPERFLATS starts from the flatfielded SCIENCE images. All astronomical sources are removed from these images. `SExtractor` is used to detect objects and flag their pixel position in the `-OBJECTS` check-image.

2. The `SExtractor` check-images are rescaled to a common median.

3. The SUPERFLAT frame is created by a median stacking of the rescaled check-images, in which flagged pixels are ignored. If not at least three input images have an unflagged pixel at a given position the mean of the median of all input images is assigned to this pixel.

4. The SUPERFLAT image is heavily smoothed by creating a `SExtractor` background check-image with a background mesh of 512 pixels.

The resulting ILLUMINATION image is the basis for removing large scale flatfield variations.

It is essential for later photometric calibration to equalize the photometric zeropoints of all CCDs. This is achieved by scaling all chips to the same sky background, in practice to the median of the CCD with the highest count-rate in a flatfield image. This is preferably the SUPERFLAT image but can be the SKYFLAT or DOMEFLAT if no SUPERFLAT is generated. The ILLUMINATION images are rescaled and the SCIENCE images are then divided by the rescaled ILLUMINATION frames. The resulting superflatted SCIENCE images have a homogeneous background level.

The way SUPERFLAT images are created imposes strict conditions on the SCIENCE images entering the process. Sufficient sky coverage for all pixels is essential if the SUPERFLAT is to provide a good estimate of the sky background at all pixels. This typically requires a series of at least 10 dithered exposures with offsets larger than the largest object in the exposure. This condition on the size of the dither pattern is easy to fulfil for empty high-galactic latitude fields but can pose serious problems for fields with extended objects like nearby galaxies or diffuse emission. Also, galactic fields, globular clusters, or nearby dwarf galaxies are often so dense that even with a large number of dithered exposures many pixels never see the sky background. If one wants to generate SUPERFLAT images for these type of observations the only choice is to observe empty fields during the same observing run. This is a serious investment of observing time and cannot be ensured for service mode observing, in which the observer has no control how many of his observing blocks (OBS) are executed per night. The latter point is also critical for the minimum number of exposures entering SUPERFLAT creation. A typical OB for WFI has 5 dithered exposures, meaning that at least two OBS need to be executed to obtain reliable background estimates for all pixels.[6]

Another problem for SUPERFLAT creation are extended halos around bright starts and extended low surface brightness structures like tidal tails. These are not reliably detected and masked by `SExtractor` and enter the SUPERFLAT, resulting in a significant overestimation of the sky level at the affected pixels. The only solution for this problem is to exclude the affected images from the SUPERFLAT creation. To this end I developed a mechanism

---

[6]The number of exposures is higher in I-band, see Sect. 3.3.2 below.

for the pipeline that lets the users specify which *images* instead of whole exposures should be excluded, but still provides proper rescaling of the SCIENCE and ILLUMINATION images to a common zeropoint. To achieve this two sets of SUPERFLAT frames are created; one set with all images, which is used to determine the factors for scaling to the same sky level, and one set containing only "good" object subtracted SCIENCE frames. The latter set is used to create the ILLUMINATION images to be applied to the flatfielded SCIENCE frames.

Finally, SUPERFLAT images can only be created if the background of the SCIENCE images is dominated by the night sky emission and not by read-out noise of the camera electronics. This is usually the case for typical exposure times of SCIENCE images in broad-band filters like Johnson-Cousins BVRI. The sensitivity of WFI in the U-band is often so low that the background is read-noise dominated. This is also the case for exposures taken with medium- and narrow-band filters, which thus cannot be flatfielded with SUPERFLAT images.

It is important to note that flatfielding with SUPERFLAT images does not correct for the spatial variation of photometric zeropoints across chips reported by Manfroid & Selman (2001) and Koch et al. (2004).[7] In fact, Manfroid & Selman argue that the aim of a flat sky background is incompatible with a constant zeropoint and superflatting exacerbates the effects of inhomogeneous illumination. The results of Koch et al. indicate that the functional dependence of the relative zeropoint change with pixel position is relatively independent of wavelength. Thus, reliable colors of objects can be measured even without illumination correction. It is then obviously imperative that all images are reduced in a homogeneous fashion, e.g., in a set of observations done in broad- and medium-band filters even the broad-band data must not be superflatted. This specific problem had to be taken into account for a study of the Fornax dwarf galaxy using the GABODS pipeline (Kayser et al., in preparation).

---

[7]Confoundingly, the technique to correct for this effect is often called "illumination correction", which is not to be confused with the ILLUMINATION image above.

3.3.2 Fringing Correction

Fringing is an additive instrumental signature in red passbands caused by diffraction of light in the CCD substrate. Fringes are most prominent in thinned CCDs optimized for observations in blue passbands. Fringes are spatially quickly varying wave-like structures on the images. The geometry of the pattern is usually constant with time but the intensity changes, sometimes on timescales of a few minutes, depending on a variety of parameters like sky brightness, airmass, position on the sky. The amplitude of the fringe pattern in WFI images is typically only ~ 1% of the sky level in R-band images but reaches up to 10% in I-band.

If the fringe intensity is sufficiently stable over all SCIENCE images in a run the following procedure effectively removes fringes:

1. The SUPERFLAT images contain the small scale additive fringing component of the SCIENCE images. Due to the heavy smoothing this signal is not anymore present in the ILLUMINATION images. FRINGE images can thus be created by subtracting the ILLUMINATION images from the SUPERFLAT images.

2. Because the FRINGE frames will be subtracted from the superflatted SCIENCE frames I divide the FRINGE images by the appropriate rescaled ILLUMINATION images. Note that this step is a deviation from the defringing procedure described in ESD. I will discuss the differences below.

3. We assume that the intensity of the fringes scales linearly with the sky brightness. The scaling factor is computed as the ratio of the medians of superflatted SCIENCE and ILLUMINATION images.

4. The scaled FRINGE frame is subtracted from the superflatted SCIENCE images.

ESD do not apply the ILLUMINATION frames as I do in step 2. This is not strictly correct as the FRINGE maps are computed from the SCIENCE images before they are superflatted, but the FRINGE maps applied are after superflatting. On the one hand the effect is relatively small but noticeable in some runs. Not performing step 2 can sometimes lead to residual fringing

with varying intensity across an image. On the other hand, the effect is in most cases smaller than the deviation from linearity assumed in step 3. Performing step 2 in these cases can harm the data quality. Extended halos around bright objects are especially prominent in red passbands. As these are often not masked during SUPERFLAT creation, they remain as artifacts in the subsequent ILLUMINATION and FRINGE images. Performing step 2 multiplies this error, leading to noticeable dark rings around bright objects. Nevertheless, during reduction of the XMM-Newton Follow-Up Survey (Chap. 5) I opted to always perform the superflatting of the FRINGE frames to achieve a homogeneous reduction.

The de-fringing algorithm of the GABODS pipeline performs very well for WFI R-band images in which no residual fringing is visible. We estimate that the amplitude of any residual fringing must be below 0.1% of the night sky brightness. For I-band images residual fringing can be as low as ∼ 0.1% if a good SUPERFLAT image can be created and the linearity assumption of step 3 holds. For the latter to be true the sky brightness must not change by more than ∼ 10%. This places strict limits on the time interval a run can cover and defines the observing strategy for I-band observations. Typical time intervals in which this condition is true do not exceed 1–2 h and should not contain the rise or set of the moon or bright planets.[8] This in turn limits the number of exposures that can enter the SUPERFLAT construction and hence the quality of the SUPERFLAT and FRINGE images, especially if bright or extended objects are in the FOV.

A typical strategy for WFI I-band would be to take 10 exposures in an OB of 1 h hour duration. Depending on the stability of the sky brightness, one or two OBs can be reduced in one run.

3.3.3 Photometric Calibration of Images

The GABODS pipeline supports an almost fully automatic photometric calibration of final coadded SCIENCE images, if at least a subset of reduced SCIENCE frames entering a coaddition stack can be photometrically calibrated. The photometric calibration of SCIENCE images is done with STANDARD frames obtained in the same night as the SCIENCE images.

---

[8] The rise or set of Venus can change the sky brightness as much as 4%.

STANDARD exposures are reduced in a fashion similar to SCIENCE exposures. They are overscan corrected, the master BIAS frame is subtracted, and flatfielded using the same master FLAT image as the SCIENCE images. If the SCIENCE images were superflatted, the STANDARD images have to be superflatted with the ILLUMINATION image created from the SCIENCE images. This is important to ensure photometric homogeneity between STANDARD and SCIENCE frames.

If necessary the FRINGE map created from the SCIENCE images is rescaled and subtracted from the superflatted STANDARD frames. Fortunately, most STANDARD images are taken with such short exposure time that the sky background cannot create a strong fringing pattern. However, if significant fringing is present in STANDARD exposures its removal is especially difficult. The reason is that STANDARD observations are usually taken at different times during the night (sometimes even in twilight), at different sky positions and various airmasses. This often leads to fringing patterns with intensities very different from those present in SCIENCE images.

To generate object catalogs that can be used for photometric calibration bad pixel masks for the STANDARD images are created. They mark pixels not suitable for photometric measurements, such as bad pixels or cosmic rays. The creation of these FLAG images is described in Sect. 3.3.4.

Using the FLAG images, object catalogs are created with SExtractor from the reduced STANDARD images. To match the found objects with standard stars from, e.g., the Landolt (1992) or Stetson (2000) catalogs, an astrometric solution for the STANDARD images has to be derived first. This is done with the LDAC astrom tools to match objects found in the STANDARD exposures to the USNO-A2 catalog (Monet et al. 1998). The number of objects found in the WFI STANDARD exposures is sufficiently high to derive a second-order astrometric solution separately for each image. This is enough to reliably match photometric standard star catalogs with our catalogs.

All fluxes in our STANDARD images are normalized to an exposure time of 1 s. From the database of matched standard stars, the coefficients of the equation

$$m - m_{\mathrm{inst}} = ZP + k \cdot \mathrm{airmass} + CT \cdot CI \, , \tag{3.1}$$

i.e., the zeropoint ZP, the extinction coefficient k, and the color term CT are determined, where m is the standard star's magnitude, m_{inst} the instru-
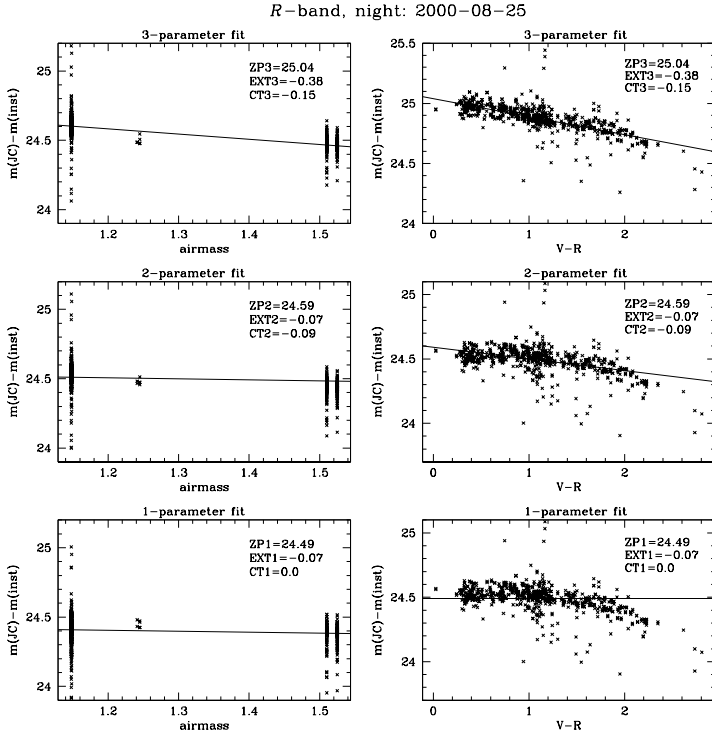
Figure 3.2: Plot showing the three different photometric solutions of a night (from Hildebrandt et al. 2006). The first row shows the results for the 3-parameter fit, the difference between instrumental magnitude (data from all eight chips) and standard star magnitude plotted versus airmass (for color zero) on the *left* and versus color (for airmass one) on the *right*. In the second and third row the same diagrams are shown for the 2- and the 1-parameter fit.

mental magnitude measured on the reduced STANDARD frame, and *CI* is a color index of the standard star, e.g., $(B - V)$. This is done using a non-linear least-squares Marquardt-Levenberg algorithm with an iterative 3σ rejection, which allows rejected points to be used again if they are compatible with later solutions. As this algorithm is not guaranteed to converge, the iteration is aborted as soon as one of the following three criteria is true:

1. The iteration converged and no new points are rejected.

2. The maximum number of iterations (set to 20) is reached.

3. More than a fixed percentage (set to 50%) of points is rejected.

In a first step all three coefficients are fit simultaneously. However, in order to reliably estimate the extinction coefficient standard star observations must be spread over a range of airmasses. This is sometimes neglected by observers or impeded by changing observing conditions. To find an acceptable solution in this case, the user can supply a default value for the extinction coefficient. The fit is then repeated with the extinction coefficient fixed at the user supplied value and the zeropoint and color term as free parameters.

Although wide-field observations of Landolt/Stetson fields typically cover a wide range of stellar colors, the user can also supply a default value for the color term. This is then used for a 1-parameter fit in which the zeropoint is the only free parameter. An example of the three different photometric solutions is given in Fig. 3.2.

In an interactive step the user can then choose between the 1-, 2-, and 3-parameter solution or reject the night as non-photometric. The FITS headers of the SCIENCE frames belonging to the same night are updated with the zeropoints and extinction coefficients of all solutions and the information which solution is the one preferred by the user.

We note that we perform the fit simultaneously for all chips. After sky background equalization the zeropoints of chips agree within 0.01–0.03 mag. We do not take into account possible color term variations between individual chips that are expected due to slightly different CCD response curves. Notable differences can occur in the U- and Z-filters that are cut off by the CCD response.

We use the `SExtractor MAG_AUTO` parameter to measure the instrumental magnitudes. Although we do not know at which aperture we finally measure the standard star's magnitude, `MAG_AUTO` turns out to be a reliable estimate for the total flux of bright sources. More importantly we do not need to manually adapt the size of the aperture for varying observing conditions, e.g., large seeing variations. We checked that our results with `MAG_AUTO` and appropriately chosen aperture magnitudes are in excellent agreement.

3.3.4 Weighting and Flagging

Not all pixels on a CCD carry values linearly related to the sky intensity imaged onto the pixel position. Defects like cold or hot pixels, or bad columns are present on all CCDs. Any pipeline reduction must be able to automatically detect and exclude them from entering the final coaddition as well as pixels affected by cosmic ray hits. The GABODS pipeline takes care of such bad pixels and other pixels with non-Gaussian noise properties in a number of ways.

Bad pixel FLAG maps are created from FLAT, SUPERFLAT, and master DARK images. The latter are created in exactly the same fashion from DARK exposures as the master BIAS frames are created from BIAS exposures. A thresholding procedure is applied and all pixels above or below the predefined thresholds are considered to be bad pixels. Using DARK images to detect bad pixels and columns is – at least for WFI – much more efficient than using BIAS frames. Many of the image defect – especially dark columns next to hot columns – appear only once a certain count level, which is well above that of BIAS exposures, is reached. In the absence of DARK exposures SKYFLAT or SUPERFLAT images can often be used to create FLAG images of sufficient quality. However, the majority of image defects is detected in the DARK images and the other two images serve mainly as a redundancy.

In addition to the bad pixel FLAG maps, which are valid per run, pixels containing unusable data are also detected per SCIENCE image to mask

1. saturated pixels, which are identified by a thresholding to the SCIENCE images;

2. cosmic rays. These are detected using `SExtractor` with a special

filter for cosmic ray detection generated with EYE (Nonino et al. 1999);

3. other extended defects like satellite tracks and ghost images or other artifacts caused by reflections from bright stars in or close to the FOV. These must be masked by hand at the end of the run processing.

Except for excluding measurements of photometric standard stars affected by flagged pixels the FLAG images are also used to create WEIGHT images described in the following paragraphs.

The gaps in multi-chip cameras, the intrinsic gain variations, and often also vignetting at the edges make the noise properties of coadded images very complex. The noise properties of each SCIENCE image is described by a WEIGHT image. The noise properties of the final coadded image are then straightforwardly obtained by a proper coaddition of the individual WEIGHT images into a combined one. See Sect. 3.4 for details of the coaddition process.

Individual weight images are created from the master FLAT frames. These are rescaled to a mode of unity. Variations in relative sensitivity and thus noise show up as variations in the FLAT images. A thresholding is applied to flag pixels of very low sensitivity and the pixels marked in the FLAG images are set to zero in the WEIGHT images.

FLAG and WEIGHT images are produced with weightwatcher from the TERAPIX software package.

3.4 Set Processing

After the end of the run processing, SCIENCE images and their associated WEIGHT images are sorted by coordinates and filter into sets. For these sets a global astrometric and relative photometric solution must be found. This is a point at which the reduction of multi-chip data becomes more complex than that of exposures from single-chip cameras.

3.4.1 Astrometric Calibration

The set processing starts with the generation of high signal-to-noise ratio (SNR) catalogs of unsaturated stars. These catalogs are used for astrometric and relative photometric calibration of SCIENCE images (see Sect. 3.4.2). To this end SExtractor with a detection threshold of typically 5 pixels 5σ above the sky background is employed. These setting provide 3–6 objects per square arcminute in high galactic latitude fields.

Astrometric calibration is implemented as a two step process. In the first step, by comparison with an astrometric standard catalog, usually the Guide Star Catalog version 2.2 (GSC-2.2), a zero-order, single shift astrometric solution is calculated for each image. CCDs in multi-chip cameras will never be perfectly aligned but show tilts and rotations with respect to each other. The difficulty of astrometric calibration is further increased by the often large dither patterns needed for the creation of SUPERFLAT images and FRINGE maps. This leads to an overlap of images with very different distortion patterns. Consequently, the simple zero-order solution cannot be more than a first approximation from which a more elaborate astrometric solution must be derived.

In the second step Astrometrix is employed to derive a 2-d third-order polynomial describing the astrometric distortions for each image. This exact solution is critical for mapping objects onto each other during the final coaddition. For this purpose all high SNR objects (stars and galaxies) are matched with each other. This includes the objects in the overlapping regions due to the dither pattern. These are important for linking astrometric solutions of the individual SCIENCE images with each other. The typical RMS of catalogs like the USNO-A2 or GSC-2.2 is about 250 mas. This is not enough for sub-pixel registration of images. Astrometrix derives the *internal* solution matching overlap objects to each other simultaneously with the *external* solution tying the images to an astrometric reference catalog. In this χ^2 minimization the error of the external reference is fixed at 300 mas so that the internal matching receives a much higher weight in the minimization procedure. Given a wide enough dither pattern to allow for generous overlaps between chips, the internal solution is typically accurate to a tenth of a pixel. The accuracy of the absolute (external) astrometry is limited by the RMS of the reference catalog with its stated typical value.

3.4.2 Photometric Calibration of Stacks

Images to be coadded are often taken under different photometric conditions, e.g., the airmass changes over the course of extended observations. In many cases images in a set were obtained in different runs and will have different absolute photometric calibrations, or only a subset will have absolute photometric calibration. Like in the case of the astrometric calibration an internal *photometric* solution allows to scale all images to a common zeropoint, while an external photometric solution allows to convert measured count rates into a standard magnitude system. The latter of course requires that at least a subset of science images in a set have been photometrically calibrated during run processing.

The internal photometric solution is computed from the measured magnitudes of overlap objects. Once the astrometric solution is known, creating a table of paired objects in all science images is possible and determining an internally consistent photometric system is straightforward. The following algorithm is implemented in the LDAC tool `relphotom`, which the pipeline uses for this purpose.

Let j and j' be two overlapping images with N sources in common. We compute the mean deviation of magnitudes

$$M_{j,j'} = \frac{\sum_{i=1}^{N} W_i (J_i - J_i')}{\sum_{i=1}^{N} W_i} \, , \qquad (3.2)$$

with $W_i = (\sigma_{J_i}^2 + \sigma_{J_i'}^2)^{-1}$, where the σ are the measurement errors of the magnitudes J_i and J_i'. The relative zeropoints ZP_l for all M overlapping images are estimated by a χ^2 minimization with respect to ZP_k,

$$\chi^2 = \sum_{j,j'=1}^{M} \left[M_{j,j'} - (ZP_j - ZP_{j'}) \right]^2 \, , \qquad (3.3)$$

with an outlier rejection in $M_{j,j'}$. To make the system non-degenerate we demand that $\sum_i ZP_i = 0$.

After defining this internally consistent photometric system, *corrected zeropoints* for absolutely calibrated images tying the set to an external reference are calculated as

$$ZP_{\text{cor}_i} = ZP + kz_i + ZP_i \, , \qquad (3.4)$$
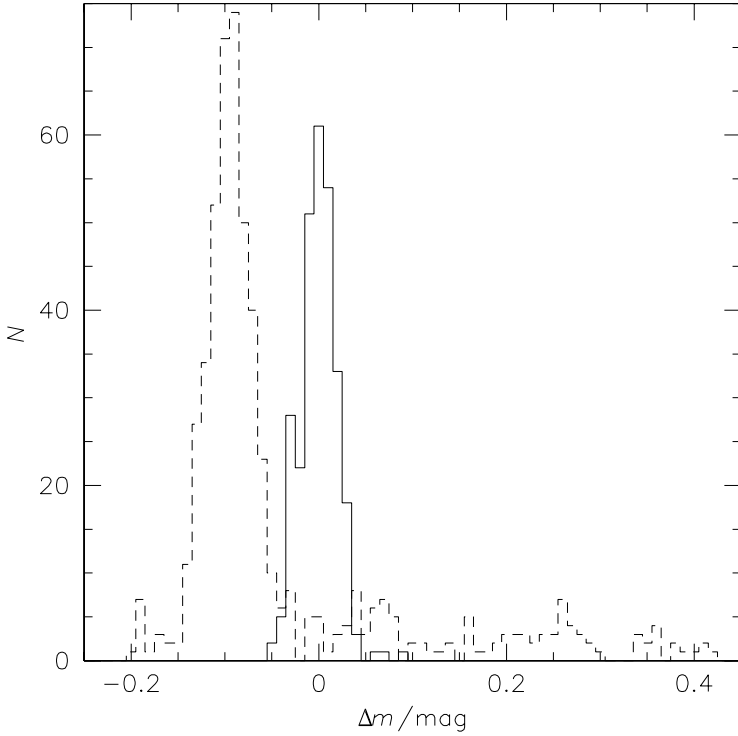
Figure 3.3: Distribution of the differences Δm between the corrected zero-points $1/N \sum_i ZP_{\mathrm{corr}_i}$ and the individual corrected zeropoints ZP_{corr_i} for a field from the Deep Public survey (Hildebrandt et al. 2006). The dashed line represents the distribution using the originally chosen photometric solution. The solid line is the distribution after manually re-choosing the photometric solutions for some nights.

where ZP and k are the zeropoint and extinction coefficient, respectively, determined for the night under consideration, and z_i is the airmass at which

the ith image was observed. The foregoing expression provides the absolute photometric calibration of an image (first term), corrects it for atmospheric extinction (second term), and ensures photometric homogeneity in the set (third term).

One expects that these corrected zeropoint coincide for all photometrically calibrated frames. This is usually true within a scatter of ∼ 0.05 mag. If, for any reason, a subset of photometrically calibrated data has a faulty external reference its corrected zeropoint will be very different from that of other data with external reference. This allows for a cross check of the photometric calibration if a set has data from different photometrically calibrated runs. This technique was successfully employed in Hildebrandt et al. (2006) as well as in the GABODS pipeline reduction of the Xmm-Newton Follow-Up Survey (see Chap. 5.2). This is also illustrated by Fig. 3.3, which is from a field of the Deep Public Survey (Hildebrandt et al. 2006). The dashed histogram shows the distribution of corrected zeropoints derived from the photometric solutions initially chosen during run processing. The scatter of corrected zeropoints is very large and shows offsets as big as 0.6 mag. This is a clear indication that at least some photometric solutions are erroneous. After further inspection of the night solutions the set of photometrically calibrated images was narrowed down. The solid histogram shows the distribution of corrected zeropoints after re-choosing the photometric solution for some nights in the set. The much narrower histogram indicates a reliable photometric calibration.

The photometric calibration of sets as it is done in the GABODS pipeline rests on the assumptions that

1. the zeropoint is spatially constant on the scale of an image. This is not necessarily true for wide-field imagers as shown by Manfroid & Selman (2001) and Koch et al. (2004) and already mentioned in Sect. 3.3.1;

2. objects of different spectral type are not differently affected by varying photometric conditions, e.g., that intervening clouds are gray.

The photometric calibration determines factors by which the fluxes in all images are multiplied. These factors are given by

$$f_i = 10^{-0.4 ZP_{\mathrm{rel}_i}} / t_i \; , \tag{3.5}$$

so that the fluxes are normalized to an exposure time of 1 s. This procedure ensures that the flux scales are determined by all images in a set and not only the photometrically calibrated images. Fixing the reference point in this way serves two purposes. First, some other pipelines rescale all images to a fixed reference point, e.g., airmass 1 or airmass 0. By doing so the rescaling becomes an extrapolation and possible errors in the extinction coefficients are multiplied more than necessary. The approach in the GABODS pipeline is in this aspect superior to the EIS/MVM pipeline that rescales all images to airmass zero (see App. C.4). Second, the pipeline allows to apply selection criteria to the images entering the final coadded image, e.g., on seeing or PSF anisotropy. Through these filters different coadditions for one field with different scientific purposes in mind may be produced. Having a reference that is determined by the entire set and not only by the images matching the selection criteria leaves the final zeropoint of the coadded frames invariant under a variation of selection criteria.

3.4.3 Image Coaddition

Before the final coaddition the sky background is subtracted from all images. A three pass process is used for this. In the first step SExtractor is used to detect all large objects. Typical SExtractor settings for WFI are to detect objects with at least 50 adjacent pixels 1.5σ above the sky background. All pixels belonging to an object are set to the mode of the SCIENCE image. From this object-masked image we create a SExtractor BACKGROUND check-image, with BACK_SIZE = 90 for WFI images. This check-image is a good description of the sky background and is subtracted from the SCIENCE image. The third step is only necessary because SExtractor has a tendency to underestimate the background, which becomes often more apparent after resampling the images to a common pixel grid.

The coaddition is carried out using SWarp from the TERAPIX package. SWarp performs a sub-pixel coaddition taking into account the full astrometric solution. The exact methods can be chosen by the user from a large variety of resampling and coaddition algorithms.

SWarp firsts resamples all SCIENCE and WEIGHT images to a common output grid according to the astrometric solution. A number of resampling kernels is built into SWarp; by default the GABODS pipeline uses the LANCZOS3 polynomial kernel.

Because after resampling with `SWarp` – at least in the version used in the GABODS pipeline – any residual background becomes more prominent, a third step of background subtraction is necessary at this point. The mode of the resampled SCIENCE images is estimated with `stats` from the `imcat` package and subtracted. The cause of the increased background in `SWarp` resampled images is not fully understood. However, the procedure described here successfully removes this effect without adversely affecting the photometric calibration.

After the final sky subtraction step, the resampled SCIENCE and WEIGHT frames are stacked using a weighted mean coaddition with the weights given by the sky noise,

$$w_i = \frac{1}{\sigma^2_{\mathrm{sky}_i} f_i^2} \; , \tag{3.6}$$

where we take into account that the noise also scales with the flux scale f_i. The output pixel values I_{out} and W_{out} of the coadded SCIENCE and WEIGHT images, respectively, are given by

$$I_{\mathrm{out}} = \frac{\sum_{i=1}^{N} I_i f_i W_i w_i}{\sum_{i=1}^{N} W_i w_i} \; , \qquad W_{\mathrm{out}} = \sum_{i=1}^{N} W_i w_i \; . \tag{3.7}$$

4

Weak Lensing Evidence for a Filament between A 222/223

The theory of cosmic structure formation predicts through N-body simulations that matter in the Universe should be concentrated along sheets and filaments and that clusters of galaxies form where these intersect (e.g., Klypin & Shandarin 1983; Davis et al. 1985; Bertschinger & Gelb 1991; Bond et al. 1996; Kauffmann et al. 1999). This filamentary structure, often also dubbed "cosmic web", has been seen in galaxy redshift surveys (e.g., Joeveer et al. 1978; de Lapparent et al. 1986; Giovanelli et al. 1986; Geller & Huchra 1989; Vogeley et al. 1994; Shectman et al. 1996) and more recently by Baugh et al. (2004) and Doroshkevich et al. (2004) in the 2dF and SDSS surveys, and at higher redshift by Möller & Fynbo (2001). Observational evidence for the cosmic web is recently also coming from X-ray observations. For example, an X-ray filament between two galaxy cluster was observed by Tittley & Henriksen (2001). Nicastro et al. (2005) reported the possible detections of a warm-hot intergalactic medium filament but this claim is disputed (Rasmussen et al. 2006; Kaastra et al. 2006).

Because of the greatly varying mass-to-light (M/L) ratios between rich clusters and groups of galaxies (Tully & Shaya 1999) it is problematic to convert the measured galaxy densities to mass densities without making further assumptions. Dynamical and X-ray measurements of the filament mass will not yield accurate values, as filamentary structures are probably not virialized. Weak gravitational lensing is a model-independent method to determine the surface mass density of clusters and filaments. Due to the random ellipticities of the unlensed faint background galaxies (FBG) every weak lensing mass reconstruction is unfortunately an inherently noisy process, and the expected surface mass density of a typical filament is too low to be detected with current telescopes (Jain et al. 2000).

Cosmic web theory also predicts that the surface mass density of a filament increases towards a cluster (Bond et al. 1996). Filaments connecting neighboring clusters should have surface mass densities high enough to be detectable with weak lensing (Pogosyan et al. 1998). Such filaments may have been detected in several weak lensing studies.

Kaiser et al. (1998) found a possible filament between two of the three clusters in the $z = 0.42$ supercluster MS 0302+17, but the detection remains somewhat uncertain because of a possible foreground structure overlapping the filament and possible edge effects due to the gap between two of the camera chips lying on the filament. Also, Gavazzi et al. (2004) could recently not confirm the presence of a filament in this system. Gray et al. (2002, G02) claim to have found a filament extending between two of the three clusters of the Abell 901/902 supercluster, but the significance of this detection is low and subject to possible edge effects, as again the filament is on the gap between two chips of the camera. Clowe et al. (1998) reported the detection of a filament extending from a high-redshift ($z = 0.809$) cluster. Due to the small size of the image it is unknown whether this filament extends to a nearby cluster.

A 222/223 are two Abell clusters at $z \approx 0.21$ separated by $\sim 14'$ on the sky, or $\sim 2800\, h_{70}^{-1}$ kpc, belonging to the Butcher et al. (1983) photometric sample. Both clusters are rich having Abell richness class 3 (Abell 1958). The Bautz-Morgan types of A 222 and A 223 are II–III and III, respectively. While these are optically selected clusters, they have been observed by ROSAT (Wang & Ulmer 1997; David et al. 1999) and are confirmed to be massive clusters. A-223 shows clear sub-structure with two distinct peaks separated by $\sim 4'$ in the galaxy distribution and X-ray emission. We will refer to these sub-clumps as A 223-S and A 223-N for the Southern and Northern clump, respectively. A 222 is a very elliptical cluster dominated by two bright elliptical galaxies of about the same magnitude.

Proust et al. (2000) published a list of 53 spectra in the field of A 222/223, 4 of them in the region between the clusters (hereafter "intercluster region") and at the redshift of the clusters. Later Dietrich et al. (2002, D02) reported spectroscopy of 183 objects in the cluster field, 153 being members of the clusters or at the cluster redshift in the intercluster region. Taking the data of Proust et al. (2000) and D02 together, 6 galaxies at the cluster redshift are known in the intercluster region, establishing this cluster system as a good candidate for a filamentary connection.

In this Chapter I present a weak lensing study of A 222/223, establishing this supercluster system as one of the best candidates for a weak lensing detected dark matter filament. This work has been published in Dietrich et al. (2005). In this paper I also discuss at length the problems of unambiguously defining what a filament is, as opposed to two overlapping halos of neighboring clusters, and how to translate this into a weak lensing detection method. This fraction of the work was part of my Diplom thesis (Dietrich 2002) and is not reproduced here. In summary it can be said that this is an extremely challenging problem because the differentiation into filaments and halos is an intuitive geometric concept that probably cannot be converted into a mathematical framework. Nevertheless, the aperture quadrupole statistic (Schneider & Bartelmann 1997) shows some promise in this area and will be used in this Chapter. Because the aperture quadrupole statistic and this application of it is relatively unknown, I give a short outline of the method in App. B.

This Chapter is organized as follows. I describe observations of the A 222/223 system in Sect. 4.1. The weak lensing analysis of this double cluster system is presented in Sect. 4.2; I compare this to the light (optical and X-ray) distribution in Sect. 4.3. Results are discussed in Sect. 4.4.

Throughout this Chapter and the other observational Chaps. 5 and 6 I will assume a ΛCDM cosmology with $H_0 = 70\,h_{70}\,\mathrm{km\,s^{-1}\,Mpc^{-1}}$, unless otherwise noted, rather than $H_0 = 100\,h\,\mathrm{km\,s^{-1}\,Mpc^{-1}}$ used in the theoretical Chaps. 1–2.

4.1 Observations of the A 222/223 System

Imaging of the A 222/223 system was performed with the Wide Field Imager (WFI) at the ESO/MPG-2.2 m telescope. In total, twenty 600 s exposures were obtained in R-band in October 2001 centered on A 223, eleven 900 s R-band exposures were taken in December 1999 centered on A 222. The images were taken with a dithering pattern filling the gaps between the chips in the coadded images of each field.

The R-band data used for the weak lensing analysis is supplemented with three 900 s exposures in the B- and V-band centered on each cluster taken from November 1999 to December 2000. The final B- and V-band images have some remaining gaps and regions that are covered by only one exposure

and – due to the dithering pattern – do not cover exactly the same region as the R-band images.

The reduction of the R-band image centered on A 222 is described in detail in D02. The R-band image centered on A 223 was reduced in the same way. The B- and V-band data were reduced using the GABODS pipeline (Chap. 3), using the USNO-A2 catalog (Monet et al. 1998) for the astrometric calibration. The B- and V-band pointings were coadded into a single frame for each color. The PSF properties of the R-band pointings were so different that they were used separately for the lensing analysis. The seeing of the coadded R-band images is 0.″9 and 0.″8 for the A 222 and A 223 pointings, respectively.

The R-band image centered on A 222 was photometrically calibrated using Landolt standard fields and corrected for galactic extinction (Schlegel et al. 1998), while the zeropoint of the R-band image centered on A 223 was fixed to match the magnitudes of objects in both fields. Because the B- and V-band data were known to be taken under non-photometric conditions, the red cluster sequence was identified in a color-magnitude diagram and its color adjusted to match those expected from elliptical galaxies at the cluster redshift, using passive evolution and K-correction on the synthetic galaxy spectra of Bruzual & Charlot (1993), to account for the additional atmospheric extinction.

Due to the greatly varying coverage of the fields, it is difficult to give a limiting magnitude for the coadded images. The number counts stop following a power law at 22.5–23.0 mag for the B- and V-band images and at 24 mag for the R-band images.

4.2 Lensing Analysis

4.2.1 Lensing Catalog Generation

Starting from the initial `SExtractor` (Bertin & Arnouts 1996) catalog which contains all objects with at least 3 contiguous pixels 2σ above the background, we measured all quantities necessary to obtain shear estimates from the KSB (Kaiser et al. 1995) algorithm. For this, we closely followed the procedure described in Erben et al. (2001).

From the KSB catalog a catalog of background galaxies used for the weak

lensing analysis was selected with the following criteria. Objects with signal-to-noise (SNR) < 2, Gaussian radius $r_g < 0.''33$ or $r_g > 1.''19$, or corrected ellipticity $\varepsilon > 0.8$ were excluded from the sample. Objects brighter than $R < 22$ were rejected as probable foreground objects, while all objects with $R > 23$ were kept as likely background galaxies. Objects between $22 < R < 23$ with colors matching those of galaxies at redshift $z < 0.5$, $-0.23 < (V-R) - 0.56 \times (B-V) < 0.67$, $0.5 < B-V < 1.6$ were not used for the lensing catalog. Objects not detected in the B-band image were kept if $V - R > 1.0$. The final catalog has 25 940 galaxies, or 13.5 galaxies arcmin^{-2}, without accounting for the area lost to masked reflection rings, diffraction spikes, and tidal tails.

The large overlap between the two R-band images allows us to test the reliability of the shear estimates and the validity of the weighting scheme we will employ in the lensing analysis. We perform these tests separately for the set of all objects found in the unmasked part of the overlap region, and the set of objects left after performing the various cuts described in the previous paragraph. The top panels of Fig. 4.1 show a comparison of the shear estimates of objects observed in the overlap region of the two R-band pointings. Overall, the two independent shear estimates agree but show a broad scatter around the ideal relation. For the set of all galaxies, we find that the mean of the differences between the two measurements is -0.01 for the ε_1 component and 0.00 for the ε_2 component. The standard deviation is 0.20 in each component. Erben et al. (2003) found an RMS scatter of 0.16 between two different lensing analyses of their VLT data. Our value seems to indicate that the additional scatter introduced by the independent observations is small compared to the uncertainties intrinsic to the shear estimation procedure. The bottom left panel of Fig. 4.1 shows the dependence of the absolute values of differences of the shear estimators $|\Delta\varepsilon|$ on the apparent R-band magnitude. As one expects, the reliability of the shear estimates drops dramatically for fainter objects. Because these are the objects we keep in our lensing catalog the RMS scatter between the two shear estimates increases to 0.25 per component for the galaxies kept in our lensing catalog. The mean for the set of galaxies in our lensing catalog stays almost unchanged at 0.01 in both components, showing that, while the shear estimates become noisier, no systematic differences between both images are present.
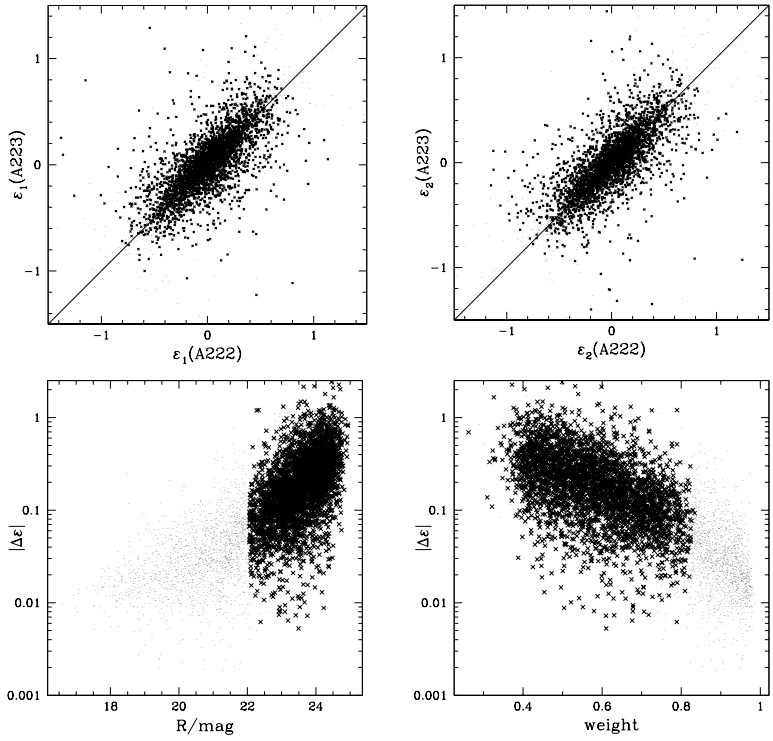
Figure 4.1: Reliability tests of the shear estimates of objects observed in the overlapping region of the two R-band pointings. All objects with shear estimates are plotted as light dots, objects surviving our various selection criteria, detailed in the text, are plotted as crosses. *Top left*: Scatter plot of the ε_1 component estimates from the exposures centered on A 222 versus the one centered on A 223. The diagonal line is not a fit but only represents the ideal relation. Although we excluded objects with corrected ellipticity $|\varepsilon| > 0.8$ from our final lensing catalog, some objects with $|\varepsilon| > 0.8$ are marked with crosses in this plot. This is because the *mean* ellipticity of their two measurements, which we employ in our selection and lensing analysis is below the chosen cut-off level. These objects are strongly down-weighted and their exclusion would not lead to significant differences in the lensing analysis. *Top right*: Same for the ε_2 component. *Bottom left*: Dependence of the absolute value of differences of the shear estimators $|\Delta\varepsilon|$ on the apparent magnitude of the object. As expected, fainter objects have less reliable shear estimates. *Bottom right*: This panel shows the correlation between $|\Delta\varepsilon|$ and the weighting scheme we employed. Objects with higher weights have more reliable shear estimates.

In the lensing reconstruction and the aperture mass maps we will assign a weight to each shear estimator. The weight is computed by

$$w = \left(\sigma_{\varepsilon_{2D}}^2 + \sigma_g^2 \right)^{-1} , \tag{4.1}$$

where $\sigma_{\varepsilon_{2D}}$ is the intrinsic 2-d ellipticity dispersion and σ_g is the error estimate of the initial ellipticity measurement of the galaxy. We set $\sigma_{\varepsilon_{2D}} = 0.38$ which is typically found in ground-based weak lensing observations (T. Erben, private communication; e.g., Clowe & Schneider 2001 who find a value of $\sigma_{\varepsilon_{2D}} = 0.42$). σ_g is computed from the uncertainty of the measurement of the quadrupole moment of the galaxy in the image. While both quantities are not independent – $\sigma_{\varepsilon_{2D}}$ is of course increased by higher errors in the initial ellipticity measurement – their relation is very complex and not readily quantifiable in the KSB algorithm. As a consequence, galaxies with low σ_g probably receive less weight than they should in an ideal weighting scheme. The large overlap and the high number of objects detected in both frames would enable us to study the shear estimation procedure in more detail and probably find a better weighting scheme than the one used in this work. This is, however, beyond the scope of this work.

The bottom right panel of Fig. 4.1 shows the correlation between our weights (normalized to be ≤ 1) and $|\Delta\varepsilon|$. This verifies that galaxies with more reliable shear estimates have a higher weight in the generation of the lensing maps, although the large variations in $|\Delta\varepsilon|$ only correspond to small relative changes in the weight w. The shear estimates with the highest weight, not part of our lensing catalog, are those which we reject as probable foreground objects because they are too bright.

4.2.2 Weak Lensing Reconstruction

Based on the lensing catalog described in the previous section, the weak lensing reconstruction in Fig. 4.2 was performed using the Seitz & Schneider (2001) algorithm adapted to the field geometry with a $\sigma = 1\farcs75$ smoothing scale on a 214×200 points grid.

Both clusters are well detected in the reconstruction, the two components of A 223 are clearly visible, and the elliptical appearance of A 222 is present in the surface-mass density map. The strong mass peak West of A 223 is most
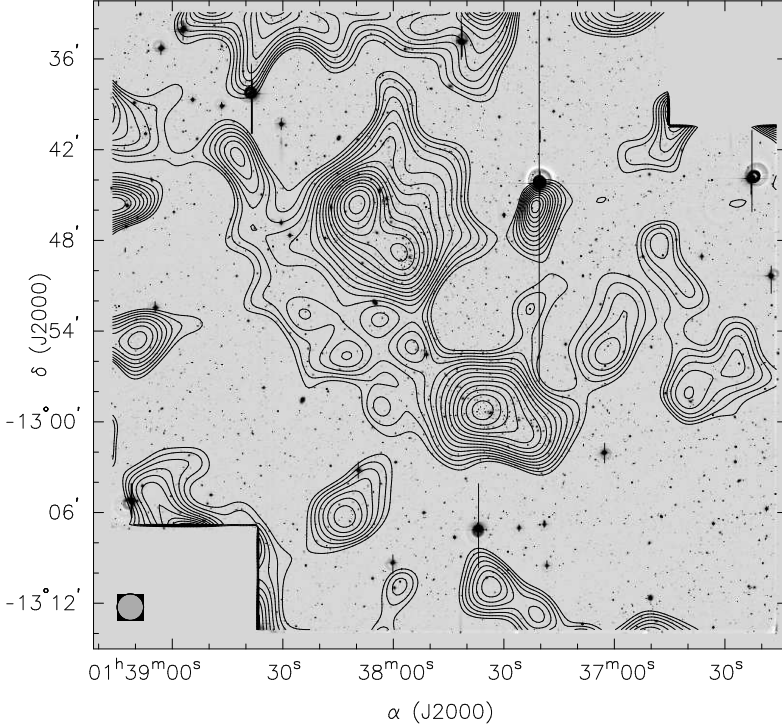
Figure 4.2: Weak lensing surface mass density contours overlaid on the R-band mosaic observed with the Wide-Field imager at the ESO/MPG-2.2 m telescope. The shear field was smoothed with a $\sigma = 1\rlap{.}'75$ Gaussian, corresponding to the diameter of the circle at the lower left corner. Each contour represents an increase in κ of 0.005 ($\sim 1.6 \times 10^{13}\ h_{70}\ M_\odot\ \mathrm{Mpc}^{-2}$, assuming $\bar{z}_{\mathrm{FBG}} = 1$) above the mean κ at the edge of the field.

likely associated with the reflection ring around the bright $V = 7.98$ mag star at that position. Although the prominent reflection ring was masked, diffuse stray light and other reflection features are visible, extending beyond the masked region, well into A 223, probably being the cause of this mass peak.

The peak positions in the weak lensing reconstruction are offset from the brightest galaxy in A 222 and the two sub-clumps of A 223. The centroid of the mass of A 222 is $57''$ South-East of the brightest cluster galaxy (BCG); the mass centroids of A 223-N and A 223-S are $86''$ and $37''$ away from the BCGs of the respective sub-clumps.

To estimate the significance of these offsets we performed lensing simulations with singular isothermal sphere (SIS) models of various velocity dispersions. The SIS models were put at the cluster redshift of $z = 0.21$; catalogs with a random distribution of background galaxies with a number density of 15 arcmin^{-2}, and 1-d ellipticity dispersion of $\sigma_{\varepsilon_{1D}} = 0.27$ were created for 200 realizations. The shear of the SIS models was applied to the galaxy ellipticity of the catalog. Weak lensing reconstructions based on these catalogs were performed with the smoothing scale set $\sigma = 1\rlap{.}'75$ to match the smoothing of our real data. Due to the lower SNR for the 550 km s^{-1} SIS, the simulations yielded only 198 reliable centroid positions, while the centroid positions of the more massive SIS could be reliably determined in all 200 realizations. Fig. 4.3 shows the cumulative fraction of reconstructed peaks found within a given distance from the true centroid position.

These simulations show that the observed offset of A 223-S is compatible with the statistical noise properties of the reconstruction. The offset of A 222, using the velocity determination of the SIS models fitted below, is significant at the 2-3σ level. The offset of A 223-N cannot be explained with the statistical noise of the reconstruction alone. It is, however, likely that the observed significant offsets are not real but linked to the influence of the bright star and its reflection rings West of A 223. Although objects coinciding with this reflection ring were excluded from the catalog, the presence of a strong mass peak on the position of the bright reflection ring is a clear indication that the shear estimates are affected by the weaker reflection features which are too numerous and large to be masked. It is difficult to guess how these reflections could contribute to the observed peak shifts. We found that varying the size of the masked region did affect the strength of the peak on the reflection ring but left the offsets of the cluster peaks essentially unchanged. Still, it is noteworthy that the mass peaks are shifted preferentially away from the star.

To avoid the mass-sheet degeneracy we estimate the cluster masses from fits of parameterized models to the shear catalog. The fits were performed
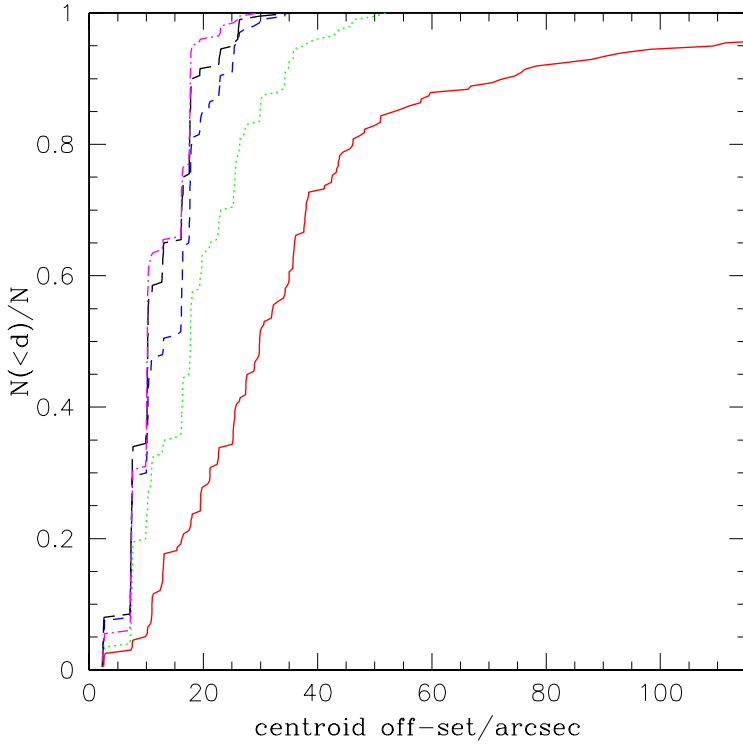
Figure 4.3: Cumulative fraction of offsets of the reconstructed centroids from the real cluster centroid. The curves display the probability of finding a reconstructed centroid of an SIS with a velocity dispersion of 550 km s^{-1} (solid), 700 km s^{-1} (dotted), 850 km s^{-1} (short dashed), 1000 km s^{-1} (long dashed), and 1150 km s^{-1} (dashed-dotted) from the real centroid position. The SIS was put at a redshift of $z = 0.21$; the number density of the input catalog was 15 arcmin^{-2}.
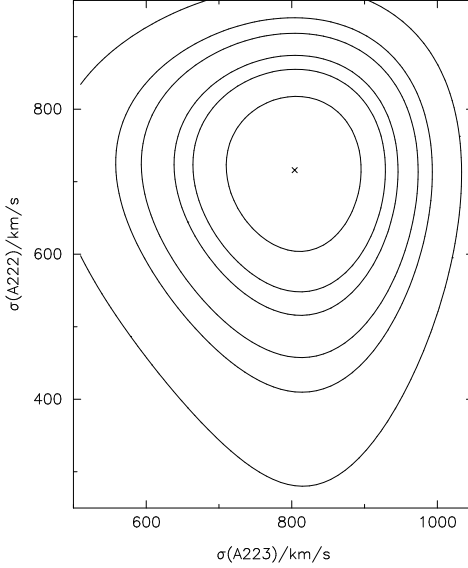
Figure 4.4: Combined confidence contours for the SIS velocity dispersion of A 222 and A 223. The contour lines are drawn for $2\Delta l = \{2.3, 4.61, 6.17, 9.21, 11.8, 18.4\}$, corresponding to the 63.8%, 90%, 95.4%, 99%, 99.73%, and 99.99% confidence levels, respectively, under the assumption that the statistic is approximately Gaussian.

minimizing the negative shear log-likelihood function (Schneider et al. 2000)

$$l_\gamma = -\sum_{i=1}^{N_\gamma} \ln p_\varepsilon(\varepsilon_i | g(\boldsymbol{\theta}_i)) \tag{4.2}$$

over the N_γ galaxy images to obtain the parameter set most consistent with the probability distribution $p_\varepsilon(\varepsilon_i | g(\boldsymbol{\theta}_i))$ of lensed galaxy ellipticities. See Schneider et al. (2000) for a detailed discussion of this maximum likelihood method for parameterized models. We fitted more than one mass profile simultaneously. Compared to a single model fit, this reduces the influence of the other cluster on the fitting procedure and result. Galaxies within distances $\theta < \theta_{min} = 3'$ from the centers of the models were ignored when fitting SIS models. Assuming a typical SIS this corresponds to roughly 10 Einstein radii and is enough to assume that all galaxies used in the fitting procedure are in the weak lensing regime. Ignoring galaxies close to the cluster centers also reduces the contamination with faint cluster galaxies. As a first approach we fit two SIS, one centered on the BCG of
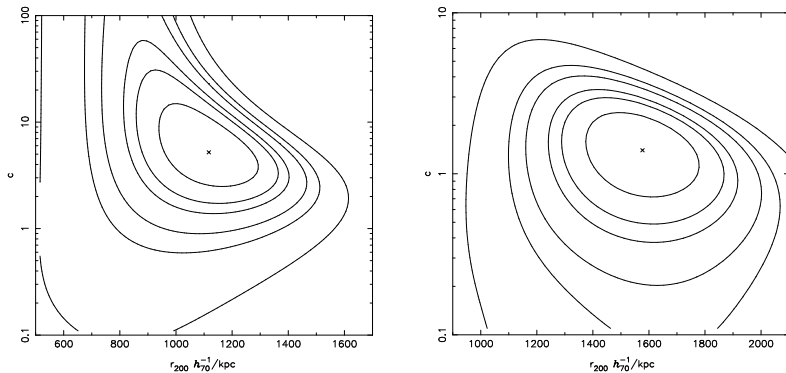
Figure 4.5: Confidence contours for the best-fit NFW parameters for A 222 (*left panel*) and A 223 (*right panel*). The contours are drawn at the same levels as in Fig. 4.4.

A 222, the other centered on the line connecting the BCGs of the two sub-clumps of A 223. The best-fit models in this case have velocity dispersions of 716^{+67}_{-74} km s^{-1} and 804^{+59}_{-64} km s^{-1}, respectively. This is considerably lower than the spectroscopic velocity dispersions of D02 of 1014^{+90}_{-71} km s^{-1} for A 222 and 1032^{+99}_{-76} km s^{-1} for A 223. It is also lower than the velocity dispersions derived from X-ray luminosities (David et al. 1999) and the $L_{X} - \sigma$ relation of Wu et al. (1999), which are $845 - 887$ km s^{-1} and $828 - 871$ km s^{-1}, respectively (D02), but the value for A 223 is consistent within the error bars. The error bars of the individual velocity dispersion were computed from $2\Delta l$, where the velocity dispersion of one component was kept fixed at its best-fit value to give the error estimate for the other component. The two component fit has a significance of 7.9σ over a model without mass. Joint confidence contours are displayed in Fig. 4.4. A three component model with an SIS centered on each BCG has a lower significance over a zero mass model than the two SIS model and does not fit the data better.

Because both clusters are elliptical and the masses determined from SIS fits differ strongly from those derived by D02, one might assume that fitting elliptical mass profiles yields a more accurate estimate of the cluster mass. To

Table 4.1: Summary of the cluster properties derived from spectroscopy, X-ray, and weak lensing observations.

	A 222	A 223
$\sigma_{\mathrm{vir}}/(\mathrm{km\ s^{-1}})$	1014^{+90}_{-71}	1032^{+99}_{-76}
$\sigma(L_{\mathrm{X}})/(\mathrm{km\ s^{-1}})$	845–887	828–871
$\sigma_{\mathrm{SIS}}/(\mathrm{km\ s^{-1}})$	716^{+67}_{-74}	804^{+59}_{-64}
$r_{200}/(\mathrm{kpc}\ h_{70}^{-1})$	1276^{+102}_{-121}	1546^{+145}_{-151}

test this, we fitted singular isothermal ellipse models to the clusters. It turned out that the 6 parameter fit necessary to model both clusters simultaneously was very poorly constrained and the fit procedure was not able to reproduce the orientation of the clusters. Results strongly depended on the initial values chosen for the minimization routines.

The best-fit NFW models have $r_{200} = 1276^{+102}_{-121}\ h_{70}^{-1}$ kpc, $c = 3.4$ and $r_{200} = 1546^{+145}_{-151}\ h_{70}^{-1}$ kpc, $c = 1.2$ for A 222 and A 223, respectively, excluding shear information at distances $\theta < 1'\!.5$ from the cluster centers. The NFW models have a significance of 5.2σ over a model with no mass. Fig. 4.5 shows confidence contours for the NFW fits to the individual clusters, computed from $2\Delta l$, while keeping the best-fit parameters for the other cluster fixed. We summarize the derived cluster properties in Tab. 4.1.

As we see from the left panel in Fig. 4.5, it can be difficult to obtain reliable concentration parameters from weak lensing data. The reason is that the shear signal is mostly governed by the total mass inside a radius around the mass center. Only in the cluster center the shear profile carries significant information about the concentration parameter. For example if we set $\theta_{\min} = 3'$ – like we did for fitting SIS models – in the minimization procedure, M_{200} remains essentially unchanged while the concentration factor can increase dramatically. The best fit parameters for A 222 in this case are $r_{200} = 1238\ h_{70}^{-1}$ kpc, $c = 7.8$. If we choose a large value for the radius $\theta_{\min}$ inside which we ignore galaxies, typical values for the scale radius $r_{\mathrm{s}} = r_{200}/c$ are contained within this radius. c is then essentially unconstrained, i.e., the minimization procedure cannot anymore distinguish between a normal cluster profile and a point mass of essentially the same mass.

The situation is different for A 223. The two sub-clumps are separated by $\sim 4'$. This means that even ignoring shear information within the larger $\theta_{min} = 3'$ radius, the outer slopes of the sub-clumps are outside θ_{min} and the determination of the concentration parameter gives a tight upper bound and does not change as dramatically when the minimization is performed only with galaxies further away from the cluster center as is the case in A 222. Because the shear outside θ_{min} is effectively that of an averaged mass profile inside θ_{min} the measured concentration parameter is very low.

The projected cluster separation is marginally smaller than the sum of the virial radii ($r_{vir} \sim r_{200}$) derived from the shear analysis; r_{200} (A 222) + r_{200} (A 223) = $2822^{+177}_{-193} \, h_{70}^{-1}$ kpc. We have to emphasize that this is only the *projected* separation. DO2 found redshifts of $z = 0.2126 \pm 0.0008$ for A 222 and $z = 0.2079 \pm 0.0008$ for A 223. Assuming that both clusters participate in the Hubble flow with no peculiar velocity, this redshift difference of $\Delta z = 0.005 \pm 0.001$ translates to a physical separation along the line of sight of $(15 \pm 3) \, h_{70}^{-1}$ Mpc. Presumably, part of the observed redshift difference is due to peculiar velocities. In any case, it is more likely that the two clusters are physically separated and the virial radii do not overlap.

In addition to the cluster peaks several other structures are seen in the reconstruction in Fig. 4.2. Using the aperture mass statistics with a $6'\!.4$ filter scale we find that the peak $\sim 13'$ SE of A 222 has a SNR of 3.5. This peak corresponds to a visually identified overdensity of galaxies.

Fig. 4.6 shows a $V - R$ vs. R color-magnitude diagram of all galaxies in a box with $170'$ side length around the brightest galaxy in this overdensity. A possible red-cluster sequence (RCS) can be seen centered around $V - R = 1.1$, which would put this mass concentration at a redshift of $z \sim 0.4$. However, the locus of the RCS is so poorly defined that this estimate has a considerable uncertainty. Assuming this redshift, the best-fit SIS model has a velocity dispersion of 728^{+101}_{-120} km s^{-1} and a significance of 3.2σ over a model without mass. The best-fit NFW model has $r_{200} = 1322 \, h_{70}^{-1}$ kpc and $c = 3.3$ and a significance of 2.8σ over a model with $r_{200} = 0$, determined from $\delta\chi^2$.

Fig. 4.7 shows a comparison of surface mass and luminosity density for this peak. Galaxies with $1.0 < V - R < 1.2$ were selected to match the tentative RCS from Fig. 4.6. The figure shows excellent agreement between the mass and light contours, unambiguously confirming that this is a weak lensing detection of a previously unknown cluster. The offset between the
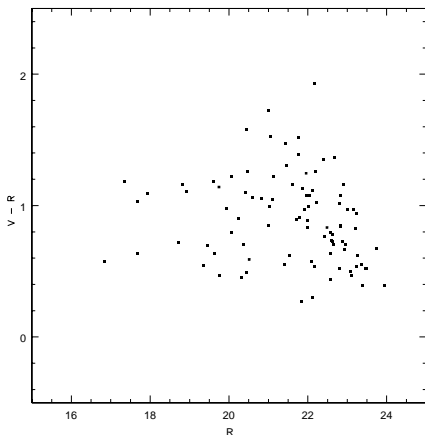
Figure 4.6: Color magnitude diagram of objects around the mass peak SE of A 222. A possible red-cluster sequence can be seen around $V - R \approx 1.1$.

mass centroid and the BCG, which is located at α=01:38:12.1, δ=−13:06:38.2, is 27″ and not significant for an SIS with a velocity dispersion of $\sim$ 730 km s^{-1} at a redshift of $z \sim 0.4$.

The mass concentration in the Western part of the possible filament reaches a peak SNR of 3.6 at a filter scale of 3.′2. We do not find an overdensity in the number or luminosity density of galaxies at this position. None of the other mass peaks seen in the reconstruction, with exception of the one on the reflection ring, is significant in filter scales > 2.′4.

Also visible in the reconstruction is a bridge in the surface mass density extending between A 222 and A 223. Although the signal of this possible filamentary connection between the clusters is very low, the feature is quite robust when the selection criteria of the catalog are varied and it never disappears. Variations on the selection criteria of the catalog let the filament shift a few arcminutes in the East-West direction. The filament strength also changes but on closer inspection this can be attributed almost entirely to variations in the mass-sheet degeneracy, which is fixed by setting the mean κ at the edge of the field to zero. Although the field is big enough to assume that the clusters have no considerable contribution to the surface mass density at the edge of the field, this is a region where the κ-map is dominated by noise.
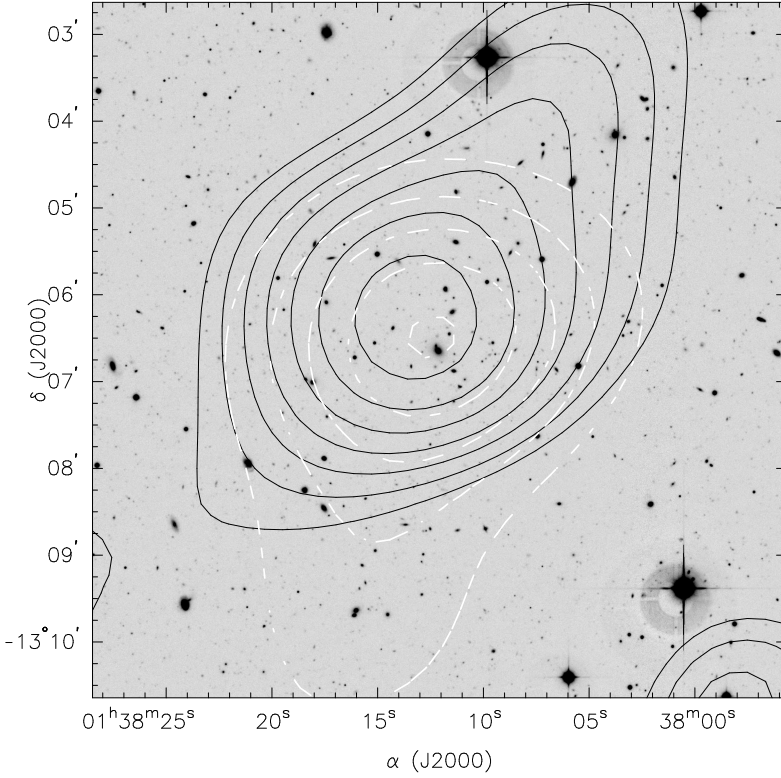
Figure 4.7: Mass and light contours in the peak SE of A 222. Black solid lines are contours of the mass reconstruction in Fig. 4.2, white dashed lines denote the luminosity density of galaxies with $1.0 < V - R < 1.2$.

Small changes in the selection criteria can change the value of the mass-sheet degeneracy by as much as $\kappa_0 = 0.02$. This illustrates that a surface mass density reconstruction is not suitable to assess the significance of structures as weak as filaments expected from N-body simulations. We thus use the aperture quadrupole statistic in an attempt to confirm the presence of a filament (Schneider & Bartelmann 1997; Dietrich et al. 2005).
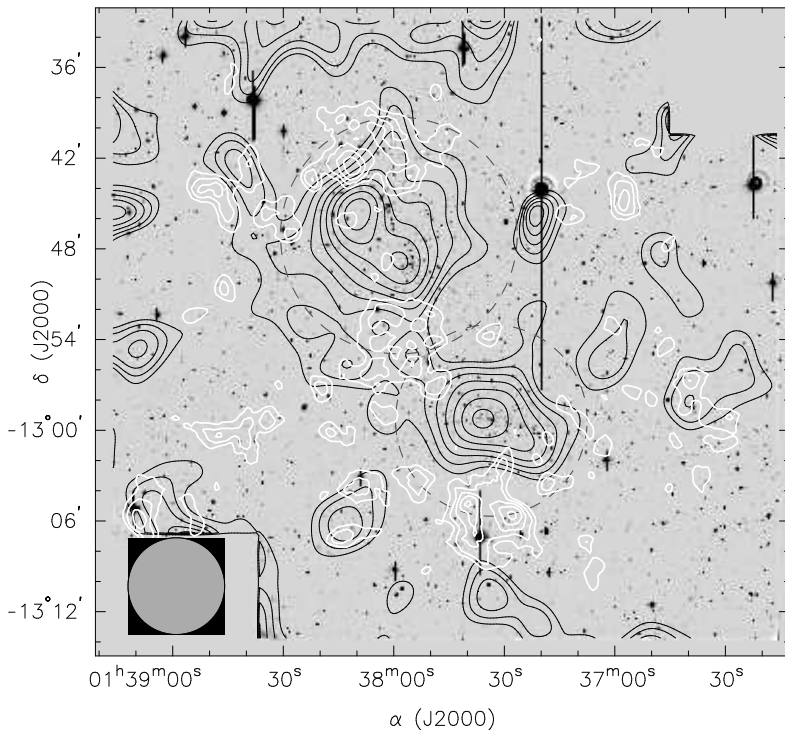
Figure 4.8: Aperture quadrupole moment map of A 222/223 in an aperture of $3\rlap{.}'2$ radius, corresponding to the radius of the circle at the lower left corner. The thick white lines are SNR contours for $|Q^{(2)}|$, the lowest contour being at 2 and higher contours increasing in steps of 0.5. The aperture quadrupole moment on the "filament" region reaches a peak SNR of 3.0. The black lines are the contours of the mass reconstruction. The dashed circles indicate the r_{200} from our best fit NFW models.

Fig. 4.8 shows a map of the absolute value of the aperture quadrupole moment, $|Q^{(2)}|$, with a weight function with $3\rlap{.}'2$ radius. The white significance contours show a quadrupole moment signal on the filament that reaches

a peak SNR of 3.0. The filter scale was chosen to be the same in which the aperture mass statistic gave the most significant signal in the intercluster region. The $|Q^{(2)}|$ signal does not fully trace the filament candidate but only the Western part of it and an extension towards the mass peak in the East. The peak SNR is most likely enhanced by the trough at the Western edge of the mass bridge. It is not surprising that the significance of the quadrupole moments on the possible filament is not very high. The aperture mass statistic already gave a relatively low SNR. The aperture quadrupole statistic uses data within the same aperture as M_{ap} but gives more information, namely instead of the mass in the aperture, it gives the mass distribution. Being generated from the same information, this naturally comes with a lower SNR.

Several other features – most of them associated with the slopes of the two massive clusters – are also seen in Fig. 4.8. Interesting in the context of quantifying filaments is the $|Q^{(2)}|$ statistics in the region between A 222 and the newly detected cluster SE of it. Indeed we see a signal with a peak signal-to-noise ratio of 2.7 extending between the two clusters. The mass reconstruction in Fig. 4.2 also shows a connection between both clusters but at a level that is dominated by the noise of the κ-map. The redshift difference between A 222 and the new cluster, inferred from the color-magnitude diagram (Fig. 4.6), makes it very unlikely that these two clusters are connected by a filament. It is much more probable that the influence of the two individual clusters leads to a quadrupole moment in the intercluster region.

4.3 Comparison of Mass and Light

Fig. 4.9 shows the number density and luminosity distribution in the A 222/ 223 system. The left panel shows the number density distribution of the color-selected ($0.78 < V - R < 0.98$) early-type galaxies. The contour lines indicate the SNR determined from bootstrap resampling the selected galaxies. It is evident that a highly significant overdensity of early-type galaxies exists in the intercluster region. The right panel shows a comparison between luminosity (background gray-scale image) and surface mass density. In general, there is good agreement between the two. We again note the offsets of the mass centroids from the light distribution, which we attribute to
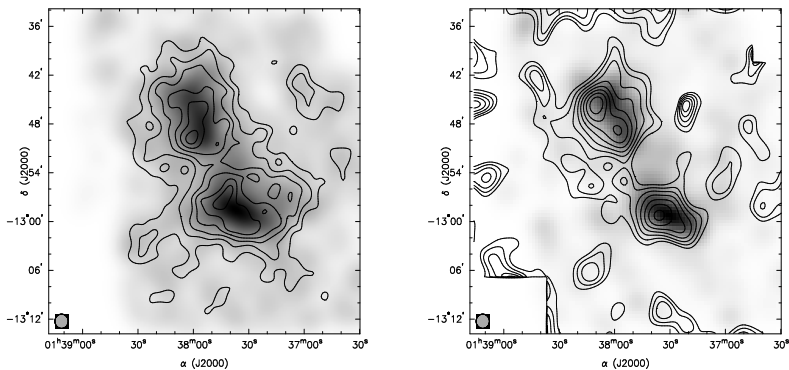
Figure 4.9: Smoothed distribution of the number density (left panel) and the luminosity density (right panel). The smoothing was done with a $\sigma = 1\rlap{.}'75$ Gaussian to match the smoothing of the weak lensing reconstruction. The diameter of the circles at the lower left corners corresponds to the FWHM of the Gaussian. The contour lines in the left panel are significance contours of the number density starting at 5σ and rising in steps of 1σ, the contour lines in the right panel are the surface mass density contours of the reconstruction.

the systematics induced by the reflection ring. The elongation of A 222 is nicely reproduced in the reconstruction. A 222 is the dominant cluster in the luminosity density map, while in the mass reconstruction A 223 appears to be more massive. We note, however, that many of the bright E/S0 galaxies in A 223 escape our color selection because they are bluer than expected for early-type galaxies at this redshift. This indicates a high amount of merger activity in this irregular system and most likely still collapsing system. As we fixed the colors such that the RCS matches the expected colors of early-type galaxies at the cluster redshift, this clearly shows that the bright central galaxies in A 223 are bluer than expected.

The overdensity in number and luminosity density is not aligned with the dark matter filament candidate. We should, however, not forget that the position of the filamentary structure is somewhat variable with varying cuts to the lensing catalog. If the reflection features West of A 223 are indeed

responsible for shifting the centroid positions of the massive clusters, their effect may be even stronger on such weak features as the mass bridge seen in the reconstruction.

We estimate the cluster luminosities by measuring the R-band luminosity density of all galaxies within r_{200} – as determined from the lens models in Sect. 4.2.2 – in excess of the luminosity density in a circle with $5'$ radius centered on (01:36:45.8, −13:07:25), which is an empty region in the sw of our field. A 222 has a luminosity $L_{R,\,r_{200}} = (2.7 \pm 0.4) \times 10^{12}\,h^{-2}\,L_\odot$ and A 223 has a luminosity of $L_{R,\,r_{200}} = (5.6 \pm 0.8) \times 10^{12}\,h^{-2}\,L_\odot$. Using the mass determined from the NFW profiles, this implies rather low M/L ratios; $M/L_R = 111^{+31}_{-34}\,h_{70}\,M_\odot/L_\odot$ for A 222 and $M/L_R = 95^{+30}_{-31}\,h_{70}\,M_\odot/L_\odot$ for A 223. The mass-to-light ratios increase to $M/L_R = 178^{+45}_{-49}\,h_{70}\,M_\odot/L_\odot$ and $M/L_R = 131^{+30}_{-31}\,h_{70}\,M_\odot/L_\odot$ for A 222 and A 223, respectively, if the mass estimates from the SIS models within r_{200} are used.

The X-ray satellite ROSAT observed the pair of galaxy clusters on 16. January 1992 using the position sensitive proportional counter (PSPC). We extracted these data from the public ROSAT archive at the MPE and analyzed the total integration time of 6780 seconds using the EXSAS software (Zimmermann et al. 1998). To avoid any confusion with diffuse soft X-ray emission and associated photoelectric absorption towards the area of interest, we focused our scientific interest on the upper energy limit of the PSPC detector. Using the pulse height invariant channels 51–201 (corresponding to $0.5\,\mathrm{keV} \leq E \leq 2.1\,\mathrm{keV}$) we calculated the photon image and the corresponding "exposure-map" according to the standard data reduction. We performed a "local" and a "map" source detection which in total yielded 42 X-ray sources above a significance threshold of ten.

By visual inspection, we selected some X-ray sources located close to the diffuse X-ray emission of the intra-cluster gas and subtracted their contribution using the EXSAS task create/bg_image. This task subtracts the X-ray photons of the point sources and approximates the background intensities via a bi-cubic spline interpolation. Finally the X-ray data were smoothed to an angular resolution of $1.'75$ using a Gaussian smoothing kernel.

Contours for this final image are shown in Fig. 4.10 overlaid on the WFI R-band mosaic and significance contours of the number density of color selected early-type galaxies. Detected X-ray sources kept in the final image
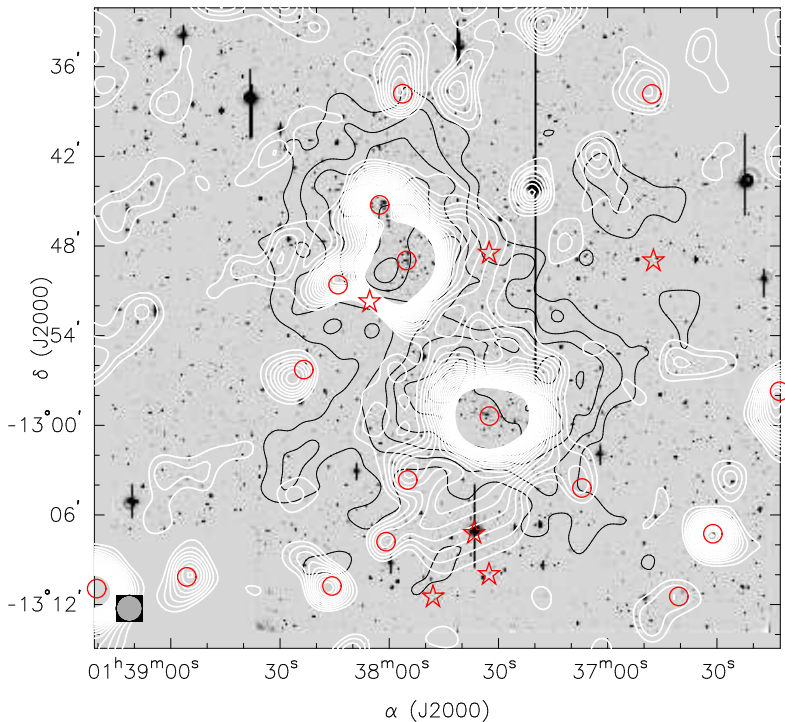
Figure 4.10: Above is an overlay of X-ray contours (white lines) over the WFI images of our field. The contour lines start at 3σ and increase in steps of 2σ. All detected X-ray sources are marked; circles correspond to sources kept, while the point sources excised from the image are marked with stars. The point source excised X-ray image was smoothed with a $\sigma = 1\!'.75$ Gaussian, corresponding to the diameter of the circle at the lower left corner. The black contours in the background are the significance contours of the number density from the left panel of Fig. 4.9.

are marked with circles; the subtracted unresolved sources are denoted by stars. The lowest contour line is at the 3σ level. Higher contours increase in

steps of 2σ. Both clusters are very well visible. As already noted by Wang & Ulmer (1997), A 223-S is by far the dominant sub-clump in A 223 in X-ray.

A bridge in X-ray emission connecting both clusters is seen at the 5σ level in this image. This possible filament is aligned with the overdensity of the number density of color selected galaxies but not with the filament candidate seen in the weak lensing reconstruction.

The Eastern spur in the X-ray emission of A 223 is caused by a point source whose removal would cut significantly into the cluster signal. We therefore decided to keep this source. Removing it does not influence the signal in the intercluster region. The Northern extension of A 223 in the κ map is blinded by the support structure of the PSPC window in the X-ray exposure.

4.4 Discussion and Conclusions

Based on observations made with WFI at the ESO/MPG-2.2 m telescope we find a clear lensing signal from the Abell clusters A 222 and A 223. Comparing our lensing analysis with the virial masses and X-ray luminosities, we find that A 222/223 forms a very complex system. Mass estimates vary considerably depending on the method. Assuming the best-fit NFW profiles of Sect. 4.2.2 $M_{200}(\text{A } 222) = 3.0^{+0.7}_{-0.8} \times 10^{14} \, h_{70}^{-1} \, M_{\odot}$ and $M_{200}(\text{A } 223) = 5.3^{+1.6}_{-1.4} \times 10^{14} \, h_{70}^{-1} \, M_{\odot}$. The masses of the best-fit SIS models within r_{200} as determined from the NFW fit are higher for both cluster but compatible within their respective error bars: $M_{\text{SIS}}(\text{A } 222) = 4.8^{+1.0}_{-1.1} \times 10^{14} \, h_{70}^{-1} \, M_{\odot}$ and $M_{\text{SIS}}(\text{A } 223) = 7.3^{+1.3}_{-1.4} \times 10^{14} \, h_{70}^{-1} \, M_{\odot}$. These mass estimates are considerably lower than those derived from the virial theorem for an SIS model. Using the velocity dispersions from DO2 we find $M_{\text{vir}}(\text{A } 222) = 9.7^{+1.9}_{-1.6} \times 10^{14} \, h_{70}^{-1} \, M_{\odot}$ and $M_{\text{vir}}(\text{A } 223) = 12.0^{+2.5}_{-2.1} \times 10^{14} \, h_{70}^{-1} \, M_{\odot}$.

The M/L ratios we found in this work are lower than the ones determined by DO2 of $M/L_R = (202 \pm 43) \, h_{70} \, M_{\odot}/L_{\odot}$ for A 222 and $M/L_R = (149 \pm 33) \, h_{70} \, M_{\odot}/L_{\odot}$ within a radius of $1.4 \, h_{70}^{-1}$ Mpc but agree within the error bars of our values for the M/L ratios determined from the SIS model masses, and in the case of A 223 also with the M/L ratio from the NFW model. Two competing effects are responsible for this difference. First and foremost, the weak lensing masses are lower than the masses DO2 used. Second, also

the luminosities determined are lower than in D02. This has two reasons. First, D02 analyze the Schechter luminosity function; this allows them to estimate the fraction of the total luminosity they observe, while we limit our analysis to the actually observed luminosity. Also, D02 correct the area available to fainter objects by subtracting the area occupied by brighter galaxies, which might obscure fainter ones. Both differences mean that we probably underestimate the total luminosity of the clusters. Our M/L ratios are already at the lower end of common M/L ratios. A higher luminosity would lead to even lower M/L value making A 222 and A 223 unusually luminous clusters, considering their mass. Although this system is complex and probably still in the process of collapsing, the M/L ratios of both clusters are very similar and do not exhibit variations like those observed by G02 in A 901/902. Variations between mass, optical, and X-ray luminosity are seen on smaller scales in A 223. A 223-N is very weak in the X-ray image, while it is the dominant sub-clump in the mass and optical luminosity density map. The latter may, however, be affected by the color selection that misses many of the unusually blue bright galaxies in A 223, especially in the Southern sub-clump.

The weak lensing mass determination depends on the redshift of the FBG which we assumed to be $\overline{z}_{\mathrm{FBG}} = 1$. This assumption is based on the redshift distribution of the Fontana et al. (1999) HDF-S photometric redshift catalog. Changes in the redshift distribution could change the absolute mass scale while leaving the dimensionless surface mass density and hence also the significance of the weak lensing signal unchanged. However, the A 222/223 clusters are at comparably low redshift and changes in $\overline{z}_{\mathrm{FBG}}$ affect the mass scale only weakly. To bring $M_{\mathrm{SIS}}(\mathrm{A}\ 222)$ to the value of $M_{\mathrm{vir}}(\mathrm{A}\ 222)$, the mean redshift of the faint background galaxies would have to move to $\overline{z}_{\mathrm{SIS}} = 0.3$. This is clearly unrealistic given the depth of our WFI images and the color selection we made. Although we cannot exclude deviations from the redshift distribution of Fontana et al. (1999), it is much more realistic to attribute the differences between virial and weak lensing masses to intrinsic cluster properties.

From the visual impression of the galaxy distribution it is already obvious that this system is far from being relaxed. This can affect the measured masses in several ways: First, the deviation from circular symmetry certainly implies that the line of sight velocity dispersion is not equal to the velocity

dispersion along other axes in the clusters. If the clusters are oblate ellipsoid with their major axis lying along the line of sight, the measured velocity dispersions will overestimate the 3-d velocity dispersion. Second, if the clusters are not virialized, estimating their masses from the virial theorem of course can give significant deviations from their actual mass. Finally, we could only successfully obtain weak lensing mass estimates with spherical models, which are probably not a good representation of the actual system. Although both clusters are clearly elliptical, fits with SIE models could not reliably reproduce the observed cluster properties. This does not come as a total surprise; King et al. (2002) already noticed that the shear log-likelihood function is much more sensitive to changes in the slope of the mass profile than to a possible cluster ellipticity. The insensitivity of the log-likelihood function to the ellipticity parameters means that the fitting procedure rather changes other cluster parameters than reproducing the actual ellipticity which we see in the parameter-free weak lensing reconstruction.

We found that the concentration parameter c of the NFW profile is poorly constrained if we omit the central regions of the cluster in order to avoid contamination with cluster galaxies. This does not significantly affect the masses determined from fitting NFW profiles and was not of prime importance to the work presented here. From varying the radius of the circles in which shear information was ignored, we saw that galaxies closer to the cluster center constrain the concentration parameter better than those at large distances from the clusters. If one wants to determine concentration parameters more reliably, the fitting procedure has to be extended to include background galaxies close in projection to the cluster centers, while ensuring that faint cluster galaxies do not have a strong influence on the shear signal.

All observations presented in this work – weak lensing, optical, and X-ray – show evidence for a "filament" between the two clusters. The most compelling evidence probably comes from the number density of color-selected early-type galaxies, which is present at the 7σ level (Fig. 4.9). The spectroscopic work of D02 and Proust et al. (2000) confirmed the presence of at least some galaxies at the cluster redshift in the intercluster region. Obtaining a larger spectroscopic sample in the intercluster region would allow us to spectroscopically confirm the significance of this overdensity and could provide insights into the correlation of star formation rates and matter density (e.g., Gray et al. 2004). The X-ray emission between the

clusters is aligned with the overdensity in galaxy number and luminosity density. This provides further evidence for a "filament" extending between A 222 and A 223.

The signal level of the possible filament in the weak lensing map Fig. 4.2 is rather low compared to the clusters. The aperture quadrupole statistics has a signal at the 3σ level on the filament candidate but this signal may already be contaminated by the outskirts of the cluster in the aperture. The most striking "feature" of the mass bridge seen in the κ map is the misalignment with respect to the possible filament seen in the optical and X-ray maps. This can be interpreted in several ways. It could suggest that the surface mass density on the "true filament" defined by the position of the optical overdensity and X-ray emission is below our detection limit and what we see in the κ map is a noise artifact. This possibility aside, the observed misalignment can have several causes. First, as we already discussed in Sect. 4.2.2, the influence of the many reflection features around the bright star West of A 223 on the weak lensing reconstruction is difficult to determine. It seems that the cluster peaks are shifted preferentially away from the reflection rings. The same could be true for the "filament" in the reconstruction. Second, the position of structures inferred from weak lensing is affected by the noise of the reconstruction. This is especially true for low mass structures and is illustrated by our simulations using SIS models to infer the positional uncertainty of weak lensing reconstructed peaks in Sect. 4.2.2. It is possible that at least part of the observed misalignment is caused by the noise of the weak lensing method. Finally, one could in principle imagine that the offset is real and a misalignment of dark and luminous matter is present. This would require complex and possibly exotic physical processes that cause galaxies to form next to a dark matter filament and not in it. At present there is no good observational support for such a scenario. We should note, however, that a misalignment between mass and light is also present in the filament candidate of G02.

As I have not found an objective way to define what a filament in a close double cluster pair is (Dietrich 2002), the question of whether what we observe in A 222/223 constitutes a filament or not can also not be answered objectively. Thus, our filament candidate is – in this respect – not very different from those of Kaiser et al. (1998) and G02. The *projected* virial radii of the clusters marginally overlap. However, (1) the redshift difference

between the clusters make an actual overlap of the clusters unlikely; (2) the projected mass in clusters falls off steeply, and weak lensing is currently not capable of mapping the cluster mass distribution out to the virial radius. A signature of a filament should thus already be present inside the virial radius.

The unambiguous weak lensing detection of a filament between two clusters would provide a powerful support for the theory of structure formation and the "cosmic web". Taking the 3σ signal of the quadrupole statistics on the filament candidate at face value, an increase of the number density of FBGs by a factor of 2.8 could give a 5σ detection. Such number densities can be reached by 8 m class telescopes. The A 222/223 system, being only the third known candidate system to host a filament connecting two clusters, would be a good target for such a study. In fact, a weak lensing study of A 222/223 using SuprimeCam at the Subaru telescope is already underway (Miyazaki et al., in preparation).

In addition to the lensing signal from Abell 222 and Abell 223 we found a significant mass peak SE of A 222. This peak coincides with an overdensity of galaxies. The color-magnitude diagram of these galaxies suggest that this newly found cluster is at a redshift of $z \sim 0.4$, but this estimate comes with a considerable uncertainty and requires spectroscopic confirmation. A maximum likelihood fit to the shear data around this mass peak leads to a best-fit SIS model with a velocity dispersion of 728^{+101}_{-120} km s^{-1}. This serendipitous detection again illustrates the power of weak lensing as a tool for cluster searches, a subject to which I will come back in Chap. 6.

5

XMM-Newton Follow-Up Survey

This chapter describes the Xmm-Newton Follow-Up Survey (xfs) that is the basis for the following chapters. The xfs has two parts, a public and a private part. The public part was carried out as collaboration between the eso Imaging Survey (eis), the Xmm-Newton Survey Science Centre (ssc), and the Institut für Astrophysik und extraterrestrische Forschung (iaef) at the University of Bonn. The data release of the public survey is described in Dietrich et al. (2006), which is the basis of Sects. 5.1, 5.3, and 5.4. The private extension of the survey, carried out as collaboration between the Astrophysikalisches Institut Potsdam (aip) and the iaef is described in Sect. 5.2. Section 5.4 in particular benefits from the collaboration with Axel Schwope at the aip who is responsible for a large fraction of that section.

The public survey was motivated by the new generation of highly sensitive X-ray observatories such as Chandra and Xmm-Newton generating large volumes of X-ray data, which through public archives are made available for all researchers. Even though all observations target a particular object, the large field of view (fov) of Xmm-Newton allows many other sources to be detected in deep exposures. These sources are the main product of the Xmm-Newton Serendipitous Sky Survey (Watson et al. 2001), which annually detects about 30 000 new X-ray sources. To fully understand the nature of these serendipitously detected sources follow-up observations at other wavelengths are needed.

The private survey is motivated by a weak lensing search for galaxy clusters. Looking for galaxy clusters on fields already observed with X-ray satellites opens the opportunity to perform a search using most of the available methods for galaxy cluster search. I will discuss this in detail in Chap. 6.

The xfs aims at obtaining optical observations of Xmm-Newton Serendipitous Sky Survey fields, publicly available in the Xmm-Newton archive, using

the wide-field imager (WFI) at the ESO/MPG 2.2 m telescope at the La Silla Observatory. The optical observations were carried out in service mode. WFI is a focal reducer-type mosaic camera mounted at the Cassegrain focus of the telescope. The mosaic consists of 4×2 CCD chips with 2048×4096 pixels with a projected pixel size of $0''\!.238$, giving a FOV of $8'\!.12 \times 16'\!.25$ for each individual chip. The chips are separated by gaps of $23''\!.8$ and $14''\!.3$ along the right ascension and declination direction, respectively (see also Fig. 3.1). The full FOV of WFI is thus $34' \times 33'$ with a filling factor of 95.9%. Thus, WFI has a FOV which is an excellent match to that of the X-ray detectors on-board the XMM-Newton satellite, making this instrument an obvious choice for this survey in the South.

5.1 Public Data Release

Based on a Call for Ideas for public surveys to the ESO community, the XMM-Newton Survey Science Centre (SSC) proposed optical follow-up observations of XMM-Newton fields for its X-ray Identification (XID) program (Watson et al. 2001; Barcons et al. 2002; Della Ceca et al. 2004). This proposal was evaluated and accepted by ESO's Survey Working Group (SWG) and turned into a proposal for an ESO large program submitted to the ESO OPC.[1]

A complementary multiband optical imaging program (to median 5σ limiting magnitudes reaching $i' = 23.1$) for over 150 XMM-Newton fields is nearing completion in the North using the similarly well matched Wide Field Camera on the 2.5 m Isaac Newton Telescope (Yuan et al. 2003; Watson et al. 2003). In order to provide data for minimum spectral discrimination and photometric redshift estimates of the optical counterparts of previously detected X-ray sources, the survey has been carried out in the B-, V-, R-, and I-passbands. The survey has been administered and carried out by the EIS team.

This section describes observations, reduction, and science verification of data publicly released as part of this follow-up survey. Section 5.1.1 briefly describes the X-ray observations while Sect. 5.1.2 focusses on the optical

---

[1]The full text of the large program proposal is available at `http://www.eso.org/science/eis/documents/EIS.2002-09-04T12:42:31.890.ps.gz`

Table 5.1: Central positions in right ascension, declination and galactic longitude and latitude of the XMM-Newton fields observed as part of the XMM-Newton Follow-Up Survey. Fields that are part of the public survey have their EIS field name given in the last column.

Target	α (J2000.0)	δ (J2000.0)	l	b	Eis-Field
BPM 16274	00:50:03.2	−52:08:17	303:26:03	−64:59:19	XMM-05
CFRS-3h	03:02:39.2	+00:07:31	177:31:03	−48:20:12	—
RX J0505.3−2849	05:05:20.0	−28:49:05	230:39:29	−34:36:50	XMM-06
RX J0720.4−3125	07:20:25.1	−31:25:49	244:09:28	−08:09:50	XMM-02
RX J0925.7−4758	09:25:46.0	−47:58:17	271:21:18	+01:53:03	XMM-01
RBS 0864	10:21:03.8	+04:26:23	239:24:11	+47:57:38	—
QSO B1030−403	01:33:01.9	−40:06:28	271:59:44	−74:25:23	—
BR 1033−0327	10:36:23.7	−03:43:20	251:06:41	+45:07:58	XMM-13
SDSS J104433.04−012502.2	10:44:33.0	−01:25:02	118:58:09	−64:14:07	—
MS 1054.4−0321	10:56:60.0	−03:37:27	256:34:30	+48:40:18	XMM-04
HE 1104−1805	11:06:33.0	−18:21:24	270:49:55	+37:53:29	XMM-03
PG 1115+080	11:18:17.0	+07:45:59	249:53:16	+60:38:41	—
CD −33 07795	11:29:27.2	−34:19:55	284:52:26	+25:27:35	XMM-15
T LEO	11:38:27.1	+03:22:10	47:57:38	+60:31:32	—
WR 46	12:05:19.0	−62:03:07	297:33:23	+00:20:14	XMM-12
IRAS 12112+0305	12:13:46.1	+02:48:41	280:59:17	+64:03:59	XMM-14
LBQS 1228+1116	12:30:54.1	+11:00:11	285:16:27	+73:10:01	—
NGC 4666	12:45:08.9	−00:27:38	299:25:55	+63:17:22	XMM-08

Table 5.1 – *continued from previous page*

Target	α (J2000.0)	δ (J2000.0)	l	b	Eis-Field
QSO B1246−057	12:49:13.9	−05:59:19	301:55:40	+56:52:43	XMM-09
Field 864-1	13:41:22.4	+00:23:52	329:08:46	+60:42:09	—
Field 864-9	13:44:36.0	−00:24:00	329:59:37	+59:38:57	—
A 1882	14:14:39.9	−00:19:07	342:23:58	+56:01:31	—
MKW 9	15:32:29.3	+04:40:54	9:52:34	+45:34:08	—
Sgr A	17:45:40.0	−29:00:28	359:56:39	−00:02:45	XMM-11
PB 5062	22:05:09.8	−01:55:18	58:03:55	−42:54:13	XMM-10
LBQS 2212−1759	22:15:31.7	−17:44:05	39:16:07	−52:55:44	XMM-07
NGC 7252	22:20:44.8	−24:40:42	28:26:20	−56:08:54	—
PHL 5200	22:28:30.4	−05:18:55	59:07:49	−49:36:14	—

imaging. In Sect. 5.1.3 the reduction and calibration of optical data are presented and the results discussed. Final survey products such as stacked images and science-grade catalogs extracted from them are presented in Sect. 5.1.4. The quality of these products is evaluated in Sect. 5.1.5 and compared to an independent reduction in Sect. 5.3. In Sect. 5.4 the results of a preliminary assessment of X-ray/optical cross-correlation are also discussed.

5.1.1 X-ray Observations

The original proposal by the SWG to the ESO OPC was to cover a total area of approximately 10 square degrees (40 fields) to a limiting magnitude of 25 (AB, 5σ, 2$''$ aperture). The OPC approved enough time to observe 12 fields, later extending the time allocation to include 3 more fields. This paper presents results for the original 12 fields for which the optical data were originally publicly released in the fall of 2004, with corrections to the weight maps released in July 2005. Table 5.1 gives the location of all fields in this survey. The 12 fields for which data was publically released are indicated in this table by their EIS field name.

These fields were selected and prioritized by the survey collaboration and an appointed committee of the SWG. These fields were selected following, as much as possible, the criteria given in the proposal, namely that: (1) the fields had to have a large effective exposure time in X-ray (ideally $t_{\mathrm{exp}} > 30$ ks) with no enhanced background; (2) the X-ray data of the selected fields had to be public by the time the raw WFI frames were to become public; (3) the original targets should not be too bright and/or extended, thus allowing a number of other X-ray sources to be detected away from the primary target; and (4) ~ 70% of the fields had to be located at high-galactic latitude. Comments on the individual fields can be found in Appendix C.1. The full list of X-ray observations in the XFS for both – public and private fields – is given in App. C.2 in Table C.1.

Combined EPIC X-ray images for the public survey fields were created from exposures taken with the three cameras (PN, MOS1, MOS2) on-board XMM-Newton. The sensitive area of these cameras is a circle with a diameter of approximately 30$'$. These cameras and their settings are described in detail in Ehle et al. (2004). For some fields additional observations were available but these were discarded mainly due to unsuitable camera settings.

The Xmm-Newton data, both in raw and pipeline reduced form, are available through the Xmm-Newton Science Archive.[2] These data were used to create a wide range of products which include:

– Combined EPIC images in the XID-band 0.5–4.5 keV (FITS);

– Combined EPIC images in the total band 0.1–12 keV (FITS);

– Color images using three sub-bands, 0.5–1.0 keV (red), 1.0–2.0 keV (green), 2.0–4.5 keV (blue), in the XID-band (JPG).

As an illustration, Fig. 5.1 shows color composites of the final combined X-ray images for the 12 fields considered. Note that the X-ray images have a non-uniform exposure time over the field of view due to (1) the arrangements of the CCDs in the focal plane, which is different for the three cameras, and (2) the vignetting of the camera optics.

5.1.2 Optical observations

As mentioned earlier the optical data for this survey were obtained with the wide-field imager at the ESO/MPG-2.2 m telescope on La Silla, Chile. The WFI data contributing to the public survey are from the following sources:

1. the ESO Large Programme 170.A-0789(A) (Principal Investigator: J. Krautter, as chair of the SWG) which has accumulated data from January 27, 2003 to March 24, 2004 at the time of writing;

2. the contributing programs 70.A-0529(A); 71.A-0110(A); 71.A-0110(B) with P. Schneider as the Principal Investigator, which have contributed data from October 14, 2002 to September 29, 2003.

Observations were performed in the B-, V-, R-, and I-passbands. These were split into OBs consisting of a sequence of five (ten in the I-band) dithered sub-exposures with the typical exposure time given in Table 5.2. The dither pattern with a radius of $80''$ was optimized for the best filling of the gaps.

---

[2]http://xmm.vilspa.esa.es/external/xmm_data_acc/xsa/index.shtml

Table 5.2: Planned observing strategy for the Xmm-Newton follow-up survey. The table gives in Col. 1 the passband; in Col. 2 the filter id adopting the unique naming convention of the La Silla Science Operations Team; in Col. 3 the total exposure time in seconds; in Col. 4 the number of observing blocks (OBS) per field; and in Col. 5 the integration time of the individual sub-exposures in the OB. The two table entries for the R-band reflect the different observing strategies of the public survey (first line) and the contributing program (second line).

Passband	Filter	$T_{\mathrm{tot}}(s)$	N_{OB}	$T_{\mathrm{exp}}(s)$
B	B/123_ESO879	1800	1	360
V	V/89_ESO843	4400	2	440
R	Rc/162_ESO844	3500	1	700
R	Rc/162_ESO844	11500	4	575
I	I/203_ESO879	9000	3	300

Filter curves can be found in Arnouts et al. (2001) and on the web page of the La Silla Science Operations Team.[3]

Even though the nominal total survey exposure time for the R-band is 3500 s, the data contributed by the Bonn group provided additional exposures totaling 11 500 s each, spread over 4 OBs. For the same reason the B-band data for the field XMM-07 has a significantly larger exposure time than that given in Table 5.2.

Service mode observing provides the option for constraints on e.g., seeing, transparency, and airmass to be specified in order to meet the requirements of the survey. The adopted constraints were: (1) dark sky with a fractional lunar illumination of less than 0.4; (2) clear sky with no cirrus though not necessarily photometric; and (3) seeing $\leq 1\rlap{.}''2$. The R-band images of the contributing program were taken with a seeing constraint of $\leq 1\rlap{.}''0$ so that the data can be used for weak lensing studies.

The total integration time in some fields may be higher than the nominal one listed in Table 5.2 because unexpected variations in ambient conditions during the execution of an OB can cause, for instance, the seeing and trans-

---

[3]http://www.ls.eso.org/lasilla/sciops/2p2/E2p2M/WFI/filters/

parency to exceed the originally imposed constraints. If this happens, the OB is normally executed again at a later time. In these cases the decision of using or not all the available data must be taken during the data reduction process. In the case of the present survey all available data were included in the reduction, which explains why in some cases the total integration time exceeds that originally planned.

The public data release describes data accumulated prior to October 16, 2003, amounting to about 80 h on-target integration. The science data comprises 720 exposures split into 130 OBs. About 15% of the B-band and 85% of the R-band data are from the contributing programs.

5.1.3 Data Reduction

The accumulated optical exposures were reduced and calibrated using the EIS Data Reduction System (da Costa et al., in preparation) and its associated image processing engine based on the C++ EIS/MVM library routines (Vandame 2004, Vandame et al., in preparation). This library incorporates routines from the multi-resolution visual model package (MVM) described in Bijaoui & Rué (1995) and Rué & Bijaoui (1997). The EIS Data Reduction System was developed by the EIS project to enable handling and reducing, using a single environment, the different observing strategies and the variety of single/multi-chip, optical/infrared cameras used by the different surveys carried out by the EIS team. The platform independent EIS/MVM image processing engine is publicly available and can be retrieved through the ESO archive.[4]

The system automatically recognizes calibration and science exposures and treats them accordingly. For the reduction, frames are associated and grouped into *Reduction Blocks* (RBs) based on the frame type, spatial separation and time interval between consecutive frames. The end point of the reduction of an RB is a *reduced image* and an associated weight map describing the local variations of noise and exposure time in the reduced image. The data reduction algorithms are fully described in Vandame (2004).

In order to produce a *reduced image*, the individual exposures within an RB are: (1) normalized to 1 s integration; (2) astrometrically calibrated with the GSC-2.2 as reference catalog, using a second-order polynomial distortion

---

[4] http://archive.eso.org/

model; (3) warped into a user-defined reference grid (pixel, projection and orientation), using a third-order Lanczos kernel; and (4) coadded, using the weight image for discarding the flux contribution from masked pixels (e.g. satellite tracks automatically detected and masked using a Hough transformation), for which the pixel value is zero. Note that individual exposures in the RB are not scaled to the same flux level. This assumes that the time interval corresponding to an RB is small enough to neglect significant changes in airmass.

The 720 raw exposures were converted into 160 fully calibrated reduced images, of which 146 were released in the B- (36), V- (32), R- (43) and I- (35) passbands. Of the remaining 14, 10 were observed with wrong coordinates, three (XMM-05 (R), XMM-06 (I), XMM-12 (V)) were rejected after visual inspection and one (XMM-12) was discarded due to a very short integration time (73 s), associated to a failed OB. The number of reduced images (150) exceeds that of OBS (130) because the RBs were built by splitting the OBS in order to improve the cosmetic quality of the final stacked images, as discussed below.

The photometric calibration of the reduced images was obtained using the photometric pipeline integrated to the EIS data reduction system as described in more detail in Appendix C.3. In particular, the XMM-Newton survey data presented here were obtained in 41 different nights of which 37 included observations of standard star fields. For these 37 nights it was attempted to obtain photometric solutions. The four nights without standard star observations are: February 2, 3 and 4, 2003 (Public Survey); and November 8, 2002 (contributing program). For the nights with standard star observations, the number of measurements ranges from a few to over 300, covering from 1 to 3 Landolt fields.

Table 5.3 summarizes the available photometric observations. For three nights (March 26, 2003; April 2, 2003; August 6, 2003) the solutions obtained in the passbands V, I, R, respectively (either 2- or 3-parameter fits) deviate from the median by -0.26, -0.5, -0.25 mag. Of those, only the I-band zeropoint obtained for April 2, 2003 deviates by more than 3σ from the solutions obtained for other nights. Note that the type of solution obtained depends on the available airmass and color coverage, which in the case of the XMM-Newton survey depends on the calibration plan adopted by the La Silla Science Operations Team.
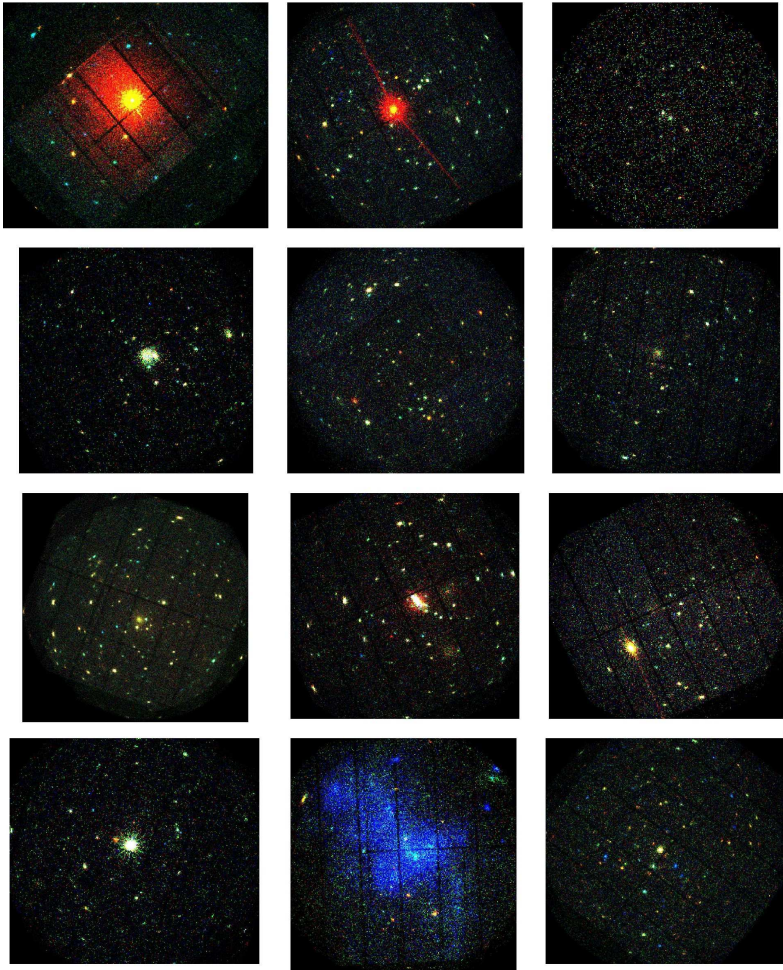
Figure 5.1: Color composite X-ray images for the 12 fields considered in the public data release (XMM-01 to XMM-12 from top left to bottom right). The color images are composites within the so-called XID-band (0.5–4.5 keV). Red, green and blue channels comprise the energy ranges 0.5–1.0 keV, 1.0–2.0 keV, and 2.0–4.5 keV, respectively. Weighting of the sub-images was done in a manner that a typical extragalactic source with a power law spectrum with photon index 1.5 and absorption column density $N_H = 1 \times 10^{20}$ cm^{-2} would have equal photon numbers in all three bands. North is up and East to the left. The size of the images is typically $30' \times 30'$ but varies slightly with camera orientation.

Table 5.3: Summary of the number of nights with standard star observations and type of solution. The table gives Col. 1 the passband; in Col. 2–5 the number of nights assigned a default solution or a 1–3-parameter solution, respectively; and in Col. 6 the total number of nights with standard star observations.

Passband	default	1-par	2-par	3-par	total
B	0	3	4	3	10
V	0	8	3	5	16
R	0	8	3	3	14
I	4	8	2	5	19

Table 5.4: Comparison between the EIS 3-parameter fit solutions and the Telescope Team's best solution. The table lists in Col. 1 the passband; in Cols. 2–4 the mean offsets in zeropoint (ZP), extinction (k) and color term (color), respectively.

Passband	ΔZP	Δk	Δcolor
B	0.00	−0.03	−0.06
V	−0.05	0.00	−0.01
R	0.00	0.10	0.00
I	−0.04	0.05	−0.02

Because the EIS Survey System automatically carries out the photometric calibrations it is interesting to compare the solutions to those obtained by other means. Therefore, the automatically computed 3-parameter solutions of the EIS Survey System are compared with the *best solution* recently obtained by the La Silla Science Operations Team. The results of this comparison are presented in Table 5.4. The agreement of the solutions is excellent for all passbands. However, it is worth emphasizing that the periods of observations of standard stars available to the two teams do not coincide.

Not surprisingly, larger offsets are found when 2- and 1-parameter fits are included, depending on the passband and estimator used to derive the estimates for extinction and color term. Finally, taking into consideration only 3-parameter fit solutions and after rejecting 3σ outliers one finds that

Table 5.5: Grades representing the visual assessment of the reduced bad images. The table, ordered by field and date, lists: in Col. 1 the field name; in Col. 2 the passband; in Col. 3 the civil date when the night started (YYYY-MM-DD); in Col. 4 the grade given by the visual inspection; and in Col. 5 the primary motive for the grade.

EIS-Field	Passband	Date	Grade	Comment
XMM-05	R	2002-10-14	D	strong stray light contamination
XMM-06	I	2003-01-29	D	inadequate fringing correction
XMM-12	I	2003-03-29	D	very short integration time
XMM-12	V	2003-09-27	D	out-of-focus
XMM-01	V	2003-02-01	C	strong shape distortions
XMM-07	R	2003-08-06	C	stray light contamination
XMM-10	R	2003-08-06	C	fringing
XMM-10	R	2003-09-23	C	fringing
XMM-10	R	2003-09-29	C	fringing
XMM-10	R	2003-09-29	C	fringing
XMM-10	R	2003-09-29	C	fringing

the scatter of the zeropoints is $\lesssim 0.08$ mag. This number is still uncertain given the small number of 3-parameter fits currently available, especially in the R-band. The obtained scatter is a reasonable estimate for the current accuracy of the absolute photometric calibration of the XMM-Newton survey data.

There are two more points that should be considered in evaluating the accuracy of the photometric calibration of the present data. First, for detectors consisting of a mosaic of individual CCDs it is important to estimate and correct for possible chip-to-chip variations of the gain. For the present data these variations were estimated by comparing the median background values of sub-regions bordering adjacent CCDs within one RB. The determined variations were used to bring the gain to a common value for all CCDs in the mosaic. This was applied to both science and standard exposures. Second, it is also known that large-scale variations due to non-uniform illumination over the field of view of a wide-field camera exist. The significance of this effect is passband-dependent and becomes more pronounced with increasing

distance from the optical axis (Manfroid & Selman 2001; Koch et al. 2004; Vandame et al. in preparation). Automated software to correct for this effect has been developed but due to time constraints it has not yet been applied to these data.

The final step of the data reduction process involves the assessment of the quality of the reduced images. Following visual inspection, each reduced image is graded, with the grades ranging from A (best) to D (worst). This grade refers only to the visual aspect of the data (e.g., background, cosmetics). Out of 150 reduced images covering (see Sect. 5.1.2) the selected Xmm-Newton fields, 104 were graded A, 35 B, 7 C and 4 D. The images with grades C and D are listed in Table 5.5. It is important to emphasize that the reduced images must be graded, as grades are used in the preparation of the final image stacks. In particular, reduced images with grade D have no scientific value and were not released and were discarded in the stacking process discussed in the next section.

The success rate of the automatic reduction process is better than 95% and most of the lower grades are associated with observational problems rather than inadequate performance of the software operating in an un-supervised mode. An interesting point is that occasionally R-band images are also affected by fringing (see Table 5.5) – for instance, in the nights of August 6 and September 23 and 29, 2003, all from the contributing program. The night of August 6 is one of the nights for which the computed R-band zeropoint deviates from the median. This points out the need to consider applying fringing correction also in the R-band, at least in some cases. The R-band fringing problem accounts for five out of seven grade C images. The remaining cases are due to stray-light and strong shape distortions.

It should also be pointed out that the reduced images show a number of cosmic ray hits. This is because the construction of rbs was optimized for removing cosmic ray features in the final stacks using a thresholding technique. To this end the number of images in an rb was minimized for some field and filter combinations to have at least three reduced images entering the stack blocks (sb).

5.1.4 Final Products

Images

The 146 reduced images with grades better than D were converted into 44 stacked (coadded) images using the EIS Data Reduction System. The system creates both a final stack, by coadding different reduced images taken of the same field with the same filter (see Appendix C.4), and an associated product log with additional information about the stacking process and the final image. Note that all stacks (and catalogs) and their associated product logs are publicly available from the EIS survey release and ESO Science Archive Facility pages.[5]

The final stacks are illustrated in Fig. 5.2 which shows cutouts from color composite images of the 12 fields. From this figure, one can easily see the broad variety of fields observed by this survey – dense stellar fields (XMM-01, XMM-02, XMM-12), sometimes with diffuse emission (XMM-11), extended objects (e.g., XMM-08), and empty fields at high galactic latitude (e.g., XMM-07). While the constraints imposed by the system normally lead to good results, visual inspection of the images after stacking revealed that at least in one case the final stacked image was significantly degraded by the inclusion of a reduced image (graded B) with high-amplitude noise. Therefore, this image was not included in the production of the corresponding stack. The reason for this problem is being investigated and may lead to the definition of additional constraints for the automatic rejection algorithm being currently used.

Before being released the stacks were again examined by eye and graded. Out of 44 stacks, 33 were graded A, 10 B, and 1 C, with no grade D being assigned. In addition to the grade a comment may be associated and a list of all images with some comment can be found in the README file associated to this release in the EIS web-pages. The comments refer mostly to images with poor background subtraction either due to very bright stars (XMM-12) or extended, bright galaxies (XMM-08, XMM-09) in the field. It is important to emphasize that the reduction mode for these data was optimized for

---

[5] http://www.eso.org/science/eis/surveys/release_XMM.html for catalogs and http://archive.eso.org/archive/public_datasets.html for the latest release of stacked images made in July 2005.

Table 5.6: Summary of available data. The table gives for each field in: Col. 1 the field identification; Cols. 2–4 for each passband the number of reduced images with the number in parenthesis being the number of independent nights in which they were observed.

Eis-Field	B	V	R	I
xmm-01	3 (1)	3 (2)	3 (1)	3 (3)
xmm-02	3 (1)	3 (1)	3 (1)	3 (1)
xmm-03	3 (1)	3 (2)	5 (3)	3 (1)
xmm-04	3 (1)	3 (2)	4 (2)	3 (2)
xmm-05	3 (1)	3 (2)	5 (1)	3 (2)
xmm-06	3 (1)	3 (2)	6 (4)	3 (2)
xmm-07	3 (2)	3 (2)	6 (4)	3 (2)
xmm-08	3 (1)	3 (1)	—	3 (2)
xmm-09	3 (1)	3 (2)	—	3 (2)
xmm-10	3 (1)	—	5 (3)	—
xmm-11	3 (1)	3 (2)	3 (1)	5 (4)
xmm-12	3 (1)	2 (1)	3 (1)	3 (2)

extragalactic, non-crowded fields, which is not optimal for some of these fields. Residual fringing is also observed in some stacks such as that of xmm-10 in the R-band and xmm-04, xmm-06 in the I-band.

As mentioned in the previous section, to improve the rejection of cosmic rays, the rbs were constructed so that in most cases the sbs consist of at least 3 reduced images as input. This allows for the use of a thresholding procedure, with the threshold set to 2.5σ, to remove cosmic ray hits from the final stacked image. Even with this thresholding the stacks consisting of only three rbs (totaling 5 exposures), mostly B-band images, still show some cosmic ray hits. This happens primarily in the regions of the inter-chip gaps, where fewer images contribute to the final stack. Also, the automatic satellite track masking algorithm has proven to be efficient in removing both bright and faint tracks. The most extreme case is 3 satellite tracks of varying intensity in a single exposure. The regions affected by satellite tracks in the original images were flagged in the weight-map images and thus are properly removed from the stacked image. Naturally, in the regions where a satellite

Figure 5.2: Above are cut-outs from color images of xmm-01 to xmm-12 (from top left to bottom right) to illustrate the wide variety of fields the pipeline can successfully handle. The color images are BVR composite where R-band data is available, BVI otherwise. The side length of the images displayed here is 7′9 × 5′6. In these images North is up and East is to the left. These composite color images also demonstrate the accuracy of the astrometric calibration independently achieved in each passband.

Table 5.7: Type of best photometric solution available for each field. The table gives: in Col.1 the field name; in Cols. 2–5 the number of free parameters in the type of the *best solution* available for the passbands indicated. Solutions with more free parameters in general indicate better airmass and color coverage, yielding better photometric calibration.

Eɪs-Field	default	1-par	2-par	3-par
xmm-01	R	BV	—	I
xmm-02	RI	BV	—	—
xmm-03	—	I	R	BV
xmm-04	—	V	—	BRI
xmm-05	—	R	I	BV
xmm-06	—	V	BR	I
xmm-07	—	I	B	VR
xmm-08	—	V	—	BI
xmm-09	—	—	B	VI
xmm-10	—	—	B	R
xmm-11	—	—	—	BVRI
xmm-12	—	BR	V	I

track was found in one of the contributing images the noise is slightly higher in the stacked image. This is also reflected in the final weight-map image.

The accuracy of the final photometric calibration of course depends on the accuracy of the photometric calibration of the reduced images which are used to produce the final coadded stacks and the number of independent photometric nights in which these were observed (see Table 5.6). The former depends not only on the quality of the night but also on the adopted calibration plan. To preview the quality of the photometric calibration, Table 5.6 provides information on the number of reduced images and number of independent nights for each passband and filter. Complementing this information, Table 5.7 shows the best type of solution available for each field/filter combination. Examination of these two tables provides some insight into the quality of the photometric calibration of each final stack, as reported below.

The main properties of the stacks produced for each field and filter are summarized in Table 5.8. The table gives: in Col. 1 the field identifier; in

Col. 2 the passband; in Col. 3 the total integration time T_{int} in seconds, of the final stack; in Col. 4 the number of contributing reduced images or RBS; in Col. 5 the total number of science frames contributing to the final stack; in Cols. 6 and 7 the seeing in arcseconds and the point-spread function (PSF) anisotropy measured in the final stack; in Col. 8 the limiting magnitude, m_{lim}, estimated for the final image stack for a $2''$ aperture, 5σ detection limit in the AB system; in Col. 9 the grade assigned to the final image during visual inspection (ranging from A to D); in Col. 10 the fraction (in percentage) of observing time relative to that originally planned.

This table shows that for most stacks the desired limiting magnitude was met in V (24.92 mag) or even slightly exceeded in B (25.20 mag). The R- and I-band images are slightly shallower than originally proposed with median limiting magnitudes of 24.66 mag and 24.39 mag. Still, when only the high-galactic latitude fields are included the median limiting magnitudes are fainter – 25.33 (B), 25.05 (V), 25.36 (R) and 24.58 (I) mag. All magnitudes are given in the AB system. The median seeing of all stacked images is $0''.94$ with the best and worst values being $0''.60$ and $1''.51$, respectively. This is significantly better than the seeing requirement of $1''.2$ specified for this survey.

Finally, the following remarks can be made concerning the image stacks and their calibration:

– XMM-01 (R) – The background subtraction near bright stars is poor. This field was observed as a single OB on February 3, 2003 for which no standard stars were observed. Since this is a galactic field there are no complementary observations from the contributing program, and therefore these observations cannot be calibrated.

– XMM-01 (I) – This field at low galactic latitude is very crowded and no acceptable fringing map could be produced from the science exposures in the field. The de-fringing was done with an *external fringing* map generated from science images taken on empty fields close in time to the XMM-01 I-band observations.

– XMM-02 (R) – The observations for this pointing and filter were done with one OB (5 exposures) on February 2, 2003 for which no standard stars observations were carried out.

– xmm-02 (I) – The observations for this pointing and filter were done with two obs (10 exposures each) on February 2, 2003 for which no standard stars observations were carried out. Like for xmm-01 (I) an external fringing map was used.

– xmm-03 (V) – The V-band calibration on the night of March 26, 2003 yields a 3-parameter fit that deviates from the median of the solutions by roughly 0.26 mag (less than 3σ).

– xmm-04 (I) – Low level fringing is still visible in the final stacked image.

– xmm-06 (I) – As in xmm-04, low level fringing is still visible in the final stack.

– xmm-07 (B) – From the three reduced images available, only two were used for stacking because of the high amplitude of noise in one of them, which greatly affected the final product.

– xmm-07 (R) – This field was observed in four nights (August 6, and September 23, 27, and 28, 2003) as part of the contributing program. For the night of August 6 a 3-parameter fit solution was obtained. However, this solution deviates by roughly 0.25 mag relative to the median of all R-band solutions.

– xmm-07 (I) – There is a visible stray light reflection at the lower right corner of the image.

– xmm-08 (V) – The bright central galaxy is larger than the dithering pattern, thus making it difficult to estimate the background in its neighborhood. As a consequence the background subtraction procedure does not work properly.

– xmm-08 (I) – The comments about the background subtraction for the V-band image also apply to the I-band. This field was observed using 3 obs (which in this case also correspond to 3 rbs) on two nights (March 30, 2003, one ob and April 2, 2003, two obs). On the night of April 2 a 3-parameter solution was obtained for which the ZP determined deviates significantly (more than 3σ) from the

median of all solutions, even though the conditions of the night seem to have been adequate. The reason for this poor solution is at present unknown. Poor fringing correction is a possibility but needs to be confirmed. The zeropoint for the two reduced images taken in this night has been replaced by a default value.

– XMM-09 (BVI) – The preceding comment about background subtraction (see XMM-08) can be repeated here for the large galaxy in the North-West corner of the image. The background subtraction procedure fails, creating a strong variation around the galaxy.

– XMM-10 (B): This stack has a shorter exposure time than the others released, leading to higher background noise.

– XMM-10 (R) – This field was observed in the nights of August 6, and September 23 and 29, 2003 as part of contributing program. As in case of XMM-07 the solution for August 6 deviates somewhat from the median.

– XMM-11 (V) – The same comments as for the photometric calibration of XMM-03 (V) apply to this image.

– XMM-11 (I) – Like for XMM-01 (I) an external fringing map was used.

– XMM-12 (BR) – The background subtraction near bright stars is poor.

– XMM-12 (V) – The preceding comment about background subtraction also applies to this image. In addition the comment about the photometric calibration of XMM-03 (V-band) applies to this image as well.

– XMM-12 (I) – The comment about background subtraction also applies to the I-band image. Like for XMM-01 (I) an external fringing map was used.

Some improvements in the image quality may be possible in the future by adopting a different observing strategy such as larger dithering patterns to deal with more extended objects or shorter exposure times to minimize the impact of fringing.

Table 5.8: Overview of the properties of the produced image stacks. Column 1 gives the EIS field name; Col. 2 the passband of the observations; Col. 3 the total exposure time of the stack in seconds; Cols. 4 and 5 list the number of reduction blocks and exposures entering the stack, respectively; Col. 6 gives the seeing of the image; Col. 7 gives RMS of PSF ellipticity; Col. 8 lists the 5σ, $2''$ aperture limiting magnitudes in the AB system; Col. 9 gives the grade assigned to stack after visual inspection; finally, Col. 10 gives the completeness of the observations with respect to the exposure time of the observing strategy defined in Table 5.2.

Eis-Field	Passband	T_{int} (s)	#RBs	#Exp.	Seeing (arcsec)	PSF RMS	m_{lim} (mag)	Grade	Completeness (%)
XMM-01	B	1800	3	5	1.19	0.056	24.94	A	100
XMM-01	V	6599	3	15	0.97	0.056	25.32	A	150
XMM-01	R	3500	3	5	0.82	0.074	23.97	B	100
XMM-01	I	8998	3	30	0.69	0.063	23.53	A	100
XMM-02	B	1800	3	5	1.17	0.051	24.51	A	100
XMM-02	V	4399	3	10	0.96	0.076	24.63	A	100
XMM-02	R	3500	3	5	0.64	0.087	24.69	A	100
XMM-02	I	5998	3	20	0.94	0.079	23.84	A	67
XMM-03	B	1800	3	5	1.01	0.031	25.44	A	100
XMM-03	V	4399	3	10	0.86	0.068	25.35	A	100
XMM-03	R	11748	5	20	0.83	0.152	25.15	A	336
XMM-03	I	9297	3	31	0.96	0.061	24.39	A	103
XMM-04	B	1800	3	5	1.17	0.041	25.22	A	100
XMM-04	V	4399	3	10	1.07	0.050	25.05	A	100

Table 5.8 – continued from previous page

Eis-Field	Passband	T_{int}	#RBs	#Exp.	Seeing	PSF RMS	m_{lim}	Grade	Completeness
XMM-04	R	11748	4	20	0.76	0.069	25.57	A	336
XMM-04	I	8998	3	30	0.87	0.066	24.83	A	100
XMM-05	B	1800	3	5	1.24	0.076	25.18	A	100
XMM-05	V	4399	3	10	1.51	0.063	24.80	A	100
XMM-05	R	12348	5	21	0.94	0.072	25.58	A	353
XMM-05	I	8998	3	30	1.09	0.056	24.58	A	100
XMM-06	B	1800	3	5	0.87	0.052	25.57	A	100
XMM-06	V	4399	3	10	0.73	0.039	25.43	A	100
XMM-06	R	14998	6	25	0.85	0.060	24.54	A	429
XMM-06	I	8998	3	30	0.74	0.044	24.40	A	100
XMM-07	B	2699	2	8	1.24	0.035	25.55	A	150
XMM-07	V	4399	3	10	1.10	0.050	25.37	A	100
XMM-07	R	15698	6	27	1.03	0.058	25.66	A	449
XMM-07	I	8998	3	30	0.95	0.048	24.96	A	100
XMM-08	B	1800	3	5	1.28	0.062	25.62	A	100
XMM-08	V	4399	3	10	1.03	0.082	24.93	A	100
XMM-08	I	8998	3	30	0.79	0.052	24.76	B	100
XMM-09	B	1800	3	5	0.94	0.045	24.59	B	100
XMM-09	V	4839	3	11	0.83	0.031	24.20	B	110
XMM-09	I	8998	3	30	0.72	0.038	23.81	B	100

Table 5.8 – *continued from previous page*

Eis-Field	Passband	T_{int}	#RBs	#Exp.	Seeing	PSF RMS	m_{lim}	Grade	Completeness
XMM-10	B	1500	3	5	1.12	0.042	24.26	B	83
XMM-10	R	11748	5	20	0.88	0.049	24.62	C	336
XMM-11	B	1800	3	5	1.09	0.058	25.25	A	100
XMM-11	V	4399	3	10	0.77	0.075	24.03	A	100
XMM-11	R	3500	3	5	0.60	0.090	23.10	A	100
XMM-11	I	12297	5	41	0.77	0.087	22.64	A	137
XMM-12	B	1800	3	5	1.09	0.087	23.41	B	100
XMM-12	V	3519	2	8	0.79	0.085	23.48	B	80
XMM-12	R	4899	3	7	0.64	0.111	23.16	B	140
XMM-12	I	3599	3	12	1.21	0.093	22.01	B	40

Catalogs

For the 8 fields located at high-galactic latitudes with $|b| > 30°$, a total of 28 catalogs were produced (not all fields were observed in all filters, see Table 5.6). Catalogs for the remaining low-galactic latitude fields were not produced since these are crowded stellar fields for which SExtractor alone is not well suited. As in the case of the Pre-FLAMES survey (Zaggia et al., in preparation), it is preferable to use a PSF fitting algorithm for them such as DAOPHOT (Stetson 1987). Details about the catalog production pipeline available in the EIS data reduction system are presented in Appendix C.5.

As mentioned earlier, the fields considered here cover a range of galactic latitudes of varying density of objects, in some cases with bright point and extended sources in the field. In this sense this survey is a useful benchmark to evaluate the performance of the procedures adopted for the un-supervised extraction of sources and the production of science-grade catalogs. This also required carrying out tests to fine-tune the choice of input parameters to provide the best possible compromise. Still, it should be emphasized that the catalogs produced are in some sense general-purpose catalogs. Specific science goals may require other choices of software (e.g. DAOPHOT, IMCAT) and/or input parameters.

A key issue in the creation of catalogs is to minimize the number of spurious detections. In general, the adopted extraction parameters successfully limit the number of spurious objects in the catalogs. However, there are unavoidable situations where this is not the case. Among these are: (1) the presence of ghost images near bright stars. Their location and size vary with position and magnitude making it difficult to deal with them in an automatic way; (2) the presence of bright galaxies because the algorithm for automatic masking does not work well in this case; (3) residual fringing in the image; (4) the presence of stray light, in particular, associated with bright objects just outside the observed field; (5) when the image is slightly rotated, the trimming procedure does not trim the corners of the image correctly, leading to the inclusion of regions with a low SNR. In these corners many spuriously detected objects are not flagged as such. The XMM-Newton fields are a good showcase for these various situations.

Another important issue to consider is the choice of the parameter that controls the deblending of sources. Experience shows that the effects of

deblending depend on the type of field being considered (e.g., empty or crowded fields, extended object, etc.) and vary across the image. Some tests were carried out but further analysis of this topic may be required.

A number of tests have also been carried out to find an adequate compromise for the scaling factor used in the calculation of the size of the automatic masks (see Appendix C.5) which depends on the passband and the magnitude of the object. While the current masking procedure generally works well, the optimal scaling will require further investigation. It is also clear that for precision work, such as, e.g., lensing studies, additional masking by hand is unavoidable. It should also be mentioned that occasionally the masking of saturated stars fails. This occurs in five out of the 28 catalogs released and only for ~ 10% of the saturated stars in them. These cases are likely to be due to stars just barely saturated, at the limit of the settings for automatic masking.

Bearing these points in mind, the following comments can be made regarding some of the released catalogs:

- XMM-03 (B) – The automatic masking misses a few saturated stars.

- XMM-06 (B) – Due to a small rotation of the image of a few degrees the trimming frame does not mask the borders completely.

- XMM-06 (V) – The deblending near bright galaxies is insufficient. Deblending near bright stars is too strong.

- XMM-06 (R) – As in the V-band image the deblending near bright galaxies is insufficient.

- XMM-06 (I) – As in the V-band image the deblending near bright galaxies is insufficient. Spurious object detections are caused by reflection features of bright stars and stray light reflections.

- XMM-07 (B) – Spurious objects in the corners are caused by insufficient trimming.

- XMM-08 (B) – Masks are missing for a number of saturated stars. XMM-08 contains an extended, bright galaxy (NGC 4666) at the center of the image, plus a companion galaxy located South-East of it. The

presence of these galaxies leads to a large number of spurious object detections in their surroundings in all bands.

– XMM-08 (VRI) – See the comments about spurious object detections for XMM-08 B-band.

– XMM-09 (B) – Cosmic rays are misidentified as real objects. The very bright galaxy located at the North-West of the image leads to the detection of a large number of spurious objects extending over a large area $(10' \times 10')$ in all bands. Even though the galaxy has been automatically masked, the affected area is much larger than that predicted by the algorithm, which is optimized for stars. Thus, additional masking by hand would be required.

– XMM-09 (VI) – See the comments about spurious object detections for XMM-09 B-band.

– XMM-10 (R) – The stacked image was graded C because of fringing. The fringing pattern causes a high number of spurious object detections along the fringing pattern, leading to a catalog with no scientific value. *This catalog is released exclusively as an illustration.*

5.1.5 Quality Checks

A key element in public surveys is to provide potential users with information regarding the quality of the products released. To this end a number of checks of the data are carried out and several diagnostic plots summarizing the results are automatically produced by the EIS Survey System. They are an integral part of the product logs available from the survey release page. Due to the large number of plots produced in the verification process these are not reproduced here. Instead a small set illustrating the results are presented.

A relatively simple statistics that can be used to check the catalogs and the star/galaxy separation criteria is to compare the star and galaxy number counts derived from the data to that of other authors and/or to model predictions. As an example, Fig. 5.3 shows the galaxy counts in different observed passbands for the field XMM-07. Here objects with CLASS_STAR < 0.95 or fainter than the object classification limit were used to create the sample of
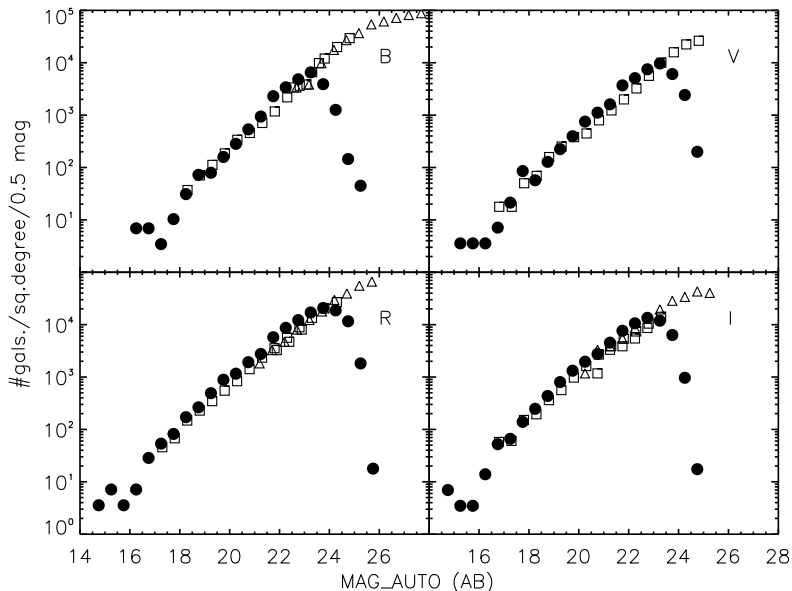
Figure 5.3: Galaxy number counts for the XMM-07 field for the different passbands as indicated in each panel. Full circles represent EIS data points, open triangles Metcalfe et al. (2001), open squares Arnouts et al. (2001).

galaxies. Note that the number counts shown in the figure take into account the effective area of the catalog, which is available in its FIELDS table (see Appendix C.5). As can be seen, the computed counts are consistent with those obtained in previous studies for all passbands (Arnouts et al. 2001; Metcalfe et al. 2001).

A complementary test is to compare the stellar counts to those predicted by models, such as the galactic model of Girardi et al. (2005, and references therein). Generally, the agreement of model predictions is excellent for B- and V-band catalogs, becoming gradually worse for R- and especially in I-band, near the classification limit, with the counts falling below model predictions (e.g., XMM-09 I-band). Note, however, that plots of CLASS_STAR

versus magnitude show a less well defined stellar locus for these bands. It is thus reasonable to assume that the observed differences between catalogs and model predictions are due to misclassification of stars as galaxies. Alternatively, these may also reflect short-comings in the model adopted. However, a detailed discussion of this issue is beyond the scope of the present work.

While useful to detect gross errors, number counts are not sufficiently sensitive to identify more subtle differences. The comparison of expected colors of stars with theoretical models provides a better test of the accuracy of the photometric calibration in the different bands. Using color transformations computed in the same way as in Girardi et al. (2002), the theoretical colors of stars can be obtained. Such comparisons were made for all five fields with data in four passbands. The results for two cases, XMM-06 and XMM-07 are illustrated in Figs. 5.4 and 5.5, respectively, which show $(B-V) \times (V-I)$ and $(V-R) \times (R-I)$ diagrams. For XMM-06 the data are in excellent agreement with the colors of stars predicted by the theoretical model, with only a small ($\lesssim 0.05$ mag) offset in $R-I$, indicating a good calibration. On the other hand, for XMM-07, one observes a significant offset (~ 0.2 mag) in $B-V$. This field was chosen because it exemplifies the worst offset observed relative to the theoretical models. Since this offset is only visible in the $(B-V) \times (V-I)$ diagram, it suggests a problem in the B-band data. Data for this field/filter combination comes from two nights 2003-06-30 and 2003-08-06. Closer inspection of the observations in the night of 2003-06-30 show that: (1) the standard stars observations span only 2 hours in the middle of the night; (2) the photometric zeropoint derived using the available measurements (24.59 mag) is reasonably close ($\sim 1\sigma$) to the median value of the long-term trend (24.71 mag); (3) the B exposures were taken close to sunrise; and (4) there was a significant increase in the amplitude of the DIMM seeing at the time the XMM-07 exposures under consideration were taken. For the night of 2003-08-06 standards cover a much larger time interval, yielding a zeropoint of 24.82 mag with comparable difference relative to the long-term median value for this filter as given above. The results suggest that the observed problem is not related to the calibration of the night, as will be seen below.

(a) *BVI* color-color plot.

(b) *VRI* color-color plot
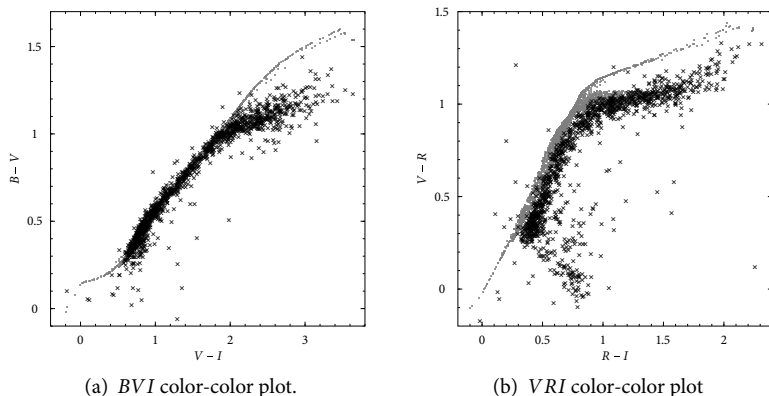
Figure 5.4: Color-color plots for stars in the xmm-06 field (black crosses) and that obtained using theoretical models (gray dots).

5.2 Private Survey Extension

In addition to the public eso survey covering 15 fields, 12 of them at high galactic latitude, a private extension of the xfs was proposed to eso (P.I. P. Schneider, Program-ids 70.A-0529, 71.A-0110, 072.A-0061, 073.A-0050). The primary aim of this survey is a combined optical, weak lensing, and X-ray search for galaxy clusters (see Chap. 6). The proposal of the private extension aimed at obtaining another 4 sq. deg. or 16 wfi pointings in B- and R-band at high galactic latitude to give a total survey area usable for weak lensing of 6 sq. deg.

The observing strategy for this extension is – as already noted in Sect. 5.1.2 – very similar to the observations for the public survey. The exposure times are given in Table 5.2. The most important difference is that the R-band data was taken with a seeing constraint of $\leq 1''$ to allow weak lensing studies.

The whole survey – public and private – was independently reduced using the gabods pipeline (esd) with the modification to the de-fringing algorithm described in Chap. 3.3.2. Fringe pattern subtration was done in the R- and I-band. This is an important difference to the eis reduction that

(a) *BVI* color-color plot.

(b) *VRI* color-color plot.
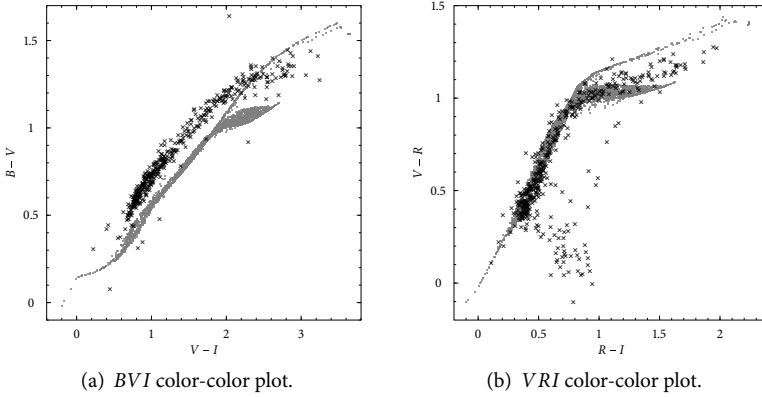
Figure 5.5: Same as Fig. 5.4 for xmm-07.

applied the de-fringing algorithm only to I-band images. The gsc-2.2 catalog was used for astrometric calibration. Photometric calibration was done using the standard star catalog of Stetson (2000). The type of photometric solution (number of free parameters for a linear fit) was decided on a case by case basis after visual inspection of the linear fits (see Fig. 3.2) and on the coincidence of relative zeropoints of data from different nights entering a coadded image. See Chap. 3.4.2 for an explanation of this procedure.

A quantitive comparison of the reduction of a subset of the public survey fields with the gabods pipeline and the eis pipeline is presented in Sect. 5.3.

A summary of all coadded images is given in Table 5.9. For a number of fields we produced different coadditions with different quality criteria to select the reduced science frames entering the coaddition. These are distinguished by their coadd id in Table 5.9. For almost all combinations of field and passband a combination with essentially all frames (denoted by the coadd id allf) was produced. These contain all images with a seeing $< 2''$ and a background < 5 counts s^{-1}. In most cases the allf coaddition indeed contains all frames. An example to the contrary is bpm 16274 R-band, which for this reason has a shorter integration time in the gabods reduction than in the eis reduction (see Table 5.8 for comparison). With

Table 5.9: Stacked images from the GABODS pipeline reduction of the XMM-Newton Follow-Up Survey. The fields are ordered by right ascension as in Table 5.1. The coadd IDs distinguish different coadditions of one field with different quality criteria for stacks entering the final stacked frame; their meaning is explained in the text. Where necessary details or deviations from the standard meaning are given in the table notes. The limiting magnitude is given in the Vega system as 5σ skylevel measured in a $2''$ diameter aperture. The grades are determined from visual inspection of the coadded images. Grade "A" is assigned to an image with no special features and an appearance typical to that band. Images with grade "B" show mostly cosmetic defects but are usable for most scientific purposes. Images with grade "C" show more severe defects. Grade "D" (not usable for scientific purposes) was not assigned. A short explantion for grades is given in the table notes. The completeness of the observations is given with respect to the planned exposure time from Table 5.2.

Field	Passband	coadd ID	T_{int} (s)	Seeing (arcsec)	m_{lim} (mag)	Grade	Completeness (%)
BPM 16274	B	ALLF	1800	1.20	25.04	A	100
BPM 16274	V	ALLF	3959	1.45	25.20	A	90
BPM 16274	R	ALLF	11748	0.88	25.38	A	102
BPM 16274	R	SE95	9349	0.87	25.32	A	81
BPM 16274	I	ALLF	8998	1.09	24.26	A	100
CFRS-3h	R	ALLF	11688	0.85	25.46	A	102
CFRS-3h	R	ELLI[a,b,c]	8999	0.83	25.33	A	78
CFRS-3h	R	SE95[d]	9599	0.83	25.36	A	83
RX J0505.3−2849	B	ALLF	1800	0.86	25.42	A	100
RX J0505.3−2849	V	ALLF	4399	0.74	25.22	A	100

Continued on next page

130

Table 5.9 – continued from previous page

Field	Passband	coadd ID	T_{int}	Seeing	m_{lim}	Grade	Completeness
RX J0505.3−2849	R	ALLF	14998	0.83	25.58	A	130
RX J0505.3−2849	R	ELLI[a,e]	6599	0.72	25.16	A	57
RX J0505.3−2849	R	SE70	3000	0.62	24.77	A	26
RX J0505.3−2849	R	SE95	9599	0.75	25.36	A	83
RX J0505.3−2849	I	ALLF	8998	0.72	23.94	A	100
RBS 0864-S	B	ALLF	1500	1.20	24.95	A	83
RBS 0864-S	R	S115	5899	1.05	25.20	A	51
RBS 0864-S	R	S130	8259	1.08	25.38	A	72
RBS 0864-S	R	ALLF	8849	1.10	25.41	A	77
RBS 0864-N	V	ALLF	8039	1.15	25.29	A	183
RBS 0864-N	R	ALLF	16078	1.01	25.53	A	140
RBS 0864-N	R	SE96	4287	0.87	24.87	A	37
QSO B1030−403	R	ALLF	4799	1.01	24.94	C⋆	42
BR 1033−403	B	ALLF	1500	1.32	24.66	A	83
BR 1033−403	V	ALLF	4399	0.85	25.15	A	100
BR 1033−403	R	ALLF	15188	0.79	25.62	A	132
BR 1033−403	R	ELLI[a,f,g]	9319	0.75	25.41	A	81
BR 1033−403	R	S120[d]	14008	0.78	25.59	A	122
BR 1033−403	R	SE95[d]	11058	0.75	25.49	A	96
BR 1033−403	I	BCK3	2999	1.05	23.69	A	33
BR 1033−403	I	BCK4	8698	0.92	24.18	A	97

Table 5.9 – continued from previous page

Field	Passband	coadd ID	$T_{\rm int}$	Seeing	$m_{\rm lim}$	Grade	Completeness
SDSS J10433.04−012502.2	R	ALLF	13398	0.79	25.44	A	117
SDSS J10433.04−012502.2	R	ELLI[g,h,i]	9799	0.78	25.29	A	85
SDSS J10433.04−012502.2	R	SE85	7399	0.73	25.16	A	64
MS 1054.4−0321	B	ALLF	1800	1.16	25.26	A	100
MS 1054.4−0321	V	ALLF	4399	1.04	25.04	A	100
MS 1054.4−0321	R	ALLF	11748	0.69	25.35	A	102
MS 1054.4−0321	R	ELLI[a,e,j]	8749	0.66	25.21	A	76
MS 1054.4−0321	I	ALLF	8998	0.87	24.06	A	100
HE 1104−1805	B	ALLF	1800	1.02	25.31	A	100
HE 1104−1805	V	ALLF	2200	0.89	24.79	A	50
HE 1104−1805	R	ALLF	11748	0.83	25.47	A	102
HE 1104−1805	R	S100	8199	0.74	25.24	A	71
HE 1104−1805	R	SE80	4699	0.67	24.97	A	41
HE 1104−1805	R	SE90	6399	0.70	25.12	A	56
HE 1104−1805	I	ALLF	9297	0.96	24.06	A	103
HE 1104−1805	I	S130	8698	0.95	24.03	A	97
PG 1115+080	B	ALLF	1500	0.83	24.91	A	83
PG 1115+080	R	ALLF	11648	0.92	25.48	A	101
PG 1115+080	R	SE96	7049	0.86	25.21	A	61
CD −33 07795	B	ALLF	1800	1.35	25.26	A	100
CD −33 07795	V	ALLF	3699	0.96	25.15	A	84

Table 5.9 – continued from previous page

Field	Passband	coadd ID	$T_{\rm int}$	Seeing	$m_{\rm lim}$	Grade	Completeness
CD −33 07795	R	ALLF	3500	0.91	25.04	B[†]	30
CD −33 07795	I	ALLF	8998	0.85	24.16	B[†]	100
T Leo	B	ALLF	1500	1.02	24.93	B[‡]	83
T Leo	R	ELLI[a,k]	8199	0.73	25.26	B[‡,§]	71
T Leo	R	SE95	11648	0.74	25.47	B[‡,§]	101
IRAS 12112+0305	B	ALLF	1500	0.98	25.03	A	83
IRAS 12112+0305	V	ALLF	4399	1.22	25.18	A	100
IRAS 12112+0305	R	ALLF	11648	0.88	25.51	A	101
IRAS 12112+0305	R	SE95	5219	0.77	25.11	A	45
IRAS 12112+0305	I	ALLF	8398	0.75	24.18	A	93
IRAS 12112+0305	I	BCK4	8098	0.77	24.18	A	90
IRAS 12112+0305	I	GOOD[l,m]	7798	0.75	24.16	A	87
LBQS 1228+1116	R	ALLF	4129	1.01	25.09	B[†]	36
NGC 4666	B	ALLF	1800	1.29	25.15	A	100
NGC 4666	V	ALLF	4399	1.02	24.80	A	100
NGC 4666	R	ALLF[b]	10948	0.87	25.43	A	95
NGC 4666	R	S110[b]	8749	0.82	25.29	A	76
NGC 4666	R	S130[b]	9849	0.85	25.37	A	86
NGC 4666	I	ALLF	8998	0.76	23.49	B[†]	100
QSO B1246−057	B	ALLF	1800	0.89	25.15	A	100
QSO B1246−057	V	ALLF	4839	0.84	24.87	A	110

Continued on next page

Table 5.9 – continued from previous page

Field	Passband	Coadd ID	T_{int}	Seeing	m_{lim}	Grade	Completeness
QSO B1246−057	R	ALLF	8499	0.80	25.21	B[†]	74
QSO B1246−057	I	ALLF	8698	0.72	24.09	B[†]	97
QSO B1246−057	I	BCK4[n]	5398	0.69	23.92	B[†]	60
FIELD 864-1	B	ALLF	1500	1.07	25.05	A	83
FIELD 864-1	R	ALLF	10823	0.88	25.45	A	94
FIELD 864-1	R	SE95	6694	0.83	25.24	A	58
FIELD 864-9	B	ALLF	2999	0.80	25.54	A	167
FIELD 864-9	R	ALLF	12208	0.84	25.56	A	106
FIELD 864-9	R	SE95	8699	0.79	25.40	A	76
A 1882	B	ALLF	1500	0.85	25.13	A	83
A 1882	R	ALLF	17548	0.72	25.73	B[†]	153
A 1882	R	ELLI[a,o]	8139	0.60	25.30	A	71
A 1882	R	SE95	9879	0.63	25.42	A	86
MKW 9	B	ALLF	4199	1.25	25.80	A	233
MKW 9	B	S120	1500	1.10	25.23	A	83
MKW 9	R	ALLF	11248	0.91	25.56	A	98
MKW 9	R	S120	8499	0.85	25.41	A	74
MKW 9	R	SE95	5749	0.80	25.24	A	50
PB 5062	B	ALLF	1500	1.13	24.28	B[¶]	83
PB 5062	V	ALLF	2879	1.58	24.72	A	65
PB 5062	R	ALLF	11748	0.87	25.27	A	102

Continued on next page

Table 5.9 – *continued from previous page*

Field	Passband	coadd ID	T_{int}	Seeing	m_{lim}	Grade	Completeness
PB 5062	R	GOOD[a,m]	7549	0.81	25.08	A	66
PB 5062	R	SE95	8149	0.81	25.10	A	71
LBQS 2212−1759	B	ALLF	3299	1.21	25.12	A	183
LBQS 2212−1759	B	BCK3	1800	1.30	24.95	A	100
LBQS 2212−1759	B	S120	1500	1.03	24.42	B[||]	83
LBQS 2212−1759	V	ALLF	4399	1.08	25.12	A	100
LBQS 2212−1759	R	ALLF	15698	0.99	25.52	A	137
LBQS 2212−1759	R	S100	8699	0.86	25.13	A	76
LBQS 2212−1759	I	ALLF	8998	0.97	24.25	A	100
NGC 7252	B	ALLF	1500	1.28	25.35	A	83
NGC 7252	R	ALLF	11498	0.70	25.57	A	100
NGC 7252	R	S100	10948	0.71	25.55	A	95
PHL 5200	B	ALLF	1500	1.48	25.23	A	83
PHL 5200	R	ALLF	2750	1.06	24.92	B[†]	24

Notes on selection criteria: [a] seeing $< 0''95$, [b] $\varepsilon_1 < 0.1$, [c] $\varepsilon_2 < 0.05$, [d] $\varepsilon_1 < 0.1$ [e] $|\varepsilon_1| < 0.045$, [f] $-0.04 < \varepsilon_1 < 0.1$, [g] $\varepsilon_2 > -0.04$, [h] seeing $< 1''$, [i] $\varepsilon_1 < 0.04$, [j] $\varepsilon_2 < 0.045$, [k] $\varepsilon_1 > -0.05$, [l] background $< 4\,\text{cts s}^{-1}$, [m] relative zeropoint > -0.2, [n] relative zeropoint > -0.05, [e] $|\varepsilon_1| < 0.04$.

Notes on grades: [*] Very uneven background, [†] Uneven background, [‡] Lower left corner cut off due to strong reflections from Jupiter, [§] CCD 3 darker than other chips, [¶] very noisy background, [||] Residual bad columns.

the weak lensing goal of the survey in mind, seeing filtered images were primarily produced in the R-band. These are denoted by coadd IDs starting with s or SE followed by the maximum allowed seeing of the input images in hundredth of an arcsecond. Sometimes input images had very elliptical PSFs. These are filtered out in the coadditions marked with ELLI. In some cases additional constraints were put on the background counts (BCKn, n being the background counts per second), primarily to avoid strong fringing in the I-band. Deviations from these criteria or additional filters are specified in Table 5.9.

All coadded images were graded after visual inspection. Grades range from "A"–"D". Grade "A" is assigned to an image with no special features and an appearance typical to that passband. Images with grade "B" show mostly cosmetic defects but are usable for most scientific purposes. Images with grade "C" show more severe defects. Grade "D" (not usable for scientific purposes) was not assigned. Out of the 69 combinations of field and passband 59 had at least one coaddition with grade "A". 9 combinations of field and filter are only available as "B"-graded coaddition. These are mostly due to situations for which the GABODS pipeline was not optimized, e.g., extended objects in the FOV, few exposures to create SUPERFLAT images, or extended diffuse emission/absorption. One coaddition has a grade "C" assigned. In this case the SUPERFLAT was created from only a few images and produced a very uneven background.

I comment on some of the fields not already discussed as part of the public data release:

– RBS 0864 – This field became part of the private XFS after it was already observed with WFI in V- and R-band by Schindler et al. because the presence of data of this target in the ESO archive was not realized by the survey team. The observations by Schindler et al. (RBS 0864-N in Table 5.9) are centered on coordinates slightly North-West of the galaxy cluster and were taken with a seeing constraint of 1.″2. The re-observation in the course of the XFS two years later (RBS 0864-S) is centered on the cluster and was observed with the seeing constraint of 1.″0 of this survey. However, most data was taken well outside the specified constraint.

– QSO B1030−403 (R-band) – The only image with grade "C". Due to

bad weather and termination of the program 70.A-0529 observations of this field were not done to the targeted depths. The remaining shallow image has a very uneven background probably due to a bad SUPERFLAT produced from only a few SCIENCE images.

– CD −33 07795 (R- and I-band) – This field is one of the three public survey fields for which no data has been released yet. It is also the only high galactic latitude field in the EIS survey that was not forseen to be part of the weak lensing survey. Thus, the R-band is relatively shallow leading to the known problems with SUPERFLAT creation if only few SCIENCE images are present. The high number of relatively bright stars in this field, including the target itself, is an additional difficulty for superflatting and FRINGE map creation.

– T LEO – The observations of this field were carried out with Jupiter ∼ 11 deg from the pointing position. The open construction of the 2.2-m telescope lead to strong reflections even at this distance in the lower left corner. This part of the mosaic was unusable and masked by hand. In the R-band data chip 3 has noticeably lower level than other chips. The cause of this is currently under investigation.

– A 1882 (R-band, ALLF) – This coaddition has an uneven background. Abell 1882 is a rich cluster at redshift $z = 0.14$. The many bright and relatively large galaxies in this system make the creation of a good SUPERFLAT image difficult. The coadditions with better grades use preferentially data from runs that contained observations of empty fields and had good SUPERFLAT images.

– PB 5062 – When this field was initially selected for the XFS wrong coordinates were passed to the EIS team. The patch of the sky located at these coordinates fulfilled the selection criteria for the optical survey. Unfortunately, the true position of the X-ray observations has a very high galactic extinction and is not suitable for extragalactic studies.

– PHL 5200 (R-band) – This target is part of the still on-going program 073.A-0050. The present observations are very shallow and do not allow the creation of a good SUPERFLAT image. The bad SUPERFLAT image made from the available data leads to an uneven background.

The high percentage of images graded "A" (86%) shows that the GABODS pipeline performs well in the cases for which it was designed, namely the reduction of data taken on deep empty fields. This is also supported by the quantitative comparison of the EIS/MVM and GABODS pipeline reduction presented in the following section. Note that the application of the de-fringing algorithm to the R-band data successfully removed the fringing pattern in PB 5062 R-band, which showed residual fringing in the EIS/MVM reduction.

So far no detailed investigation into the quality of the photometric cal-ibration of the data, not part of the comparison in the next section, has been done. Comparison of observed stellar colors with those derived from models is a sensitive test for all fields observed in more than two passbands. This is planned for the future. By design, however, most fields were only observed in B- and R-band. In the absence of primary or secondary photo-metric standards on the fields themselves, the only available methods is the rather insensitive comparison of galaxy number counts with those obtained on other fields. This is done as a standard procedure in the GABODS pipeline and generally shows good agreement between the observed and expected number counts. In some cases the XFS overlaps with the Sloan Digital Sky Survey (SDSS). If color transformations between SDSS and WFI filters are known, the SDSS sources with good photometry can be used as secondary photometric standards to check the calibration of our reduction.

5.3 Comparison of Optical Data

As shown in Sect. 5.1.5, comparison of different statistics, based on the sources extracted from the final image stacks, to those of other authors and to model predictions provide an internal means to assess the quality of the data products. However, in the particular case of this survey one can also benefit from the fact that about one third of the accumulated data had been independently reduced by the Bonn group in charge of the contributing program (Sect. 5.1.2) by the time the public data release was being prepared. The images in common are used in this section to make a direct comparison of the astrometric and photometric calibrations. A total of 15 stacked images in the B-, V-, and R-bands were compared to those produced by the EIS/MVM pipeline.

Table 5.10: Summary of the astrometric and photometric comparison. All differences were computed EIS−GABODS. The errors given in the last three columns are the 1σ scatter of the differences in the respective quantities. They are not the external error of the calibration.

Eis-Field	Target	Passband	$\Delta\alpha\cos(\delta)$ (arcsec)	$\Delta\delta$ (arcsec)	Δm (arcsec)
XMM-03	HE 1104−1805	B	0.02 ± 0.04	−0.01 ± 0.03	0.13 ± 0.02
XMM-03	HE 1104−1805	R	0.02 ± 0.05	−0.01 ± 0.05	0.01 ± 0.04
XMM-04	MS 1054.4−0321	B	0.00 ± 0.05	0.00 ± 0.05	0.12 ± 0.04
XMM-04	MS 1054.4−0321	V	0.02 ± 0.05	−0.00 ± 0.05	0.00 ± 0.04
XMM-04	MS 1054.4−0321	R	0.03 ± 0.06	0.00 ± 0.06	0.00 ± 0.03
XMM-05	BPM 16274	B	0.00 ± 0.06	−0.01 ± 0.06	0.05 ± 0.04
XMM-05	BPM 16274	R	0.03 ± 0.09	−0.01 ± 0.09	0.18 ± 0.04
XMM-06	RX J0505.3−2849	B	0.02 ± 0.04	0.00 ± 0.04	0.00 ± 0.02
XMM-06	RX J0505.3−2849	V	0.02 ± 0.04	−0.01 ± 0.04	−0.04 ± 0.04
XMM-06	RX J0505.3−2849	R	0.01 ± 0.03	0.01 ± 0.04	0.05 ± 0.03
XMM-07	LBQS 2212−1759	B	0.02 ± 0.06	−0.02 ± 0.06	0.34 ± 0.04
XMM-08	NGC 4666	B	0.00 ± 0.06	−0.01 ± 0.05	0.00 ± 0.03
XMM-08	NGC 4666	V	0.00 ± 0.06	−0.01 ± 0.05	−0.01 ± 0.03
XMM-09	QSO B1246−057	B	0.02 ± 0.06	−0.01 ± 0.05	0.02 ± 0.02
XMM-10	PB 5062	B	−0.03 ± 0.05	−0.01 ± 0.07	0.05 ± 0.02

To carry out the comparison of the data products, catalogs were produced from the EIS and GABODS images using the same extraction parameters. These catalogs were associated with each other to produce a merged catalog for each field and passband. The results of this comparison for all the available images in common are presented in Table 5.10. The table gives: in Col. 1 the field name; in Col. 2 the original target name; in Cols. 3 and 4 the mean offset and standard deviation in right ascension and declination in arcseconds; in Col. 5 the mean and standard deviation of the magnitude differences as measured within an aperture of 3″. The mean and standard deviation of the magnitude differences were determined in the interval $17 < m < 21$. This range was chosen to avoid saturated objects at the bright end and to limit the comparison to objects whose estimated internal error in magnitude is smaller than about 0.01 mag at the faint end. An iterative 5σ rejection, which allowed rejected points to re-enter if they are compatible with later determinations of the mean and variance, was employed to ignore obvious outliers in the computation of the mean and the standard deviation.

Fig. 5.6 illustrates the results obtained from the comparison of the position of sources extracted from images produced by the two pipelines for the particular case of XMM-06 in R-band. From the figure one can see that the positions of the sources agree remarkably well. In fact, as summarized in Table 5.10, the typical mean deviation is ~ 20 mas with a standard deviation of ~ 50 mas, confirming the excellent agreement in the *external* (absolute) astrometric calibration to be distinguished from the *internal* calibration discussed later.

Fig. 5.7 shows a plot of the magnitude differences measured on the GABODS R-band image of the field MS 1054.4−0321 (XMM-04) versus the magnitudes measured on the corresponding EIS image. This field shows that the photometry of both reductions agree remarkably well. The measured scatter of the magnitude differences is small (~ 0.03 mag) for this as well as for most other fields. This result indicates that the internal procedures used by the two pipelines to estimate chip-to-chip variations are consistent. Moreover, inspection of the last column of Table 5.10 shows that for 11 out of 15 cases the mean offsets are ≲ 0.05 mag. This is reassuring for both pipelines considering all the differences involved in the process, which include differences in the routines, procedures and the standard stars used. It is important to emphasize that differences in the computed zeropoint of the photometric
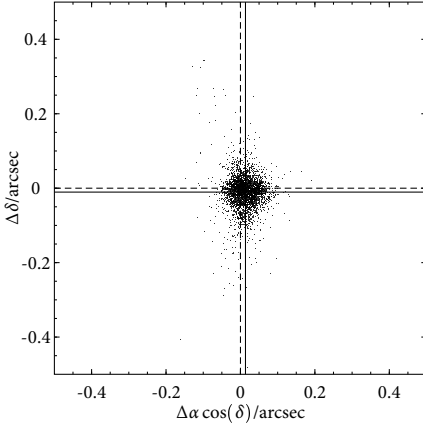
Figure 5.6: Comparison of astrometry for the R-band image of XMM-06 (RX J0505.3−2849), selected to represent a typical case. The offsets are as computed EIS−GABODS. The dashed lines are centered on $(0, 0)$, while the solid lines denote the actual barycenter of the points.

solutions are $\lesssim 0.08$ mag, even for the cases with the largest differences such as XMM-05 (R) and XMM-07 (B). The value of 0.08 mag is consistent with the scatter measured from the long-term trend shown by the zeropoints computed over a large time interval, as presented in the EIS release of WFI photometric solutions, thus representing the uncertainty in the photometric calibration. Therefore, the offsets reported in the table cannot be explained by differences in the photometric calibration alone. This point is investigated in more detail for XMM-05 R-band and XMM-07 B-band.

All R-band images for XMM-05 were taken in one night and the photometric solutions determined by both teams agree very well. While the source of the discrepancy has not yet been identified, the stellar locus in the $(B - V) \times (V - I)$ and $(V - R) \times (R - I)$ diagrams based on the source catalog extracted from the EIS images yield results which are consistent with model predictions, suggesting that the problem may lie in the Bonn reductions. On the other hand, the large offset (0.34 mag) between the B-band observations of the field XMM-07 is most likely caused by the data taken in the night 2003-06-30. While the standard star observations in this night suggest relatively good photometric conditions, the available measurements span only about 2 hours in the middle of the night, while the science exposures were taken at the very end of the night. Inspection of the ambient condition shows a rapid increase in the amplitude of the DIMM seeing which could
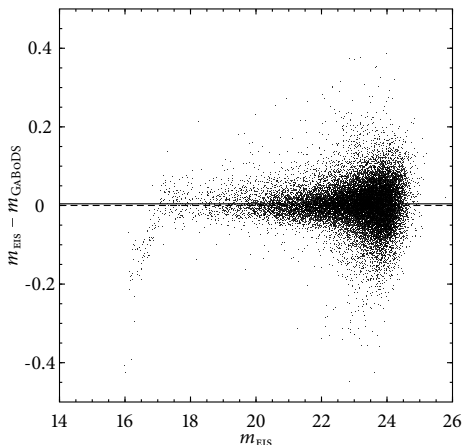
Figure 5.7: Comparison of aperture magnitudes ($3''$ aperture) measured on the R-band image of the field XMM-04 (MS 1054.4–0321). The dashed line is at a magnitude difference of 0, while the solid line denotes the actual offset between the EIS and the GABoDS reduction. The difference at the bright end is caused by different treatments of saturated objects in both pipelines.

be related to a localized variation in the transparency. In fact, the Bonn pipeline, which monitors the relative differences in magnitude for objects extracted from different exposures in an OB, finds strong flux variations that could be caused by changes in the sky transparency or by the twilight at sunrise. The latter could also account for the fact that these observations were later repeated in August of that year. The important point is that the Bonn group discarded the calibration of the frames taken in 2003-06-30, while the automatic procedure adopted by EIS did not.

In addition to evaluating the accuracy of the image registration and photometric calibration, the independent reductions also offer the possibility to evaluate the shape of the images. To this end the PSF of bright, non-saturated stars on the R-band images for XMM-04 (MS 1054.4–0321) and XMM-06 (RX J0505.3–2849) were measured and compared. These are the only two cases in which the final stacked images were produced by using exactly the same reduced images. The difference in the number of images entering a stacked image is caused by the differences in the criteria adopted in building the SBS. In the case of XMM-06, one finds that the size and pattern of the PSF are in good agreement and both reductions yield a smooth PSF with no obvious effects of chip boundaries over the whole field. The situation
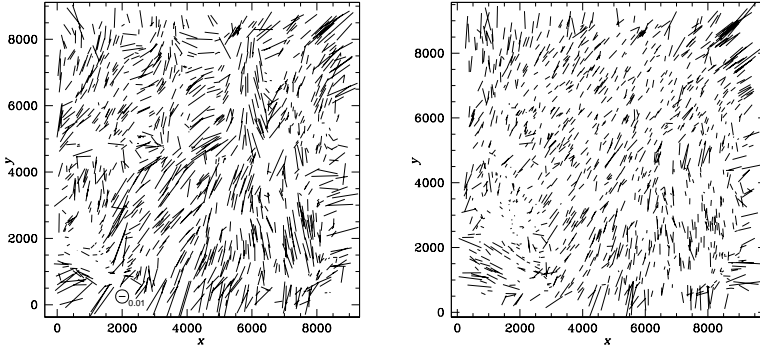
Figure 5.8: Stellar PSF pattern in the R-band images of the field MS 1054.4–0321 in the EIS reduction (left panel) and the GABODS reduction (right panel). The encircled stick in the left panel denotes an ellipticity of $\varepsilon = 0.01$. Both plots have the same scale.

is different for XMM-04 as can be seen in Fig. 5.8, which shows a map of the PSF distortion obtained by the EIS (left panel) and Bonn (right panel) groups. While the overall pattern of distortion is similar, the amplitude of the PSF distortion of the EIS reduction is significantly larger and exhibits jumps across chip borders. Although the effect is small in absolute terms, it should be taken into account for applications relying on accurate shape measurements. The reason for these differences is likely due to the fact that the astrometric calibration in the EIS pipeline is done for each chip relative to an absolute *external* reference, without using the additional constraint that the chips are rigidly mounted to form a mosaic. By neglecting this constraint, the solution for each chip in the mosaic may vary slightly, depending on the dithered exposure being considered and the density and spatial distribution of the reference stars in and around the field of interest. Since the accuracy of the GSC-2.2 of 250 mas is approximately equal to the pixel size of WFI of $0\rlap{.}''238$, in addition to the absolute calibration of the image centroid, finding an *internal* relative astrometric solution further ensures that images in different dithered exposures map more precisely onto each other during coaddition.

Imperfections in the *internal* relative astrometry result in objects not being matched exactly onto each other, thereby degrading the PSF of the coadded image.

5.4 X-Ray Catalogs

As pointed out before, the ultimate goal of the XFS has been to provide catalogs from which one can identify and characterize the optical properties of X-ray sources detected with deep XMM-Newton exposures.

X-ray source lists for the public high-galactic latitude fields were produced by the AIP-node of the SSC. These are based on pipeline processed event lists which were obtained with the latest official version of the Software Analysis System (SAS-v6.1) available at the time this work was carried out. Stacked X-ray images of multiple observation were not produced for this data release.

Source detection was performed as a three-stage process using `ebox-detect` in local and in map mode followed by a multi-PSF fit with `eml-detect` for all sources present in the initial source lists. The multi-PSF fit invoked here works on 15 input images, i.e. 5 per EPIC camera. The five energy bands used per camera cover the ranges: (1) 0.1–0.5 keV; (2) 0.5–1.0 keV; (3) 1.0–2.0 keV; (4) 2.0–4.5 keV; and (5) 4.5–12.0 keV.

The SAS task `eposcorr` was applied to the X-ray source list. Eposcorr correlates the X-ray source positions with the positions from an optical source catalog, in this case the EIS catalog, to improve the relatively poor astrometry of the X-ray catalogs, assuming that a significant fraction of the true counterparts are contained in the reference catalog.

The source detection scheme used here is very similar to the pipeline implemented for the production of the second XMM-Newton catalog of X-ray sources to be published by the SSC (Watson et al., in preparation). This approach is superior to that used for the creation of source lists which are currently stored in the XMM-Newton Science Archive since it makes use of X-ray photons from all cameras simultaneously. It also distinguishes between point-like and extended X-ray sources. In this section we only consider point-like sources. Extended sources at high galactic latitudes are almost exclusively galaxy clusters and cannot be matched with individual

objects in the optical catalogs. Examining their properties is beyond the scope of the work presented in this Chapter. We will return to the subject of extended X-ray sources in the XFS in Chap. 6.1.

In carrying out the matching between the XMM-Newton source lists and those extracted from the optical images, it is important to note that the X-ray images lie fully within the FOV of the WFI images. Hence an optical counterpart can be potentially found for any of the X-ray sources.

There are 2 fields in the high-galactic latitude sample of the public survey with more than one observation (see Table C.1). However, for XMM-05 only the two available observations with good time $t > 10$ ks were considered.[6] One of them had technical problems that prevented it from being used for catalog extraction. For XMM-09 the source list created contained many spurious sources due to remaining calibration uncertainties in the pipeline processed images and was not considered further. Figures showing the results of the source detection process with all sources indicated on an image in TIFF format, the composite X-ray images, and the source lists can be found on the web-page of the AIP-SSC-node.[7] Below these source lists are used to identify their optical counterparts.

The extraction yields 995 point-like X-ray sources. This number includes multiple detections of individual sources from the three independent observations of the field XMM-07. 742 of these sources are *unique*, i.e., free of multiple detections of a source. The mean flux of these 742 unique X-ray sources is $F_{\mathrm{mean}}(0.5\text{--}2.0\,\mathrm{keV}) = 8.5 \times 10^{-15}$ erg cm^{-2} s^{-1}, the median flux in this band is $F_{\mathrm{med}}(0.5\text{--}2.0\,\mathrm{keV}) = 3.7 \times 10^{-15}$ erg cm^{-2} s^{-1}. Sources with $F(0.5\text{--}2.0\,\mathrm{keV}) = 4 \times 10^{-15}$ erg cm^{-2} s^{-1} are detected already with an exposure time of 5 ks, while the limiting flux in the EIS-XMM fields at the deepest exposure levels is $F_{\mathrm{lim}} \simeq 3 \times 10^{-16}$ erg cm^{-2} s^{-1}.

Nearly all the X-ray source lists were matched to catalogs extracted from the R-band images, with the exception of the field XMM-08, which was correlated with the I-band. Two search radii, $2''$ and $5''$, were used. The larger value reflects the typical statistical error in X-ray source position determination (typically in the range $\sim 0.5''\text{--}2''$), coupled with an additional systematic error component ($\sim 1''$) in the attitude of the spacecraft. Hence,

---

[6]*Good time* is the exposure time not affected by flares.

[7]http://www.aip.de/groups/xray/XMM_EIS/

Table 5.11: Contents of X-ray source lists for high-latitude XMM-EIS fields.

Field (1)	Obs. ID (2)	N_s (3)	Passband (4)	N_m (5)	N_1 (6)	(N_1/N_s)(%) (7)	N_{all} (8)	$N_{1,all}$ (9)	B (10)	V (11)	I (12)	BV (13)	BI (14)	BVI (15)
XMM-03	0112630101	69	R	92	61	88	62	47	1	1	1	0	0	0
		69		36	35	51	27	27	0	0	0	0	0	0
XMM-04	0094800101	101	R	156	91	90	84	68	0	0	1	1	0	0
		101		74	73	72	57	57	0	1	1	0	0	1
XMM-05	0125320401	89	R	130	79	89	52	42	1	0	1	0	0	0
		89		59	57	64	37	37	1	0	2	1	0	0
XMM-06	0111160201	110	R	173	101	92	105	79	1	1	0	0	0	0
		110		76	72	65	61	58	3	0	1	0	0	0
XMM-07	0106660101	144	R	191	119	83	84	66	3	0	2	1	0	2
		144		82	81	56	52	52	2	2	1	1	0	1
XMM-07	0106660201	110	R	134	91	83	65	53	3	0	2	1	0	2
		110		62	61	56	39	39	1	0	2	2	0	0
XMM-07	0106660601	162	R	211	139	86	93	76	1	0	1	2	1	0
		162		100	98	60	59	59	1	1	1	2	0	0
XMM-08	0110980201	123	I	130	97	79	82	70	1	0	—	0	1	—
		123		73	73	59	58	58	0	2	—	1	—	—
XMM-10	0012440301	88	R	113	76	86	50	46	1	—	—	—	—	—
		88		57	56	64	35	34	3	—	—	—	—	—

a matching radius of $5''$ corresponds to roughly a 2–3σ uncertainty for most of the sources. The smaller correlation radius is justified by the distribution of the positional accuracy of the X-ray sources, which peaks at $\sim 1\overset{''}{.}3$. It extends up to $3''$ with the majority of sources (92%) being within $2''$.

One X-ray source may be matched to more than one optical source. This is especially true for the larger search radius. The number of matches an X-ray source has is called its *multiplicity*, denoted by m. If $m > 1$ the closest optical match is called the $m = 1$ source, the second closest match is the $m = 2$ source, and so on. If an X-ray source has only one optical counterpart this is automatically an $m = 1$ source.

The results of X-ray source extraction and their cross-identification with their optical counterparts for 7 high-galactic latitude fields (9 observations) are summarized in Table 5.11. For each field two rows are given: the first row refers to the matching done with a $5''$ search radius, in the second row the numbers for the smaller $2''$ search radius are reported. The table lists: in Col. 1 the field name; in Col. 2 the Obs. ID of the XMM-Newton observation; in Col. 3 the number of detected X-ray point sources with a likelihood of existence larger than `detml` = 6, N_s; in Col. 4 the passband of the catalog used as the optical reference for matching. Column 5 lists the total number of matches, N_m within $5''$ ($2''$). This number includes multiple matches of optical sources to one X-ray source. Column 6 gives the number of X-ray sources which could be matched to at least one optical source N_1. Column 7 then gives the identification rate N_1/N_s, i.e., the fraction of X-ray sources for which an optical counterpart could be found. Column 8 lists the number of X-ray sources, which have at least one counterpart in the optical reference catalog indicated by Col. 4, and are also detected in all other available optical passbands. This is a subset of the objects listed in Col. 5. Column 9 contains the same quantity as the previous column but for the $m = 1$ optical counterparts, $N_{1,all}$. This in turn is a subset of the objects listed in Col. 6. Finally, Cols. 10–15 give the number of optical counterparts in other passbands, which are not detected in the reference catalog, i.e., the number of X-ray sources with no counterpart in the reference catalog but with counterparts in other passbands. In Cols. 13–15 BV, BI and BVI refer to objects which are simultaneously detected in the respective passband but do not correspond to matches of X-ray sources with the reference catalog. Because we only list objects *without* match in the reference catalog the

number of objects reported in Cols. 10–15 is in some cases higher in the second row than in the first row. These are X-ray sources with matches in B-, V-, or I-band within a circle of 2″ having matches in the reference catalog only in the larger 5″ search radius.

The results of the X-ray/optical cross-correlation for all fields with available R-band catalogs, i.e., all fields listed in Table 5.11 with the exception of xmm-08, are displayed in Fig. 5.9. This encompasses 619 unique sources; the 742 total unique sources minus the 123 sources in xmm-8. The figure shows: (top left) the multiplicity function; (top right) the cumulative fraction of X-ray sources with optical counterparts in a 5″ search radius (dashed line) and a 2″ search radius (straight line); (bottom left) the distribution of the positional offsets between X-ray and optical sources; and (bottom right) the corresponding scatter plot in the $\alpha \times \delta$ plane. Note that in three panels all $m = 1$ matches are represented by filled histograms and/or larger symbols.

Inspection of Fig. 5.9 shows that: (1) about 87% (61%) of the X-ray point sources have at least one optical counterpart within the search radius of 5″ (2″) down to $R \sim 25$ mag, and very few sources have more than 3 matches. In only very few cases one finds up to five associated optical sources, i.e., potential physical counterparts; (2) only about 15% of the X-ray sources have counterparts down to the Digitized Sky Survey magnitude limit ($R \sim 20.5$ mag), underscoring the need for dedicated optical imaging in order to identify the X-ray source population; (3) the distribution of the X-ray/optical positional offset peaks at around 1″ for the sources with $m = 1$. The $m = 1$ matches are well concentrated within a circle of 2″. The distribution is almost flat if all associations are considered. This underlines that the true physical counterparts to the X-ray sources will be found predominantly among the $m = 1$ sources, i.e., the nearest and in most cases single associated optical sources; (4) the positional differences between X-ray and optical coordinates seem to be randomly distributed.

The statement that the additional correlations found within the greater search radius are chance alignments is strengthened by an estimate of the number of random matches between X-ray and optical sources. Using an average of 110 X-ray sources per field we can compute the total area covered by the search circles with 5″ (2″) radius. Multiplying this with the typical number density of sources in the optical catalogs ($30\ \mathrm{arcmin}^{-2}$) we estimate 70 (12) random matches for an average field. The number of random matches
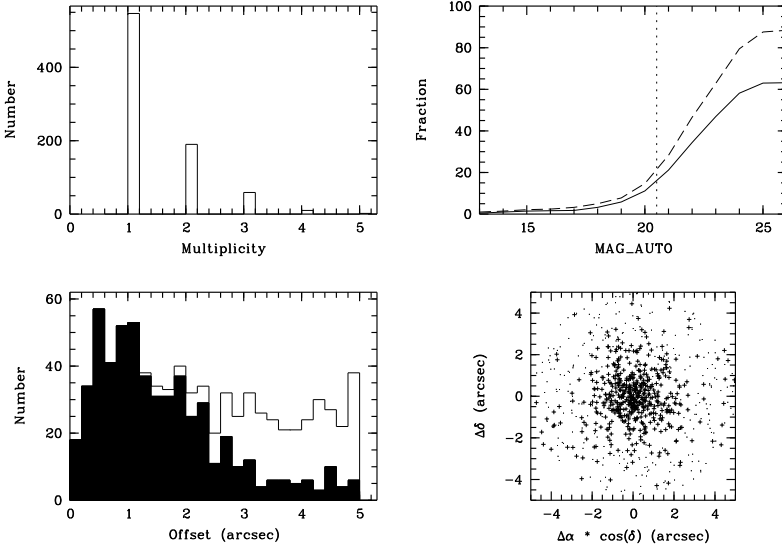
Figure 5.9: X-ray/optical R-band positional correlation. (*top left*) number of correlated optical sources to X-ray sources within 5″; (*top right*) cumulative fraction of X-ray sources with optical counterparts in the R-band catalog. The dashed line is for the 5″ search radius, the straight line for the 2″ search radius. The vertical short-dashed line denotes the approximate limit of the DSS; (*bottom left*) distribution of X-ray minus optical positional offset of all sources (open histogram) and the *m* = 1 sources (solid histogram); (*bottom right*) distribution of positional offsets in the right ascension – declination plane.

within the smaller correlation radius is well below the observed number of optical/X-ray counterparts.

In addition, from this preliminary analysis the following conclusions can be drawn: (1) about 39% of the X-ray sources have no associated optical source within 2″. This optical identification completeness is comparable with that found by Eckart et al. (2005) in a similar study of X-ray source samples, but there may also be small contributions from sources with larger

offsets than allowed by the adopted search radius, contamination by spurious X-ray sources, and random matches with the optical catalogs; (2) over 50% of the $m = 1$ sources are detected in all the other bands available, within 1″ of the R-band position; (3) correlations which occur at search radii greater than 2″ are most likely random correlations with the comparably dense optical catalogs; (4) all sources which are detected in RI are also detected in BV, indicating that the optical counterparts of the X-ray sources are not excessively red or, even if they are red, the blue images are sufficiently deep to detect them; (5) the small number of X-ray sources matched with objects in the B- and V-band catalogs without matches in the R-band catalog suggests that we are also not dealing with excessively blue objects. Figure 5.10 shows color-color diagrams for the field XMM-06 for stars and galaxies in the field and compares it with the optical colors of X-ray sources matching objects in the optical catalogs. Stars and galaxies were selected using the SExtractor `CLASS_STAR` classifier with the cuts made at `CLASS_STAR` < 0.1 and `CLASS_STAR` > 0.99 for galaxies and stars, respectively. These diagrams show that, as one would expect, no specific sub-population of stars or galaxies can be identified with the X-ray sources.

5.5 Summary

In this chapter I have described the XMM-Newton Follow-Up survey, consisting of a public and a private part. Section 5.1 describes the data products – reduced and stacked images as well as science-grade catalogs extracted from the latter – produced and released as part of the ESO Imaging Survey project. The survey was carried out as a collaboration between the EIS, XMM-Newton-SSC and IAEF-Bonn groups. At the time of writing 15 WFI fields (3.75 square degrees) have been observed for the public survey of which 12 were released in the fall of 2004, with corrections to the weight maps in July 2005. These are described in Sect. 5.1 paper. For the 8 fields at high galactic latitude catalogs are also presented.

The images were reduced employing the EIS/MVM image processing library and photometrically calibrated using the EIS data reduction system. The EIS system was also used to produce more advanced survey products (stacks and catalogs), to assess their quality, and to make them publicly available
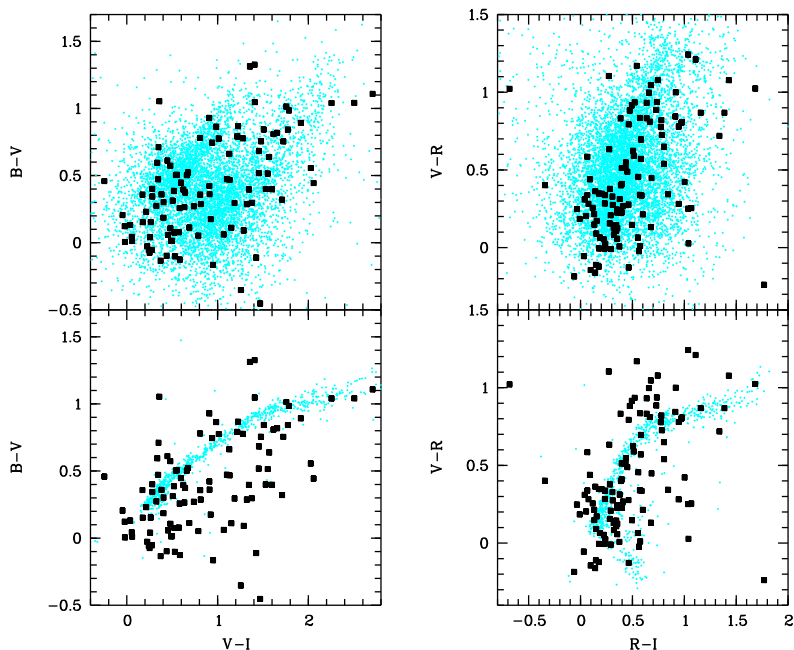
Figure 5.10: Optical colors for galaxies (top panels) and stars (bottom panels) in the field xmm-06. The black squares mark X-ray sources in this field with matches to the optical catalogs in all four passbands.

via the web, together with comprehensive product logs. The quality of the data products reported in the logs is based on the comparison of different statistical measures such as galaxy and star number counts and the locus of stars in color-color diagrams with results obtained in previous works as well as predictions of theoretical models calibrated by independent studies. These diagnostics are regularly produced by the system forming an integral part of it.

Section 5.2 then describes the private survey extension aimed at obtaining 6 square degrees of deep R-band data for a weak lensing search of galaxy clusters, with shallower B-band data to derive color information. Although

the survey is still on-going due to weather and scheduling problems a sizeable fraction of the original targets has been observed, albeit not always to the intended depth or with the desired color coverage. Section 5.2 provides on overview of the reduced data at hand together with a short evaluation of the quality of this data.

Section 5.3 uses the opportunity to test the performance of the two independent data reduction pipelines used by the EIS team and the group at the IAEF and assess the quality of their data products. From this comparison one finds that the position of the sources extracted from images produced for the same field/filter combination by the different pipelines are in excellent agreement with a mean offset of ~ 20 mas and a standard deviation of ~ 50 mas. Comparison of the magnitudes of the extracted sources shows that in general the mean offset is ≲ 0.05 mag, consistent with the estimated error of the photometric calibration of about 0.08 mag. Cases with larger deviations were investigated further and the problem with the two most extreme cases were found to be unrelated to the calibration procedure. Instead, it demonstrates the need for the implementation of additional procedures to cope with the specific situation encountered and the need for a better calibration plan. This discussion illustrates a couple of important points. First, that while an automatic process is prone to errors in dealing with extreme but rare situations, reductions carried out with human intervention are prone to random errors which can never be eliminated. Second, more robust procedures can always be added or existing ones tuned to deal with exceptions once they are found. However, as always when dealing with automatic reduction of large volumes of data, the real issue is to decide on the trade-off between coping with these rare exceptions and the speed of the process and margin of failures one is willing to accept.

Finally, a comparison of the PSF distortions suggests that some improvement could be achieved by requiring the EIS/MVM to impose an additional constraint on the astrometric solution to improve the *internal* registration.

Preliminary catalogs were also extracted from the available X-ray images and cross-correlated with the source lists produced from the R-band images in Sect. 5.4. From this analysis one finds that about 61% of the X-ray sources have an optical counterpart within 2″, most of which are unique. Out of these about 70% are detected in all the available passbands. Combined, these results indicate that the adopted observing strategy successfully yields the ex-

pected results of producing a large population of X-ray sources (~ 300) with photometric information in four passbands, therefore enabling a tentative classification and redshift estimation, sufficiently faint to require follow-up observations with the VLT.

6

Cluster Search in the XMM-Newton Follow-Up Survey

Clusters of galaxies are the most massive bound objects in the Universe.[1] They can be detected by optical or X-ray emission, weak lensing (e.g., Schneider 1996), and – using future surveys – the Sunyaev-Zeldovich effect (SZE). SZE, optical, and X-ray selection of clusters depend on the baryonic content of clusters, which – compared to the predicted dark matter density – is a minor fraction of the clusters' constituents. Optical selection depends on the star formation history, and X-ray and SZE detections require a hot intra-cluster medium (ICM). All these methods are sensitive in different redshift regimes. Optical surveys based on the red sequence method can be effective up to very high redshifts but optical selection is in principle prone to projection effects. SZE is a very promising method because it is almost redshift independent but increasing projections with higher redshifts and a yet unknown contamination from point sources may limit its ability to detect clusters. X-ray, like optical selection, depends on the luminosity distance of clusters, but has the unique advantage that it depends on the square of the number density of the hot ICM. Weinberg & Kamionkowski (2002) predict that up to 20% of all weak lensing clusters have not heated their ICM to a level detectable with current X-ray missions. Weak lensing surveys with the depth achievable with today's ground based telescope are sensitive to cluster mass concentrations in the redshift range $0.15 < z < 0.8$.

The XMM-Newton Follow-Up Survey (XFS) described in Chap. 5 was designed with the goal in mind to perform galaxy cluster searches in parallel with as many methods as possible. In this Chapter we will present the results

---

[1] I'm sorry. I just had to say this.

of cluster searches done with X-rays (Sect. 6.1), an optical matched filter algorithm (Sect. 6.2), and weak gravitational lensing (Sect. 6.3). We will give a summary in Sect. 6.4.

6.1 X-ray Detection

The hot gas trapped in the deep potential well of a galaxy cluster emits thermal bremsstrahlung in the X-ray regime. Because the X-ray luminosity of this intracluster gas scales with the square of its density X-ray detections of clusters of galaxy are relatively insensitive to projection effects. The high sensitivity of XMM-Newton allows us to find clusters out to very high redshifts. Two of the three most distant and spectroscopically confirmed clusters were found serendipitously with XMM-Newton. These are at redshift $z = 1.39$ (Mullis et al. 2005) and $z = 1.45$ (Stanford, private communication), the latter being located in the public XFS field LBQS 2212−1759.

6.1.1 X-ray Data Reduction

The archival XMM-Newton data of the XFS were reduced with the latest version of the Science Analysis System available at that time (SAS-6.5.0), with some exceptions described when they become relevant later in this section. Reduction of data of targets covered by only one observation is relatively straightforward and follows the steps outlined in Chap. 5.4 and is discussed in some more detail below. Three XFS fields were covered by more than one observation, leading to significantly deeper exposures. These are BPM 1627, LBQS 2212−1759, and PG 1115+080. For the purpose of the cluster search, combined images of the individual observations were created. Before we discuss the special treatment of these three data sets, we will describe the standard procedure adopted to go from raw telemetry data in FITS format to catalogs of extended X-ray sources.

Standard Processing

Starting from the raw Observation Data Files (ODF) the SAS tasks `emchain` and `epchain` are used to generate calibrated event lists and ancillary files

for the MOS and PN detectors, respectively. These are complex pipeline tasks that by themselves make use of a large number of SAS tasks. Among other things they need to take the attitude of the space craft, its tracking history, bad pixels, instrumental gains, and information on background flares into account. A detailed description of these tasks is provided in the SAS User's Guide (Loiseau 2005).

The background light curves were inspected for flare activity and if necessary maximal acceptable count rates for the MOS and PN detectors were determined for later processing. This step provides additional security for obtaining clean data products in addition to the *good time intervals* (GTI) already automatically determined by the radiation monitoring on-board the spacecraft. The information about GTIs is stored in files created by the `tabgtigen` task.

FITS images for five energy bands ranging from 0.1–0.5 keV, 0.5–1.0 keV, 1.0–2.0 keV, 2.0–4.5 keV, and 4.5–12.0 keV are generated for each of the three cameras from the event lists with the task `evselect`. Event lists are filtered by `evselect` according to the GTI information, photon energy, charge patterns, and the SAS macros `#XMMEA_EM` for the MOS detectors and `#XMMEA_EP` for the PN detector. The macros filter out artefacts based on flags set in the event list, e.g., events on bad pixels or charge patterns classified as cosmic ray events. Depending on how an X-ray photon hits the CCD detector, charge may be deposited in more than one pixel for a single events.

Charge patterns have been defined that correspond to valid and well calibrated X-ray events. For the PN detector we impose additional selection criteria on patterns to the ones of the `#XMMEA_EP` macro. For the two lowest energy bands we accepted only single events; for the three highest energy bands only events not depositing charge in more than two neighboring pixels are kept.

We also exclude the energy range of 7.8—8.2 keV from the PN data to avoid the complex of Ni-Kα, Cu-Kα, and Zn-Kα fluorescence lines of the detector and surrounding structure.

Exposure maps, i.e., FITS images describing the spatial variation of the instruments' efficiency, with and without the vignetting of the FOV taken into account are generated with the task `eexpmap`. The unvignetted exposure maps are used to create mask images with `emask`. These mask images have

a pixel values of 1 everywhere except at pixel positions that should be ignored for source detection, which have pixel value 0.

Using the 15 images generated with `evselect` (5 images per camera and 3 cameras), the mask images, and the vignetted exposure maps, `eboxdetect` in local mode is run to generate a first source list. The minimum likelihood for a detection in this step is set to 5. The sources are excised from the image by `esplinemap` to model the background of the images. The task `esplinemap` allows to describe the background either by a two component model (low and high energy contribution) based on ray-tracing of the instruments or by a 2-d spline with a user-defined number of nodes. For the xfs the decision which approach to use was based on visual inspection of the data.

With these background maps `eboxdetect` can now be run in map mode to create another source list. The minimum likelihood for source detection is set to 4 in this step. This list is given together with the science images, masks, and background maps to `emldetect` that performs a simultaneous maximum likelihood multi-source PSF fitting in all energy bands. The free parameters `emldetect` fits are source position, source extent (core radius of a β-model), and source count rate in each energy band and instrument. Derived parameters are total source count rate, total likelihood of detection and likelihood of detection per energy band, likelihood of source extent, and four hardness ratios between the input energy bands. In our reduction we let `emldetect` fit up to two sources to one source position reported by `eboxdetect`. The minimum likelihood for a detection was set to 6, and the minimum extent likelihood for a source to be considered as an extended source to 4.

The source positions in the `emldetect` catalog have statistical errors on the order of $1''$–$2''$ plus a systematic error due to an uncertainty in the attitude of the spacecraft, which is of the same size. The latter can be corrected by cross-correlating the X-ray source positions with the more accurate positions of optical sources. The task `eposcorr` is used to carry out this cross-correlation with R-band catalogs on all fields. The production of the optical catalogs is described in detail in Sect. 6.2.1.

Changes for Bright Extended Sources

Very bright extended sources like massive galaxy cluster are often not fully detected by `eboxdetect`. Typically, `eboxdetect` places a large number of point and extended sources on these objects. Still the wings of such bright objects are often not sufficiently covered with `eboxdetect`ed objects to enable `esplinemap` to make a reliable model of the background. To avoid a large number of spurious source detections in these cases we manually mask very bright and extended sources before the first `eboxdetect` run.

The masks were produced as DS9 region file, converted with `ds9tocxc` to FITS `REGION` tables (McDowell & Rots 1998). Using a development version of `emask` not yet publically available, the masked regions were marked as such in the FITS mask images.

Combination of Observations

Multiple observations of one field are in general taken at different roll angles and – since the center of rotation is not the center of the FOV – different positions. The first step in combining observations is thus to bring them all to a common nominal position. This is done with the SAS task `attcalc`, which computes sky coordinates for event files.

From these new event lists FITS images, exposure maps, and masks are created for the individual observations as described above. Science images and exposure maps are coadded weighted by the masks of the respective observation. The masks themselves are combined with logical or.

The source extraction continues on the combined images, exposures maps, and masks as described above.

6.1.2 Catalog of Extended X-ray Sources

Catalogs of cluster candidates were generated from the `emldetect` source list. Sources with a detection of likelihood > 6 and extent likelihood > 4 were considered as potential cluster candidates. Remaining large scale inhomogeneities in the background are sometimes detected as spurious sources and the best fit model of `emldetect` is often one whose extent reaches the maximum value of 30 pixels. Hence only sources with an extent <30 pixels

were kept in the final catalog. The extended X-ray sources found in this way were visually screened and obvious artefacts, often due to out-of-time (OOT) events or remaining background structure were manually rejected. The optical images were visually inspected for possible counterparts of extended sources. In this step extended sources obviously associated the nearby galaxies were removed from the catalog. Grades were assigned to the quality of a cluster detection based on visual inspection of the optical and X-ray images. Cluster candidates with grade "+" are obvious real cluster, often the ones one would select by eye. Extended X-ray sources graded with "∘" are possible clusters but not as prominent as those graded with "+". This grade is assigned to clusters without a very obvious optical counterparts but a reliable X-ray detection. In some cases these may be systems at very high redshift just barely visible on the optical images. Clusters graded "−" appear to be unreliable in the optical and X-ray images, but were not rejected as obvious spurious sources based on their visual impression in the X-ray images.

The full cluster catalog is given in App. D.1. Cluster candidates in this catalog follow the naming scheme BLOX JHHMM.m+DDMM, where BLOX is the IAU registered acronym for "Bonn Lensing, Optical, X-ray" detected cluster candidates.

In the following we give comments on individual fields when appropriate.

– BPM 16274 – The X-ray observation with the observing ID 0125320401 was discarded due to problems in the data reduction.

– RX J0505.3−2849 – Two extended X-ray peaks are found on both previously known RX J clusters in this field. In the case of RX J 0505.3−2849 we only list one; the other is probably associated with a bright foreground galaxy.

– RBS 0864 – Two reductions of this field were made. One reduction excluded the target cluster excluded from the analysis, while the other one was made with the cluster remaining in the data. A large number of spurious detections associated with OOT events were manually rejected.

– SDSS J104433.04−012502.2 – Due to problems in the processing of the PN and MOS1 data in this field, only the MOS2 detector was utilized.

- MS 1054.3−0321 – Two extended X-ray sources were detected on the target cluster.

- HE 1104−1805 – The only extended X-ray source found in this field coincides with a bright star.

- PG 1115+080 – The X-ray data on this field is a combination of several individual observations. Due to problems in modelling the background in the combined data, a large number of spurious sources was rejected after visual screening.

- LBQS 1228+1116 – The X-ray data on this field is strongly affected by background flares. No clusters were found in the remaining shallow data.

- MKW 9 – The target cluster dominates the center and several extended sources are detected in the cluster region, some of them on bright and large galaxies.

- LBQS 2212−1759 – Like PG 1115+080 the X-ray data on this field is a combination of several observations, again leading to some problems in the determination of the background structure. A number of spurious sources has been rejected after visual inspection. The combined data set, however, is truly deep and a large number of possible high redshift clusters is detected in this field.

- QSO B1246−057 – The calibration problem that prevented the X-ray data on this field from being included in the public data release (see Chap. 5.4) were solved and the field could be included in the cluster search.

- FIELD 864-9 – Only the X-ray observation with the observing ID 0111282501 was used for the cluster search.

- A 1882 – The X-ray image of this cluster shows three very extended sources centered around the nominal position of the cluster of Abell (1958). The regions of extended X-ray emission have been excluded from the analysis.

- NGC 7252 – No extended targets were found in this field.

6.2 Optical Matched Filter Detection

Clusters of galaxies can be optically selected in a multitude of ways, either from one passband alone or by combining color information from two or more passbands with the positional information on galaxies used in all methods. A review of a large number of optical detection methods has recently been published by Gal (2006).

Optical detection of clusters of galaxies in the XFS so far has only been performed with one method, the matched filter detection algorithm of Postman et al. (1996, P96) . The P96 method was chosen because it is well tested and efficient, works on a single passband catalogs, and can thus be used for the entire area of the XFS.

6.2.1 Optical Catalog Creation

The starting point for any optical cluster search method is a catalog of galaxies. It is thus only prudent to discuss the creation of such catalogs in some detail before turning to a short description of the matched filter algorithm and its implementation for this survey.

Unfortunately, WFI images are especially prone to internal reflections, producing prominent reflection rings around all saturated stars with blooming in the core. The brightest stars show more than one reflection ring, with increasing sizes and offsets from the position of the source. Additionally, extended halos and diffraction spikes occur around bright sources. The catalog creation tries to mask regions affected by these problems automatically as much as possible but still requires a large amount of manual masking.

The catalog production uses SExtractor (Bertin & Arnouts 1996) and starts with a very low SNR catalog. The WEIGHT images produced by the GABODS pipeline are used in all steps of the catalog creation. The sole purpose of this first catalog is to identify regions that should be masked. Masked regions will be passed on to SExtractor in a FLAG image.

All objects of the initial catalog are put into cells of a grid whose size is chosen such that the average number of objects per cell is 2. This grid is smoothed with a Gaussian kernel with a FWHM of 1.4 pixels. We call the smoothed array $\mathcal{S}$. Automatically adjusting the grid size such that a fixed number of galaxies per cell is reached on average, allows one to keep the

size of the Gaussian, which is necessary to reach the desired SNR in the object density distribution, fixed in the program. The main advantage of this approach is that the values of the kernel can be stored in a matrix (fixed to a 5×5 array in the program). The convolution of the density grid with the kernel matrix is computationally much faster than re-evaluating the Gaussian kernel at every grid cell. In the next step the dynamic range $\mathcal{S}$ is limited. Every pixel with a value > 1.5 is set to 2. Every pixel with a value < 1 is set to zero; these pixels will be masked because they are either in very low SNR ratio parts of the image, such as the edges, or they are covered by extended objects, such as large foreground galaxies or very bright stars. The resulting array is called $\mathcal{D}$.

Additionally, any rapid change of object density in $\mathcal{D}$, such as seen at the edges of reflection rings, is detected with a Sobel edge detection, i.e., an array containing the absolute values of the gradient of the array $\mathcal{D}$. The gradient computation is implemented as a convolution of $\mathcal{D}$ with the two 3×3 convolution kernels that correspond to finite second-order, two-sided differentiation. Every pixel exceeding a threshold in $\mathcal{D}$ is flagged in the output image.

Finally, the FLAG array, containing only values of 1 for pixels to be flagged and 0 for all other pixels, is smoothed again with the 1.4 pixels FWHM Gaussian to account for the fact that the initial smoothing shrunk the areas not covered by objects. Every pixel with a non-zero flag value will be flagged in the output FLAG image, which is expanded to the size of the original WFI image from which the catalog was created.

FLAG images created through this procedure reliably mask extended objects, bright stars, and the most prominent reflection rings. Exceptionally empty regions on the sky are only rarely masked erroneously. However, fainter reflection rings and stars of intermediate magnitude must still be masked by hand. Files describing the regions masked manually – either by circles or polygons for more complex shapes – must be generated by the user with tools such as the image viewer DS9. From them and the automatically generated FLAG image, the final FLAG image used in further steps of the catalog production, is created.

The image seeing is determined from a high SNR catalog. A histogram of the FWHM of all objects with $0\overset{\prime\prime}{.}3 < $ FWHM $ < 3\overset{\prime\prime}{.}0$ is created and the image seeing is set equal to the FWHM of the bin with the most objects. The seeing

is used as input for `SExtractor`'s star-galaxy classifier `CLASS_STAR`. Since we are only interested in galaxies and not in stars, reliably separating them in the science grade catalogs is important for galaxy cluster searches.

Finally, two science grade catalogs are created with `SExtractor`. Their only difference is the filter with which the detection image is convolved. The catalog for the optical matched filter search is made using a Gaussian kernel with a FWHM of 4 pixels. This kernel ensures that relatively few spurious detections of faint objects are made but it has a lower completeness at the low SNR ratio end with a tendency to miss very small objects. Another catalog with `SExtractor`'s default filter – a 3×3 pixel pyramidal kernel – is created as starting point for the weak lensing catalog creation (see Sect. 6.3).

6.2.2 The Postman Matched Filter

The Postman matched filter algorithm is described in detail in P96. We will only give a short overview here. The main features of the matched filter algorithm separating it from other single-band cluster detection schemes are: (1) it is optimal for identifying weak signals in a noise dominated background; (2) photometric information is used in an optimal way; (3) the contrast of structures which approximate the filter shape with the background is maximized; (4) redshift and richness estimates of cluster candidates are produced as a byproduct; (5) the algorithm performs well over a large range of redshifts. The main disadvantage is that a particular radial profile and luminosity function must be assumed. Clusters deviating from the expected profile will be detected only at lower significances or suppressed.

The P96 filter is constructed as a maximum likelihood estimator for the presence of a cluster at a given position. It assumes a fiducial cluster model embedded in a noisy background. The model is described by

$$
\begin{aligned}
D(r, m) &= \text{background} + \text{cluster} \\
&= b(m) + \Lambda_{\text{cl}} P(r/r_{\text{c}}) \phi(m - m^*) ,
\end{aligned}
\tag{6.1}
$$

where $D(r, m)$ is the total number of galaxies per magnitude per unit area at a given distance $r = |\boldsymbol{r} - \boldsymbol{r}_0|$ from the cluster center $\boldsymbol{r}_0$ and magnitude m; $b(m)$ is the number density per magnitude of field galaxies contributing to the noise background. $P(r/r_{\text{c}})$ is the projected number density profile of

the galaxy cluster, $\phi(m - m^*)$ is the differential cluster luminosity function, and Λ_{cl} is a measure of the cluster's richness. The parameter r_c is a characteristic length scale of the cluster seen in projection (the core radius); m^* is the apparent magnitude corresponding to the characteristic luminosity of galaxies in the cluster. We denote the physical core of the cluster by R_c and the absolute magnitude corresponding to m^* with M^*.

Using this model an approximate expression for the likelihood can be derived,

$$\ln \mathcal{L}(r, m; z, \boldsymbol{r}_0) \propto \int \mathrm{d}^2 r \, \mathrm{d}m \, P(r/r_c(z)) \frac{\phi(m - m^*(z))}{b(m)} D(r, m) \,, \quad (6.2)$$

giving the likelihood of finding a cluster at a given position $\boldsymbol{r}_0$ and redshift z. The dependence on the redshift enters Eq. (6.2) implicitly through the r_c and m^*, which both depend on it. Because the galaxy distribution is a set of discrete positions and magnitudes, the function $D(r, m)$ can be represented as a series of δ functions. Thus, an estimator S of the integral (6.2) can be computed on grid positions (i, j) as a sum over all galaxies in a field,

$$S(i, j; z) = \sum_{k=1}^{N_g} P\left[r_k(i, j)\right] L(m_k) \,, \quad (6.3)$$

where $r_k(i, j)$ is the distance of the kth galaxy from the grid point (i, j) scaled with the core radius r_c, and m_k is the apparent magnitude of this galaxy. $P(r_k)$ is the spatial weight function of Eq. (6.2) and $L(m_k) = \phi(m_k - m^*)/b(m_k)$ is the luminosity weight function. Again, the redshift dependency of this estimator enters implicitly through $r_c(z)$ and $m^*(z)$. The sum is evaluated for different redshifts, while the fiducial cluster model specifying the characteristic length scale and luminosity of the cluster in physical units is kept fixed. The corresponding observables r_c and m^* are varied according to the specified cosmology. The redshift dependence of m^* also includes a k-correction.

The grid S computed in this way is a likelihood map in which cluster candidates correspond to peaks in the likelihood map. A redshift estimate of such a cluster candidate is obtained by varying the redshift for which S is computed and maximizing the value of S at the peak position.

When the luminosity function ϕ is chosen to be the Schechter (1976) function, the integral over $L(m) = \phi(m - m^*)/b(m)$ in Eq. (6.2) diverges at faint magnitudes. The solution P96 propose is an exponential cutoff of the luminosity function of the form $10^{-\beta(m-m^*)}$ so that with $\beta = 0.4$ an additional weighting with the flux of the galaxy is performed. The filter $L(m)$ then reads

$$L(m) = c_L \frac{\phi(m - m^*)10^{-\beta(m-m^*)}}{b(m)} , \qquad (6.4)$$

where c_L is a normalization factor.

The spatial filter $P(r/r_c)$ is chosen to be a modified Hubble profile

$$P(r/r_c) = \begin{cases} c_P \left(\dfrac{1}{\sqrt{1+(r/r_c)^2}} - \dfrac{1}{\sqrt{1+(r_\infty/r_c)^2}} \right) & r < r_\infty , \\ 0 & \text{otherwise} , \end{cases} \qquad (6.5)$$

where r_∞ is an arbitrary cutoff radius and c_P is a normalization constant. The filter $P(r/r_c)$ is circularly symmetric. However, if the cutoff radius is much bigger than the core radius, systems which are not circularly symmetric are still detected, albeit at a lower significance.

These weight functions are normalized by choosing the factors c_L and c_P such that the following conditions are satisfied:

$$\int_0^{r_\infty} \mathrm{d}r \, 2\pi r P(r/r_c) = 1 , \qquad (6.6)$$

and

$$\int_{-\infty}^{m_{\mathrm{lim}}} \mathrm{d}m \, \Phi(m - m^*) = c_L \int_{-\infty}^{m_{\mathrm{lim}}} \mathrm{d}m \, \phi(m - m^*)10^{-\beta(m-m^*)} = 1 , \quad (6.7)$$

where the upper limit of the integration of the luminosity function is determined by the limiting magnitude m_{lim} of the sample. With this normalization the "background level" of the filtered images should be $S(i, j) = S_{\mathrm{bg}} = 1$. However, the mode of the filtered images is in practice not exactly unity but varies slightly with redshift. This is because the background $b(m)$ is estimated as the total number of galaxies (background and clusters) in the field.

These two components cannot be separated a priori. The normalization in Eq. (6.7) is strictly correct only in the case of a pure background population and still appropriate if the number of cluster galaxies is small compared to the number of background galaxies. However, when a significant fraction of the Schechter function is truncated by the limiting magnitude, a bias in the estimated redshift of a cluster candidate is introduced. We correct for this bias according to the prescription of P96 by computing

$$S_{\mathrm{cor}}(i,j) = \frac{S(i,j) - S_{\mathrm{bg}}}{\mathrm{CSC}} \; , \tag{6.8}$$

where CSC is the *cluster signal correction*

$$\mathrm{CSC} = \frac{\int_{-\infty}^{m_{\mathrm{lim}}} \mathrm{d}m \; \phi_{\mathrm{cl}}(m - m^*)\Phi(m - m^*)/b(m)}{\int_{-\infty}^{m_{\mathrm{lim}}} \mathrm{d}m \; \Phi(m - m^*)}$$
$$\Bigg/ \frac{\int_{-\infty}^{\infty} \mathrm{d}m \; \phi_{\mathrm{cl}}(m - m^*)\Phi(m - m^*)/b(m)}{\int_{-\infty}^{\infty} \mathrm{d}m \; \Phi(m - m^*)} \; , \tag{6.9}$$

and ϕ_{cl} is the luminosity function of the fiducial cluster model. The full derivation of this expression is given in P96. The CSC also depends through m^* implicitly on the redshift.

The only parameter in Eq. (6.1) that we have not discussed until now is the cluster richness Λ_{cl}. The total luminosity in the area of a cluster, i.e., the luminosity of the cluster L_{cl} plus the background is

$$L_{\mathrm{tot}} = \mathrm{constant} + \Lambda_{\mathrm{cl}}10^{-0.4m^*} \; , \tag{6.10}$$

as was shown by P96. Therefore, the cluster luminosity is $L_{\mathrm{cl}} = \Lambda_{\mathrm{cl}}10^{-0.4m^*} = \Lambda_{\mathrm{cl}}L^*$. Thus, Λ_{cl} is the equivalent number of L^* galaxies in the cluster yielding the luminosity of the cluster.

6.2.3 Matched Filter Pipeline

A series of programs and shell scripts is used to go from the object catalogs described in Sect. 6.2.1 to a catalog of cluster candidates. The input catalog is filtered such that only objects which have a high probability of being

galaxies are kept. To this end only objects with a CLASS_STAR value < 0.5 are kept. At the faint end the catalog is cut at a magnitude 10σ above the sky background as measured in a $2''$ aperture to ensure a high completeness of the catalog. Objects brighter than 17 mag are also filtered. These are often bright stars, which are not correctly identified as such by SExtractor and would cause a serious contamination of the input catalog. If any of these objects with $m < 17$ are bright, nearby cluster members, the matched filter signal of the cluster is decreased. However, the fainter cluster galaxies usually still lead to a significant detection of the galaxy cluster but with a redshift bias. This bias is introduced because omitting the bright cluster galaxies modifies the luminosity function. This redshift bias introduced by the cut on the bright galaxies is marginal, at least on the redshift range considered here.

FITS images of the likelihood array S are produced for a number of redshifts. Because at this point we have no reliable determination of the actual background the CSC is computed but not applied. We store it in the header of the output FITS files. Here we compute S with a spacing in redshift of $\Delta z = 0.1$, starting at $z = 0.1$ and up to the last output grid in which the m^* of the fiducial cluster model shifted to that redshift is not fainter than the limiting magnitude of the input catalog. For the XFS R-band observations this is typically up to $z = 0.9$. We base our approach on that of Olsen et al. (1999, henceforth O99) and assume a fiducial cluster model at at $z = 0.6$ with a Schechter luminosity function with $M_R^* = -21.63$ mag, faint end slope $\alpha = -1.1$, and a Hubble profile with physical core radius $R_c = 0.1\,h_{70}$ Mpc integrated out to cutoff radius $r_\infty = 10 R_c$. We keep the pixel size of the output grid constant at $0.5\,\mathrm{pix}/R_c$ at $z = 0.6$ but vary the area required for a detection in the output images with redshift. The k-correction needed for the redshift dependence of m^* is computed for an elliptical galaxy with no evolution.

Having created the likelihood maps we are now faced with the problem of identifying clusters of galaxies in them, i.e., we have to decide which peaks are reliable candidates for galaxy clusters. Peaks in the likelihood maps are detected with SExtractor. The main SExtractor detection parameters were adopted from O99 and are set as follows:

- The minimum area for a detection MIN_AREA scales with the redshift and corresponds to πr_c^2, i.e., the area corresponding to the projected cluster core in the model;

– The detection threshold `DETECT_TRESH` is set to 2;

– No deblending of peaks is performed (`DEBLEND_MINCONT=1`), so that all contiguous pixels above the detection threshold are counted as one cluster candidate.

– A global background is estimated from the image.

Most objects in the catalogs created in this way have a very low SNR and the catalogs contain many spurious sources. Before developing criteria for rejecting them, a few derived quantities are computed. The `SExtractor` estimated background level is used as S_{bg}. The redshift dependent value of the CSC is stored in the FITS header of every output grid. The significance of a detection is calculated by dividing the peak signal above the background by the standard deviation of the background level as determined by `SExtractor`.

Catalogs from the individual output grids at different redshifts are then matched by position using the LDAC program `associate`. Peaks present in at least 3 output grids with a minimum significance of at least 3.5σ in one of them were kept as reliable cluster candidates. These parameters are slightly different from the ones adopted by O99, who used a threshold of 3σ, a detection in at least 4 output grids, and a minimum value of the richness parameter Λ_{cl}. The reason for different selection criteria are the different redshift regions of interest in the study of O99 and the work presented here. While O99 are chiefly interested in high redshift clusters, our search mainly aims for intermediate redshift clusters accessible with weak lensing, i.e., most of these clusters will be at redshifts $z = 0.2 \ldots 0.3$. Several of the criteria adopted by O99 bias against the search of clusters at intermediate redshifts.

The significance of a cluster signal drops sharply once we look at output grids at redshifts higher than the cluster's redshift because the power law cutoff of the luminosity filter strongly suppresses signals from lower redshifts. For clusters at lower redshifts the number of output grids at redshifts smaller or equal to the cluster redshift is small. The requirement of O99 that a cluster candidate be detected in at least 4 output grids thus heavily biases against the detection of clusters at the redshift interval we are especially interested in. We therefore relaxed the requirement on the number of output grids in which a cluster must be detected to 3, and have the lowest redshift output grid at $z = 0.1$ instead of $z = 0.2$. To compensate for the higher number of spurious

detections caused by this less stringent cut the minimum significance to be reached in at least one output grid was increased from 3 to 3.5.

We do not make any cuts on the richness parameter Λ_{cl}. Clusters at higher redshifts need to be much more luminous than clusters at lower redshifts to be detectable. Consequently, the average richness parameter of clusters at higher redshift is much larger than that of lower redshift clusters. Imposing a minimum value for Λ_{cl} would create a strong bias against low and intermediate redshift systems.

The selection criteria adopted by O99 have proven to be very successful by a high rate of spectroscopically confirmed clusters found in the EIS wide survey (e.g., Hansen et al. 2002; Olsen et al. 2003; Benoist et al. 2002) and we are thus confident that our slightly modified criteria are also successful. However, we have to note that the simulations on which these criteria were developed are not able to predict the number of spurious detections. O99 attempted to simulate a pure background population of galaxies by randomizing the position of galaxies while keeping their magnitude fixed. This randomized population has a much smoother distribution than the field population of galaxies. The reason is that the distribution of field galaxies is not a random field with white noise, but shows clustering and correlation.

6.2.4 Matched Filter Catalog

To generate catalogs of galaxy cluster candidates, object catalogs were produced as described in Sect. 6.2.1 for the R-band data of all fields. For the matched filter cluster search the deepest coaddition available was used when more than one coaddition was present. This is in most cases the image denoted by the ALLF coaddition ID; see Table 5.9 for comparison. These catalogs were given to the matched filter pipeline with the setup described in the previous section.

The resulting catalog is presented in App. D.2. It lists 116 candidate clusters over 23 fields of the XFS. The field PB 5062 was excluded from this analysis as the galactic extinction in this field is too high. 13 of the systems in this catalog have been previously found by other authors and have either spectroscopic or photometric redshift information. All cluster candidates were visually inspected and graded similar to the grades given to the X-ray detected clusters. Grades are listed in Table D.2. Cluster candidates with grade "+"
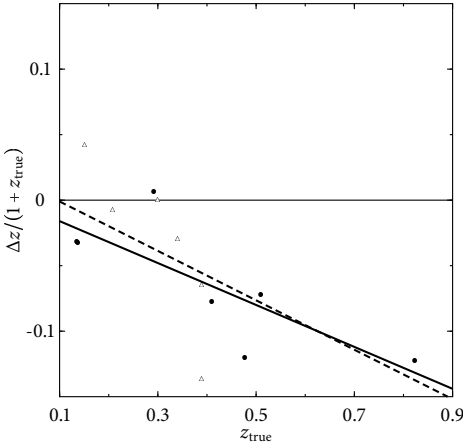
Figure 6.1: Comparison of redshift estimates obtained from the matched filter with literature values. Solid circles denote data points with spectroscopic redshift information; open triangles are photometric redshift estimates from the literature. The matched filter underestimates the redshift as is shown by the best fit lines to the spectroscopic sample (solid line) and the full sample (dashed line).

are obvious real cluster, often the ones one would select by eye, or have extended X-ray sources as counterpart. Matched filter peaks graded "∘" are probable detections but less prominent than those graded "+" and may be more prone to projection effects. Candidates with a "−" grade are most likely artefacts or maybe in some cases very poor clusters or groups.

Out of the total of 116 matched filter peaks 50 were graded "+", 41 "∘", and 25 received a grade of "−". There is a clear correlation between the significance of a cluster candidate and its grade. The average SNR of a "+" rated cluster is 5.4σ and include the highest SNR detections; "∘" graded cluster candidates have an average significance of 5.0, while the unlikely candidates rated with "−" have an average value of $\overline{\sigma}_{max} = 4.4$.

A comparison of the matched filter estimated redshifts of the 13 previously found systems with their redshift values found in the literature is provided by Fig. 6.1. Clusters with spectroscopic redshift information are presented as solid circles while open triangles denote clusters whose redshift information is based on photometry. These "photometric redshifts" are not photometric redshifts in the classical sense of, e.g., template fitting but are the redshift estimators of other cluster finding methods. This is most notably the redshift
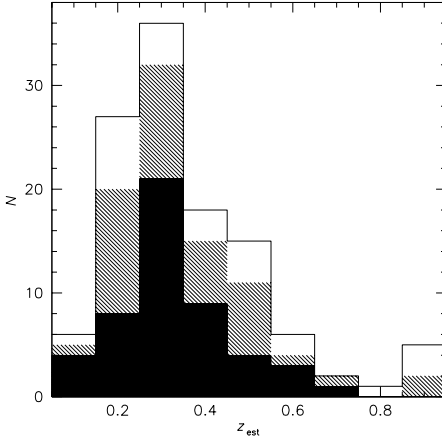
Figure 6.2: Histogram of the estimated redshift distribution of the matched filter detected clusters. The open histogram represents all cluster candidates, the shaded histogram the "+" and "∘" rated candidates, and the solid histogram only the "+" rated clusters.

estimator of the "cut-and-enhance method" of Goto et al. (2002), which provides 4 redshifts in this sample. The mean offset from the zero line for the spectroscopic sample is marginally significant with $\langle \Delta z/(1 + z_{\text{true}}) \rangle = -0.06 \pm 0.05$, while the mean offset of the whole sample $\langle \Delta z/(1 + z_{\text{true}}) \rangle = -0.05 \pm 0.05$ is consistent with zero, where the error is simply the standard deviation of the scatter. The relatively small deviation from zero hides a significant bias of the matched filter redshifts towards lower redshifts. The solid line in Fig. 6.1 is the best linear fit to the spectroscopic data points. The line is described by $\Delta z/(1 + z_{\text{true}}) = (0.00 \pm 0.03) + (-0.16 \pm 0.06)z_{\text{true}}$. Thus, the deviation from the ideal relation is significant at the 2.7σ level. The bias increases marginally if the photometric data points are included in the analysis (dashed line in Fig. 6.1). The best fit line is then described $\Delta z/(1 + z_{\text{true}}) = (0.02 \pm 0.02) + (-0.21 \pm 0.06)z_{\text{true}}$.

Since the clusters were found on different fields with independent photometric calibration, errors in the photometric calibration can be excluded as the source of this systematic difference. Possible sources of the underestimated redshifts are (1) the k-correction, which depends on the adopted galaxy model, and (2) the luminosity function of the fiducial cluster model, specifically the value of M^*. We note that the most discrepant value is the

highest redshift point. Our flux filter was constructed under the assumption of no evolution and thus stronger discrepancies are indeed expected at higher redshifts. This was already noted by P96, who also found the estimated redshifts of higher redshift cluster to be systematically too low by about $\Delta z = 0.1\ldots 0.2$.

6.3 Weak Lensing Detection

Through the differential deflection of light, cluster mass concentrations induce a measurable tangential alignment of the images of background galaxies around the mass in the foreground. This distortion can be used to detect galaxy clusters based solely on their mass, or more precisely on their gravitational shear (see Chap. 2 for a more detailed discussion). A number of galaxy clusters have been found using weak gravitational lensing in recent years: in the FORS1 cosmic shear survey (Maoli et al. 2001; Hetterscheidt et al. 2005) one mass peak clearly coincides with an overdensity of galaxies. Dietrich et al. (2005, see also Chap. 4) found a cluster in the background of the super-cluster system A 222/223. Recently, Wittman et al. (2005) published a sample of 6 new weak lensing detected clusters from their Deep Lens Survey, increasing the number of clusters selected by this method in the literature by about 50%. These examples clearly demonstrate that this method of cluster detection in fact works.

The selection of clusters of galaxies by weak lensing, however, also faces significant methodological challenges. Even before the first spectroscopically confirmed weak lensing detected cluster was detected (Wittman et al. 2001), Erben et al. (2000) reported a highly significant tangential alignment of galaxies around an empty spot on the sky (see also von der Linden et al. 2005). Two more of these *dark clumps* have been reported in the literature (Umetsu & Futamase 2000; Miralles et al. 2002, but see also Erben et al. 2003). Of course, the reality of these dark clump detections has to be considered with caution, given that even one of them would have profound impact on our understanding of the evolution of dark and baryonic matter in the Universe.

Several theoretical studies have recently shed some light on the problem of dark clump detection in weak lensing surveys. Among them are Hamana et al. (2004, H04) and HS05 who have both used ray-tracing simulations

through N-body simulations to study the *efficiency* and *completeness* of the detection of clusters of galaxies in weak lensing surveys. If f_+ is the fraction of false positives, i.e., the fraction of shear selected mass peaks that do not correspond to a dark matter halo, the efficiency is defined as $e = 1 - f_+$. Conversely, if f_- is the fraction of false negatives, i.e,. the fraction of cluster mass halos that does not correspond to a shear selected peak, the completeness is defined as $c = 1 - f_-$. Completeness and efficiency are obviously functions with a complex dependence on cluster mass, redshift of the cluster, redshift distribution and number density of the background population, cosmology, and selection criteria. An important result of HS05 is that the efficiency, even in the limiting case of no intrinsic ellipticity, does not increase beyond $e \sim 0.85$. The remaining 15% of shear selected peaks are due to projections of the large scale structure along the line of sight and will be seen as dark clumps. These could very well account for the dark clumps reported so far in the literature. The efficiency naturally further drops if realistic noise properties of the background galaxies are assumed. The completeness was studied in more detail by H04, who find that even with low significance thresholds in the selection process shear selected samples will be incomplete, except at the highest masses.

Both of these theoretical studies used a number density of background galaxies of $n = 30\,\text{arcmin}^{-2}$ that is achievable with 8 m class telescope but out of reach for the 2.2 m telescope with which the XFS was observed. Typical number densities in the XFS will not exceed $15\,\text{arcmin}^{-2}$. Consequently, efficiency and completeness of the weak lensing selected cluster sample in the XFS will be lower than the predictions of H04 and HS05.

6.3.1 Signal and Noise of the Aperture Mass

Before we apply the aperture mass statistic to the XFS data we need to understand the properties of the aperture mass function (Chap. 2.4) in some more detail. Equations (2.47) and (2.48) allow us to compute the SNR of M_{ap} as

$$S = \frac{\sqrt{2}\sum_i Q_i \varepsilon_{\text{t}i}}{\sqrt{\sum_i Q_i^2 \varepsilon_i^2}} \, , \tag{6.11}$$

where Q_i is the weight assigned to the ith galaxies by the radially symmetric weight function $Q(\vartheta)$. This expression, however, considers only the noise caused by the random ellipticities and not the shot noise of the finite sampling of the M_{ap} statistic by the population of background galaxies.

We use ray-tracing simulations to examine these effects in detail. These were generated by tracing light rays through the ΛCDM N-body simulation of the VIRGO consortium (Jenkins et al. 1998). These N-body simulations were carried out with the following parameters: $\Omega_{\mathrm{M}} = 0.3$, $\Omega_{\Lambda} = 0.7$, $h_{70} = 1$, $\sigma_8 = 0.9$, $\Gamma = 0.21$, and the index of the primordial power spectrum $n_{\mathrm{s}} = 1$. The population of background galaxies was assumed to be a δ function peaked at $z = 1$. From the source redshift to redshift 0, 1024^2 light rays were traced through 16 slices of 202.9 h_{70}^{-1} Mpc thickness onto an output grid of 1×1 square degree. Each redshift slice corresponds to one output box of the N-body simulations. 50 different realization of the ray-tracing were made by randomly shifting and rotating the lens planes. The details of the ray-tracing algorithm are given in Hartlap (2005). The output of these simulations are noiseless maps of the surface mass density and the two shear components.

Lensing catalogs were created by randomly distributing galaxies with an ellipticity dispersion of $\sigma_{\varepsilon} = 0.38$ over the output grid of the ray-tracing simulations on areas corresponding to the sizes of actual XFS fields until the number density of the respective XFS field was reached. When placing galaxies, the masks used in the catalog generation of the real data were applied to simulated catalogs as well, to realistically model the effect of holes in the field. Three different masks and number densities were taken from the XFS data. All masks were put on each of the 50 ray-tracing realization to obtain a high number of lensing simulations. The effective (unmasked) area and number densities of these fields are 970 arcmin^2 and 13.4 arcmin^{-2}, 1022 arcmin^2 and 17.7 arcmin^{-2}, and 981 arcmin^2 and 18.2 arcmin^{-2}.

With typical sizes of the XFS fields of $35' \times 35'$ the individual lensing simulations are not totally independent but have some overlap because the side length of one raytracing simulation is only $60'$, not enough to accommodate two XFS masks next to each other. The catalogs were placed on the ray-tracing simulations such that this overlap is minimized. While not completely independent these overlapping areas were covered by catalogs with different masking, different number densities, and different realizations of Gaussian noise so that for our purpose – understanding the noise proper-

Table 6.1: Filter radii for M_{ap} computation and corresponding virial mass.

Radius (kpc/h_{70})	M_{vir} ($10^{14}\,h_{70}^{-1}\,M_{\odot}$)
1000	0.76
1247	1.5
1493	2.5
1740	4.0
1986	6.0
2233	8.5
2479	12.0
2726	15.0
2972	20.0

ties of M_{ap} from realistic simulations – no significant correlation between individual lensing simulations is expected.

We compute the aperture mass for 9 different filter scales and the filter functions proposed by Schirmer (2004) and Maturi et al. (2005) from the same catalogs. As both filter functions are based on an NFW model of a cluster we choose the filter radii based on an assumed fiducial cluster model. In this model the cluster is at redshift $z = 0.3$, the redshift at which we expect the lens strength in our survey to be maximized. Table 6.1 gives these filter radii and the corresponding virial mass if they are interpreted as virial radius of the cluster. We also need to fix the the redshift of the source galaxies to model the lens strength of the fiducial cluster in the Maturi filter (see Chap. 2.4 for details of the construction of this filter). We assume that all background galaxies are at $z_{\mathrm{s}} = 0.8$ and the number density of background galaxies is $n = 18\,\mathrm{arcmin}^{-2}$. M_{ap} is computed on a grid. We set the pixel size in this grid such that one pixel corresponds to $50\,h_{70}^{-1}$ kpc at the redshift of the fiducial cluster model.

For all lensing simulations and filter scales we compute M_{ap} and $-M_{\mathrm{ap}}$ for both filter functions from the input catalog, and M_{ap} after rotating (1) all galaxies by 45°; (2) every galaxy by a random angle for the Schirmer filter. Maps of the aperture mass and their SNR (S-maps), which are computed as well, are saved as FITS images.

As for the detection of peaks in the matched filter maps, we use `SExtractor` to identify shear selected peaks in the M_{ap}-maps. For this purpose we run `SExtractor` in dual-image mode with the M_{ap}-map as detection image and the S-map as measurement image. This means that the SNR of a M_{ap} peak is computed with Eq. (6.11) and not determined by `SExtractor`. This is a small difference from the matched filter pipeline, in which we did not use the P96 likelihood to determine a significance but used `SExtractor` detection significances.

The detection threshold is set to 2σ and the minimum detection area scales with the filter such that it corresponds to the pixels covered by a circle with a radius twice as large as the filter scale. `SExtractor` is run without deblending, i.e., every contiguous area above the detection threshold is counted as one object. Peaks found in this way in different filter radii were associated based on positional coincidence.

We first examine the results obtained with the Schirmer filter before comparing these to the ones obtained with the Maturi filter.

Positional offsets between the weak lensing peak positions and the position of the BCG or the center of X-ray emission from the hot intracluster gas are commonly observed (Wittman et al. 2005) and expected (Dietrich et al. 2005). The size of the offsets was studied for the case of an isolated SIS by Dietrich et al. (2005, see also Fig. 4.3). The ray-tracing simulations used here allow us to study the additional effect of large-scale structure along the line of sight.

The catalogs of weak lensing halos produced in this way from the M_{ap} images were associated with a catalog of actual dark matter halos in the VIRGO simulation. For this purpose we only considered halos with masses in excess of $10^{14}\,M_{\odot}$ and with redshifts $0.1 < z < 0.7$ as these are roughly the ones to which we expect to be sensitive in our galaxy cluster survey. The maximum distance allowed for a match between halo position and M_{ap} peak is determined by the virial radius of the halo and the size of the M_{ap} peak as determined by `SExtractor`. Note that the position of the halo was derived from the most-bound particle in that halo identified by the friend-of-friend halo finder employed to generate the halo catalog. In rare cases this is in the center between what one by eye would identify as two separate halos.

In the ray-tracing simulations 434 peaks in the M_{ap}-maps could be associated with dark matter halos in the VIRGO simulation. Figure 6.3 shows the
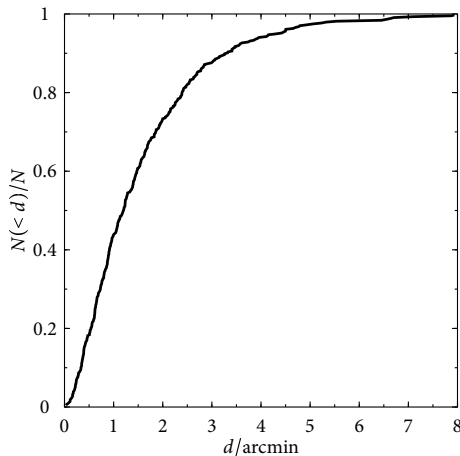
Figure 6.3: Cumulative distance distribution of the 434 M_{ap} peaks that could be associated to a dark matter halo in the VIRGO simulation. 75% of all matches are made within a $2\!'\!.15$ radius.

cumulative distribution of their positional differences. From the number of density of M_{ap} peaks and the average size of the association radius we estimate that ~ 100 or $\sim 25\%$ of those matches are chance coincidences. Inspection of Fig. 6.3 shows that 75% of all positional offsets are smaller than $2\!'\!.15$, which is the maximum offset we will allow from here on. Note that this is on the one hand significantly smaller than the $3'$ matching radius adopted by HS05 who used a higher number density and a smaller ellipticity dispersion. On the other hand it is significantly larger than the offsets found for an isolated SIS in Chap. 4.2.2. This possibly indicates a non-negligible influence of large-scale structure along the line of sight on the weak lensing peak positions of dark matter halos. One, however, has to be careful when drawing this conclusion as we are looking at halos at very different redshifts, while we studied only systems at one redshift in Chap. 4.2.2.

Aperture mass peaks not associated with dark matter halos can be caused either by projections of large structure mimicking a shear signal of a cluster or by the shape noise background galaxies that can cause random tangential alignments. In real data the measured ellipticities must be corrected for atmospheric seeing and PSF distortions of the instrument. Residuals in this correction can also lead to spurious alignments of background galaxies.

This remaining systematic is sometimes seen in cosmic shear surveys as non-curl-free shear field (*B-modes*). Opposed to B-modes, lensing can only create curl-free shear fields (*E-modes*). B-modes are usually seen only on scales smaller than relevant for our M_{ap} kernels (e.g., Van Waerbeke et al. 2005, Hetterscheidt et al. in preparation) and we can thus safely apply the results of our ray-tracing simulations to the XFS. E-modes are transformed into B-modes (and vice versa) by rotating all galaxies by 45°.

Figure 6.4 shows the significance distribution of shear selected peaks in the different kind of aperture mass maps created with the Schirmer filter. If a peak was found in more than one filter scale the significance is the highest from all filter scales. The solid black line is the distribution of peak significances for all M_{ap} peaks created from the ray-traced catalog, i.e., those peaks one would find in real data. The long dashed green line represents negative peaks or, considering how the peak finding pipeline is run, peaks found in $-M_{ap}$-maps. The short dashed red line is for peaks found in B-mode M_{ap}-maps, i.e., maps of aperture mass created after all galaxies in the ray-traced catalog were rotated by 45°. Blue dot-dashed lines are from mock catalogs with random ellipticities. It is important to emphasize that the random seed was kept fixed so that when computing M_{ap} on different filter scales the orientation of galaxies in the input catalog remained unchanged. The solid pink line corresponds to those weak lensing peaks that could be associated with dark matter halos within a matching radius of $2'.15$.

A number of features in Fig. 6.4 are worth a more detailed discussion. First, we note that the number density of peaks in the M_{ap}- and $-M_{ap}$-maps declines towards lower significances, while the number density of peaks in the B-mode and mock maps remains roughly constant below 3.25σ. Naively, one would expect an increase in all curves towards lower significances. The observed behavior is due to a selection bias when running `SExtractor` on the FITS images. The detection threshold is derived from the standard deviation of the background in these images. The B-mode and mock maps are overall flatter than the E-mode M_{ap}-maps. This leads to a detection threshold at which peaks of lower significance in the S-maps are detected in the M_{ap}-maps for mock and B-mode maps than for E-mode maps.

Second, the number of E-mode peaks is higher than the number of B-mode and mock peaks in all significance bins in which the aforementioned selection effect plays no role. However, the numbers of E-mode, B-mode,
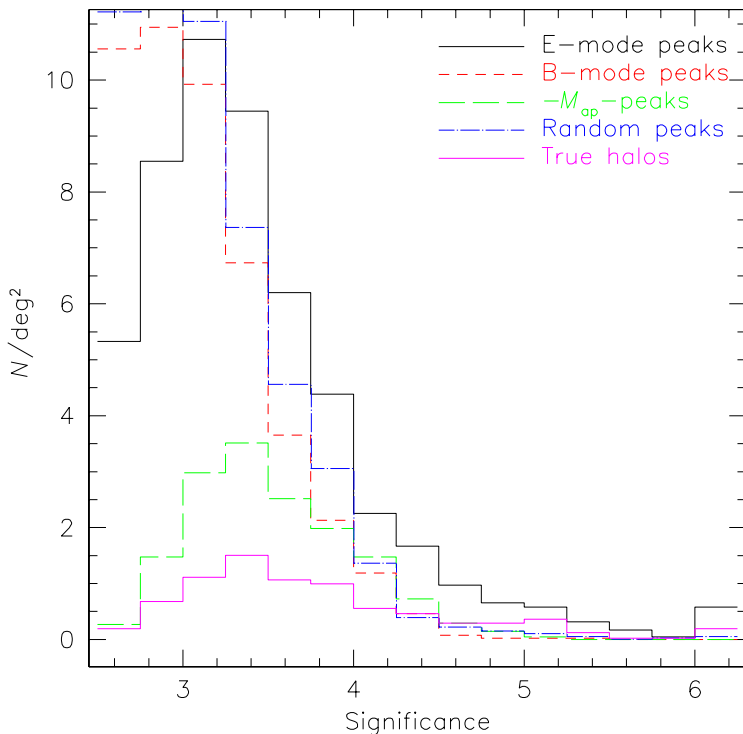
Figure 6.4: Peak significances of shear selected peaks in the maps of M_{ap} (black solid), $-M_{\mathrm{ap}}$ (green long dashed), B-mode M_{ap} (red short dashed), and mock catalogs (blue dot-dashed). The solid pink line corresponds to peaks successfully associated to dark matter halos within $2'.15$.

and mock peaks are consistent with each other at all significances $> 3\sigma$, if one assumes Poissonian statistic. This means that we can expect a significant fraction of spurious peaks at almost all significances, a result that is compatible with earlier findings of H04 and HS05.
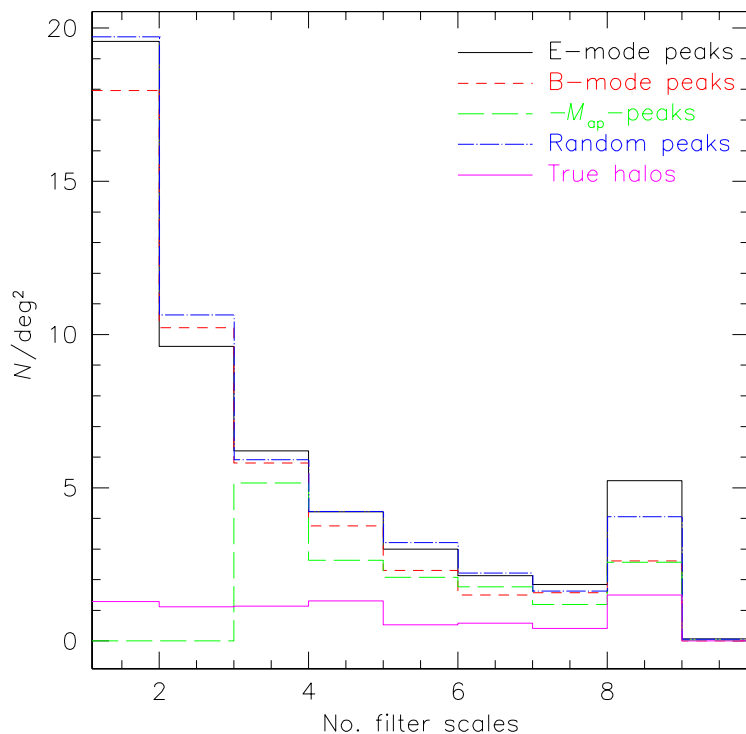
Figure 6.5: Number density of filter scales a lensing peak is detected in. The color/line-style coding is the same as in Fig. 6.4. Dark matter halo peaks show virtually no dependence on the number of filter scales, while the number density of spurious peaks sharply declines with a requirement on minimum number of filter scales.

Third, the number densities of mock and B-mode peaks are very similar, with the latter being slightly smaller. As we did not simulate the systematic influence of instrumental PSF corrections, the only sources of B-modes are

the shape noise of background galaxies and finite field effects in the M_{ap} estimator. The effect of shape noise alone is simulated by the mock catalogs, while the B-mode peaks are a combination of shape noise and systematic effects due to the finiteness of the field and holes in the data. The fact that the number density of B-mode peaks is compatible with the number density of mock peaks shows that systematic effects contributing to B-modes are not an important noise source. This is confirmed by a visual inspection of the peak distribution indicating that B-mode peaks do not show an obvious behavior to appear close to holes in or edges of the data field.

Fourth, negative peaks are relatively rare. The two effects leading to this result are best understood in terms of the filter function U that is related to Schirmer's Q_{NFW} function by Eq. (2.46) and acts on the surface mass density. U has a narrow positive peak close to the origin with extended and shallow negative wings to satisfy the condition in Eq. (2.42). The comparably low number density of $-M_{\mathrm{ap}}$ peaks is then caused by (1) the shallowness of negative wings, which will limit the peak strengths of negative peaks; and (2) by U acting as a bandpass filter for structures with the same size as the characteristic filter scale. The large extent of the negative wings will make negative peaks more extended than positive peaks, naturally leaving less space for other peaks.

By associating peaks found in different filter scales with each other we can also examine whether the number of filter scales n_{f} a peak is detected in says something about the correspondence of the lensing signal to a dark matter halo. Figure 6.5 shows the number density of peaks detected in the ray-tracing simulations as a function of n_{f} these peaks are detected in for peaks detected in at least 2 filter scales. The color/line-style coding is the same as in Fig. 6.4. One clearly sees that the number density of lensing peaks associated with a dark matter halo is virtually independent of the number of filter scales the M_{ap} peak appears in. Real dark matter halos show up as often only in 3 filter scales as in 9. This contradicts the conclusion of Schirmer (2004), who claims that the lensing signal of clusters is generally seen in many filter scales.

The behavior of spurious peaks is very different. Their number falls off monotonously as a function of n_{f}, with an exception in the last bin, i.e., the peaks that are detected in all filter scales. This dependence can be used to impose a selection criterion to decrease the contamination of shear selected

clusters with spurious lensing peaks by requiring that a M_{ap} peak must occur in at least a given number of filter scales. However, as stated above, this will always exclude a number of real clusters as well. As a compromise between efficiency and completeness we impose the condition that $n_f \geq 3$ in the xfs.

We briefly compare these results to the ones obtained with the Maturi filter Q_{Lss} on the same catalogs. It is claimed by Maturi et al. (2005) that their filter gives fewer spurious peaks and increases the signal-to-noise ratio, thereby increasing the number of real cluster detections. We find that the results of the Schirmer and Maturi filters are entirely consistent for our survey parameters. The number of M_{ap} peaks associated to dark matter halos within the $2.\!'15$ matching radius (316) is contrary to expectations slightly smaller than for the Schirmer filter (325). The difference might well be due to a smaller contamination with spurious peaks. The observed peak offsets from the dark matter halo positions are consistent with the Schirmer filter. We compare the peak significances of M_{ap} peaks related to dark matter halo computed with both filter and find $\langle S(Q_{Lss}) - S(Q_{NFW}) \rangle = -0.06 \pm 0.27$, i.e., the peak significances are consistent with each other, non-significantly favoring the Schirmer filter. As a result of this comparison we limit the weak lensing cluster search in the xfs to the Schirmer filter that is less complex and faster to compute.

6.3.2 Weak Lensing Catalog

Based on the optical catalogs created with `SExtractor`'s default convolution kernel (Sect. 6.2.1) we create lensing catalogs. We use the ksb algorithm (Kaiser et al. 1995) to obtain shear estimates closely following the procedure described by Erben et al. (2001). From the ksb catalogs we construct catalogs of probable background galaxies that are reliable shear estimators by imposing the following selection criteria: Objects with snr< 2, Gaussian radius $r_g < 0.\!''33$ or $r_g > 1.\!''19$, or corrected ellipticity $\varepsilon > 1.0$ were deleted from the catalog. We also deleted objects whose pre-seeing shear polarisability tensor P^γ has a negative trace, and bright galaxies with $R < 21$ mag.

We compared catalogs created from different coadditions on fields with known clusters to decide what the best compromise between number density of background galaxies and image seeing is to obtain high snr detections of

galaxy clusters. This comparison shows that typically the higher number density achievable from the ALLF coaddition outweighs the better seeing in other coadditions. We thus use the ALLF coaddition where available or otherwise the deepest coaddition, with the exceptions of RBS 0864-S where we use the S130 coaddition, and BR 1033−0327 where we used the S120 coaddition. The field PB 5062 was again excluded due to high galactic extinction rendering it unusable for a weak lensing analysis.

Table 6.2 gives the effective (unmasked) area of all XFS fields used for the weak lensing cluster search as well as their number density of galaxies in the weak lensing catalogs. The total area used for weak lensing is 5.8 sq. deg. The number density of background galaxies averaged over this area is 13.9 arcmin^{-2}.

The aperture mass statistic with the Schirmer filter function was estimated from these resulting catalogs on the filter scales listed in Table 6.1. No weighting of individual galaxies was done. Peaks in the M_{ap}-maps were detected as described in the previous section. The final catalog lists all aperture mass peaks with maximum SNR ≥ 5, or with maximum SNR ≥ 3 if the peak has an X-ray or matched filter counterpart, or was previously reported as cluster (candidate) within 2.′15 radius from the lensing position. All shear peaks must be present in at least 3 filter scales.

- T Leo – No association could be found for the 4 M_{ap} peaks with $\sigma_{\mathrm{max}} > 3$ and $n_{\mathrm{f}} > 2$ in this field.

- Field 864-1 – None of the 5 M_{ap} peaks with $\sigma_{\mathrm{max}} > 3$ and $n_{\mathrm{f}} > 2$ could be associated with X-ray or matched filter clusters.

- Field 864-9 – This field contains the only weak lensing selected cluster candidate that was previously identified as cluster candidate but not found by the matched filter or in X-ray. The candidate BLOX J1343.5−0022 is outside the FOV of Xmm-Newton. The cluster candidate is very elongated and might for this reason be missed by the matched filter pipeline.

- LBQS 2212−1759 – None of the 8 M_{ap} peaks with $\sigma_{\mathrm{max}} > 3$ and $n_{\mathrm{f}} > 2$ could be identified with clusters selected by other methods.

- PHL 5200 – This field is too shallow for a weak lensing analysis.

Table 6.2: Effective area and number density of galaxies of xfs fields used in the weak lensing cluster search. The last line gives the total area and the average number density over this area.

Field	Area (arcmin^2)	Number Density (arcmin^{-2})
BPM 16274	1011	15.6
CFRS-3h	965	12.1
RX J0505.3−2849	981	18.2
RBS 0864-N	948	13.0
QSO B0130−403	925	7.8
BR 1033−0327	1037	16.8
SDSS J104433.04−012502.2	997	16.9
MS 1054.4−0321	1022	17.7
HE 1104−1805	1030	13.4
PG 1115+080	1051	12.3
CD −33 07795	927	6.1
T Leo	1005	18.6
IRAS 12112+0305	1028	13.9
LBQS 1228+1116	1014	8.4
NGC 4666	1074	10.7
QSO B1246−057	869	13.0
Field 864-1	1058	16.8
Field 864-9	1045	16.9
A 1882	1019	18.6
MKW 9	1032	10.7
LBQS 2212−1759	970	12.6
Total/average	21010	13.9

We select a total of 28 cluster candidates using the aperture mass method on 22 wfi fields. The full catalog is given in App. D.3. There we list the position of the M_{ap} peaks, the significance of their detection, the number of filter scales a cluster was detected in, and the filter scale in which the snr of a peak was maximized.

6.4 Summary

In this Chapter we have selected galaxy cluster candidates independently with three different methods: optical matched filter algorithm, extended X-ray emission, and the shear signal induced by massive foreground structures.

We found a total of 158 cluster candidates on 23 WFI fields, or 25.8 cluster candidate per square degree. Most cluster candidates were found with the optical matched filter (116), followed by X-ray emission (66). As was previously shown (H04; HS05) and confirmed by our lensing simulations using ray-tracing simulations (Sect. 6.3.1) the efficiency of weak lensing for cluster selection is relatively low. To avoid being dominated by spurious weak lensing signals, we limited the catalog of weak lensing selected cluster candidates to those that have an optical or X-ray counterpart, either found in our own survey or previously reported in the literature. We found significant lensing signals for 28 cluster candidates, of which 9 are previously known cluster (candidates). 7 of the weak lensing selected clusters were detected with the matched filter and X-ray emission; 4 of these are previously unknown cluster candidates.

Comparing the redshift estimates of the matched filter method to spectroscopically measured redshifts or other photometric estimates we find that these work surprisingly well. The mean difference of redshifts $\langle \Delta z / (1 + z_{\text{true}}) \rangle$ is marginally significant only for the spectroscopic sample with -0.06 ± 0.05 , and consistent with zero if we also trust the redshifts of the photometric sample which gives $\langle \Delta z / (1 + z_{\text{true}}) \rangle = 0.05 \pm 0.05$. Considering that we use only one passband to derive the redshift of matched filter clusters, this result compares favorably to what is achievable with more colors. For example, Goto et al. (2002) report a mean Δz for their "cut-and-enhance" method of 0.02 using four colors, but only after outliers with $\Delta z > 0.1$ have been rejected. However, the matched filter estimated redshift come with a significant bias, which puts higher redshift cluster at redshifts which typically too low by $\Delta z = 0.1 \ldots 0.2$.

We have in detail described how we developed the selection criteria for our weak lensing sample using ray-tracing simulations. We find that – at least for the comparatively low number densities we are dealing with – the dominant source of noise is the shape noise of the background population and not projections of the large scale structure. The M_{ap} kernel developed

by Maturi et al. (2005) to minimize the effect of large-scale structure on weak lensing cluster searched thus could not perform better than the filter function proposed by Schirmer (2004) used in this work.

The number density of weak lensing selected cluster candidates is 4.8 per square degree. This is slightly lower than the number density of $M_{\rm ap}$ peaks with a halo counterpart in the ray-tracing simulations, which is 6.1/sq. deg. However, the average number density in the XFS data is only 13.9 arcmin^{-2}; this is somewht lower than in the ray-tracing simulations, which had an average number density of 16.5 arcmin^{-2}. Whether this difference can really be attribtuted to the difference in number density should be checked by adjusting the simulation parameters to better match the XFS observtions. The trend to slightly lower number densities is present if we select only $M_{\rm ap}$ peaks with a higher SNR> 4. The XFS contains 9 of these highly significant peaks associated with a matched filter or X-ray cluster candidate. This corresponds to 1.6/sq. deg., compted to 2.3/sq.,deg. in the raytracing simulations.

With the cluster sample presented here we have built a solid foundation to study possible selection effects in either method. This will be the subject of a follow-up paper (Dietrich et al., in preparation).

7

Summary

In the following I will summarize the content and main results of the individual Chapters in this work.

Chapter 1: Cosmological Framework

I briefly review the fundamentals of our cosmological model. Starting from the Robertson-Walker metric the expansion history of the Universe is described by the Friedmann Equations together with the equations of state of the various components contributing to the energy density of the Universe. I define the standard density parameters of cosmology and the dependence of the expansion rate (the Hubble parameter) on them. Distance definitions in curved space-time are not unambiguous and I review the definition and differences of the comoving, angular diameter, and luminosity distances.

The evolution of massive structures from tiny density perturbation is a very complex process and I provide only a brief glimpse into the complications of structure formation. Describing the density fluctuations with linear perturbation theory, the linear growth of structures can be studied. The full complexity of cosmological structure formation can, however, only be studied numerically with N-body simulations. Every N-body simulation only gives one specific realization of an initial Gaussian random density field. They can only be statistically compared to observations of our Universe, e.g., through the power spectrum of density fluctuations.

For some cases, simple analytical models of structure formation give surprisingly good results. One example is the spherical collapse model of halo formation that was used in the first derivation of the mass function of galaxy clusters. Only 24 years later a better mass function was found using N-body simulations.

Chapter 2: Gravitational Lensing

After deriving the lens equation, two fundamental quantities in gravitational lensing, the dimensionless surface mass density κ and the shear γ are defined and their influence on the image of faint background galaxies are explained. The ellipticity ε of these images is an unbiased estimator for the reduced shear g.

I review how the surface mass density distribution can be – up to an additive constant – reconstructed from the measurements of the ellipticity of faint background galaxies. First, using the classical algorithm of Kaiser & Squires (1993) and then with data only available on finite fields using the algorithm of Seitz & Schneider (2001).

I continue this Chapter with the aperture mass statistic M_{ap} (Schneider 1996). By appropriately choosing the filter function, with which the shear field is convolved during the computation of the aperture mass, M_{ap} becomes a matched filter method for galaxy cluster searches with weak lensing. I present two proposals for such weight functions.

Chapter 3: Image Reduction Pipeline

The advent of wide-field imagers created not only data volumes for which the astronomical community was not prepared but also necessitated the development of new reduction methods taking into account the additional complexity of mosaic cameras as opposed to single-chip cameras. The "Garching-Bonn Deep Survey" (GABODS) pipeline was developed to provide an almost fully automatic reduction environment for wide-field imaging data. Although the pipeline was primarily developed for the reduction and calibration of data coming from the Wide-Field Imager (WFI) at the ESO/MPG-2.2 m telescope, it has been successfully tested with data from a number of instruments, e.g., CFH12K (CFHT), FORS1/2 (VLT), SUPRIMECAM (SUBARU), WFC (INT), and WFC (WHT). The pipeline is fully described in Erben et al. (2005). This Chapter gives an overview of the complete pipeline but concentrates on the areas in which I contributed most, namely the photometric calibration of single and stacked images and strategies for de-fringing images.

One first deviation from the standard processing of single-chip cameras is the application of *superflats* to correct for large variations in the background

intensity. Superflats are created from the data themselves by masking objects in dithered exposures and stacking these exposures. The resulting image should have a good estimate of the sky on every pixel. Large or bright objects on single chips of a multi-chip camera during some pointings in an observing run can make these chips unusable for superflat creation. I describe our approach to excluding these data while ensuring photometric homogeneity of the data set.

Fringe maps are created from the superflat images to remove the additive effect caused by the diffraction of light in the substrate of the CCDs. In a deviation from the de-fringing procedure described in Erben et al. (2005) I apply the superflats also to the fringe maps. The rationale behind this procedure is that the fringe maps are created before the large scale variations are taken out by the superflats but applied to the science images only after superflatting. This means that these large scale variations are present in the fringe maps and not corrected for in the reduction procedure of Erben et al. (2005).

Single images are calibrated on a nightly basis with observations of photometric standard stars. Three different solutions with varying numbers of free parameters are computed. It is up to the user to decide whether all three parameters of a photometric solution (zeropoint, extinction coefficient, and color term) can be reliably determined from observations of a given night, or whether some of them should be replaced by default values. The nightly solutions are propagated to the step of *set processing*, in which observations of a single target from different observing runs are combined. The full set is photometrically calibrated using the frames with external (standard) calibration as a reference. The photometric calibration of stacked images with the GABODS pipeline is also described in Hildebrandt et al. (2006).

Final coadded images and weight images describing the noise variations across the image are produced by the pipeline by resampling all images in a set to a common reference grid. An accurate internal astrometric solution is necessary to preserve the shape of objects during this coaddition. We show that we typically achieve an internal accuracy of a tenth of a pixel. The accuracy of the external astrometric solution is limited by the accuracy of the reference catalog, which is typically 300 mas.

Chapter 4: Weak Lensing Evidence for a Filament between A 222/223

The theory of cosmic structure formation predicts through N-body simulations that matter in the Universe is arranged in sheets and filaments and that galaxy clusters form where these filaments intersect. These filaments have been seen in galaxy redshift surveys. We try to directly map the dark matter in the filament expected to connect the close pair of galaxy clusters Abell 222/223 at $z = 0.21$. The weak lensing mass reconstruction provides evidence for a mass bridge extending between the two cluster, albeit at a low significance of $\sim 3\sigma$. The problem of assigning a significance to a filament detection is non-trivial and discussed in detail by Dietrich (2002) and Dietrich et al. (2005). Thus, the quoted value should be used with care. Supporting evidence for a filamentary connection extending between A 222/223 comes from a 7σ overdensity of color selected galaxies between the clusters, extended X-ray emission at the 5σ level found in archival ROSAT PSPC data, and spectroscopically confirmed galaxies at the cluster redshift between the clusters. Although still not conclusive, the weak lensing filament candidate between A 222/223 is "arguably one of the best to date" (Pimbblet 2005).

Model fitting and mass determination reveals significant differences between weak lensing masses of the clusters and masses obtained with other methods. We discuss the possible sources of these discrepancies.

Additionally, we report the serendipitous weak lensing detection of galaxy cluster SE of A 222. The red sequence in a color-magnitude diagram suggests that this cluster is at a redshift of $z \sim 0.4$, but this estimate comes with a considerable uncertainty.

The work in this Chapter was published in Dietrich et al. (2005).

Chapter 5: XMM-Newton Follow-Up Survey

In the framework of ESO's public survey program the ESO Imaging Survey (EIS) team has conducted the XMM-Newton Follow-Up Survey (XFS). This public survey is complemented by a private extension. The optical survey with the ESO Wide-Field Imager (WFI) is conducted on deep public XMM-Newton fields. Chapter 5 describes the XFS, the optical and X-ray observations, the data reduction and calibration, quality control of the reduced data, and a cross-correlation of optical and X-ray catalogs.

Reduced and calibrated coadded images and single passband catalogs that are part of the public survey were released to the world-wide astronomical community. The core of this Chapter is the accompanying data release paper (Dietrich et al. 2006).

An important part of the quality checks performed on the WFI images reduced with the EIS/MVM pipeline (Vandame 2004) is the comparison to our independent reduction with the GABODS pipeline (Chap. 3). The results show very good agreement between the astrometric and photometric calibration of both pipelines. Remaining uncertainties in the photometric calibration of some frames could be traced to calibration data obtained under non-photometric conditions rather than problems in any of the pipelines.

In the cross-correlation of optical and X-ray catalogs about 61% of all X-ray sources have an optical counterpart. Out of these ~ 70% are detected in all four passbands of the XFS. This means that for ~ 300 X-ray sources photometric information is available from four passbands, therefore enabling a tentative classification and photometric redshift estimation. The vast majority of these sources is so faint that spectroscopic observations of them require the light gathering power of the VLT. Thus, a major goal of the public survey was met.

Chapter 6: Cluster Search in the XMM-Newton Follow-Up Survey

We conducted a search for galaxy clusters on the public and private parts of the XFS using three different techniques: optical matched filter, extended X-ray emission, and weak gravitational lensing.

We found a total of 158 cluster candidates on 23 WFI fields, or 25.8 cluster candidates per square degree. Most cluster candidates were found with the optical matched filter (116), followed by X-ray emission (66). 28 lensing detected peaks had matched filter or X-ray counterparts, or were previously reported in the literature. Out of these, 9 are previously known cluster (candidates). 7 of the weak lensing selected clusters were detected with the matched filter and X-ray emission; 4 of these are previously unknown cluster candidates.

We extensively tested the aperture mass method to select galaxy clusters by their gravitational shear with ray-tracing simulations. We find that – at least for the comparatively low number densities we are dealing with – the

dominant source of noise is the shape noise of the background population and not projections of the large-scale structure.

The number density of clusters found with the aperture mass is somewhat lower than expected from the ray-tracing simulations. However, the number density of faint background galaxies (FBG) in the XFS is lower than in the ray-tracing simulations. This may well account for the small difference but requires further investigation.

We compare the redshifts of clusters estimated with the matched filter algorithm to spectroscopic or photometric redshifts obtained with other methods. We find that these matched filter redshifts give a fair estimate for low to medium redshift cluster but show a significant towards lower redshifts for high redshift systems. This confirms earlier findings of Postman et al. (1996).

With the cluster sample presented in Chap. 6 we have built a solid foundation to study possible selection effects in either method. The work in this Chapter will be submitted for publication to Astronomy & Astrophysics. A detailed comparison of the cluster samples will be the subject of a follow-up paper (Dietrich et al., in preparation).

8

Outlook

This thesis touched on a large number and variety of topics. I will try to give a short overview of how the work and results presented here will be relevant for future work.

The GABODS pipeline has now been used for a number of publications (e.g., Dietrich et al. 2006; Hildebrandt et al. 2006; Bouy et al. 2006). It has proven to be an efficient tool for the data reduction of small and medium size projects and will certainly be used in a number of other projects, some of them already being conducted. For projects of the size of KIDS a pipeline with capabilities to organize the data and track the history of pipeline products is needed. This is something the GABODS pipeline does not provide. KIDS will be reduced with the AstroWise Environment (AWE) pipeline, which automatically keeps track of every frame and its history through a database. However, AWE is a fairly new system with relatively little testing and verification done so far. Existing pipelines like GABODS will play an important role in the science verification of the first reduced KIDS images.

Work on the GABODS pipeline is not finished. Adoption to more instruments and more extensive tests of data from other cameras than WFI should be done. A correction for the effect of varying zeropoints across the FOV ("illumination correction") is under development.

We plan to make a public data release of the public XFS fields not released by the EIS team, as well as of our private extension, once the still on-going observations are finished and the data products are verified.

Weak lensing filaments have proven to be extremely hard to be detected reliably. No study in this field has as of yet produced a definite detection of CDM filaments between two clusters of galaxies. The existing studies have been done with telescopes in the 2–4 m class. Wide-field cameras mounted on 8 m class telescopes might produce the number densities of

FBGs necessary for a $> 5\sigma$ detection of a mass bridge between two galaxy clusters. We are currently working on a study of the $z = 0.6$ double cluster system RX J1419.9+0634/1419.3+0638 observed with WFI, FORS, and XMM-Newton. More extended filaments in the field are so weak that they will require number densities only achievable from space. Until then, we can study filaments by other means. A few examples are given below.

Surprisingly few papers dealing with filaments are available in the literature. Only recently the interest in this subject started to surge (see, e.g., the review by Pimbblet 2005). We have successfully proposed multi-object spectroscopy with VIMOS of A 222/223 but the majority of the granted observing time was lost to bad weather and scheduling problems. The available data cover A 222 and part of the optical/X-ray filament candidate. A proposal for 130 ks X-ray spectroscopy of the filament candidate with RGS on-board XMM-Newton was accepted but only with low priority.

The XFS provides a wealth of information that awaits exploitation. The cluster catalogs presented in Chap. 6 will form the basis for detailed comparison of the properties of clusters selected with different methods. We have obtained observing time to spectroscopically confirm some of the cluster candidates detected in the XFS and have applied for more observing time for further spectroscopic confirmation.

The existing data set itself can be used to demonstrate that shear selected clusters can be used to constrain cosmological models. Due to the problems with efficiency and completeness in weak lensing cluster searches this must be done by comparing the observed number counts of weak lensing peaks against ray-tracing simulations for a number of cosmological models.

The part of the XFS that is covered with observations in BVRI can be used to test the proposed tomographic peak finder of HS05 that makes use of photometric redshifts. It is expected to somewhat reduce the problem of projections of the large-scale structure and at the same time give rough redshift estimates for shear selected cluster candidates.

Various optical selection methods can be tested on the multi-color data of the XFS. An overwhelming number of optical cluster selection methods is available and new ones seem to pop up constantly (e.g., Postman et al. 1996; Gladders & Yee 2000; Goto et al. 2002; Miller et al. 2005) but almost no comparison of their efficiency, completeness, and accuracy of redshift determination has been done.

A

Pipeline Data Format

Below is an example of a standardized FITS header generated by the GABODS pipeline in the first step of run-processing (see Chap. 3.3).

```
SIMPLE  =                     T  /
BITPIX  =                    16  /
NAXIS   =                     2  /
NAXIS1  =                  2142  /
NAXIS2  =                  4128  /
BSCALE  =                    1.  /
BZERO   =                32768.  /
CTYPE1  =            'RA---TAN'  /
CTYPE2  =            'DEC--TAN'  /
CRPIX1  =                -2552.  /
CRPIX2  =                 3893.  /
CD1_1   =             -6.61E-05  /
CD2_2   =              6.61E-05  /
CD1_2   =                    0.  /
CD2_1   =                    0.  /
CRVAL1  =             190.62779  /
CRVAL2  =              -0.64277  /
RADECSYS=                 'FK5'  /
FILTER  =    'BB#Rc/162_ESO844'  /
AIRMASS =              1.189382  /
EXPTIME =                 9.917  /
EQUINOX =                 2000.  /
IMAGEID =                     5  /
GABODSID=                  2351  /
```

```
EISID    =                        0   /
OBJECT   =                    'STD'   /
ZP       =                      -1.   /
COEFF    =                      -1.   /
DUMMY0   =                        0   /
DUMMY1   =                        0   /
DUMMY2   =                        0   /
DUMMY3   =                        0   /
         .
         .
         .
```

The IMAGEID, GABODSID, and EISID keyword are unique identifiers for the chip position within the mosaic, the night of the observation, and the image, respectively. The ZP and COEFF keywords are placeholdes for the zeropoint and extinction coefficient to be filled during the photometric calibration. At the end 20 DUMMY keywords are introduced which are partly used to hold information generated during the pipeline processing. The remaining DUMMY keywords can be used at the discretion of the pipeline user.

B

The Aperture Quadrupole Method

In analogy to the aperture mass (Chap. 2.4), Schneider & Bartelmann (1997) define the complex nth-order aperture multipole moment by

$$Q^{(n)}(\boldsymbol{\theta}_0) = \int_0^\infty \mathrm{d}^2\theta\,\theta^n\,U(|\boldsymbol{\theta}|)\,\mathrm{e}^{ni\varphi}\kappa(\boldsymbol{\theta}_0 + \boldsymbol{\theta})\,, \qquad \text{(B.1)}$$

with a radially symmetric weight function $U(|\boldsymbol{\theta}|)$. For $n = 2$ Eq. (B.1) expresses the aperture quadrupole moment in terms of the surface mass density. As for M_{ap} an expression for aperture moments in terms of the shear can be found,

$$
\begin{aligned}
Q^{(n)}(\boldsymbol{\theta}_0) = {} & \frac{1}{\bar{n}}\sum_{i=1}^N \mathrm{e}^{ni\varphi_i} \\
& \times \left\{ \vartheta_i^n U(\vartheta_i)\varepsilon_{ti} + i\frac{\vartheta_i^n\left[nU(\vartheta_i) + \vartheta U'(\vartheta_i)\right]}{n}\varepsilon_{\times i} \right\}\,, \quad n \neq 0\,, \quad \text{(B.2)}
\end{aligned}
$$

where $\bar{n}$ is the number density of galaxies in the aperture, (ϑ_i, φ_i) are the polar coordinates of the ith galaxy with respect to $\boldsymbol{\theta}_0$, and $\varepsilon_{ti} = -\mathfrak{R}(\varepsilon_i \mathrm{e}^{-2i\varphi_i})$ and $\varepsilon_{\times i} = -\mathfrak{I}(\varepsilon_i \mathrm{e}^{-2i\varphi_i})$ are the tangential and cross components of the shear estimate, respectively, with respect to $\boldsymbol{\theta}_0$. Here $U'(\vartheta)$ is the derivative of the weight function.

The weight function chosen in Chap. 4 is,

$$U(\vartheta) = \begin{cases} 1 - \left(\dfrac{\vartheta}{\vartheta_{\mathrm{max}}}\right)^2 & \vartheta \leq \vartheta_{\mathrm{max}}\,, \\ 0 & \text{otherwise}\,. \end{cases} \qquad \text{(B.3)}$$

While this weight function is clearly not ideal as it does not closely follow the expected mass profiles of a filament, it is sufficient to identify all relevant features in quadrupole moment maps.
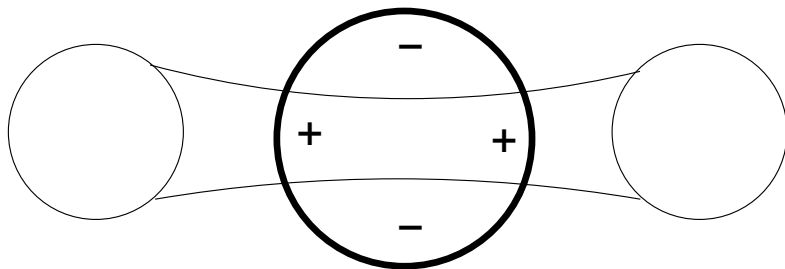
Figure B.1: Toy model of two galaxy clusters connected by a filament. The aperture (thick circle) placed on the filament illustrates why a quadrupole moment is expected in the filament region.

The complex aperture quadrupole moment gives strength and orientation of the quadrupole moment of the mass distribution inside the aperture. The quadrupole maps in Chap. 4 show only the absolute value $|Q^{(2)}|$.

Figure B.1 illustrates why an aperture quadrupole moment is expected on the filament between two galaxy clusters. Note, however, that a quadrupole signal would also be generated in the absence of filament if the aperture is sufficiently large compared to the clusters' separation. This is discussed in detail in Dietrich (2002) and Dietrich et al. (2005).

C

Public Follow-Up Survey

C.1 Field Description

Below a broad overview of the 12 public survey fields covered by the data release of Dietrich et al. (2006) is given. It includes a description of their nature and the original target of the X-ray observations. Details about the exposure time per camera per observation are given on the public data release web-page (see Chap. 5).

1. XMM-01/RX J0925.7−4758 – The original target was the ROSAT-discovered, galactic supersoft X-ray binary RX J0925.7−4758, also known as MR VEL (Motch et al. 1994). The X-ray image is a superposition of two medium deep (~ 60 ks) observations with EPIC-PN in large window, EPIC-MOS1 in full frame, and EPIC-MOS2 in small window mode. This results in a reasonably deep (~ 115 ks) exposure in the common PN and MOS area (less than half of the field of view).

2. XMM-02/RX J0720.4−3125 – Targeting the ROSAT-discovered isolated neutron star RX J0720.4−3125 (Haberl et al. 1997), the X-ray image is a superposition of three medium deep observations with all cameras in full frame. The bright target of the observation causes visible out-of-time events (OOT) in the X-ray images leading to bright stripes through the target. These stripes are fixed in detector coordinates, hence they do not coincide in sky coordinates resulting in three different OOT stripes.

3. XMM-03/HE 1104−1805 – The primary target of this XMM-Newton observation was the double lensed quasar HE 1104−1805 (Wisotzki

et al. 1993). This is an empty field at high galactic latitude. The X-ray image is a combined image of the three EPIC cameras during the single observation of the target. Bad space weather resulted in a loss of ∼ 65% of the total exposure and a rather shallow resulting image (∼ 10 ks).

4. XMM-04/MS 1054.4−0321 – The galaxy cluster MS 1054.4−0321 at redshift of $z = 0.83$ is the most distant cluster in the Einstein Medium Sensitive Survey and among the most massive ones (Gioia et al. 1990; Stocke et al. 1991; Gioia & Luppino 1994). The X-ray image is a combined image of the three EPIC cameras of the single observation of the target, all taken in full frame mode.

5. XMM-05/BPM 16274 – The white dwarf BPM 16274 is at high galactic latitude. This field is used for calibrations of the optical monitor onboard the XMM-Newton satellite. The X-ray image is a superposition of six observations in full frame mode of all three cameras. The archive contains already many more data sets with other camera settings and the observations in this field are on-going.

6. XMM-06/RX J0505.3−2849 – This is a field at high galactic latitude. The galaxy cluster RX J0505.3−2849 in the center was detected as part of the SHARC survey (Burke et al. 2003) at a redshift of $z = 0.509$. The X-ray image is the superposition of all three EPIC cameras, which were all operated in full frame mode. Only the PN suffered significantly from high background, resulting in a medium deep X-ray image (∼ 45 ks).

7. XMM-07/LBQS 2212−1759 – In order to avoid potential damage from the Leonid meteors when XMM-Newton intersects their trajectories annually, the spacecraft is oriented in the anti-Leonid direction for safety reasons. The field then repeatedly chosen for observation was centered on the $z = 2.217$ quasar LBQS 2212−1759 (Barkhouse & Hall 2001). The X-ray image is a superposition of five observations with all cameras in full frame mode. Enhanced background affected less than 15% of the observations resulting in a truly deep field with more than 200 ks net exposure in all three cameras. The nominal target of the observations was not discovered, the image is thus dominated by the

serendipitous source content. The most prominent source is a new cluster of galaxies close to the center of the field.

8. XMM-08/NGC 4666 – The target of this field was the almost edge-on spiral galaxy NGC 4666 which dominates the center of the field. Although the target was optically and X-ray extended, the target was included in the public survey since the target blocks only about 5% of the field of view. The X-ray image is a combined image of the three EPIC cameras of the single observation of the target, all taken in full frame mode.

9. XMM-09/QSO B1246−057 – The target was the broad absorption line quasar B1246−057. The XMM-Newton observation of the target was published by Grupe et al. (2003). The X-ray image is a combined image of the three EPIC cameras of the single observation of the target, all taken in full frame mode. The field is unusual, about one quarter of the field in the NE corner is almost devoid of X-ray sources. The dominant point-like object is the X-ray counterpart of the Algol binary HD 111487 (RBS 1165).

10. XMM-10/PB 5062 – PB 5062 (also known as QSO B2202−0209) is a quasar at redshift $z = 1.77$ (Yuan et al. 1998). The X-ray image is a combined image of the three EPIC cameras of the single observation of the target, all taken in full frame mode.

11. XMM-11/Sgr A – The target of this field is the center of our Milky Way. The X-ray image is a superposition of five observations with all cameras in full frame mode. The observations were severely affected by background flares resulting in a loss of more than 50% of the observation time. Nevertheless, repeated observations of the field resulted in a medium deep exposure with more than 40 ks exposure in all three cameras. The image is dominated by diffuse emission from the galactic center region. In addition there are two classes of point-sources, heavily absorbed, i.e., likely background sources with hard X-ray spectra and foreground sources with soft X-ray spectra.

12. XMM-12/WR 46 – This object, also known as HD 104994, is a Wolf-Rayet star. The X-ray image is a combined image of the three EPIC cameras

of the single observation of the target, all taken in full frame mode. Data loss due to enhanced background is insignificant resulting in a medium deep field with more than 70 ks exposure in each camera.

C.2 X-ray Observations

Table C.1 gives a summary of the EPIC X-ray observations contributing to the XFS. The table gives for each field: in Col. 1 the field name; in Col. 2 the XMM-Newton observation ID; in Col. 3 the nominal exposure time in seconds; in Col 4–6 the settings for each of the cameras. Here (E)FF indicates (extended) full frame readout, LW large window mode and SW small window mode. These cameras and their settings are described in detail in Ehle et al. (2004). For some fields additional observations were available but these were discarded mainly due to unsuitable camera settings.

"FIELD 864" is a mosaic of 3×3 XMM-Newton observations. The name was assigned by the principal investigator. FIELD 864-6 is not part of the optical survey but the X-ray observations overlaps the WFI observations of FIELD 864-9.

Table C.1: Information about X-ray imaging in the XFS. The Table lists in Col. 1 the field name; in Col. 2 the XMM-Newton observation ID; in Col. 3 the nominal exposure time; and in Cols. 4–6 the EPIC camera settings.

Field	Obs. ID	T_{exp}/s	Camera settings		
BPM 16274	0125320401	33728	EPN EFF	MOS1 FF	MOS2 FF
	0125320501	7845	EPN FF	MOS1 FF	MOS2 FF
	0133120301	12022	EPN FF	MOS1 FF	MOS2 FF
	0133120401	13707	EPN FF	MOS1 FF	MOS2 FF
	0125320701	45951	EPN FF	MOS1 FF	MOS2 FF
	0153950101	5156	EPN FF	MOS1 FF	MOS2 FF
CFRS-3h	0041170101	51724	EPN EFF	MOS1 FF	MOS2 FF
RX J0505.3−2849	0111160201	49616	EPN EFF	MOS1 FF	MOS2 FF
RX J0720.4−3125	0164560501	50059	EPN FF	MOS1 FF	MOS2 FF
	0156960201	30243	EPN FF	MOS1 FF	MOS2 FF
	0156960401	32039	EPN FF	MOS1 FF	MOS2 FF
RX J0925.7−4758	0111150201	62067	EPN LW	MOS1 FF	MOS2 SW2
	0111150101	61467	EPN LW	MOS1 FF	MOS2 SW2
RBS 0864	0108670101	56459	EPN FF	MOS1 FF	MOS2 FF
QSO B0130−403	0112630201	37870	EPN FF	MOS1 FF	MOS2 FF
BR 1033−0327	0150870401	31418	EPN FF	MOS1 FF	MOS2 FF
SDSS J104433.04−012502.2	0125300101	62310	EPN FF	MOS1 FF	MOS2 FF
MS1054.4−0321	0094800101	41021	EPN FF	MOS1 FF	MOS2 FF
HE 1104−1805	0112630101	36428	EPN FF	MOS1 FF	MOS2 FF

Continued on next page

Table C.1 – *continued from previous page*

Field	Obs. ID	T_{exp}/s	Camera settings		
PG 1115+080	0082340101	63358	EPN FF	MOS1 FF	MOS2 FF
	0203560201	86649	EPN FF	MOS1 FF	MOS2 FF
	0203560401	86515	EPN FF	MOS1 FF	MOS2 FF
CD −33 07795	0112880101	29921	EPN FF	MOS1 FF	MOS2 FF
T Leo	0111970701	12866	EPN FF	MOS1 SW3	MOS2 SW2
WR 46	0109110101	76625	EPN EFF	MOS1 FF	MOS2 FF
IRAS 12112+0305	0081340801	23206	EPN FF	MOS1 FF	MOS2 FF
LBQS 1228+1116	0145800101	107002	EPN FF	MOS1 FF	MOS2 FF
NGC 4666	0110980201	58237	EPN EFF	MOS1 FF	MOS2 FF
QSO B1246−057	0060370201	41273	EPN FF	MOS1 FF	MOS2 FF
FIELD 864-1	0111281001	10377	EPN EFF	MOS1 FF	MOS2 FF
FIELD 864-9	0111281801	8315	—	MOS1 FF	MOS2 FF
	0111282501	8623	EPN EFF	MOS1 FF	MOS2 FF
FIELD 864-6	0111281501	8650	EPN EFF	MOS1 FF	MOS2 FF
A 1882	0145480101	23567	EPN FF	MOS1 FF	MOS2 FF
MKW 9	0091140401	45414	EPN EFF	MOS1 FF	MOS2 FF
PB 5062	0012440301	35366	EPN FF	MOS1 FF	MOS2 FF

Table C.1 – *continued from previous page*

Field	Obs. ID	T_{exp}/s	Camera settings		
LBQS 2212−1759	0106660501	11568	EPN FF	MOS1 FF	MOS2 FF
	0106660401	35114	—	MOS1 FF	MOS2 FF
	0106660101	60508	EPN FF	MOS1 FF	MOS2 FF
	0106660201	53769	EPN FF	MOS1 FF	MOS2 FF
	0106660601	110168	EPN FF	MOS1 FF	MOS2 FF
NGC 7252	0049340201	28359	EPN FF	MOS1 FF	MOS2 FF
PHL 5200	0100440101	46681	EPN FF	MOS1 FF	MOS2 FF

C.3 Photometry

The photometric calibration is done in a fully automated way by the EIS Data Reduction System (da Costa et al., in preparation) calibrating all data to the Vega magnitude system. The photometric pipeline extracts catalogs from the standard star fields, and measures fluxes at different apertures to allow for a growth curve inspection. The positions and flux measurements for each object are cross-correlated with those corresponding to known standard stars as stored in a database. The matched standard stars are then used to determine the photometric zeropoint, extinction and color term from a linear fit. Finally, the zeropoint for each science frame is derived from standard star observations obtained in the same night.

Calibrations for the public EIS data release have been based on observations of Landolt (1992) standard star fields. The magnitudes were measured in $6''$ apertures, which from monitoring the growth curve of all measured stars proved to be adequate. The linear fits had from one to three free parameters depending on the available airmass and color coverage provided by the calibration plan. In cases where the airmass and/or color coverage is insufficient, pre-specified values for the extinction and color term, either determined from other solutions or from theoretical models, are used.

The photometric pipeline computes photometric parameters for all possible types of fits (one to three free parameters) and chooses the solution with the smallest rms to be the *best solution* for the night. A night is considered photometric if this scatter is less than a pre-defined value, which at the present time is taken to be 0.1 mag. If none of the solutions satisfies this criterion and/or the solution found yields unrealistic results (e.g. negative extinction) then the night is considered non-photometric and a default value for the zeropoint is adopted and its error set to -1. For nights without observation of standard star fields, a default zeropoint and an error of -2 are assigned to the image. Finally, during quality assessment of the data, calibrated images with zeropoints that deviate significantly from a reference value have the zeropoint in the header changed to a default value and its error set to -3. When a default value is assigned all images will have the same zeropoint in the header regardless of the airmass at which they were observed. For homogeneity, the default value normally adopted is the median of the zeropoints reported in the trend analysis kept by either the

telescope team (depending on the instrument) or the internal EIS database. In the case of WFI, only one solution is currently reported on the WFI WWW pages.[1]

The derived photometric solutions were used to calibrate the reduced images. The zeropoint in the header of a reduced image is given by

$$ZP = ZP' - kX \tag{C.1}$$

where ZP' is the zeropoint at zero airmass (determined from the linear fit as described above), k is the extinction coefficient and X is the airmass at which the frame was observed. Using this definition the Vega magnitude can computed by

$$m_{\text{Vega}} = -2.5\log(f) + ZP \tag{C.2}$$

where f is the flux in number of counts directly measurable on the image (note that the reduced images are normalized to 1 s).

C.4 Image stacks

Most fields are covered by more than one reduced image. These are coadded to create the final image product. The following steps are involved in the creation of a final stacked image:

– Grouping: reduced images are grouped into *stacking blocks* (SBs) according to position (with a minimum distance between centers of 0.25 times the field-of-view), and filter.

– Validation: as the coaddition is carried out in pixel space it is required that all images have been warped to the same reference grid. Therefore, images in a SB must share the same reference grid (projection, reference position, pixel scale and orientation). In addition, the images contributing to an SB, or their original RBs, are checked to ensure that they appear only once in the SB. Images in the SB are also checked to ensure that their flux scale has been properly normalized to 1 s, and if not they are re-normalized accordingly.

[1] http://www.ls.eso.org/lasilla/sciops/2p2/E2p2M/WFI/zeropoints/

- – Constraints: images in an SB are checked to ensure that they meet certain constraints, for instance on the value of seeing, the rms of the PSF distortion and grade. In principle a raw exposure may be part of more than one RB. The contributing images to an SB, or their original RBs, are checked to prevent the repetition of raw exposures. Images not satisfying the constraints are discarded from the SB.

- – PSF homogenization: all images in the SB are convolved by a Gaussian with a FWHM corresponding to the largest seeing value computed for the contributing images.

- – Flux scale determination: before the images can be coadded, which is done using a weighted mean procedure, it is necessary to have all images at the same flux level. This is done by scaling photometric frames to zero airmass using the extinction coefficients from the photometric solutions. The non-photometric frames are scaled to the zero airmass level of the photometric frames (see below)

- – Coaddition: images in a validated SB are coadded using a weighted mean. The weight images reflect the exposure times of their associated science image. Therefore, the weight of each image is a combination of exposure time and noise. However, the weight images also contain information about the location of bad pixels and masks which are set to zero weight and thus do not contribute to the final image. In the coaddition process, performed by the routine add-mosaic of the EIS/MVM library, a sigma-clipping procedure is employed to remove cosmic ray hits.

The image coaddition uses a weighted mean combination. The weighting is done with the weight images produced by the image reduction. Additionally, a thresholding procedure is employed to remove cosmic rays if at least 5 images are coadded. In general, the use of weight maps and cosmic ray hits removal produces very clean final images.

As mentioned above, all images in an SB have to be scaled to a common flux level before the coaddition to assure the photometric calibration of the final, stacked image. For this rescaling, one has to consider two cases:

1. *SB with at least one photometric frame* – In this case the reference flux level is obtained from the combination of all contributing photometric frames. First, all photometrically calibrated frames are scaled to the flux level that would have been obtained at zero airmass. This is done using the extinction coefficients of their respective photometric solutions. Second, by computing a weighted average of all scaled images a reference image is created. For the final coaddition all input images (photometric and non-photometric) are scaled to the flux level of the reference image. The scaling factors are determined by comparing object magnitudes. Naturally, in cases where only one photometric frame is available, this one is used as the reference.

2. *SB with no photometric frames* – Occasionally, none of the reduced images in an SB are photometrically calibrated (e.g., no standards were observed in the night, observations in non-photometric nights). In such cases, all images are scaled to the flux level of an arbitrarily chosen reference image from the SB. The zeropoint of the final stacked image is then the zeropoint of the adopted reference image. The zeropoint of the output image is that of the arbitrarily chosen reference. These frames can be identified by the negative zeropoint error assigned to these cases, as described above.

C.5 Catalog production

The final processing step in the EIS Data Reduction system is the creation of source catalogs by standardized procedures, resulting in catalogs containing enough information to be directly usable for scientific applications. Here the production of catalogs for deep, sparse fields is discussed. The production of catalogs for crowded fields, which are not included in the public data release of Dietrich et al. (2006), will be described in Zaggia et al. (in preparation).

The EIS catalog production is based on `SExtractor` and a common configuration file for all catalogs with a minimum number of adjustments to be made for individual images. For each image the appropriate values for the seeing and magnitude zeropoints as well as the weight-map associated to each image are used. Other parameters are the same for all catalogs.

The catalog production starts with a very low SNR catalog, which contains a large number of spurious objects. To produce a science-grade catalog a number of steps are taken. First, the catalog is pruned of objects with a SNR (determined from the `MAGERR_AUTO`) below a user-defined level, which was set to 5 for the public data release of the XFS. The object magnitudes are converted to the AB system according to the response function of the optical system and corrected for galactic extinction. At present, this correction is applied to the magnitudes of all objects, including stars. To facilitate the use of the catalogs 14 flags are added for each object as described below.

The saturation level of the final image stack is difficult to determine from the input images due to variations in integration time and possibly seeing. Therefore, the saturation level is determined from the extracted catalog. The method is based on the FWHM and peak flux of bright objects. The distribution of the FWHM is determined and sigma-clipped to exclude bright galaxies from the sample. Among the remaining objects those with FWHM deviating more than 3σ are taken to be the saturated objects. The saturation level is set to the minimum peak value among these objects. This value is used to set the saturation flag.

To be able to remove objects close to bright stars masks can be created in two ways: by an automatic routine or by hand using a Skycat plug-in. The automatic masking adds masks around saturated objects as well as around objects brighter than a user-specified magnitude. The size of the mask scales with the major-axis of the object, as computed by `SExtractor`. The scaling factor is specified by the user. The adopted shape of the masks is a square with one of the diagonals oriented north-south in an attempt to mask the diffraction spikes. The parameters used in the mask definition are reported in the product log. The positions of all masks are reported in the `MASKS` table in the catalog.

Note that except for objects with SNR less than that required, no object is removed from the catalog. If necessary, more objects can be pruned by the user according to the flags described below. In addition, the default magnitude system adopted for the objects can be changed using the information available in the `FIELDS` table.

The catalogs produced by the EIS Data Reduction system are in FITS format, based on the "Leiden Data Analysis Center" (LDAC) convention originally adopted by the DENIS project and later expanded in the course

of the EIS project. The FITS catalog file in its current form contains the following tables: FIELDS, OBJECTS, MASK, and FILTER.

The FIELDS table contains general information for all objects in the catalogs. It consists of 109 columns including: (1) basic information set by the LDAC library; (2) keywords taken from the FITS header of the image from which the catalog was extracted; (3) the main SExtractor configuration parameters used; and (4) information computed by the EIS Data Reduction system. The latter includes, for instance:

- the diameter of the 10 apertures used for aperture magnitudes, ranging from $1''$ to $5''$ in steps of $0''\!.5$ and a large aperture of $10''$;

- the WCS coordinates of the corners of the original image and of the trimmed area, i.e., the area in which the weight exceeds a minimum value;

- the extinction correction. This is computed as the average of the value of the extinction in cells of $3' \times 3'$, distributed over the trimmed image;

- the value added to the original magnitude of the extracted objects in the Vega system to produce the reported magnitudes in the catalog in the AB system;

- an estimate of the fudge factor used to multiply the errors reported by SExtractor to correct for the correlated noise introduced by the re-sampling kernel;

- total and trimmed areas.

Some of the information contained in the FIELDS table is also available in the *Product Logs* which are available on the EIS XMM-Newton follow-up survey release pages.

The OBJECTS table reports the parameters characterizing the individual extracted objects as computed by SExtractor. It has 69 columns, some being vectors (e.g. aperture magnitudes), describing the main geometric and photometric properties of the objects. The parameters were chosen as a compromise between the total number of parameters and the most frequently requested parameters from survey product users. The choice

of apertures and the flags defined are the result of suggestions made by users of EIS data products. In addition to the SExtractor flag, which are described in the SExtractor manual, 14 other flags have been defined to facilitate the filtering of the catalogs. These are

- FLAG_SEX1–FLAG_SEX128 – 8 flags individually representing the various SExtractor flag components;

- FLAG_SAT – set to 1 if the object is saturated;

- FLAG_TRIM – set to 1 if the object is inside a trimmed area;

- FLAG_MASK – set to 1 if the object is inside a masked area;

- EISFLAG – sum of FLAG_TRIM and FLAG_MASK

- FLAG_STATE – 1 if any of the above flags are set

- FLAG_STAR – 1 if star, 0 if galaxy, based on the SExtractor stellarity parameter CLASS_STAR. The value used for separation and the magnitude down to which a classification was attempted are reported in the product log.

The MASK table gives the number and coordinates of the vertices of both automatically created masks as well as those drawn by hand using a Skycat plug-in.

The FILTER table gives the filter transmission curve and their convolution with the optical system response function.

D

Cluster Catalogs

This appendix lists the cluster catalogs derived from X-ray, optical, and weak lensing analyses of the xfs. Their production is described in detail in Chap. 6.

D.1 X-ray Cluster Catalog

The following table provides the catalog of extended X-ray sources described in Chap. 6.1.2. The table lists in Col. 1 a sequential number of the X-ray selected cluster candidate. Column 2 gives the blox name of the cluster candidate. Note that in some cases slight offsets between the X-ray position and the matched filter position (Table D.2) might in principle give raise to different names. In these cases the blox name was determined from the position that was deemed to be the most reliable one after visual inspection of the data. These cases are indicated in the table notes (Col. 11). The cluster position in right ascension and declination is given in Col. 3 and 4. The detection and extent likelihood as determined by `emldetect` are listed in Col. 5 and 6, respectively. Column 7 gives the extent of the source in Xmm-Newton pixels. The total count rate of all three cameras and five energy bands is listed in Col. 8. Cross-references to the sequence numbers of matched filter (Table D.2) and weak lensing (Table D.3) detected cluster candidates are provided in Col. 9 and 10, respectively. References to additional notes at the bottom of the table are provided by Col. 11. Grades based on visual inspection of the X-ray and optical data were assigned to the cluster detections and are listed in Col. 12. See Chap. 6.1.2 for an explanation of how the grades were assigned.

Table D.1: This table lists clusters detected in the xrs as extended X-ray sources. Column 1 gives a sequential number to the galaxy cluster candidates found in X-ray observations. The name of the cluster candidates is given in Col. 2. The position of the extended X-ray source is given in Col. 3 and 4. The detection and extension likelihood are given in Col. 5 and 6, respectively. The extent measured in XMM-Newton pixels is given in Col. 7. The total count rate of all cameras and channels is given in Col. 8. Columns 9 and 10 provide cross-references to the sequence numbers of Table D.2 (optical matched filter detected clusters) and Table D.3 (weak lensing detected clusters). Column 11 provides references to additional remarks at the bottom of the table. Finally, Col. 12 lists grades assigned to cluster candidates based on visual inspection of the optical and X-ray data.

Seq. Nr.	Cluster	α (J2000.0)	δ (J2000.0)	detml	extml	ext (pix)	rate (10^{-2}/s)	MF	M_{ap}	Notes	Grade
					BPM 16274						
1	BLOX J0048.7−5214	00:48:42.1	−52:14:26	14.6	7.1	11.1	12.6 ± 2.9	—	—	—	−
2	BLOX J0050.8−5213	00:50:51.8	−52:13:25	32.4	20.3	5.9	2.6 ± 0.4	4	—	—	+
					CFRS-3h						
3	BLOX J0302.0−0000	03:02:05.6	−00:00:05	114.7	63.5	7.0	4.9 ± 0.5	9	—	1	+
4	BLOX J0302.2−0001	03:02:12.1	−00:01:33	72.2	25.5	3.2	1.7 ± 0.2	—	—	—	○
5	BLOX J0302.2+0006	03:02:13.2	+00:06:01	25.6	4.2	2.4	0.5 ± 0.1	—	—	—	○
6	BLOX J0302.9+0019	03:02:55.9	+00:19:27	12.9	4.7	2.0	1.4 ± 0.3	—	—	—	−
					RX J0505.3−2849						
7	BLOX J0504.6−2853	05:04:41.0	−28:53:45	15.4	10.3	11.5	4.8 ± 1.3	—	—	—	−
8	BLOX J0505.0−2846	05:05:04.0	−28:46:53	15.2	4.7	2.4	0.9 ± 0.2	—	—	—	+
9	BLOX J0505.3−2849	05:05:19.4	−28:48:52	935.2	447.8	5.3	8.2 ± 0.3	14	4	2,3	+
10	BLOX J0506.0−2840	05:06:04.3	−28:40:42	30.3	18.6	11.0	5.7 ± 1.1	16	—	1,4	+
12	BLOX J0506.1−2842	05:06:07.6	−28:42:45	36.9	6.4	5.7	3.1 ± 0.5	—	5	5	+

Table D.1 – continued from previous page

Seq. Nr.	Cluster	α (J2000.0)	δ (J2000.0)	detml	extml	ext	rate	MF	M_{ap}	Notes	Grade
13	BLOX J1023.6+0411	10:23:39.7	+04:11:11	10^6	10^5	3.5	786.9 ± 1.5	18	6	6	+
14	BLOX J1024.0+0402	10:24:00.5	+04:02:23	87.4	54.8	5.0	2.2 ± 0.2	20	—	—	+
	RBS 0864										
	QSO B1030−403										
15	BLOX J0132.6−4011	01:32:39.8	−40:11:08	27.7	5.8	4.1	2.2 ± 0.4	—	—	—	−
16	BLOX J0133.3−4019	01:33:20.1	−40:19:23	32.2	6.8	1.7	3.4 ± 0.6	—	—	—	−
	BR 1033−403										
17	BLOX J1035.9−0331	10:35:54.2	−03:31:58	71.1	31.6	5.0	4.0 ± 0.5	26	8	1	+
18	BLOX J1036.6−0333	10:36:36.1	−03:33:01	34.2	12.1	3.4	1.5 ± 0.3	—	—	—	+
	SDSS J104433.04−012502.2										
19	BLOX J1044.7−0120	10:44:43.3	−01:19:50	34.9	14.5	3.4	0.7 ± 0.1	30	—	2	+
20	BLOX J1044.9−0131	10:44:56.1	−01:31:29	60.9	15.2	2.3	0.8 ± 0.1	—	9,10	—	−
	MS 1054.3−0321										
21	BLOX J1056.4−0335	10:56:25.1	−03:35:05	162.2	79.6	4.5	6.2 ± 0.5	39	12	—	+
22	BLOX J1056.9−0337	10:56:58.3	−03:37:33	6778.5	2850.5	8.0	50.6 ± 0.8	40	13	7,8	+
23	BLOX J1056.9−0337	10:57:01.0	−03:37:34	357.7	188.3	4.4	9.9 ± 0.4	40	13	7,8	+
	PG 1115+080										
24	BLOX J1117.4+0743	11:17:25.8	+07:43:38	1229.3	530.3	5.2	8.4 ± 0.3	53	—	9	+
25	BLOX J1117.4+0746	11:17:30.0	+07:46:23	289.1	155.7	4.5	3.0 ± 0.2	—	—	—	+
26	BLOX J1117.6+0742	11:17:41.8	+07:42:03	20.5	8.2	2.5	0.4 ± 0.1	—	—	—	+
27	BLOX J1118.2+0743	11:18:16.2	+07:43:36	26.6	21.8	5.8	0.6 ± 0.1	55	15	10	+
28	BLOX J1118.3+0747	11:18:23.6	+07:47:12	35.2	24.9	5.5	0.6 ± 0.1	—	—	—	−
29	BLOX J1118.5+0744	11:18:34.7	+07:44:35	280.2	102.8	3.3	1.2 ± 0.1	55	—	—	+

Table D.1 – *continued from previous page*

Seq. Nr.	Cluster	α (J2000.0)	δ (J2000.0)	detml	extml	ext	rate	MF	M_{ap}	Notes	Grade
30	BLOX J1118.8+0735	11:18:48.1	+07:35:22	15.0	6.1	3.4	1.1 ± 0.2	—	—	—	−
31	BLOX J1119.2+0743	11:19:14.2	+07:43:22	141.9	103.0	15.4	18.2 ± 1.5	—	—	—	−
	CD −33 07795										
32	BLOX J1132.4−3434	11:32:27.5	−34:34:04	46.0	13.2	2.6	1.5 ± 0.2	—	—	—	○
33	BLOX J1132.5−3443	11:32:32.0	−34:43:48	606.3	320.6	6.5	11.4 ± 0.6	59	16	—	+
	T LEO										
34	BLOX J1138.0+0315	11:38:04.4	+03:15:23	51.5	18.0	4.0	4.9 ± 0.6	61	—	1	+
35	BLOX J1138.7+0315	11:38:43.9	+03:15:38	514.3	193.0	6.2	21.6 ± 1.2	—	—	11	+
	IRAS 12112+0305										
36	BLOX J1213.0+0258	12:13:04.3	+02:58:17	14.1	4.1	2.2	2.7 ± 0.5	—	—	—	−
37	BLOX J1213.5+0253	12:13:34.6	+02:53:47	1640.5	999.2	8.3	25.8 ± 0.8	65	17	12	+
	NGC 4666										
38	BLOX J1244.8−0019	12:44:48.7	−00:19:48	61.2	23.7	3.2	1.3 ± 0.2	—	—	—	○
39	BLOX J1244.8−0033	12:44:51.3	−00:33:30	200.1	166.3	10.1	5.6 ± 0.4	—	19	13, 14	+
40	BLOX J1244.9−0026	12:44:54.2	−00:26:39	213.9	118.7	7.6	4.0 ± 0.3	—	—	15	+
41	BLOX J1244.9−0033	12:44:55.1	−00:33:35	81.3	58.3	6.4	2.8 ± 0.3	—	19	13, 14	+
42	BLOX J1245.7−0030	12:45:45.8	−00:30:20	37.0	8.1	2.4	1.2 ± 0.2	—	—	—	−
	QSO B1246−057										
43	BLOX J1249.3−0610	12:49:19.7	−06:10:40	24.7	6.7	1.9	1.7 ± 0.3	—	—	—	○
44	BLOX J1249.4−0600	12:49:28.5	−06:00:04	89.0	59.3	7.0	4.6 ± 0.5	80	20	—	+
	FIELD 864-1										
45	BLOX J1341.6+0018	13:41:38.6	+00:17:19	117.4	82.9	10.8	15.5 ± 1.4	84	—	2, 16,17	+
46	BLOX J1341.6+0018	13:41:41.2	+00:18:36	9.9	7.6	5.2	3.1 ± 0.6	84	—	16,17	+

Continued on next page

Table D.1 – *continued from previous page*

Seq. Nr.	Cluster	α (J2000.0)	δ (J2000.0)	detml	extml	ext	rate	MF	M_{ap}	Notes	Grade
			FIELD 864-9								
47	BLOX J1345.2−0008	13:45:14.6	−00:08:42	16.6	4.8	3.5	6.3 ± 1.2	—	—	18, 19	+
			A 1882								
48	BLOX J1414.1−0016	14:14:08.8	−00:16:19	69.7	31.5	6.2	6.9 ± 0.8	92	24	20	+
49	BLOX J1414.8−0017	14:14:51.8	−00:17:34	25.3	14.1	4.4	1.6 ± 0.3	—	—	21	+
50	BLOX J1414.8−0037	14:14:52.7	−00:37:54	30.7	5.9	1.7	3.3 ± 0.5	—	—	—	○
			MKW 9								
51	BLOX J1531.8+0443	15:31:48.4	+04:43:20	49.5	11.2	2.3	2.3 ± 0.3	—	27	—	○
52	BLOX J1532.5+0440	15:32:31.9	+04:40:54	10^5	6163.1	9.4	100.4 ± 1.1	—	—	22	+
			LBQS 2212−1759								
53	BLOX J2214.7−1753	22:14:47.6	−17:53:25	77.5	6.6	2.6	0.7 ± 0.1	—	—	—	−
54	BLOX J2215.0−1750	22:15:00.8	−17:50:34	88.1	48.8	7.2	1.6 ± 0.2	102	—	1	+
55	BLOX J2215.0−1752	22:15:03.6	−17:52:12	23.6	14.3	7.3	1.0 ± 0.2	—	—	—	+
56	BLOX J2215.1−1747	22:15:07.5	−17:47:06	48.3	27.5	8.9	1.4 ± 0.2	—	—	—	−
57	BLOX J2215.6−1745	22:15:36.9	−17:45:33	2614.2	816.1	4.4	5.4 ± 0.1	103	—	—	+
58	BLOX J2215.8−1739	22:15:48.6	−17:39:51	20.3	6.5	5.5	0.8 ± 0.1	—	—	—	−
59	BLOX J2215.9−1751	22:15:56.9	−17:51:37	98.4	46.7	3.7	1.0 ± 0.1	—	—	—	○
60	BLOX J2215.9−1740	22:15:57.7	−17:40:28	210.9	104.6	4.3	1.6 ± 0.1	—	—	—	○
61	BLOX J2215.9−1738	22:15:58.7	−17:38:09	882.1	276.9	3.2	3.1 ± 0.1	—	—	23	+
62	BLOX J2216.1−1739	22:16:07.7	−17:39:23	67.3	34.8	10.0	1.9 ± 0.3	—	—	—	−
63	BLOX J2216.3−1736	22:16:20.8	−17:36:22	44.4	18.5	11.2	3.1 ± 0.6	—	—	—	−
64	BLOX J2216.3−1732	22:16:21.2	−17:32:31	31.7	11.5	3.0	0.7 ± 0.1	—	—	—	−

Continued on next page

Table D.1 – *continued from previous page*

Seq. Nr.	Cluster	α (J2000.0)	δ (J2000.0)	detml	extml	ext	rate	MF	M_{ap}	Notes	Grade
				PHL 5200							
65	BLOX J2228.3−0507	22:28:18.6	−05:07:49	42.3	7.0	2.2	0.9 ± 0.2	113	—	1	+
66	BLOX J2228.3−0520	22:28:22.5	−05:20:31	653.2	231.7	4.6	5.9 ± 0.3	114	—	—	+

[1] Name of this cluster based on the X-ray position, [2] Name of this cluster based on matched filter position, [3] This is RX J0505.3−2849 at $z = 0.509$ of Burke et al. (2003), [4] This is RX J0505.9−2841 of Vikhlinin et al. (1998); Mullis et al. (2003) at $z = 0.136$, [5] Probably part of BLOX J0506.0−2840, [6] This is cluster RBS 0864 of Allen et al. (1992), [7] This is cluster MS 1054.3−0321 of Gioia et al. (1990); Gioia & Luppino (1994), [8] Cluster 22 and 23 are the same object, [9] This is RX J1117.4+0743 of Vikhlinin et al. (1998), [10] The matched filter detected cluster BLOX J1118.3+0743 is probably merged by detection of X-ray clusters 27 and 29, [11] This is RX J1138.7+0315 (Vikhlinin et al. 1998) at $z = 0.127$ (Mullis et al. 2003), [12] This is cluster RX J1213.5+0253 at $z = 0.409$ of Vikhlinin et al. (1998); Mullis et al. (2003), [13] Cluster 39 and 41 are the same object, [14] This is SDSS CE J191.220871−00.560489 at $z = 0.231$ of Goto et al. (2002), [15] This is SDSS CE J191.220749−00.444507 at $z = 0.220$ of Goto et al. (2002), [16] Cluster 45 and 46 are the same object, [17] This cluster is SDSS CE J205.412231+00.303271 at $z = 0.390$ of Goto et al. (2002), [18] Found on X-ray observations of neighboring FIELD 864-6, [19] This is XMM2DF J134511.9−000953 at $z = 0.12$ of Basilakos et al. (2004), [20] This is SDSS CE J213.532593−00.276487 at $z = 0.152$ of Goto et al. (2002), [21] Possibly associated with A 1882, [22] This is MKW 9 at $z = 0.040$, [23] This is a high redshift cluster at $z = 1.45$ (Stanford, private communication),

D.2 Optical Matched Filter Catalog

The following table provides the optical matched filter catalog generated with the P96 algorithm from the R-band data of the XFS. The table lists in Col. 1 a sequential numbering of the cluster candidates, and in Col. 2 their names within the XFS. The positions of the matched filter selected candidate clusters in right ascension and declination are given in Col. 3 and 4, respectively. The maximum detection significance over all redshift slices is listed in Col. 5. The redshift and richness parameter estimated from the matched filter pipeline output are given in the next two columns. Columns 8 and 9 provide cross-references to the sequence numbers of X-ray (Table D.1) and weak lensing (Table D.3) detected cluster. If the cluster was previously detected either as cluster or candidate cluster, the best redshift estimate from the literature is provided in Col. 10. Column 11 gives references to additional notes at the end of the table. Finally, Col. 12 contains a grade to indicate the quality of the cluster detection based on visual inspection. See Sect. 6.2.4 for an explanation of how the grades were assigned.

Table D.2: The table lists cluster candidates detected in the XFS using the optical matched filter method. Column 1 gives a sequential number to the galaxy cluster candidates, their name in the XFS is given in Col. 2. The position of the matched filter peak in right ascension and declination is listed in Col. 3 and 4, respectively. Note that the name in Col. 2 may be based on other position estimators like X-ray. The maximum detection significance over all redshift slices is given in Col. 5., the redshift and richness parameters estimated from the matched filter algorithm Col. 6 and 7, respectively. The next two columns provide cross-references to the sequence numbers of Table D.1 (X-ray detected clusters) and Table D.3 (weak lensing detected clusters). In case the cluster candidate was previously identified as such or confirmed as cluster, Col. 10 gives the best redshift estimate from the literature. Column 11 provides references to additional remarks. Finally, Col. 12 lists grades assigned to the cluster candidates based on visual inspection.

Seq. Nr.	Cluster	α (J2000.0)	δ (J2000.0)	σ_{max}	z_{est}	Λ_{cl}	X-ray	M_{ap}	z_{lit}	Notes	Grade
			BPM 16274								
1	BLOX J0048.3−5156	00:48:20.3	−51:56:14	4.7	0.3	35.8	—	—	—	—	+
2	BLOX J0049.7−5221	00:49:45.8	−52:21:26	6.3	0.2	23.9	—	—	—	—	∘
3	BLOX J0050.6−5204	00:50:36.6	−52:04:15	3.5	0.5	93.9	—	—	—	—	∘
4	BLOX J0050.8−5213	00:50:53.9	−52:13:05	5.5	0.2	21.9	2	—	—	—	+
5	BLOX J0051.3−5206	00:51:19.3	−52:06:36	3.9	0.5	102.9	—	1	—	—	+
6	BLOX J0051.4−5153	00:51:25.4	−51:53:23	8.2	0.3	62.7	—	—	—	—	+
			CFRS-3h								
7	BLOX J0301.7+0001	03:01:46.8	+00:01:51	4.8	0.2	15.1	—	2	—	—	−
8	BLOX J0302.0−0005	03:02:02.0	−00:05:45	4.7	0.2	15.0	—	—	0.209	1	+
9	BLOX J0302.0−0000	03:02:07.1	−00:00:24	4.8	0.4	48.5	3	—	—	—	+
10	BLOX J0302.2+0010	03:02:14.2	+00:10:34	3.6	0.9	424.4	—	—	—	—	∘
11	BLOX J0303.1−0000	03:03:07.1	−00:00:54	6.2	0.2	19.6	—	—	—	—	∘
12	BLOX J0303.3+0012	03:03:18.3	+00:12:49	3.6	0.5	65.9	—	3	—	—	+

Continued on next page

Table D.2 – *continued from previous page*

Seq. Nr.	Cluster	α (J2000.0)	δ (J2000.0)	σ_{max}	z_{est}	Λ_{cl}	X-ray	M_{ap}	z_{lit}	Notes	Grade
			RX J0505.3−2849								
13	BLOX J0504.6−2902	05:04:41.7	−29:02:22	4.6	0.2	25.4	—	—	—	—	+
14	BLOX J0505.3−2849	05:05:20.3	−28:49:10	6.5	0.4	85.0	9	4	0.509	2	+
15	BLOX J0505.7−2832	05:05:44.7	−28:32:28	3.8	0.3	32.6	—	—	—	—	○
16	BLOX J0506.0−2839	05:06:04.1	−28:39:49	6.8	0.1	17.3	—	—	0.136	3	+
			RBS 0864								
17	BLOX J1022.9+0412	10:22:54.9	+04:11:57	3.6	0.3	24.5	—	—	—	4	+
18	BLOX J1023.6+0411	10:23:39.0	+04:11:13	12.4	0.3	111.0	13	6	0.291	4,5	+
19	BLOX J1023.9+0424	10:23:54.9	+04:24:22	7.8	0.1	14.7	—	—	—	—	+
20	BLOX J1024.0+0402	10:24:00.0	+04:02:17	4.2	0.4	60.0	14	—	—	—	+
			QSO B1030−403								
21	BLOX J0132.9−4016	01:32:59.3	−40:16:01	3.5	0.5	88.0	—	—	—	—	−
22	BLOX J0133.7−4010	01:33:45.0	−40:10:39	8.8	0.2	23.1	—	—	—	—	○
23	BLOX J0133.8−4015	01:33:51.6	−40:15:53	4.3	0.3	34.4	—	7	—	—	+
			BR 1033−403								
24	BLOX J1035.3−0336	10:35:22.5	−03:36:45	4.4	0.5	100.7	—	—	—	—	○
25	BLOX J1035.8−0357	10:35:49.9	−03:57:18	6.6	0.3	42.9	—	—	—	—	+
26	BLOX J1035.9−0331	10:35:50.9	−03:31:39	4.3	0.4	52.7	17	8	—	—	+
27	BLOX J1036.2−0352	10:36:17.9	−03:52:12	4.0	0.3	26.1	—	—	—	—	○
28	BLOX J1037.1−0356	10:37:09.3	−03:56:11	4.2	0.3	27.6	—	—	—	—	○
29	BLOX J1037.1−0353	10:37:11.3	−03:53:11	6.2	0.2	18.9	—	—	—	—	+
			SDSS J104433.04−012502.2								
30	BLOX J1044.7−0120	10:44:43.3	−01:20:05	3.7	0.7	201.4	19	—	—	—	+
31	BLOX J1044.7−0120	10:44:44.8	−01:20:57	3.8	0.6	125.0	—	—	—	—	+

Table D.2 – *continued from previous page*

Seq. Nr.	Cluster	α (J2000.0)	δ (J2000.0)	σ_{max}	z_{est}	Λ_{cl}	X-ray	M_{ap}	z_{lit}	Notes	Grade
32	BLOX J1044.7−0137	10:44:44.8	−01:37:38	6.5	0.3	37.6	—	—	—	—	+
33	BLOX J1044.7−0112	10:44:46.8	−01:12:29	4.4	0.3	25.6	—	—	—	—	+
34	BLOX J1044.8−0137	10:44:49.8	−01:37:38	5.2	0.4	51.3	—	—	—	—	○
35	BLOX J1045.2−0108	10:45:15.2	−01:08:59	3.8	0.3	21.7	—	—	—	—	—
36	BLOX J1045.5−0129	10:45:22.7	−01:29:03	3.7	0.6	119.5	—	11	—	—	—
37	BLOX J1045.6−0121	10:45:35.2	−01:21:19	8.6	0.2	30.4	—	—	—	—	○
	MS 1054.3−0321										
38	BLOX J1056.0−0347	10:56:03.5	−03:47:21	3.7	0.3	28.7	—	—	—	—	○
39	BLOX J1056.4−0335	10:56:25.0	−03:35:16	3.7	0.6	125.5	21	12	—	—	+
40	BLOX J1056.9−0337	10:56:59.9	−03:37:23	3.7	0.6	122.9	22	13	0.823	6	+
41	BLOX J1057.2−0340	10:57:16.9	−03:40:37	3.7	0.5	75.0	—	—	—	—	+
42	BLOX J1057.3−0325	10:57:18.4	−03:25:40	5.5	0.2	24.2	—	—	—	—	○
43	BLOX J1057.5−0321	10:57:32.9	−03:21:19	4.4	0.3	33.7	—	—	—	—	+
	HE 1104−1805										
44	BLOX J1106.0−1823	11:06:05.0	−18:23:30	4.2	0.3	31.8	—	—	—	—	—
45	BLOX J1106.2−1824	11:06:12.9	−18:24:59	6.9	0.2	27.2	—	—	—	—	○
46	BLOX J1106.5−1805	11:06:32.8	−18:05:41	3.9	0.2	15.5	—	—	—	—	○
47	BLOX J1106.8−1828	11:06:48.1	−18:28:14	4.0	0.4	52.9	—	14	—	—	+
48	BLOX J1106.9−1809	11:06:57.5	−18:09:10	3.9	0.4	52.3	—	14	—	—	—
49	BLOX J1107.0−1805	11:07:02.2	−18:05:41	7.3	0.2	28.7	—	—	—	—	—
50	BLOX J1107.1−1832	11:07:07.0	−18:32:57	3.8	0.4	51.4	—	—	—	—	—
51	BLOX J1107.3−1813	11:07:20.6	−18:13:39	5.5	0.1	7.6	—	—	—	—	○
	PG 1115+080										
52	BLOX J1117.3+0759	11:17:19.8	+07:59:01	3.5	0.4	42.2	—	—	—	—	+

Table D.2 – *continued from previous page*

Seq. Nr.	Cluster	α (J2000.0)	δ (J2000.0)	σ_{max}	z_{est}	Λ_{cl}	X-ray	M_{ap}	z_{lit}	Notes	Grade
53	BLOX J1117.4+0743	11:17:25.4	+07:43:34	13.3	0.3	90.2	—	—	0.477	7	+
54	BLOX J1117.9+0744	11:17:58.6	+07:44:04	5.7	0.4	68.4	—	—	—	—	○
55	BLOX J1118.3+0743	11:18:23.7	+07:43:20	3.8	0.5	86.5	—	—	—	—	○
			CD −33 07795								
56	BLOX J1130.8−3436	11:30:51.6	−34:36:26	4.9	0.3	40.8	—	—	—	—	○
57	BLOX J1131.5−3440	11:31:35.8	−34:40:56	4.2	0.4	62.0	—	—	—	—	−
58	BLOX J1132.1−3422	11:32:09.0	−34:22:29	5.1	0.1	8.8	—	—	—	—	−
59	BLOX J1132.5−3443	11:32:31.5	−34:43:32	3.8	0.5	97.6	33	16	—	—	+
60	BLOX J1132.8−3421	11:32:51.9	−34:21:36	8.2	0.2	36.1	—	—	—	—	○
			T LEO								
61	BLOX J1138.0+0315	11:37:59.6	+03:16:02	4.1	0.4	56.1	34	—	—	—	+
62	BLOX J1138.4+0320	11:38:26.0	+03:20:24	6.7	0.4	92.7	—	—	—	—	+
			IRAS 12112+0305								
63	BLOX J1212.8+0301	12:12:53.2	+03:01:17	5.7	0.2	20.7	—	—	—	—	−
64	BLOX J1212.9+0302	12:12:58.7	+03:02:47	4.4	0.4	51.5	—	—	—	—	○
65	BLOX J1213.5+0253	12:13:34.1	+02:53:49	8.0	0.3	52.2	37	17	0.409	8	+
66	BLOX J1214.0+0237	12:14:03.6	+02:37:08	4.1	0.3	27.0	—	—	0.34	9	+
67	BLOX J1214.6+0240	12:14:40.5	+02:40:22	3.7	0.2	13.5	—	—	—	—	○
			LBQS 1228+1116								
68	BLOX J1230.2+1116	12:30:15.9	+11:16:37	8.0	0.4	114.5	—	—	—	—	○
69	BLOX J1230.6+1113	12:30:38.7	+11:13:23	3.7	0.2	21.3	—	—	—	—	○
70	BLOX J1230.8+1058	12:30:51.9	+10:58:41	3.7	0.4	52.3	—	18	—	—	○
71	BLOX J1231.3+1114	12:31:21.9	+11:14:23	3.6	0.6	127.6	—	—	—	—	○
72	BLOX J1231.3+1112	12:31:22.9	+11:12:31	3.6	0.5	79.8	—	—	—	—	−

Table D.2 – *continued from previous page*

Seq. Nr.	Cluster	α (J2000.0)	δ (J2000.0)	σ_{max}	z_{est}	Λ_{cl}	X-ray	M_{ap}	z_{lit}	Notes	Grade
73	BLOX J1231.7+1112	12:31:43.2	+11:12:08	5.1	0.3	46.8	—	—	—	—	+
			NGC 4666								
74	BLOX J1244.0−0037	12:44:04.1	−00:37:03	4.2	0.5	78.9	—	—	—	—	—
75	BLOX J1244.7−0035	12:44:48.0	−00:35:18	7.2	0.2	29.4	—	—	—	—	○
76	BLOX J1245.8−0039	12:45:48.3	−00:39:54	3.6	0.5	67.1	—	—	—	—	○
			QSO B1246−057								
77	BLOX J1249.2−0607	12:49:15.9	−06:07:20	4.1	0.2	16.9	—	—	—	—	—
78	BLOX J1249.3−0611	12:49:22.9	−06:11:20	4.3	0.9	499.0	—	—	—	—	○
79	BLOX J1249.3−0600	12:49:23.9	−06:00:07	3.7	0.9	425.8	—	—	—	—	—
80	BLOX J1249.4−0600	12:49:27.4	−06:00:07	4.4	0.3	31.4	44	—	—	—	+
81	BLOX J1249.9−0551	12:49:55.0	−05:51:39	5.1	0.2	21.3	—	—	—	—	—
82	BLOX J1250.1−0555	12:50:11.5	−05:55:00	4.0	0.3	28.1	—	—	—	—	○
			FIELD 864-1								
83	BLOX J1341.4+0023	13:41:27.6	+00:23:52	6.1	0.2	22.3	—	—	—	—	—
84	BLOX J1341.6+0018	13:41:40.0	+00:18:01	6.1	0.3	51.4	45, 46	—	0.390	10	+
			FIELD 864-9								
85	BLOX J1343.6−0011	13:43:38.6	−00:11:10	4.0	0.9	509.0	—	—	—	—	—
86	BLOX J1343.7−0030	13:43:44.5	−00:30:44	4.5	0.3	34.4	—	—	—	11	+
87	BLOX J1343.9−0011	13:43:59.5	−00:11:25	4.3	0.3	33.3	—	—	—	—	○
88	BLOX J1344.2−0010	13:44:17.4	−00:10:18	5.8	0.2	27.1	—	22	0.390	12	+
89	BLOX J1344.9−0020	13:44:54.8	−00:20:53	4.2	0.5	94.6	—	23	—	—	○
90	BLOX J1344.9−0038	13:44:55.3	−00:38:50	4.3	0.5	96.0	—	—	—	—	○
91	BLOX J1345.4−0026	13:45:26.7	−00:26:52	6.0	0.3	46.2	—	—	0.3	13	+

Table D.2 – *continued from previous page*

Seq. Nr.	Cluster	α (J2000.0)	δ (J2000.0)	σ_{max}	z_{est}	Λ_{cl}	X-ray	M_{ap}	z_{lit}	Notes	Grade
			A 1882								
92	BLOX J1414.1−0016	14:14:08.8	−00:16:32	4.7	0.2	55.8	—	—	0.152	14	+
93	BLOX J1414.9−0021	14:14:56.6	−00:21:38	4.5	0.1	31.2	—	25,26	0.137	15	+
			MKW 9								
94	BLOX J1532.0+0449	15:32:00.2	+04:49:57	5.6	0.4	69.0	—	—	—	—	+
95	BLOX J1532.4+0444	15:32:24.7	+04:44:14	5.6	0.2	28.5	—	—	—	16	+
96	BLOX J1532.5+0447	15:32:31.2	+04:47:50	3.6	0.9	319.8	—	—	—	—	−
97	BLOX J1532.7+0444	15:32:47.7	+04:44:06	4.8	0.5	94.5	—	—	—	16	○
98	BLOX J1532.9+0440	15:32:56.7	+04:40:44	4.7	0.1	9.1	—	—	—	16	+
99	BLOX J1533.0+0432	15:33:03.7	+04:32:16	3.7	0.5	72.7	—	—	—	—	−
100	BLOX J1533.2+0438	15:33:16.7	+04:38:30	3.8	0.6	125.7	—	—	—	—	−
			LBQS 2212−1759								
101	BLOX J2214.4−1728	22:14:24.9	−17:28:07	4.4	0.2	15.2	—	—	—	—	○
102	BLOX J2215.0−1750	22:14:59.3	−17:50:26	5.5	0.3	29.5	54	—	—	—	+
103	BLOX J2215.6−1745	22:15:36.5	−17:45:42	7.9	0.3	42.1	57	—	—	—	+
			NGC 7252								
104	BLOX J2220.2−2426	22:20:13.5	−24:26:23	6.7	0.2	25.0	—	—	—	—	+
105	BLOX J2220.5−2450	22:20:33.7	−24:50:18	5.0	0.2	18.6	—	28	—	—	−
106	BLOX J2221.3−2445	22:21:21.4	−24:45:26	4.3	0.3	26.6	—	—	—	—	−
107	BLOX J2221.4−2425	22:21:27.4	−24:25:38	3.5	0.4	32.9	—	—	—	—	○
108	BLOX J2221.6−2441	22:21:37.9	−24:41:42	4.0	0.3	24.3	—	—	—	—	○
			PHL 5200								
109	BLOX J2227.4−0530	22:27:26.9	−05:30:48	6.0	0.3	38.6	—	—	—	—	○
110	BLOX J2227.5−0506	22:27:31.9	−05:06:53	6.4	0.3	42.6	—	—	—	—	○

Table D.2 – continued from previous page

Seq. Nr.	Cluster	α (J2000.0)	δ (J2000.0)	σ_{max}	z_{est}	Λ_{cl}	X-ray	M_{ap}	z_{lit}	Notes	Grade
111	BLOX J2227.8−0517	22:27:52.9	−05:17:14	5.5	0.3	37.1	—	—	—	—	−
112	BLOX J2228.2−0524	22:28:13.9	−05:24:57	4.2	0.8	334.2	—	—	—	—	−
113	BLOX J2228.2−0508	22:28:17.9	−05:08:16	3.9	0.3	26.0	65	—	—	—	○
114	BLOX J2228.3−0520	22:28:21.9	−05:20:28	6.7	0.3	44.7	66	—	—	—	+
115	BLOX J2228.5−0503	22:28:33.4	−05:03:47	4.0	0.7	216.7	—	—	—	—	○
116	BLOX J2229.4−0531	22:29:27.0	−05:31:56	4.3	0.3	28.6	—	—	—	—	○

Notes on table: [1]Cluster 8 is SDSS CE J045.509975−00.099065 of Goto et al. (2002), [2]This is RX J0505.3−2849 of Burke et al. (2003), [3]Cluster 16 is RX J0505.9−2841 of Vikhlinin et al. (1998) with spectroscopic redshift from Mullis et al. (2003), [4]Properties derived from the matched filter are averages of the independent detections in RBS 0864-N and RBS 0864-S, [5]This cluster is RBS 0864 of Allen et al. (1992), [6]This is MS 1054.3−0321 (Gioia & Luppino 1994; Gioia et al. 1990; Gioia & Luppino 1994), [7]This is RX J1117.4+0743 of Vikhlinin et al. (1998) with spectroscopic redshift from Mullis et al. (2003), [8]This is the cluster RX J1213.5+0253 of Vikhlinin et al. (1998) with spectroscopic redshift from Mullis et al. (2003), [9]This is NCSC J121407+023642 of Lopes et al. (2004) with a photometric redshift estimate, [10]This cluster is SDSS CE J205.412231+00.303271 of Goto et al. (2002), [11]This is J1836.14RC of Lidman & Peterson (1996), [12]This is SDSS CE J206.064102−00.169585 of Goto et al. (2002), [13]This is BPG2004 J206.363−00.438 of Basilakos et al. (2004), [14]This cluster is SDSS CE J213.533593−00.276487 of Goto et al. (2002), [15]This cluster is part of the A 1882 complex, [16]Probably part of MKW 9 at z=0.040,

D.3 Weak Lensing Cluster Catalog

The following table lists cluster candidates detected in the xfs using the aperture mass method. Column 1 gives a sequential number to the galaxy cluster candidates, their name blox name xfs is given in Col. 2. Due to the large positional uncertainty the blox name is not derived from the weak lensing position but rather from the X-ray of matched filter position when available. The position of the aperture mass peak in right ascension and declination is listed in Col. 3 and 4, respectively. The maximum detection significance over all filter scales is given Col. 5. The filter scale in which the detection snr was maximized is given in Col. 6. Column 7 gives the number of filter scales in which a peak was detected. The next two columns provide cross-references to the sequence numbers of Table D.1 (X-ray detected clusters) and Table D.2 (matched filter detected clusters). The last column provides references to additional notes at the end of the table.

Table D.3: The table lists cluster candidates detected in the XFS using the aperture mass method. Column 1 gives a sequential number to the galaxy cluster candidates, their name in the XFS is given in Col. 2. The position of the aperture mass peak in right ascension and declination is listed in Col. 3 and 4, respectively. Note that the name in Col. 2 is based on the X-ray or matched filter position, if available. The maximum detection significance over all filter scales is given Col. 5. The filter scale in which the detection SNR was maximized is given in Col. 6. Column 7 gives the number of filter scales in which a peak was detected. The next two columns provide cross-references to the sequence numbers of Table D.1 (X-ray detected clusters) and Table D.2 (matched filter detected clusters). The last column provides references to additional notes at the end of the table.

Seq. Nr.	Cluster	α (J2000.0)	δ (J2000.0)	σ_{max}	$r/(h_{70}^{-1}$ kpc)	n_f	X-ray	MF	Notes
			BPM 16274						
1	BLOX J0051.3−5153	00:51:24.1	−52:05:48	3.2	1000	8	—	5	—
			CFRS-3h						
2	BLOX J0301.7+0001	03:01:50.1	+00:00:10	3.1	1247	4	—	7	1
3	BLOX J0303.2+0012	03:03:26.6	+00:13:04	3.4	1247	6	—	12	—
			RX J0505.3−2849						
4	BLOX J0505.3−2849	05:05:18.5	−28:49:32	4.2	2726	9	9	14	2
5	BLOX J0506.2−2843	05:06:15.6	−28:43:55	3.1	1247	6	12	—	—
			RBS 0864						
6	BLOX J1023.6+0411	10:23:38.3	+04:11:16	6.2	2479	9	13	18	3,4
			QSO B1030−403						
7	BLOX J0133.8−4015	01:33:51.3	−40:15:40	3.4	1493	9	—	23	—
			BR 1033−403						
8	BLOX J1035.9−0331	10:35:55.8	−03:31:10	3.7	1000	3	17	26	—

Table D.3 – *continued from previous page*

Seq. Nr.	Cluster	α (J2000.0)	δ (J2000.0)	σ_{max}	r	n_f	X-ray	MF	Notes
			SDSS J104433.04−012502.2						
9	BLOX J1044.9−0131	10:44:51.9	−01:32:51	3.3	1493	5	20	—	5
10	BLOX J1044.8−0132	10:44:51.9	−01:32:51	3.3	1493	5	20	—	5
11	BLOX J1045.5−0129	10:45:17.3	−01:27:26	3.5	1493	8	—	36	—
			MS 1054.3−0321						
12	BLOX J1056.4−0335	10:56:29.6	−03:34:46	3.3	1247	4	21	8	—
13	BLOX J1056.9−0337	10:56:55.0	−03:38:08	4.3	2972	10	22	40	6
			HE 1104−1805						
14	BLOX J1106.9−1807	11:06:58.10	−18:07:39	3.6	1000	4	—	48,49	7
			PG 1115+080						
15	BLOX J1118.2+0742	11:18:11.2	+07:42:53	3.6	1247	4	27	—	8
			CD −33 07795						
16	BLOX J1132.5−3443	11:32:32.7	−34:43:49	3.8	1986	9	33	59	—
			IRAS 12112+0305						
17	BLOX J1213.5+0253	12:13:34.6	+02:54:13	4.7	2972	10	37	65	9
			LBQS 1228+1116						
18	BLOX J1230.8+1058	12:30:51.10	+11:00:01	4.0	1000	9	—	70	—
			NGC 4666						
19	BLOX J1244.8−0033	12:44:52.9	−00:32:53	3.2	1000	8	39,41	—	—
			QSO B1246−057						
20	BLOX J1249.4−0600	12:49:36.5	−06:00:41	3.8	1247	4	44	—	10
			FIELD 864−9						
21	BLOX J1343.5−0022	13:43:33.2	−00:22:53	4.8	1000	7	—	—	11

Table D.3 – *continued from previous page*

Seq. Nr.	Cluster	α (J2000.0)	δ (J2000.0)	σ_{max}	r	n_f	X-ray	MF	Notes
22	BLOX J1344.2−0010	13:44:16.6	−00:08:52	3.7	1000	6	—	88	12
23	BLOX J1344.9−0038	13:44:50.2	−00:20:50	3.8	1740	6	—	89	—
			A 1882						
24	BLOX J1414.1−0016	14:14:02.8	−00:14:56	4.0	1000	7	48	—	13,14
25	BLOX J1414.9−0021	14:14:52.2	−00:19:48	3.2	2479	7	—	93	15
26	BLOX J1414.9−0021	14:14:59.6	−00:21:51	5.0	1247	9	—	93	15
			MKW 9						
27	BLOX J1531.7+0442	15:31:46.3	+04:42:54	4.0	1247	8	51	—	—
			NGC 7252						
28	BLOX J2220.5−2450	22:20:33.7	−24:49:39	4.1	1493	9	—	105	—

Notes on table: [1] 2′.0 from SDSS CE J045.290550−00.086673 at $z = 0.333$ of Goto et al. (2002), [2] This is RX J0505.3−2849 at $z = 0.509$ of Burke et al. (2003), [3] This cluster is RBS 0864 of Allen et al. (1992), [4] We list the properties derived from the RBS 0864-N pointing, [5] Probably chance alignment with a low quality X-ray cluster candidate, [6] This is MS 1054.3−0321 at $z = 0.823$ (Gioia et al. 1990; Gioia & Luppino 1994), [7] BLOX name derived from lensing position due to uncertain association, [8] X-ray cluster 27 is probably matched filter cluster 55, which is 3′.2 from the lensing peak, [9] This is the cluster RX J1213.5+0253 at $z = 0.409$ of Vikhlinin et al. (1998); Mullis et al. (2003), [10] X-ray cluster 44 is associated with matched filter cluster 80, which is 2′.3 from the M_{ap} peak, [11] This is LP96 Cl 1341−0006 of Lidman & Peterson (1996), [12] This is SDSS CE J206.064102−00.169585 at $z = 0.390$ of Goto et al. (2002), [13] Matched filter cluster 92 is associated with X-ray cluster 48 but 2′.18 from the M_{ap} peak position, [14] This cluster is SDSS CE J213.532593−00.276487 at $z = 0.152$ of Goto et al. (2002), [15] This cluster is part of the A 1882 complex at $z = 0.137$,

Bibliography

Abazajian, K., Adelman-McCarthy, J. K., Agüeros, M. A. et al. 2003, AJ, 126, 2081

Abell, G. O. 1958, ApJS, 3, 211

Allen, S. W., Edge, A. C., Fabian, A. C. et al. 1992, MNRAS, 259, 67

Arnouts, S., Vandame, B., Benoist, C. et al. 2001, A&A, 379, 740

Bacon, D. J., Refregier, A. R., & Ellis, R. S. 2000, MNRAS, 318, 625

Barcons, X., Carrera, F. J., Watson, M. G. et al. 2002, A&A, 382, 522

Barkhouse, W. A. & Hall, P. B. 2001, AJ, 121, 2843

Bartelmann, M. 1996, A&A, 313, 697

Bartelmann, M. & Schneider, P. 2001, Physics Report, 340, 291

Basilakos, S., Plionis, M., Georgakakis, A. et al. 2004, MNRAS, 351, 989

Baugh, C. M., Croton, D. J., Gaztañaga, E. et al. 2004, MNRAS, 351, L44

Benoist, C., da Costa, L., Jørgensen, H. E. et al. 2002, A&A, 394, 1

Bertin, E. 2005, SExtractor User Manual

Bertin, E. & Arnouts, S. 1996, A&AS, 117, 393

Bertin, E., Mellier, Y., Radovich, M. et al. 2002, in ASP Conf. Ser. 281: Astronomical Data Analysis Software and Systems XI, ed. D. A. Bohlender, D. Durand, & T. H. Handley, 228

Bertschinger, E. & Gelb, J. M. 1991, Computers in Physics, 5, 164

Bijaoui, A. & Rué, F. 1995, Signal Processing, 46, 345

Bond, H., Kofman, L., & Pogosyan, D. 1996, Nature, 380, 603

Bouy, H., Martín, E. L., Brandner, W. et al. 2006, A&A, 451, 177

Bruzual, A., G. & Charlot, S. 1993, ApJ, 405, 538

Burke, D. J., Collins, C. A., Sharples, R. M., Romer, A. K., & Nichol, R. C. 2003, MNRAS, 341, 1093

Butcher, H., Wells, D. C., & Oemler, A. 1983, ApJS, 52, 183

Carroll, S. M., Press, W. H., & Turner, E. L. 1992, ARA&A, 30, 499

Clowe, D., Luppino, G. A., Kaiser, N., Henry, J. P., & Gioia, I. M. 1998, ApJ, 497, L61

Clowe, D. & Schneider, P. 2001, A&A, 379, 384

Colless, M., Dalton, G., Maddox, S. et al. 2001, MNRAS, 328, 1039

Croft, R. A. C., Weinberg, D. H., Katz, N., & Hernquist, L. 1998, ApJ, 495, 44

David, L. P., Forman, W., & Jones, C. 1999, ApJ, 519, 533

Davis, M., Efstathiou, G., Frenk, C. S., & White, S. D. M. 1985, ApJ, 292, 371

de Lapparent, V., Geller, M. J., & Huchra, J. P. 1986, ApJ, 302, L1

Della Ceca, R., Maccacaro, T., Caccianiga, A. et al. 2004, A&A, 428, 383

Devillard, N. 2001, in ASP Conf. Ser. 238: Astronomical Data Analysis Software and Systems X, ed. F. R. Harnden, F. A. Primini, & H. E. Payne, 525

Dietrich, J. P. 2002, Diplomarbeit, Universität Bonn, Germany

Dietrich, J. P., Clowe, D. I., & Soucail, G. 2002, A&A, 394, 395 (D02)

Dietrich, J. P., Miralles, J.-M., Olsen, L. F. et al. 2006, A&A, 449, 837

Dietrich, J. P., Schneider, P., Clowe, D., Romano-Díaz, E., & Kerp, J. 2005, A&A, 440, 453

Doroshkevich, A., Tucker, D. L., Allam, S., & Way, M. J. 2004, A&A, 418, 7

Dyson, F., Eddington, A., & Davidson, C. 1920, Mem. R. Astron. Soc., 62, 291

Eckart, M. E., Laird, E. S., Stern, D. et al. 2005, ApJS, 156, 35

Ehle, M., Breitfellner, M., González Riestra, R. et al. 2004, XMM-Newton Users' Handbook

Eisenstein, D. J. & Hu, W. 1998, ApJ, 496, 605

Eke, V. R., Cole, S., & Frenk, C. S. 1996, MNRAS, 282, 263

Epchtein, N., de Batz, B., Capoani, L. et al. 1997, The Messenger, 87, 27

Erben, T., Miralles, J. M., Clowe, D. et al. 2003, A&A, 410, 45

Erben, T., Schirmer, M., Dietrich, J. P. et al. 2005, Astronomische Nachrichten, 326, 432 (ESD)

Erben, T., Van Waerbeke, L., Bertin, E., Mellier, Y., & Schneider, P. 2001, A&A, 366, 717

Erben, T., van Waerbeke, L., Mellier, Y. et al. 2000, A&A, 355, 23

Fontana, A., D'Odorico, S., Fosbury, R. et al. 1999, A&A, 343, L19

Freedman, W. L., Madore, B. F., Gibson, B. K. et al. 2001, ApJ, 553, 47

Gal, R. R. 2006, astro-ph/0601195

Gavazzi, R., Mellier, Y., Fort, B., Cuillandre, J.-C., & Dantel-Fort, M. 2004, A&A, 422, 407

Geller, M. J. & Huchra, J. P. 1989, Science, 246, 897

Gioia, I. M. & Luppino, G. A. 1994, ApJS, 94, 583

Gioia, I. M., Maccacaro, T., Schild, R. E. et al. 1990, ApJS, 72, 567

Giovanelli, R., Myers, S. T., Roth, J., & Haynes, M. P. 1986, AJ, 92, 250

Girardi, L., Bertelli, G., Bressan, A. et al. 2002, A&A, 391, 195

Girardi, L., Groenewegen, M. A. T., Hatziminaoglou, E., & da Costa, L. 2005, A&A, 436, 895

Gladders, M. D. & Yee, H. K. C. 2000, AJ, 120, 2148

Gnedin, N. Y. & Hamilton, A. J. S. 2002, MNRAS, 334, 107

Goto, T., Sekiguchi, M., Nichol, R. C. et al. 2002, AJ, 123, 1807

Gray, M. E., Taylor, A. N., Meisenheimer, K. et al. 2002, ApJ, 568, 141 (G02)

Gray, M. E., Wolf, C., Meisenheimer, K. et al. 2004, MNRAS, 347, L73

Grupe, D., Mathur, S., & Elvis, M. 2003, AJ, 126, 1159

Haberl, F., Motch, C., Buckley, D. A. H., Zickgraf, F.-J., & Pietsch, W. 1997, A&A, 326, 662

Hamana, T., Takada, M., & Yoshida, N. 2004, MNRAS, 350, 893 (H04)

Hamilton, A. J. S., Kumar, P., Lu, E., & Matthews, A. 1991, ApJ, 374, L1

—. 1995, ApJ, 442, L73

Hansen, L., Olsen, L. F., & Jørgensen, H. E. 2002, A&A, 388, 1

Harrison, E. R. 1970, Phys. Rev. D, 1, 2726

Hartlap, J. 2005, Diplomarbeit, Universität Bonn, Germany

Hennawi, J. F. & Spergel, D. N. 2005, ApJ, 624, 59 (HS05)

Hetterscheidt, M., Erben, T., Schneider, P. et al. 2005, A&A, 442, 43

Hildebrandt, H., Erben, T., Dietrich, J. P. et al. 2006, A&A accepted, also astro-ph/0509882

Hoekstra, H., Mellier, Y., van Waerbeke, L. et al. 2005, astro-ph/0511089

Jain, B., Seljak, U., & White, S. 2000, ApJ, 530, 547

Jenkins, A., Frenk, C. S., Pearce, F. R. et al. 1998, ApJ, 499, 20

Jenkins, A., Frenk, C. S., White, S. D. M. et al. 2001, MNRAS, 321, 372

Joeveer, M., Einasto, J., & Tago, E. 1978, MNRAS, 185, 357

Kaastra, J. S., Werner, N., den Herder, J. W. A. et al. 2006, astro-ph/0604519

Kaiser, N. 1995, ApJ, 439, L1

Kaiser, N. & Squires, G. 1993, ApJ, 404, 441 (KS93)

Kaiser, N., Squires, G., & Broadhurst, T. 1995, ApJ, 449 (KSB), 460

Kaiser, N., Wilson, G., Luppino, G. et al. 1998, astro-ph/9809268

Kauffmann, G., Colberg, J. M., Diaferio, A., & White, S. D. M. 1999, MNRAS, 303, 188

King, L. J., Clowe, D. I., & Schneider, P. 2002, A&A, 383, 118

Klypin, A. A. & Shandarin, S. F. 1983, MNRAS, 204, 891

Koch, A., Odenkirchen, M., Grebel, E. K., & Caldwell, J. A. R. 2004, Astronomische Nachrichten, 325, 299

Landolt, A. U. 1992, AJ, 104, 340

Lidman, C. E. & Peterson, B. A. 1996, AJ, 112, 2454

Loiseau, N. 2005, User's Guide to the XMM-Newton Science Analysis System

Lopes, P. A. A., de Carvalho, R. R., Gal, R. R. et al. 2004, AJ, 128, 1017

Möller, P. & Fynbo, J. U. 2001, A&A, 372, L57

Manfroid, J. & Selman, F. 2001, The Messenger, 104, 16

Maoli, R., Van Waerbeke, L., Mellier, Y. et al. 2001, A&A, 368, 766

Maturi, M., Meneghetti, M., Bartelmann, M., Dolag, K., & Moscardini, L. 2005, A&A, 442, 851

McDowell, J. & Rots, A. 1998, FITS REGION Binary Table Design, Technical Report ASC-FITS-REGION-1.0, Chandra Science Center

Metcalfe, N., Shanks, T., Campos, A., McCracken, H. J., & Fong, R. 2001, MNRAS, 323, 795

Miller, C. J., Nichol, R. C., Reichart, D. et al. 2005, AJ, 130, 968

Miralles, J.-M., Erben, T., Hämmerle, H. et al. 2002, A&A, 388, 68

Monet, D., Bird A., Canzian, B. et al. 1998, The USNO-A2.0 Catalogue (U.S. Naval Observatory, Washington DC)

Motch, C., Hasinger, G., & Pietsch, W. 1994, A&A, 284, 827

Mullis, C. R., McNamara, B. R., Quintana, H. et al. 2003, ApJ, 594, 154

Mullis, C. R., Rosati, P., Lamer, G. et al. 2005, ApJ, 623, L85

Navarro, J. F., Frenk, C. S., & White, S. D. M. 1997, ApJ, 490, 493 (NFW)

Nicastro, F., Mathur, S., Elvis, M. et al. 2005, ApJ, 629, 700

Nonino, M., Bertin, E., da Costa, L. et al. 1999, A&AS, 137, 51

Olsen, L. F., Hansen, L., Jørgensen, H. E. et al. 2003, A&A, 409, 439

Olsen, L. F., Scodeggio, M., da Costa, L. et al. 1999, A&A, 345, 681 (O99)

Peacock, J. A. 1999, Cosmological physics (Cambridge University Press)

Peacock, J. A. & Dodds, S. J. 1996, MNRAS, 280, L19

Peebles, P. J. E. 1980, The large-scale structure of the universe (Princeton University Press)

—. 1993, Principles of physical cosmology (Princeton Series in Physics, Princeton, NJ: Princeton University Press)

Perlmutter, S., Aldering, G., Goldhaber, G. et al. 1999, ApJ, 517, 565

Pimbblet, K. A. 2005, Publications of the Astronomical Society of Australia, 22, 136

Pogosyan, D., Bond, J. R., Kofman, L., & Wadsley, J. 1998, in Wide Field Surveys in Cosmology, 14th IAP meeting held May 26-30, 1998, Paris. Publisher: Editions Frontieres, 61

Postman, M., Lubin, L. M., Gunn, J. E. et al. 1996, AJ, 111, 615 (P96)

Press, W. H. & Schechter, P. 1974, ApJ, 187, 425

Press, W. H., Teukolsky, S. A., Vetterling, W. T., & Flannery, B. P. 1992, Numerical recipes in C. The art of scientific computing (Cambridge: University Press, 2nd ed.)

Proust, D., Cuevas, H., Capelato, H. V. et al. 2000, A&A, 355, 443

Rasmussen, A. P., Kahn, S. M., Paerels, F. et al. 2006, astro-ph/0604515

Riess, A. G., Filippenko, A. V., Challis, P. et al. 1998, AJ, 116, 1009

Rué, F. & Bijaoui, A. 1997, Experimental Astronomy, 7, 129

Schechter, P. 1976, ApJ, 203, 297

Schirmer, M. 2004, PhD thesis, Universität Bonn, Germany

Schlegel, D. J., Finkbeiner, D. P., & Davis, M. 1998, ApJ, 500, 525

Schneider, P. 1996, MNRAS, 283, 837

Schneider, P. 2006, in Saas Fee Advanced Course 33: Gravitational Lensing: Strong, Weak and Micro, ed. P. Schneider, C. Kochanek, & J. Wambsganss

Schneider, P. & Bartelmann, M. 1997, MNRAS, 286, 696

Schneider, P., King, L., & Erben, T. 2000, A&A, 353, 41

Schneider, P., van Waerbeke, L., Jain, B., & Kruse, G. 1998, MNRAS, 296, 873

Seitz, C. & Schneider, P. 1997, A&A, 318, 687

Seitz, S. & Schneider, P. 1996, A&A, 305, 383

—. 2001, A&A, 374, 740

Semboloni, E., Mellier, Y., van Waerbeke, L. et al. 2005, astro-ph/0511090

Shectman, S. A., Landy, S. D., Oemler, A. et al. 1996, ApJ, 470, 172

Sheth, R. K., Mo, H. J., & Tormen, G. 2001, MNRAS, 323, 1

Sheth, R. K. & Tormen, G. 1999, MNRAS, 308, 119

Smith, R. E., Peacock, J. A., Jenkins, A. et al. 2003, MNRAS, 341, 1311

Soucail, G., Fort, B., Mellier, Y., & Picat, J. P. 1987a, A&A, 172, L14

Soucail, G., Mellier, Y., Fort, B., Mathez, G., & Hammer, F. 1987b, A&A, 184, L7

Spergel, D. N., Verde, L., Peiris, H. V. et al. 2003, ApJS, 148, 175

Stetson, P. B. 1987, PASP, 99, 191

—. 2000, PASP, 112, 925

Stocke, J. T., Morris, S. L., Gioia, I. M. et al. 1991, ApJS, 76, 813

Tittley, E. R. & Henriksen, M. 2001, ApJ, 563, 673

Tully, B. & Shaya, E. 1999, in Evolution of Large Scale Structure : From Recombination to Garching, 296

Umetsu, K. & Futamase, T. 2000, ApJ, 539, L5

van Waerbeke, L. 2000, MNRAS, 313, 524

Van Waerbeke, L., Mellier, Y., Erben, T. et al. 2000, A&A, 358, 30

Van Waerbeke, L., Mellier, Y., & Hoekstra, H. 2005, A&A, 429, 75

Vandame, B. 2004, Traitements d'images a grand-champs et multi-longeurs d'ondes. Application aux relevés "ESO Imaging Survey" (PhD-thesis, Université de Nice)

Vikhlinin, A., McNamara, B. R., Forman, W. et al. 1998, ApJ, 502, 558

Vogeley, M. S., Park, C., Geller, M. J., Huchra, J. P., & Gott, J. R. I. 1994, ApJ, 420, 525

von der Linden, A., Erben, T., Schneider, P., & Castander, F. J. 2005, astro-ph/0501442

Walsh, D., Carswell, R. F., & Weymann, R. J. 1979, Nature, 279, 381

Wang, L. & Steinhardt, P. J. 1998, ApJ, 508, 483

Wang, Q. D. & Ulmer, M. P. 1997, MNRAS, 292, 920

Watson, M. G., Auguères, J.-L., Ballet, J. et al. 2001, A&A, 365, L51

Watson, M. G., Pye, J. P., Denby, M. et al. 2003, Astronomische Nachrichten, 324, 89

Weinberg, N. N. & Kamionkowski, M. 2002, MNRAS, 337, 1269

Wisotzki, L., Koehler, T., Kayser, R., & Reimers, D. 1993, A&A, 278, L15

Wittman, D., Dell'Antonio, I. P., Hughes, J. P. et al. 2005, ArXiv Astrophysics e-prints

Wittman, D., Tyson, J. A., Margoniner, V. E., Cohen, J. G., & Dell'Antonio, I. P. 2001, ApJ, 557, L89

Wittman, D. M., Tyson, J. A., Kirkman, D., Dell'Antonio, I., & Bernstein, G. 2000, Nature, 405, 143

Wright, C. O. & Brainerd, T. G. 2000, ApJ, 534, 34

Wu, X., Xue, Y., & Fang, L. 1999, ApJ, 524, 22

Yuan, W., Brinkmann, W., Siebert, J., & Voges, W. 1998, A&A, 330, 108

Yuan, W., McMahon, R. G., Watson, M. et al. 2003, Astronomische Nachrichten, 324, 178

Zeldovich, Y. B. 1970, A&A, 5, 84

—. 1972, MNRAS, 160, 1P

Zimmermann, U., Boese, G., Becker, G. et al. 1998, EXSAS User's Guide

Zwicky, F. 1937, ApJ, 86, 217

Bibliography

Acknowledgement

No man is an Iland, intire of itselfe.
John Donne (1572–1631)

Peter, Thomas, Axel. Georg, Hendrik, Doug, Jürgen, Jan, Emilio. Tim, Oliver, Martin, Patrick, Tim, Anja. The rest of the lensing group. Olli, Ole, Günther Lay, Kathy. Ania, Ursula. Matthias. Meine Eltern. Monika.